

UNCLASSIFIED

AD NUMBER

ADB014124

LIMITATION CHANGES

TO:

Approved for public release; distribution is unlimited.

FROM:

Distribution authorized to U.S. Gov't. agencies only; Test and Evaluation; MAR 1976. Other requests shall be referred to Air Force Materials Lab., Wright-Patterson AFB, OH 45433.

AUTHORITY

AFWAL ltr 19 Nov 1982

THIS PAGE IS UNCLASSIFIED

THIS REPORT HAS BEEN DELIMITED  
AND CLEARED FOR PUBLIC RELEASE  
UNDER E.O. DIRECTIVE 5200.20 AND  
NO RESTRICTIONS ARE IMPOSED UPON  
ITS USE AND DISCLOSURE.

DISTRIBUTION STATEMENT A

APPROVED FOR PUBLIC RELEASE,  
DISTRIBUTION UNLIMITED.



2

AFML-TR-76-16

28

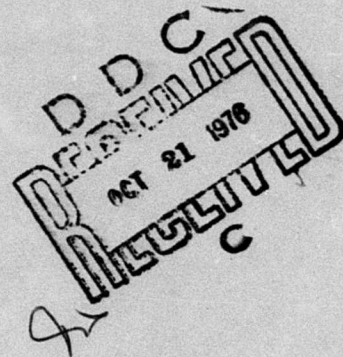
AD B014124

## CHARACTERIZATION OF TRANSPARENT MATERIALS FOR EROSION RESISTANCE

TEXTRON'S BELL AEROSPACE COMPANY

MARCH 1976

TECHNICAL REPORT AFML-TR-76-16  
SUMMARY REPORT FOR PERIOD MAY 1974 - DECEMBER 1975



Distribution limited to U.S. Government Agencies only; (test and evaluation); March 1976. Other requests for this document must be referred to the Air Force Materials Laboratory, Nonmetallic Materials Division, Elastomers and Coatings Branch, AFML/MBE, Wright-Patterson Air Force Base, Ohio 45433.

AIR FORCE MATERIALS LABORATORY  
AIR FORCE WRIGHT AERONAUTICAL LABORATORIES  
AIR FORCE SYSTEMS COMMAND  
WRIGHT-PATTERSON AIR FORCE BASE, OHIO 45433

## NOTICES

When Government drawings, specifications, or other data are used for any purpose other than in connection with a definitely related Government procurement operation, the United States Government thereby incurs no responsibility nor any obligation whatsoever; and the fact that the government may have formulated, furnished, or in any way supplied the said drawings, specifications, or other data, is not to be regarded by implication or otherwise as in any manner licensing the holder or any other person or corporation, or conveying any rights or permission to manufacture, use or sell any patented invention that may in any way be related thereto.

This report covers a period from 1 May 1974 to 31 December 1975.

This technical report has been reviewed and is approved for publication.

*T. L. Peterson*

T. L. PETERSON  
Project Monitor

FOR THE COMMANDER

*M. L. Minges*

M. L. MINGES, CHIEF  
Elastomers and Coatings Branch  
Nonmetallic Materials Division  
Air Force Materials Laboratory

Approved for	Radio Station	<input type="checkbox"/>
WHS	Ball Station	<input type="checkbox"/>
BY	DISTRIBUTION/AVAILABILITY CODES	
JUSTIFICATION	BY	
	DATE	BY

Copies of this report should not be returned unless return is required by security considerations, contractual obligations, or notice on a specific document.



UNCLASSIFIED

SECURITY CLASSIFICATION OF THIS PAGE (When Data Entered)

19 REPORT DOCUMENTATION PAGE		READ INSTRUCTIONS BEFORE COMPLETING FORM	
18 1. REPORT NUMBER AFML TR-76-16	2. GOVT ACCESSION NO.	3. RECIPIENT'S CATALOG NUMBER 9 kept	
4. TITLE (and Subtitle) CHARACTERIZATION OF TRANSPARENT MATERIALS FOR EROSION RESISTANCE		5. TYPE OF REPORT & PERIOD COVERED Summary May 1974 Dec 75	
7. AUTHOR(s) 10 William F. Adler Stephen V. Hooker		6. PERFORMING ORG. REPORT NUMBER	
9. PERFORMING ORGANIZATION NAME AND ADDRESS Textron's Bell Aerospace Company P.O. Box One Buffalo, New York 14240		8. CONTRACT OR GRANT NUMBER(s) 15 F33615-73-C-5057	
11. CONTROLLING OFFICE NAME AND ADDRESS MBE Air Force Materials Laboratory Wright-Patterson AFB Ohio 45433		10. PROGRAM ELEMENT, PROJECT, TASK AREA & WORK UNIT NUMBERS Project: 7340 Task No: 734007	
14. MONITORING AGENCY NAME & ADDRESS (if different from Controlling Office) 16 AF-7340		12. REPORT DATE 11 Mar 76	
17 734007		13. NUMBER OF PAGES 297	
		15. SECURITY CLASS. (of this report) Unclassified	
		15a. DECLASSIFICATION/DOWNGRADING SCHEDULE	
16. DISTRIBUTION STATEMENT (of this Report) Distribution limited to US Government agencies only; (test and evaluation), March 1976. Other requests for this document must be referred to Air Force Materials Laboratory, Nonmetallic Materials Division, Elastomers and Coatings Branch, AFML/MBE, Wright-Patterson AFB, Ohio 45433.			
17. DISTRIBUTION STATEMENT (of the abstract entered in Block 20, if different from Report)			
18. SUPPLEMENTARY NOTES			
19. KEY WORDS (Continue on reverse side if necessary and identify by block number) Rain Erosion Impact Ceramic Materials Subsonic Polymeric Materials Stress Waves Inorganic Glasses Materials Characterization			
20. ABSTRACT (Continue on reverse side if necessary and identify by block number) This program is directed toward an assessment of the effects of rain erosion damage on loss in transmission of radiation through window materials. The general influence of the progression of the material removal process on the spectral transmittance of polymeric materials (polymethylmethacrylate, polysulfone, polycarbonate, and nylon) and soda lime glass was evaluated for wavelengths from 0.5 to 2.1 microns. Erosion mechanism evaluations were made for the window materials (Chemcor, Cortran,			

DD FORM 1 JAN 73 1473 EDITION OF 1 NOV 65 IS OBSOLETE

UNCLASSIFIED

SECURITY CLASSIFICATION OF THIS PAGE (When Data Entered)

408855

over  
JB

UNCLASSIFIED

SECURITY CLASSIFICATION OF THIS PAGE (When Data Entered)

20. (Continued)

spinel, and borosilicate glass) and the infrared transmitting materials (zinc sulfide, arsenic trisulfide, germanium, and sapphire), however mechanical difficulties were encountered in the AFML/Bell rotating arm apparatus before the transmittance measurements as a function of the exposure to the rain environment were completed. The materials evaluated were exposed to the standard rainfield of 1.8 mm water drops at an impact velocity of 730 fps. ←

The dynamic stress analysis for an idealized model of liquid drop impacts has been programmed for digital computer computations of the transient stresses in an elastic half-space. The spatial and temporal distributions of the transient stresses generated in deformable bodies with the elastic properties of zinc selenide, polymethylmethacrylate, and soda lime glass have been evaluated. The dynamic stresses are found to rapidly approach the equivalent static values at locations directly under the expanding contact zone, however the radial tensile stresses outside the contact area for the dynamic case can be many times the corresponding static stress values.

The erosion parameters of primary interest were the sequential formation of damages, the optical transmittance, and the incubation period for mass loss. The following rain erosion ranking in order of increasing resistance was observed: arsenic trisulfide glass, zinc selenide, germanium, zinc sulfide, spinel, and sapphire for the infrared transmitters; borosilicate glass, soda lime glass, thermally tempered soda lime glass, calcium aluminosilicate glass, and ion-exchanged glass for the oxide-based glasses; and polysulfone and polymethylmethacrylate were less resistant whereas nylon and polycarbonate were more resistant. For all material classes the observed erosion modes and rates depended sensitively upon the drop diameters, impact velocity, material fabrication, and surface preparation. However, the fractures in the inorganic materials and glasses produced by multiple water drop impacts were found to propagate by the same mechanisms as observed for quasistatic loadings. The fracture morphologies and stresses associated with pointed and spherical indenters provided the most useful basis for interpreting the erosion sequence. In the materials of low to moderate fracture strength, initial drop impacts produced an array of partial and complete rings whose centers resisted damage and whose perimeters consisted of annular crack arrays. During this stage, cracks were initiated at scratch and flaw sites by the dynamic tensile stresses and pits were initiated by lateral outflow impact against surface discontinuities. Continued exposure gradually developed an array of interconnected cracks and cavities which extended into the interior. During this stage, hydraulic loading produced by water penetration into cracks and flaws was the dominant damage propagation mechanism. Increased optical degradation was observed during this stage. In the final stage, mass loss occurred as impacts dislodged undercut surface fragments.

An analogous erosion sequence occurred in the plastics in which crevice propagation was also important. For very resistant materials an array of minute pits and polishing digs were observed after extended exposure at higher velocity (845 fps).

UNCLASSIFIED

SECURITY CLASSIFICATION OF THIS PAGE (When Data Entered)

## FOREWORD

This summary report was prepared by Bell Aerospace Company, Buffalo, New York under contract F33615-73-C-5057 with the Air Force Materials Laboratory, Wright-Patterson Air Force Base, Ohio. George F. Schmitt, Jr., of the Elastomers and Coatings Branch, MBE Nonmetallic Materials Division, was the laboratory project monitor until 1 February 1975 at which time Timothy L. Peterson assumed the responsibilities of project monitor.

The authors gratefully acknowledge the helpful technical discussions they have had during the course of this research with C. Preece, Materials Science Department, State University of New York at Stony Brook, J. Wurst, University of Dayton, and S. Freiman, J. Mecholsky, and P. Becher at the U.S. Naval Research Laboratory. The excellent cooperation and understanding provided by G. Schmitt and T. Peterson throughout the period this work was underway are especially appreciated: in particular with regard to their support during the extended period when the AFML/Bell rotating arm was not operational.

## TABLE OF CONTENTS

SECTION	PAGE
I INTRODUCTION	1
II ANALYSIS OF SINGLE PARTICLE IMPACTS	8
A. COLLISION OF A LIQUID DROP WITH A PLANE SURFACE	10
B. STRESSES GENERATED IN AN ELASTIC HALF-SPACE DUE TO PARTICULATE IMPINGEMENT	16
1. Mathematical Models	18
2. Comparison of Liquid Drop and Spherical Solid Particle Impacts	32
a. Solid Particle Impingement	33
b. Liquid Drop Impingement	38
C. RING FRACTURE FORMATIONS ON MATERIAL SPECIMENS	42
1. Zinc Selenide	58
2. Polymethylmethacrylate	65
3. Soda Lime Glass	79
4. Discussion	86
III MICROSCOPIC EXAMINATION OF PROGRESSIVELY ERODED SPECIMENS	97
A. TRANSPARENT POLYMERS	97
1. Polysulfone	97
2. Polycarbonate	104
3. Nylon	115
4. Polymethylmethacrylate	124
B. INFRARED TRANSMITTING MATERIALS	133
1. Zinc Selenide and Zinc Sulfide	134
2. Arsenic Trisulfide	155
3. Germanium	162
4. Sapphire and Spinel	184
C. OXIDE-BASED GLASSES	187
1. Annealed Soda Lime Glass	193
2. Thermally-Tempered Soda Lime Glass	207
3. Borosilicate Glass	212
4. Ion-Exchanged Glass	221
5. Calcium Aluminosilicate Glass	226



## TABLE OF CONTENTS

SECTION		PAGE
IV	TRANSMISSION CHARACTERISTICS OF WINDOW MATERIALS	234
	A. MEASUREMENTS OF TRANSMISSION LOSSES	234
	B. INFLUENCE OF EROSION DAMAGE ON TRANSMISSION	263
V	INDENTATION EVALUATIONS	265
VI	SUMMARY	276
VII	CONCLUSIONS	285
VIII	RECOMMENDATIONS	289
	REFERENCES	292

# LIST OF ILLUSTRATIONS

FIGURE		PAGE
1	Comparison of the Exact and Approximate Relations Describing the Rate of Expansion of the Contact Area for a Compressible Drop Striking a Rigid Plane	20
2	One-Dimensional Shock Wave Relations for a Liquid Drop Striking a Plane Surface	22
3	Shock Velocity as a Function of Particle Velocity for Water	24
4	Comparison of Transient and Static Radial Stress Components Evaluated $0.125a_1$ Below the Surface on an Elastic Half-Space Loaded by a Uniform Pressure over a Circular Domain	34
5	Temporal Development of the Transient Radial Stress Component in an Elastic Half-Space	36
6	Comparison of Radial Expansion of Contact Area for Liquid Drop and Rigid Sphere Impact Models	37
7	Temporal Development of the Transient Radial Stress Component for $Z=0.0195\text{mm}$ When $a_1 = 0.156\text{mm}$	39
8	Temporal Development of the Principal Radial Stress Component for $Z = 0.0195\text{ mm}$ When $a_1 = 0.156\text{ mm}$	40
9	Spatial Distribution of the Transient Radial Stress Component When $a_1 = 0.156\text{ mm}$	41
10	Comparison of Static and Dynamic Radial Stress Components when $a_1 = 0.156\text{ mm}$	43
11	Temporal Development of the Transient Radial Stress Component for $Z = 0.0195\text{ mm}$ when $a_1 = 0.380\text{ mm}$	44
12	Temporal Development of the Principal Radial Stress Component for $Z = 0.0195\text{ mm}$ When $a_1 = 0.380\text{ mm}$	45
13	Spatial Distribution of the Transient Radial Stress Component When $a_1 = 0.380\text{ mm}$	46
14	Comparison of Static and Dynamic Radial Stress Components When $a_1 = 0.380\text{ mm}$	47
15	Multiple Ripple Formation on Polysulfone Due to a Single $1.8\text{ mm}$ Water Drop Impacting at $730\text{ fps}$	49



# LIST OF ILLUSTRATIONS

FIGURE		PAGE
16	Imprint on the Surface of Polymethylmethacrylate Due to a Single 1.8 mm Water Drop Impacting at 730 fps	50
17	Ring Crack Formation on Zinc Sulfide due to 1.8mm Water Drops Impacting at 730 fps	52
18	Ring Crack Formations in Borosilicate Glass for 1.8mm Water Drops Impacting at 730 fps	55
19	Distribution of Tensile Radial Stresses in Zinc Selenide When $\phi = 20^\circ$	60
20	Distribution of Tensile Stresses in Zinc Selenide When $\phi = 25^\circ$	61
21	Variation of Radial Stress Component (at $z = 10\mu\text{m}$ ) with Drop Diameter for Impacts at 730 fps on ZnSe ( $\phi=25^\circ$ )	63
22	Variation of Radial Stress Component (at $z = 10\mu\text{m}$ ) with Drop Diameter Impacts at 1100 fps on ZnSe	64
23	Temporal Development of Principal Radial Stress Component in Zinc Selenide at $z = 10\mu\text{m}$ when $\phi=25^\circ$ and the Impact Velocity is 730 fps	66
24	Variation of Principal Radial Stress Component in Zinc Selenide When $\phi=25^\circ$	67
25	Temporal Development of Principal Radial Stress Component in Zinc Selenide When Impacted by 2.5 mm Drop at 730 fps ( $\phi = 25^\circ$ )	68
26	Variation of Principal Radial Stress Component in Zinc Selenide with Depth for 2.5 mm Drop Impacting at 730 fps ( $\phi = 25^\circ$ )	69
27	Temporal Development of Principal Radial Stress Component in Zinc Selenide for 2.5 mm Drop Impacting at 730 fps ( $\phi = 10^\circ$ )	70
28	Variation of Principal Radial Stress Component in Zinc Selenide with Depth for 2.5 mm Drop Impacting at 730 fps ( $\phi = 10^\circ$ )	71
29	Variation of Normal Stress Component (at $r = 0$ ) with Depth in Zinc Selenide	72

# LIST OF ILLUSTRATIONS

FIGURE		PAGE
30	Variation of Radial Stress Component in PMMA with Critical Contact Angle at $z = 10\mu\text{m}$	74
31	Variation of Radial Stress Component in PMMA with Depth when $\phi = 20^\circ$	75
32	Temporal Development of Radial Stress Component in PMMA at $z = 10\text{ m}$ when $\phi = 20^\circ$	76
33	Temporal Development of Radial Stress Component in PMMA at $z = 5\text{ m}$ When $\phi = 25^\circ$	77
34	Variation of Normal Stress Component (at $r = 0$ ) with Depth in PMMA	78
35	Distribution of Tensile Stress in Soda Lime Glass when $\phi = 15^\circ$	80
36	Distribution of Tensile Stresses in Soda Lime Glass when $\phi = 20^\circ$	81
37	Distribution of Tensile Stresses in Soda Lime Glass when $\phi = 25^\circ$	82
38	Variation of Radial Stress Component in Soda Lime Glass with Critical Contact Angle at $z = 10\mu\text{m}$	83
39	Temporal Development of Radial Stress Component in Soda Lime Glass at $z = 10\mu\text{m}$ when $\phi = 20^\circ$	84
40	Variation of Normal Stress Component (at $r = 0$ ) with Depth in Soda Lime Glass	85
41	Schematic Profile of Damage Site in PMMA Impacted by a 2mm Water Drop at 1000 fps	87
42	Variation of Radial Stress Component at $z = 10\mu\text{m}$ for 1.8 mm Water Drop Impacting Various Materials at 730 fps ( $\phi = 20^\circ$ )	90
43	Variation of Normal Stress Component (at $r=0$ ) with Depth for 1.8 mm Water Drop Impacting Various Materials at 730 fps ( $\phi=20^\circ$ )	92
44	Computed Temporal Profiles of Water Drops Striking a Rigid Plane	93
45	Internal Fracture Originating at Scratch on Surface of Polysulfone Specimen After a 2-minute Exposure to Standard Rainfield	99

# LIST OF ILLUSTRATIONS

FIGURE		PAGE
46	Ductile Nature of Polysulfone in Vicinity of Pits Formed Along Surface Scratches	100
47	Initial Stage of Pit Nucleation in Polysulfone	101
48	General Surface Condition of Polysulfone Specimen After 4-Minute Exposure to Standard Rainfield	102
49	Particle Removal from Surface of Polysulfone Specimen	103
50	General Character of Eroded Surface of Polysulfone after a 6-Minute Exposure	105
51	Polycarbonate after 2-Minute Exposure to Standard Rainfield	106
52	Comparison of Polycarbonate and Polysulfone Surface after 6-Minute Exposure	108
53	Crack Formation within Locally Deformed Regions on the Surface of Polycarbonate Specimen	109
54	Crevice Distribution Associated with Ductile Deformations of Polycarbonate	110
55	Pit Formation on Surface of Polycarbonate Specimen After 6-Minute Exposure to Standard Rainfield	112
56	Characteristics Erosion Pits on Polycarbonate Specimen after 6-Minute Exposure	113
57	Particle Removal from Surface of Polycarbonate Specimen After 10-Minute Exposure to Standard Rainfield	114
58	Comparison of Surface Features for Coated and Uncoated Polycarbonate After 6-Minute Exposure	116
59	General Character of Erosion Pits on Surface of Coated Polycarbonate Specimen	117
60	Material Removal Through Intersection of Fracture Surfaces	119
61	Surface Condition of Nylon Specimen after 3-Minute Exposure to Standard Rainfield	121

# LIST OF ILLUSTRATIONS

FIGURE		PAGE
62	Fine-scale Damage on Nylon After 2-Minute Exposure to Standard Rainfield	122
63	Intermediate Stage of Material Removal Process	123
64	Intersection of Droplet Impacts Initiating Material Removal on Surface of Polymethylmethacrylate	129
65	Fracture Sites Initiated at Surface Scratches on Surface of Polymethylmethacrylate Specimen	130
66	General Pattern of Material Removed from the Surface of a Polymethylmethacrylate Specimen After a 45-Second Exposure to the Standard Rainfield	131
67	Condition of Surface of Polymethylmethacrylate After 75-Second Exposure to Standard Rainfall	132
68	Scanning Electron Micrographs of Arc and Ring Fractures in CVD Zinc Selenide After 10 Minutes Exposure to 1 in/hr Rainfall at 690 fps in AFML Facility	136
69	Optical Micrograph in Bright Field Reflected Light of CVD Zinc Selenide After 10 Minutes Exposure to 1 in/hr Rainfall at 690 fps in AFML Facility	137
70	Scanning Electron Micrograph of Erosion Pit in CVD Zinc Selenide After 10 Minutes Exposure to 1 in/hr Rainfall at 690 fps in AFML Facility	141
71	Scanning Electron Micrograph of Bend Bar Fracture of CVD Zinc Selenide	142
72	Optical Micrograph in Bright Field Reflected Light of CVD Zinc Sulfide After 20 Minutes Exposure to 1 in/hr Rainfall at 690 fps in AFML Facility	144
73	Scanning Electron Micrograph of Erosion Pit in CVD Zinc Sulfide after 20 Minutes Exposure to 1 in/hr Rainfall at 690 fps in AFML Facility	146
74	Scanning Electron Micrograph of Bend Bar Fracture in CVD Zinc Sulfide	148



# LIST OF ILLUSTRATIONS

FIGURE		PAGE
75	Optical Micrograph in Bright Field Reflected Light of Ring Crack Pattern and Associated Cavity in Hot-Pressed Zinc Sulfide After 40 Sec. Exposure to Standard Rainfield	149
76	Optical Micrograph in Bright Field Reflected Light of Erosion Cavities in Hot-Pressed Zinc Sulfide After 20 Sec. Exposure to Standard Rainfield	149
77	Optical Micrographs of Ring Crack Pattern in Hot-Pressed Zinc Sulfide After 20 Sec. Exposure to Standard Rainfield	150
78	Optical Micrographs in Transmitted Light of Hot-Pressed Zinc Sulfide After 40 Sec. Exposure to Standard Rainfield	153
79	Scanning Electron Micrographs of Hot-Pressed Zinc Sulfide After 40 Sec. Exposure to Standard Rainfield	154
80	Optical Macrograph in Transmitted Light of Arc and Ring Crack Patterns in Arsenic Trisulfide Glass After 5 Sec. Exposure to Standard Rainfield at 500 fps	157
81	Optical Micrograph in Dark Field Reflected Light of Subsurface Conchoidal Fractures in Arsenic Trisulfide Glass After 5 Sec. Exposure to Standard Rainfield at 500 fps	157
82	Optical Micrographs of Ring Crack Pattern Formed in Arsenic Trisulfide After 5 Sec. Exposure to Standard Rainfield	159
83	Optical Micrographs in Oblique Reflected Light of Perimeter Sectors (Contained in Fig. 82) in Arsenic Trisulfide After 5 Sec. Exposure to Standard Rainfield	161
84	Optical Macrograph in Bright Field Reflected Light of Zones in Polycrystalline Germanium After Etching	164
85	Optical Micrograph in Oblique Reflected Light of Etch Pits in Polycrystalline Germanium Near $\langle 111 \rangle$ Orientation After Etching	164

# LIST OF ILLUSTRATIONS

FIGURE		PAGE
86	Optical Micrographs in Oblique Reflected Light of Typical Grain Structures in Polycrystalline Germanium	166
87	Optical Micrograph in Nomarski Interference Contrast of Crystallographic Slip and Conchoidal Fracture of Polycrystalline Germanium After 40 Sec. Exposure to Standard Rainfield	167
88	Optical Micrograph in Nomarski Interference Contrast of Possible Ring Crack Pattern in Polycrystalline Germanium After 20 Sec. Exposure	167
89	Optical Micrograph in Nomarski Interference Contrast of Conchoidal Fracture and Surface Removal in Polycrystalline Germanium After 20 Sec. Exposure to Standard Rainfield	168
90	Optical Micrograph in Nomarski Interference Contrast of a Compact Fracture Site in Polycrystalline Germanium After 40 Sec. Exposure to Standard Rainfield	168
91	Optical Micrograph in Nomarski Interference Contrast of Erosion Pit Formed by Crushing in Polycrystalline Germanium After 40 Sec. Exposure to Standard Rainfield	169
92	Scanning Electron Micrograph of Surface Relief Fractures Originating at a Microhardness Indentation in Polycrystalline Germanium	169
93	Optical Micrograph in Oblique Reflected Light of Cleavage Traces and Crack Array in Polycrystalline Germanium After 6 Sec. Exposure to 1 in/hr Rainfall at 730 fps in AFML Facility	174
94	Optical Micrograph in Oblique Reflected Light of Cleavage Traces in Polycrystalline Germanium After 36 Sec. Exposure to 1 in/hr Rainfall at 730 fps in AFML Facility	175
95	Optical Micrograph in Oblique Reflected Light of Cavity Initiation and Scratch Initiated Damage in Polycrystalline Germanium After 36 Sec. Exposure to 1 in/hr Rainfall at 730 fps in AFML Facility	175
96	Optical Micrographs in Oblique Reflected Light of Initial Damage in <111> Orientation Germanium After 36 Sec. Exposure to 1 in/hr Rainfall at 730 fps in AFML Facility	177

# LIST OF ILLUSTRATIONS

FIGURE		PAGE
97	Optical Micrograph in Oblique Reflected Light of Etched Polycrystalline Germanium After 36 Sec. Exposure to 1 in/hr Rainfall at 730 fps in AFML Facility	178
98	Optical Micrograph in Oblique Reflected Light of an Etched Cross-Section of Polycrystalline Germanium After 20 Sec. Exposure to 1 in/hr Rainfall at 730 fps in AFML Facility	178
99	Optical Micrographs in Oblique Reflected Light of Etched $\langle 111 \rangle$ Orientation Germanium After 36 Sec. Exposure to 1 in/hr Rainfall at 730 fps in AFML Facility	180
100	Optical Micrographs in Oblique Reflected Light of Etched $\langle 111 \rangle$ Orientation Germanium After 36 Sec. Exposure to 1 in/hr Rainfall at 730 fps in AFML Facility	181
101	Optical Micrographs in Oblique Reflected Light of an Etched Cross-Section of Polycrystalline Germanium After 20 Sec. Exposure to 1 in/hr Rainfall at 730 fps in AFML Facility	183
102	Optical Micrographs in Oblique Reflected Light of Sapphire After 60 Sec. Exposure to Standard Rainfield	188
103	Optical Micrographs in Oblique Reflected Light of Spinel After 90 Sec. Exposure to Standard Rainfield	189
104	Soda Lime Glass After 3 Min. Exposure to 1 in/hr Rainfall at 730 fps in AFML Facility	196
105	Soda Lime Glass After 3 Min. Exposure to 1 in/hr Rainfall at 730 fps in AFML Facility	197
106	Optical Micrograph in Oblique Reflected Light of Erosion Cavity in Soda Lime Glass After 10 Min. Exposure to 1 in/hr Rainfall at 730 fps in AFML Facility	199
107	Optical Micrograph in Oblique Reflected Light of Linear Crack Array in Soda Lime Glass After 10 Min. Exposure to 1 in/hr Rainfall at 730 fps in AFML Facility	199

# LIST OF ILLUSTRATIONS

FIGURE		PAGE
108	Soda Lime Glass Exposed to 1 in/hr Rainfall at 730 fps in AFML Facility	201
109	Influence of Surface Scratches on Erosion of Soda Lime Glass Exposed to 1 in/hr Rainfall at 730 fps in AFML Facility	203
110	Optical Micrographs in Oblique Reflected Light of Typical Scratch Initiated Damage in Scratched Soda Lime Glass After 4 Min. Exposure to 1 in/hr Rainfall at 730 fps in AFML Facility	204
111	Optical Micrographs of Cavity and Associated Crack Network Formed in Soda Lime Glass After 2 Min. Exposure to Standard Rainfield	206
112	Optical Micrograph of Network of Cavities and Cracks in Soda Lime Glass After 4 Min. Exposure to Standard Rainfield	208
113	Optical Micrographs of Cavity and Associated Crack Network in Tempered Soda Lime Glass After 4 Min. Exposure to Standard Rainfield	209
114	Optical Micrograph in Nomarski Interference Contrast of Crack Network Formed in Tempered Soda Lime Glass After 4 Min. Exposure to Standard Rainfield	210
115	Optical Micrographs of a Crack Network in Borosilicate Glass After 10 Sec. Exposure to Standard Rainfield	213
116	Optical Micrographs in Oblique Reflected Light of Borosilicate Glass After 20 Sec. Exposure to Standard Rainfield	216
117	Optical Micrographs of Bulk Damage in Borosilicate Glass After 10 Sec. Exposure to Standard Rainfield	217
118	Optical Micrographs of Ring Crack Pattern Formed in Borosilicate Glass After 30 Sec. Exposure to Standard Rainfield	218
119	Optical Micrograph in Nomarski Interference Contrast of Surface Damage Formed in Ion Exchanged Glass After 50 Sec. Exposure to Standard Rainfield	222



# LIST OF ILLUSTRATIONS

FIGURE		PAGE
120	Optical Micrograph in Bright Field Reflected Light of Surface Relief Fracture Formed in Ion-Exchanged Glass After 60 Sec. Exposure to Standard Rainfield	224
121	Optical Micrographs in Oblique Reflected Light of Grooves and Surface Relief Fractures Formed in Calcium Aluminosilicate Glass After 60 Sec. Exposure to Standard Rainfield	227
122	Optical Micrographs in Green Reflected Light Illustrate Interference Fringes Formed in Calcium Aluminosilicate Glass After 20 Sec. Exposure to Standard Rainfield	229
123	Scanning Electron Micrographs of Surface Relief Fractures After 20 Sec. Exposure to Standard Rainfield	232
124	Resolution Target	235
125	Initial Transmittance Characteristics for Infrared Window Materials	237
126	Rain Erosion of Annealed Soda Lime Glass	238
127	Rain Erosion of Tempered Soda Lime Glass	239
128	Rain Erosion of Polymethylmethacrylate	240
129	Rain Erosion of Polysulfone	241
130	Rain Erosion of Polycarbonate	242
131	Rain Erosion of Coated Polycarbonate	243
132	Rain Erosion of Nylon	244
133	Mass Loss as a Function of Exposure Time for Soda Lime Glass	245
134	Mass Loss as a Function of Exposure Time for Polymeric Materials	246
135	Resolution Pattern Viewed Through Eroded Specimens of Annealed Soda Lime Glass	248
136	Resolution Pattern Viewed Through Eroded Specimens of Tempered Soda Lime Glass	249

# LIST OF ILLUSTRATIONS

FIGURE		PAGE
137	Resolution Pattern Viewed Through Eroded Specimens of Polymethylmethacrylate	250
138	Resolution Pattern Viewed Through Eroded Specimens of Polysulfone	251
139	Resolution Pattern Viewed Through Eroded Specimens of Polycarbonate	252
140	Resolution Pattern Viewed Through Eroded Specimens of Coated Polycarbonated	253
141	Resolution Pattern Viewed Through Eroded Specimens of Nylon	254
142	Spectral Transmittance of Annealed Soda Lime Glass	255
143	Spectral Transmittance of Tempered Soda Lime Glass	256
144	Spectral Transmittance of Polymethylmethacrylate	257
145	Spectral Transmittance of Polysulfone	258
146	Spectral Transmittance of Polycarbonate	259
147	Spectral Transmittance of Coated Polycarbonate	260
148	Spectral Transmittance of Nylon	261
149	Experimental Arrangement for Indentation Test Evaluations	266
150	Fracture Loads and Ring Fracture Diameters for Fused Silica	268
151	Cumulative Distribution for Indenter Loads for Ring Fracture Initiation in Fused Silica	269
152	Cumulative Distribution for Ring Fracture Diameters in Fused Silica	270
153	Static and Dynamic Ring Fracture Diameters due to 290-Micron Glass Bead in Borosilicate Glass and Fused Silica	273

# LIST OF TABLES

TABLE		PAGE
1	Materials Tested in Standard Rainfield	2
2	Properties of Polymeric Materials Tested	3
3	Properties of Glasses Tested	5
4	Properties of Infrared Window Materials	6
5	Critical Contact Radii and Elapsed Times for Liquid Drop Impacts on Rigid Surfaces	14
6	Summary of Erosion Behavior of Transparent Materials Exposed to Standard Rainfield at 730 fps	53
7	Rain Erosion of Borosilicate Glass Specimens	54
8	Dilatational and Shear Wave Speeds for Window Materials	57
9	Location of Shear and Dilatational Wave Fronts (1.8 mm Drop at 730) fps on Plane $Z=0$	59
10	Transmittance Degradation After 40 Sec. Exposure to Standard Rainfield	172
11	Average Values of Fracture Loads and Ring Diameters	271

## I. INTRODUCTION

Bell Aerospace Company has been actively engaged in identifying the erosion mechanisms responsible for material removal<sup>(1-4)</sup> and in analytical modeling of the overall response of materials to multiple particle impacts.<sup>(5-8)</sup> The current program is directed toward an assessment of the effects of rain erosion damage on loss in transmission of electromagnetic radiation through window materials. The general influence of the progression of the material removal process on the spectral transmittance of polymeric materials (polymethylmethacrylate, polysulfone, polycarbonate, and nylon) and soda lime glass was evaluated for wavelengths from 0.5 to 2.1 microns. Similar evaluations were to be made for the window materials (Chemcor, Cortran, spinel, and borosilicate glass) and the infrared transmitting materials (zinc sulfide, arsenic trisulfide, germanium, and sapphire) listed in Table 1, however mechanical difficulties were encountered in the AFML/Bell rotating arm apparatus during the early stages of the current funding period which terminated the testing program before the transmittance measurements as a function of the exposure to the rain environment were completed. The AFML/Bell erosion facility was not operational during the remainder of the current funding period. The use of the AFML rotating arm facility for limited rain erosion evaluations required to complete the work on the erosion mechanisms in brittle materials is gratefully acknowledged.

Specimens of the materials listed in Table 1 were exposed to the standard rainfield in the AFML/Bell erosion facility (a one-inch per hour rainfall of 1.8 mm water drops) at an impact velocity of 730 fps. All of the specimens were rectangular parallelepipeds 1.5 in. x 0.875 in. with the thickness specified in Table I for each material.

General properties taken from the supplier's literature for the polymeric materials in Table 1 are listed in Table 2. These properties are provided for general reference. Correlations

TABLE 1

## MATERIALS TESTED IN STANDARD RAINFIELD

<u>Material Designation</u>	<u>Supplier</u>	<u>Trade Name</u>	<u>Specimen Thickness (in.)</u>
Polymethylmethacrylate	Rohm and Haas	Plexiglas II UVA	0.375
Polycarbonate	General Electric	Lexan 9030	.50
Coated Polycarbonate	General Electric	Malamine coated Lexan MR-4000	.50
Polysulfone	Union Carbide	UDEL P-3500	.50
Nylon	Dyanmit Nobel of America, Inc.	Trogamid T	.25
Chemcor	Corning Glass Works	Chemcor (Corning Code 0319)	.250
Cortran	Corning Glass Works	Cortran (Corning Code 9753)	.375
Borosilicate Glass	Corning Glass Works	Pyrex (Corning Code 7740)	.375
Soda Lime Glass	Corning Glass Works	Corning Code 0080	.375
Sapphire	Union Carbide	Linde Cz	.375
Spinel	Union Carbide	-	.375
Arsenic Trisulfide	Servofax	-	.250
Zinc Sulfide	Eastman Kodak Company	Irtran 2	.250
Germanium	Exotic Materials	-	.318



TABLE 2  
PROPERTIES OF POLYMERIC MATERIALS TESTED

	<u>Polymethyl- methacrylate</u>	<u>Polysulfone</u>	<u>Polycarbonate</u>	<u>Nylon</u>
Density (g/cc)	1.19	1.24	1.20	1.12
Hardness Rockwell	M104	M69(R120)	M70(R118)	M93
Young's Modulus (psi)	450,000	360,000	340,000	450,000
Poisson's Ratio	0.35	0.37		
Tensile Strength (psi)	10,500	10,200	9,500	9,750
Elongation at Yield (percent) at Break (percent)	- 4.9	5-6 50-100	5-7 110	8.8 132
Izod Impact (ft.lb/in. notch)	0.4(a)	1.3(b)	16(c)	no failure(d)
Water Absorption 24 hr. @ 73°F (percent)	0.20	0.30	0.15	0.41

(a) 0.5" x 0.5" section  
(b) specimen cross section unspecified  
(c) 0.125" x 0.125" section  
(d) unnotched specimen

of the erosion behavior with these or other properties of the materials tested will be made on the basis of the dominant microscopic erosion mechanisms, since it has already been demonstrated that the steady-state erosion rates for a variety of different polymers could not be correlated with their gross mechanical and physical properties.<sup>(2)</sup> Subsequent work in this area will be directed toward correlating the general microscopic features of the erosion damage with particular material properties and structural parameters for the restricted classes of polymeric materials considered here.

The dynamic stress analysis for an idealized model of liquid drop impacts has been programmed for digital computer computations of the transient stresses in an elastic half-space. The computational procedure which is now operational was proposed in an earlier report.<sup>(6)</sup> Comparisons are made between the dynamic stress analysis and the equivalent static analysis in order to see if the static solutions are representative of the loadings imposed by liquid drops as suggested by Peterson.<sup>(9)</sup> The dynamic stresses are found to rapidly approach the static values at locations directly under the expanding contact zone, however the radial tensile stresses outside the contact area for the dynamic case can be many times the corresponding static stress values. A number of cases are considered for the standard 1.8 mm water drops used in the AFML/Bell erosion facility and the glass bead environments used in the development of an analytical model for the erosion of brittle materials.<sup>(5-7)</sup> The material properties for the brittle materials used in this program are listed in Tables 3 and 4.

The fracture behavior of inorganic glasses due to indentation by rounded spherical indenters from 150 to 550 microns in diameter has been evaluated to extend the data base required in analyzing the erosion of fused silica and borosilicate glasses due to multiple collisions with glass beads.<sup>(5-6)</sup> The indentation loads for fracture initiation in a variety of inorganic glasses are being used to differentiate differences in the erosive

TABLE 3  
PROPERTIES OF GLASSES TESTED

Glass	Density (g/cc)	Young's Modulus ( $\times 10^4$ MPa)	Poisson's Ratio	Elastic Wave Velocities		Knoop Hardness (100g)	Fracture Stress (MPa)	Fracture Energy (J/m <sup>2</sup> )
				Dila- tation (mm/ $\mu$ s)	Shear (mm/ $\mu$ s)			
Fused Silica Corning 7940	2.20	7.21	0.16	5.93	3.78	489	78.2	3.7
Soda Lime Corning 0080	2.47	7.0	0.22	5.71	3.43	465	-	-
PPG	-	-	-	-	-	-	83.7	3.5
Corning 0319	2.46	7.1	0.21	5.71	3.33	590	-	-
Borosilicate Corning 7740	2.23	6.37	0.20	5.65	3.46	418	87.6	4.0
Calcium Aluminosilicate Corning 9753	2.80	9.9	0.28	6.74	3.72	658	-	5.0
Arsenic Trisulfide	3.20	1.61	0.24	2.44	1.50	109	18.6	2.1



TABLE 4  
PROPERTIES OF INFRARED WINDOW MATERIALS

	Zinc Selenide		Zinc Sulfide		<u>Sapphire</u>	<u>Germanium</u>
	<u>Raytheon (CVD)</u>	<u>Kodak Irtran 4 (Hot Pressing)</u>	<u>Raytheon (CVD)</u>	<u>Kodak Irtran 2 (Hot Pressing)</u>		
Density (gm/cc)	5.27	5.27	4.08	4.09	3.98	5.32
Refractive Index (8-13 $\mu$ m)	2.40	2.85 - 2.32	2.20	2.29 - 2.15	-	4
Transmission Limits ( $\mu$ m)	0.5 - 22	0.5 - 22	0.5 - 14	0.4 - 14.5	0.15 - 6	1.8 - 25
Hardness (Knoop 50 gm)	100	150	265	249	1900 $\pm$ 300	-
Grain Size ( $\mu$ m)	70	50 - 100	2 - 10	1 - 2	single crystal	-
Flexural Strength (psi) 8,500		7,500 (250°C) 6,000 (RT)	16,000	13,500 (250°C) 14,100 (RT)	65,000	10,500
E(psi x 10 <sup>6</sup> ) 9.75		10.3	10.8	10.6 (250°C) 14.0 (RT)	53.0	14.9

response of these glasses subjected to both water drop and glass bead impacts. The indentation test with appropriate indenter radii provides a mechanical test procedure which most closely approximates the inhomogeneous stresses generated during particle impacts. Our preliminary results indicate that the fracture loads obtained by this procedure do approximate the relative erosion resistance of several inorganic glasses which have approximately the same fracture stress levels when tested by other fracture evaluation procedures. Correlations based on the microscopic observations of the erosion mechanisms in organic and inorganic glasses and ceramic materials are beginning to provide the understanding required to model the erosion process in selected materials. A materials characterization effort has also been initiated to correlate the general microscopic features of the erosion damage with particular material properties and structural parameters.

## II. ANALYSIS OF SINGLE PARTICLE IMPACTS

The erosion damage observed in brittle materials during the early stages of the overall erosion process is a complex phenomenon. A single particle impact may or may not be damaging depending on the impact velocity. Consider a small volume of the specimen which includes a portion of the surface several times the cross sectional area of the impacting particle. In the initial stages of the erosion process an impacting particle can (1) leave the initial condition of this volume unchanged, (2) produce structural changes within the volume, (3) nucleate a subcritical crack, (4) extend a crack nucleated during a previous impact, or (5) nucleate a critical crack. The extent to which any of these possibilities occur is governed by the magnitude of the impact velocity of the particle, with event number (1) being most probable at low velocities (well below the threshold for fracture initiation) and event number (5) being the immediate consequence at high impact velocities. In the intermediate range of impact velocities a number of particle impacts are required before the integrity of the material is adversely affected. The most challenging problems occur in the low to intermediate velocity range where damage to the material occurs through the cumulative damage of numerous particle impacts.

This level of abstraction is not very useful in developing a viable analytical model of the erosion process, however microscopic examinations of lightly eroded specimens have revealed individual water drop imprints on some of the materials tested at a water drop impact velocity of 730 fps: polysulfone, polymethylmethacrylate, zinc selenide, zinc sulfide, and to a lesser extent polycarbonate and nylon. The erosion of arsenic trisulfide was quite rapid, however the very early stages of the erosion process in this material showed well-defined multiple ring fractures at a drop impact velocity of 500 fps. These ring fracture formations can be contrasted with the random fracture development observed in most of the inorganic glasses tested with the exception of arsenic trisulfide. The ring fractures represent a

definable damage mode which can be related to the parameters associated with an impacting drop. Such relationships are significant in developing an analytical model of the erosion process, since the generation of a random array of cracks whose relationship to the impacting drops is not known is a considerably more difficult process to represent as a definitive model.

The basic element for the initiation of erosion damage by rounded solid particles is the cone fracture. The diameter of the ring and penetration of the conical fracture surface extending into the glass specimens have been measured for a range of impact conditions.<sup>(7)</sup> The mode of material removal for spherical solid particles near the velocity threshold for cone crack initiation is seen to depend on the cone depth which is a function of the radius of the impacting glass bead. Although static stress evaluations are not applicable to the highly transient loading conditions imparted to the solid during the collision process, the Hertzian predictions for the diameter of the contact zone as a function of impact velocity appear to be consistent with the measured ring fracture diameters. The formation and interaction of ring fractures in brittle materials provide the basis for an analytical model for erosion due to rounded particles.

In the intermediate range of impact velocities described above the experimental results indicate that a number of particle impacts are required before the infrared transmission characteristics of the materials tested are changed. To investigate the mechanisms responsible for the loss of infrared transmission, it is necessary to consider the effect of the pressure distribution from several overlapping but non-concentric particle impacts on the surface of a small volume of material,  $\Delta V$ . Once a particle impact produces damage in  $\Delta V$  the local properties of  $\Delta V$  are modified. The evaluation of the effect of the next impact must account for the change in the constitution of  $\Delta V$ .

Several features of the general erosion process will be reviewed as a continuation of our efforts to relate materials properties to the microscopic erosion mechanisms and the concomitant reduction in the transmittance of electromagnetic radiation through specimens exposed to multiple particle impingement.

#### A. Collision of a Liquid Drop with a Plane Surface

Detailed knowledge of the flow patterns and impact pressures developed during the collision of a liquid drop and a deformable plane surface is still unavailable. The qualitative details of a liquid drop impact have been obtained from a number of high-speed photographic studies.<sup>(11-14)</sup> The experimental data on spherical drops striking a solid surface still cannot provide a quantitative description of the temporal magnitude and distribution of the liquid/solid interfacial pressure; however, direct pressure measurements over a very small region of the contact area of an impacting drop<sup>(15-17)</sup> are beginning to supply the required information. In general little agreement can be found in the literature concerning the analysis of the sequence of events which take place at a solid surface impacted by a liquid drop.

The damage produced on solid surfaces due to liquid drop impingement arises from two sources: the direct pressure generated over the expanding impact area in order to bring the drop to a sudden stop and the high-velocity lateral outflow of the liquid subsequently escaping from the high pressure zone. Huang<sup>(18)</sup> developed a fluid mechanics analysis with computer solutions to indicate the time-evolution of the impact pressures and lateral outflow at impact velocities of 980 and 2450 fps. Huang's calculations support Engel's contention<sup>(19)</sup> that the pressure buildup and lateral outflow occur simultaneously after the initial contact is made, although the jetting is not appreciable during the early stage of impact. This contradicts the opinions of Morris,<sup>(1)</sup> Heymann,<sup>(20)</sup> and Bowden and Field<sup>(30)</sup> that lateral flow cannot begin before the compression wave in



the fluid moves ahead of the circular boundary between the drop and the solid surface. At approximately 300 fps these calculations indicate that the critical edge angle is on the order of a few degrees. Brunton and Camus<sup>(14)</sup> however, provide photographic evidence that under these conditions, the critical angle,  $\phi$ , falls in the range of from  $13^\circ$  to  $19^\circ$ , or the radius of the contact area at this point is from 0.23 to 0.33 times the radius of the drop. Using high-speed photography, Rochester and Brunton<sup>(16)</sup> determined that lateral outflow initiated at a critical angle  $\phi=11^\circ$  at an impact velocity of 300 fps. They found that the value of  $\phi$  did not vary for drop diameters ranging from 2 to 9 mm. It is to be noted in the experiments of Brunton and Camus<sup>(14)</sup> and Rochester and Brunton<sup>(16)</sup> that the drop is a disk of liquid generally 5 mm in diameter and 1.5 mm thick. The relation between the observations for a disk-shaped drop with lateral constraint and a spherical drop remains to be established. Rochester and Brunton suggest that lateral outflow is observed at  $\phi=11^\circ$ , since this is the angle at which the outward edge velocity between the drop and solid falls below the maximum possible jet velocity. Until this condition occurs the liquid cannot escape from under the drop.

Huang<sup>(21)</sup> has provided a plausible explanation for the discrepancy between the predicted and observed values of  $\phi$ . His description of spherical drop impingement involves a three-stage impact process. The first stage, the center stamping zone, is equivalent to that assumed by Bowden and Field,<sup>(12)</sup> but with internal radial flow already occurring within the drop. At the first contact of the drop with the solid, the maximum contact pressure is not reached instantaneously, but begins to build up toward the maximum pressure as the contact time increases. Pressure buildup initiates in the liquid in the drop at a slightly later time corresponding to the expansion of the contact area between the drop and the plane surface. This time difference due to the curvature of the drop creates radial pressure gradients which in turn produce internal radial flow. The angle at which the compressional wave front in the liquid just overtakes the

expanding boundary of the contact area is designated the critical angle,  $\phi_{1c}$ . This is the condition for the lateral outflow used by Morris,<sup>(1)</sup> Heymann,<sup>(20)</sup> and Bowden and Field<sup>(12)</sup> in their analyses. As the compressional wave front overtakes the interfacial perimeter lateral jetting begins. However, at this point the lateral jetting velocity is still not sufficient to overtake the velocity of the expanding contact area. The second critical angle,  $\phi_{2c}$ , is the value of the contact angle at which the velocity of lateral jetting overtakes the velocity of the expanding contact area which is decreasing as the contact time increases. It is this second critical angle which is observed in the high-speed photographic studies.

On the other hand, Rochester and Brunton<sup>(16)</sup> agree with Huang's analysis for the center stamping zone but describe different conditions in the zone of constrained lateral flow when  $\phi_{1c} < \phi \leq \phi_{2c}$ . Since the compression wave in the fluid is able to reach a point on the free surface of the drop before that point is overtaken by the expanding contact perimeter, a release wave is generated which propagates back into the liquid in the drop. The compression wave and attached release wave propagate along the curved wall of the drop altering its sphericity to some extent. According to Rochester and Brunton the release waves will not reduce the pressure along the axis of the drop which is still increasing. This pressure will not decrease until the edge pressure is reduced by the onset of lateral outflow, which occurs when the two release waves (for the disk shaped drop) intersect at the center of impact.

With this background the effect of a variation in the radius and velocity of an impacting water drop on the erosion behavior of window materials transparent to radiation in the visible and near infrared wavelengths will be considered in terms of simple models. To be specific, drop diameters of 0.5 mm, 1.8 mm and 2.5 mm at impact velocities of 300 fps (0.0914 mm/ $\mu$ s) and 730 fps (0.2225 mm/ $\mu$ s) and 1120 fps (0.3355 mm/ $\mu$ s) will be investigated.

When a liquid drop first strikes a plane surface, the boundary of the contact area will be traveling at supersonic speeds with respect to the dilatational wave speed for the impacted body. For a homogeneous and isotropic elastic material the period of time the radial velocity of the contact zone exceeds the dilatational wave speed will depend on the radius and initial impact velocity of the liquid drop and the compressibility of the elastic material. The time-dependent radius of the contact area during the collision of a completely compressible liquid drop with a rigid surface is given by

$$a(t) = [2RV_0 t - (V_0 t)^2]^{1/2} \quad (1)$$

where  $V_0$  is the impact velocity,  $R$  is the radius of the spherical drop, and  $t$  is the time elapsed from the initial contact.

Based on the available experimental evidence and analyses, it will be assumed that the lateral outflow is not significant for spherical drops impacting at the designated velocities until the critical contact angle,  $\varphi_{2c}$ , falls in the range  $10^\circ \leq \varphi_{2c} \leq 25^\circ$ . Using the idealized liquid drop model, the contact radii for this condition are listed in Table 5. Eq. (1) is then used to compute the approximate time after initial contact at which lateral outflow would take place.

The above summarizes some of the current thoughts on the mechanics of liquid drop impacts on rigid surfaces. However, relatively little unanimity can be found in the literature concerning the nature of the pressure distribution which develops at a solid surface impacted by a liquid drop.

Considering impact velocities which are less than 1000 fps, Heymann's analysis<sup>(20)</sup> predicts a maximum pressure of approximately  $3\rho_0 C_0 V_0$  which occurs at the periphery of the contact area between the drop and a rigid surface where  $\rho_0, C_0, V_0$  are the density, acoustic velocity, and impact velocity of the liquid drop. A paraboloidal pressure distribution is obtained



TABLE 5  
CRITICAL CONTACT RADII AND ELAPSED TIMES FOR  
LIQUID DROP IMPACTS ON RIGID SURFACES

	Drop Diameter		
	0.5 mm	1.8 mm	2.5 mm
Volume (mm <sup>3</sup> )	0.654	3.05	8.19
Mass Ratio	1	4.66	12.50
Maximum Contact Radius (mm)			
$\phi = 10^\circ$	0.0434	0.156	0.217
$\phi = 15^\circ$	.0646	.233	.324
$\phi = 20^\circ$	.0855	.308	.427
$\phi = 25^\circ$	.1058	.380	.529
Time in Microseconds Required to Reach Maximum Contact Radius When			
$V_o = 300 \text{ fps } (0.0914 \text{ mm}/\mu\text{s})$			
$\phi = 10^\circ$	0.041	0.148	0.206
$\phi = 15^\circ$	.0914	.330	.459
$\phi = 20^\circ$	.160	.576	.799
$\phi = 25^\circ$	.244	.879	1.22
$V_o = 730 \text{ fps } (0.2225 \text{ mm}/\mu\text{s})$			
$\phi = 10^\circ$	0.0169	0.0609	0.0848
$\phi = 15^\circ$	.0376	.1358	.189
$\phi = 20^\circ$	.0658	.237	.330
$\phi = 25^\circ$	.1008	.361	.503
$V_o = 1100 \text{ fps } (0.3355 \text{ mm}/\mu\text{s})$			
$\phi = 10^\circ$	0.0112	0.0402	0.056
$\phi = 15^\circ$	.0248	.0896	.125
$\phi = 20^\circ$	.0435	.157	.218
$\phi = 25^\circ$	.0665	.239	.332

by Heymann with the minimum pressure occurring along the axis of spherical drop passing through the point of contact.

Huang's numerical approach,<sup>(18)</sup> devised for obtaining quantitative estimates for the pressure distribution associated with a compressible liquid drop striking a rigid surface, indicates that a hemispherical pressure distribution predominates during the very early stages of the collision. The maximum value of the pressure is reached under these conditions. As compression of the drop continues, the distribution becomes more uniform with a very slight increase in the magnitude of the pressure at the periphery of the contact area. The magnitude of the maximum value in the pressure distribution decreases as lateral outflow becomes more dominant. Huang's numerical results indicate that the maximum pressure does not exceed  $0.8 \rho_0 C_0 V_0$  for a 2 mm water drop impacting at 980 fps.

The magnitudes of the pressure given by Heymann<sup>(20)</sup> and Huang<sup>(18)</sup> were obtained for a rigid surface and, therefore, represent the maximum values that are likely to occur. As the pressure increases on a deformable surface, the localized contact zone will be depressed; hence, the relative velocity of approach of the liquid is less than what it would be for a rigid surface.

Hwang<sup>(22)</sup> recently investigated the stresses generated by a liquid drop impact on an elastically-deformable half-space using the same computational scheme as Huang. Hwang's results for a 2 mm water drop impacting a rigid plane at 980 fps show that the maximum pressure of  $0.755 \rho_0 C_0 V_0$  occurs at a radius near  $0.5 R_0$  which revises Huang's earlier numerical analysis. Hwang finds that the pressure distribution on a deformable solid surface is lower and more uniform than for a rigid surface. The stress state beneath the contact zone is mainly compressive with the greatest tensile stresses occurring on the surface of the half-space slightly beyond the contact zone.

Using microtransducers, Rochester and Brunton<sup>(16)</sup> were able to obtain the spatial distribution of direct and shear surface stresses when a solid surface impacts a disk-shaped water drop 5 mm in diameter and 1.5 mm thick. The shear stresses for smooth surfaces are negligible with respect to the magnitude of the applied pressure. The peak pressure is approximately  $1.8 \rho_0 C_0 V_0$  and occurs at the edge of the impact area where  $\phi = \phi_{2c}$ . Rochester and Brunton comment on the high edge pressures. For  $\phi_{1c} < \phi < \phi_{2c}$ , a particle in the front surface of the drop is stopped by direct contact with the solid surface, the rate of change of momentum for such a collision will be higher than for a similar particle for which  $\phi > \phi_{2c}$ . For  $\phi > \phi_{2c}$ , the particle is separated from the solid by intervening jets carrying liquid from the center of the drop. Accordingly, the rate of change of momentum for this particle is reduced and it does not come into direct contact with the solid.

#### B. Stresses Generated in an Elastic Half-Space Due to Particulate Impingement

The review in the previous section shows that the sequence of events associated with a liquid drop striking a deformable surface at subsonic to low supersonic velocities is still a matter of speculation. In qualitative terms the liquid/solid interfacial pressure rapidly increases nonuniformly over a rapidly expanding contact area, reaches a peak value, and then decreases to a lower value while the contact zone continues to grow. The entire sequence of events is completed within one microsecond for 1.8 mm water drops impacting at high subsonic to low supersonic velocities. It was previously proposed<sup>(6)</sup> that an analytical solution to the drop impact problem derived by Blowers<sup>(23)</sup> be used in conjunction with the pressure-particle velocity relations for water to estimate the transient stresses in an elastic solid due to an increasing pressure distribution over a radially increasing contact zone. A computer program for the evaluation of Blowers' analytical solution of the liquid drop impact problem is now operational and the transient stress

distributions within the elastic half-space can be determined. The program computes the four nonvanishing stress components, the principal normal stresses, and the principal shear stresses in cylindrical coordinates. Some results from this program will be described for the evaluation of critical stress conditions within the half-space and a comparison will be made between dynamic and static stress distributions due to localized loads on the surface of a half-space. This latter problem is posed since it would be much easier to undertake static as opposed to transient stress analyses in establishing potential failure modes in a particular material and since a significant number of incorrect estimations of the stress levels a material experiences when exposed to particulate impacts have appeared in the erosion literature.

Peterson<sup>(9)</sup> has already reduced the transient problem of liquid drop impact to the evaluation of the stresses in an elastic half-space by assuming a static pressure distribution is applied over a circular region on the surface of the half-space. In actuality he has evaluated the stress field due to a spherical, rigid indenter pressed against a thick elastic plate (the Hertzian contact problem in the theory of elasticity<sup>(7)</sup>). Peterson refers to Huang's computer solutions<sup>(18)</sup> for the temporal and spatial distribution of pressure when a spherical drop strikes a rigid surface in support for the hemispherical pressure distribution used in his analysis. The hemispherical distribution of pressure in the early stages of the impact has been questioned by several investigators. Recent computer results by Kreyenhagen, et.al.,<sup>(24)</sup> for a water drop striking a rigid surface show that the maximum pressures occur at the boundary of the contact zone in the early stages of the impact and then move to the axis of symmetry passing through the initial point of contact during the later stages of the collision process.

Due to the level of uncertainty in all of the work done on this problem to date, simple models will be considered here only to obtain an estimate of the stress conditions



particular material specimens experience when exposed to a rain environment in conjunction with experimental observations of the failure modes in a variety of brittle solids. The response of materials to subsonic water drop impacts is quite complex as shown for the case of inorganic glasses to be described in Section III.C. Glasses with essentially the same gross mechanical properties display significant differences in their erosion behavior. The reasons for these differences are being explored in terms of a materials-oriented program, since the material characteristics which influence the erosion behavior have not been identified.

#### 1. Mathematical Models

Blowers<sup>(23)</sup> investigated the propagation of stress waves in an elastic half-space subjected to a uniform pressure  $p$  distributed over an expanding circular region on its surface whose time-dependent radius is deduced from the idealized model of a compressible liquid drop given in Eq.(1) where

$$a(t) = [2RV_0 t - (V_0 t)^2]^{1/2} \approx \sqrt{2RV_0} t^{1/2} = kt^{1/2} \quad (2)$$

The radius of the contact area,  $a(t)$ , increases with time according to the relation in Eq. (1) which was subsequently described by Engel.<sup>(25)</sup> The pressure distribution on the surface of the solid used by Blowers in his analysis is of the form

$$\begin{aligned} p(r,t) &= p \text{ for } r \leq kt^{1/2} \\ &= 0 \text{ for } r > kt^{1/2} \end{aligned} \quad (3)$$

The magnitude of  $p$  is assumed to be a known quantity which has to be prescribed.

The accuracy of the approximation used by Blowers corresponding to a compressible drop striking a rigid plane given in Eq.(2) will be evaluated. The general relation can be rewritten

$$t^2 - \frac{2R}{V_0} t + \left(\frac{a}{V_0}\right)^2 = 0 \quad (4)$$

which yields

$$\frac{v_o t}{R} = 1 - \sqrt{1 - \left(\frac{a}{R}\right)^2} \quad (5)$$

On the other hand Blower's approximation becomes

$$\frac{v_o t}{R} = \frac{1}{2} \left(\frac{a}{R}\right)^2 \quad (6)$$

For comparison Eq.(5) and (6) are plotted in Fig. 1. It is seen that the approximation in Eq.(2) is a good representation of the exact relation for values of  $(a/R)$  less than 0.5. Eq. (3) will therefore be applicable to the largest contact radii listed in Table V for which it is believed lateral outflow will occur.

The velocity of the expanding circular boundary defined by Eq.(2) is initially supersonic but decreases as  $t^{-1/2}$ . The disturbance experienced by the solid medium will then be due to the propagation of a dilatation wave traveling at a velocity,  $C_1$ , the propagation of a distortional, or shear, wave traveling at a velocity,  $C_2$ , and a Rayleigh wave propagating along the surface at a velocity  $C_R$  which is slightly less than  $C_2$ . As long as the boundary of the loaded region is moving at a velocity  $\dot{a}(t) \geq C_1$ , the radius of the disturbance will be the same as that of the loaded area. When  $\dot{a}(t) < C_1$ , the disturbance will move ahead of the load and will continue to travel at the sonic velocity of the medium. The time at which  $\dot{a}(t) = C_1$  can be determined from Eq.(2)

$$\tau_1 = \left(\frac{k}{2C_1}\right)^2 \quad (7)$$

Correspondingly the shear wave will move ahead of the loaded region when

$$\tau_2 = \left(\frac{k}{2C_2}\right)^2 \quad (8)$$

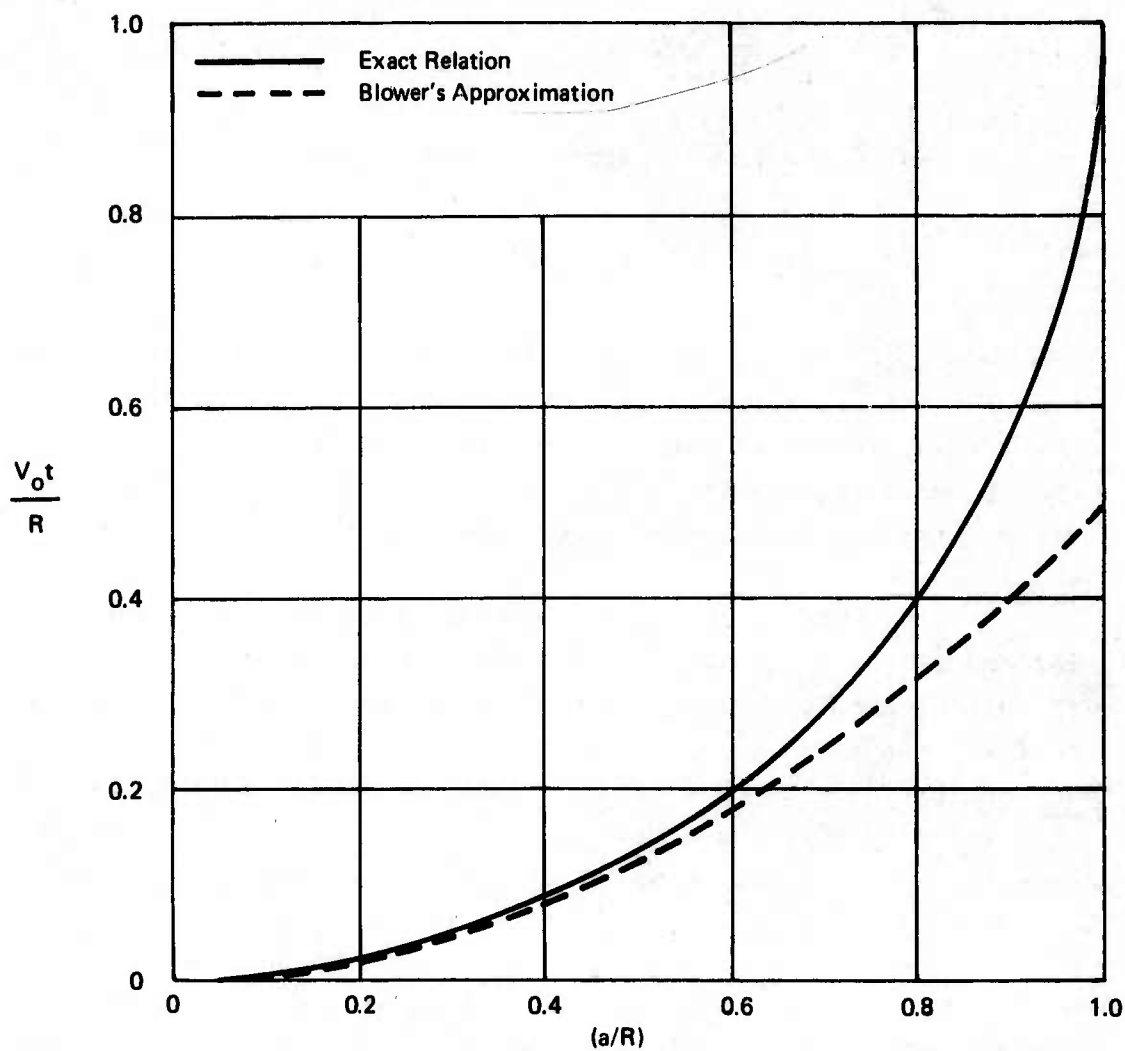


Figure 1. Comparison of the Exact and Approximate Relations Describing the Rate of Expansion of the Contract Area for a Compressible Drop Striking a Rigid Plane

where

$$c_1^2 = \left(\frac{E}{\rho}\right) \left(\frac{1-\nu}{(1+\nu)(1-2\nu)}\right) \quad (9)$$

$$c_2^2 = \left(\frac{E}{\rho}\right) \left(\frac{1}{2(1+\nu)}\right) \quad (10)$$

E is Young's modulus

$\nu$  is Poisson's ratio

$\rho$  is the density of the medium

Although the exact spatial and temporal distribution of the pressure over the contact zone,  $p(r,t)$  in Eq.(3) is not known, the one-dimensional shock wave relations for water striking a deformable substrate will provide general order of magnitude approximations to  $p$ . The balance of mass and momentum equations corresponding to the condition depicted in Fig. 2 are

$$\rho_w U_w = \rho'_w (U_w + (V_o - V_w)) \quad (11)$$

$$p_w = \rho_w U_w (V_o - V_w) \quad (12)$$

and

$$\rho_s U_s = \rho'_s (U_s - V_s) \quad (13)$$

$$p_s = \rho_s U_s V_s \quad (14)$$

The water drop strikes the target with an impact velocity  $V_o$ . A shock wave is transmitted into the drop at a velocity  $U_w$ , and a second shock wave is propagated into the substrate at a velocity  $U_s$  across the water/substrate interface. The particle velocities for the water and substrate are denoted by  $V_w$  and  $V_s$ , respectively. Continuity of the pressures and particle velocities at the water/substrate interface requires  $p_s = p_w$  and  $V_s = V_w$ . Only the momentum equations, Eq.(12) and (14), are required



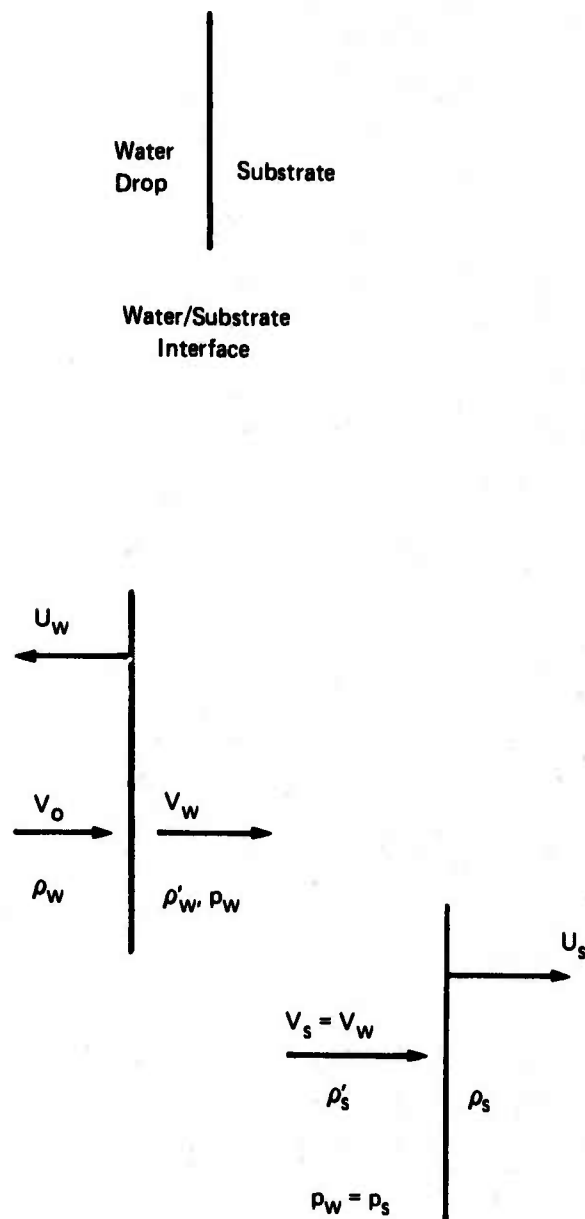


Figure 2. One-Dimensional Shock Wave Relations for a Liquid Drop Striking a Plane Surface

to evaluate the magnitude of the pressure pulse applied to the substrate. Setting  $V_s = V_w$  in the relation  $p_s = p_w$  yields

$$V_w = \frac{V_o}{1 + \frac{\rho_s U_s}{\rho_w U_w}} \quad (15)$$

The relation between the shock velocity and particle velocity is known for water. When the shock velocity as a function of the particle velocity is known for the substrate, Eq.(15) can be solved for  $V_w$ . Then, using either Eq.(12) or (14), the pressure at the water/substrate interface can be determined.

$$p_w = \frac{\rho_w U_w V_o}{1 + \frac{\rho_w U_w}{\rho_s U_s}} \quad (16)$$

When the water drop impact velocity is small in comparison to the acoustic velocities of water and the substrate, the respective particle velocities are also negligible with respect to the acoustic velocities and Eq.(16) reduces to

$$p_w = \frac{\rho_w C_w V_o}{1 + \frac{\rho_w C_w}{\rho_s C_s}} \quad (17)$$

where  $C_w$  and  $C_s$  are the acoustic velocities for water and substrate, respectively, at zero particle velocity.

The variation in the acoustic and shock velocities for water as a function of the particle velocity is given in Fig. 3 based on the tabulated data of Rice and Walsh.(27) The expression

$$U_w = C_o + 2V_w - 0.1 \left( \frac{V_w}{C_o} \right) V_w \quad (18)$$

derived by Huang(18) is also plotted in Fig. 3. The shock data

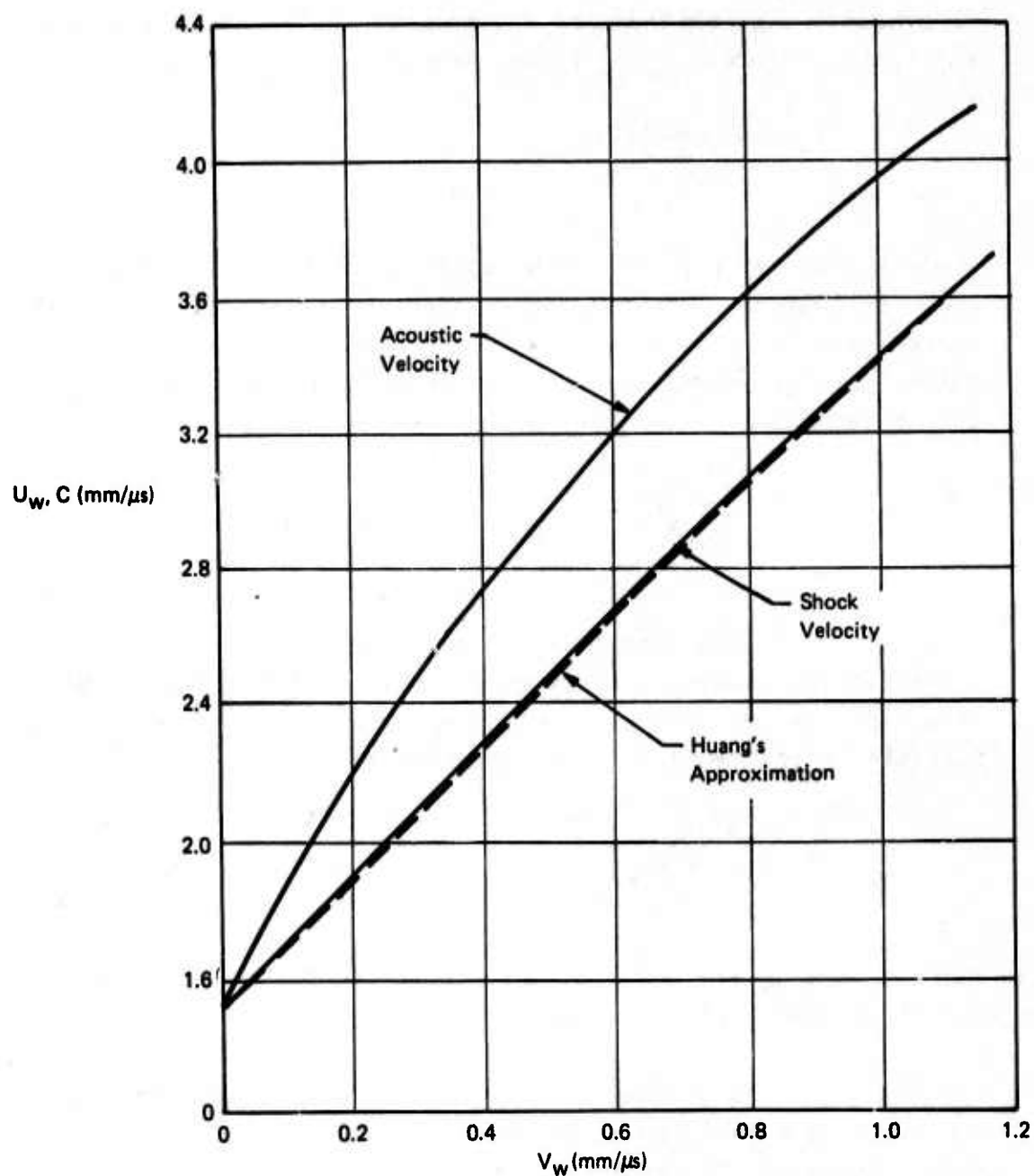


Figure 3. Shock Velocity as a Function of Particle Velocity for Water

for water will be used subsequently to evaluate the pressure applied to selected target materials by an impacting water drop.

Limited numerical results are provided in Blowers' paper for the case when Poisson's ratio  $\nu=0.3$ . Blowers shows that the transient radial and azimuthal surface stresses at time  $t = 8\tau_1$  are primarily compressive with extremely high tensile stresses found only in a narrow band immediately behind the Rayleigh wave front. Blowers comments that although extreme radial tensions arise, the radial dimensions in which they occur are always quite small. Thus, each point experiences the critical tension for an extremely short duration. Blowers conjectures that this result of the analysis tends to raise doubt in the effectiveness of the Rayleigh wave as the cause of liquid impact erosion damage. The stress states associated with the Rayleigh wave have been proposed by Bowden and Field<sup>(12)</sup> as initiating fracture in glass specimens impacted by a water jet at 1970 fps.

More extensive computations to be described shortly, using Blowers' analysis indicate that this conclusion regarding the duration of critical tensile stresses may have been premature. These computations indicate that there are locations in the interior of the half-space where significant tensile stresses develop for a reasonable length of time in relation to the duration of the impact event. The stresses associated with a 1.8mm water drop striking zinc selenide, polymethylmethacrylate, and soda lime glass at 730 fps are computed to cover a range of material response and to compare the results from these computations with the actual damage observed on these materials. In addition, numerical computations were carried out for the range of drop diameters and velocities listed in Table 5 for a half-space having the elastic properties of zinc selenide.

The numerical solutions for Blowers' equations provide the stresses at all points within the elastic half-space except in the vicinity of the Rayleigh surface wave at and near the surface where a non-removable singularity in the equations



prevails. Many attempts were made to overcome this difficulty in the numerical computations, but without success. The computed results reported here are given at locations within a few microns below the surface of the half-space where the calculated stresses are reasonably well-behaved including the regions in the vicinity of the Rayleigh wave front.

The stress distribution associated with the contact of two elastic bodies was first derived by Hertz.<sup>(28)</sup> The problem originally considered by Hertz was to determine for the case of two elastic isotropic bodies which touch each other over a very small part of their surface and exert upon each other a finite pressure distributed over the common area of contact, the form of the common surface, the distribution of pressure over it, and a relation between the distance the bodies approach each other and the pressure existing on the contacting surface of each body. The results given here will be restricted to the case of a spherical elastic body indenting an elastic half-space. A detailed account of the stress distribution for this case was given by Huber:<sup>(29)</sup> the specialized theory is often referred to as the Hertz-Huber theory.

The non-vanishing stress components for the Hertz-Huber theory are evaluated from the expressions given below<sup>(30)</sup>

$$\begin{aligned}\sigma_{\rho\rho} &= \frac{3P}{2\pi a^2} \left\{ \frac{(1-2\nu)a^2}{3\rho^2} \left[ 1 - \left(\frac{Z}{V}\right)^3 \right] + \left(\frac{Z}{V}\right)^3 \frac{a^2 V^2}{V^4 + a^2 Z^2} \right. \\ &\quad \left. + \frac{Z}{V} \left[ \frac{(1-\nu)V^2}{a^2 + V^2} + \frac{(1+\nu)V}{a} \tan^{-1} \left(\frac{a}{V}\right) - 2 \right] \right\} \\ \sigma_{\theta\theta} &= - \frac{3P}{2\pi a^2} \left\{ \frac{(1-2\nu)a^2}{3\rho^2} \left[ 1 - \left(\frac{Z}{V}\right)^3 \right] + \right. \\ &\quad \left. + \frac{Z}{V} \left[ \frac{(1-\nu)V^2}{a^2 + V^2} - \frac{(1+\nu)V}{a} \tan^{-1} \left(\frac{a}{V}\right) + 2\nu \right] \right\}\end{aligned}\tag{19}$$

$$\sigma_{\rho Z} = \frac{-3P}{2\pi a^2} \frac{\rho Z^2}{V^4 + a^2 Z^2} \frac{a^2 V}{(a^2 + V^2)}$$

$$\sigma_{ZZ} = \frac{3P}{2\pi a^2} \left(\frac{Z}{V}\right)^3 \frac{a^2 V^2}{V^4 + a^2 Z^2}$$

where  $V^2$  is the positive root from

$$V^2 = \frac{1}{2} \left[ (\rho^2 + Z^2 - a^2) \pm \left( (\rho^2 + Z^2 - a^2)^2 + 4a^2 Z^2 \right)^{1/2} \right] \quad (20)$$

and the direction of  $Z$  is perpendicular to the plane of the specimen.

The radius  $a$  of the circle of contact and the distance of approach  $\alpha$  for an elastic sphere indenting a thick elastic plate are given by

$$a = (KPR)^{1/3} \quad (21)$$

$$\alpha = \frac{a^2}{R} \quad (22)$$

where  $P$  is the normal load on the indenter,  $R$  is the indenter radius, and

$$K = \frac{3}{4} \left[ \left( \frac{1-\nu_1^2}{E_1} \right) + \left( \frac{1-\nu_2^2}{E_2} \right) \right] \quad (23)$$

where  $\nu_1$ ,  $E_1$  are Poisson's ratio and Young's modulus for the sphere and  $\nu_2$ ,  $E_2$  are the elastic constants for the half-space. If the magnitude of the maximum pressure is scaled to the radius of the contact area, the pressure distribution over the contact area is shown to be hemispherical for the particular case under consideration.

Knowing the magnitude of the contact surface and the pressure acting on it, the elastic stress distribution in the half-space can be evaluated. The above system of equations, Eq.(19) to (23), have been programmed for digital computer computations along with evaluation of the principal normal and shear stresses.

Hertz<sup>(31)</sup> assumed that the collision of two bodies could be regarded as a statical problem; the compression at the place of contact is regarded as gradually produced and as subsiding completely by reversal of the process by which it was produced. To study the impact of a spherical body on an elastic surface, the previous relations from the Hertzian theory are restated in terms of the velocity of approach  $V_0$  instead of the load  $P$  which is now an unknown. In order to establish a relation between  $P$  and  $V_0$ , the kinetic energy of the impacting sphere is equated to the strain energy at the time of maximum impression.

$$\frac{1}{2} \left( \frac{4}{3} \rho_1 \pi R^3 \right) V_0^2 = \int_0^{\alpha_{\max}} P(\alpha) d\alpha \quad (24)$$

where  $\rho_1$  is the density of the impacting sphere. Using Eq.(22)

$$P_{\max} = \left( \frac{5}{3} \pi \rho_1 \right)^{3/5} K^{-2/5} V_0^{6/5} R^2 \quad (25)$$

The duration of contact  $T$  between the two impacting bodies is given by

$$T = 2.943 \left( \frac{5}{3} \pi \rho_1 K \right)^{2/5} \frac{R}{V_0^{1/5}} \quad (26)$$

Analysis of the elastic waves generated when a rounded rigid projectile impacts an elastic half-space is provided by Tsai.<sup>(32)</sup> Tsai obtained transient stress distributions by solving the three-dimensional equations of motion after writing the stresses as the sum of the Hertz contact stresses and the effect of stress waves. The solution to the problem including the wave effects is compared with results from the corresponding Hertzian theory of impact.

The time-dependent pressure distribution,  $p$ , and distance of approach,  $\alpha$ , corresponding to the static contact problem of a rigid sphere impressing a half-space are

$$p(r, t) = \frac{4G}{(1-\nu)\pi R} [a(t)^2 - r^2] \quad (27)$$

$$\alpha(t) = \frac{a(t)^2}{R} \quad (28)$$

where  $G, \nu$  are the shear modulus and Poisson's ratio, respectively  
 $R$  is the radius of the sphere  
 $r$  is the radial distance from the point of contact to an arbitrary point within the expanding contact circle of radius  $a$ .

Tsai introduces the approximate form of  $a(t)$  given by

$$a(t) = (0.995)^{1/2} a_1 \sin^{1/2} \left( \frac{\pi t}{T} \right) \quad (29)$$

where  $a_1$  is the maximum radius of contact and  $T$  is the duration of contact. The expression for  $a_1$  can be written in terms of the impact velocity  $V_0$  and the mass,  $m$ , of the impacting sphere.

$$a_1^5 = \frac{15(1-\nu)m}{32G} R^2 V_0^2 \quad (30)$$

The basis for Tsai's comparison with the Hertzian theory is the evaluation of the radial stress component at the boundary of the contact zone, however due to the complexity of the solution only limited numerical results are provided. The value of the radial stress component at the circle of contact is computed for values of  $T$  from 10 to 200  $\mu s$ . After an elapse time of 1  $\mu s$  the ratio of the dynamic stress to the Hertzian stress increase rapidly with increasing  $a_1$  and decreasing  $T$ . At  $T/2$  it is shown that the ratio decreases if  $a_1$  increases and  $T$  decreases. For relatively small  $a_1$  and large  $T$  the radial stress components converge to the Hertzian values.

When the total load is the same for a hemispherical and a uniform pressure distribution applied to a circular region, the static stresses within an elastic half-space are identical except in the vicinity of the boundary of the loaded region. Hence the results obtained for a uniform pressure distribution should also be applicable to the hemispherical pressure distribution corresponding to the Hertz-Huber equations. The stress distributions within an elastic half-space due to a uniform pressure  $p$  distributed over a circle of radius  $a$  can be evaluated.<sup>(30)</sup> The computed dynamic stresses obtained from



Blowers' analysis<sup>(23)</sup> and the corresponding static stress distributions can therefore be compared directly. The governing equations for a uniform pressure  $p$  distributed over a circular region are as follows.

$$\begin{aligned}\sigma_{\rho\rho} &= \frac{p}{2\pi} \left( 2\nu \frac{\partial V}{\partial Z} - (1-2\nu) \frac{\partial^2 \chi}{\partial \rho^2} - Z \frac{\partial^2 V}{\partial \rho^2} \right) \\ \sigma_{\theta\theta} &= \frac{p}{2\pi} \left( 2\nu \frac{\partial V}{\partial Z} - (1-2\nu) \frac{1}{\rho} \frac{\partial \chi}{\partial \rho} - \frac{Z}{\rho} \frac{\partial V}{\partial \rho} \right) \\ \sigma_{\rho Z} &= \frac{-pZ}{2\pi} \left( \frac{\partial^2 V}{\partial \rho \partial Z} \right) \\ \sigma_{ZZ} &= \frac{p}{2\pi} \left( \frac{\partial V}{\partial Z} - Z \frac{\partial^2 V}{\partial Z^2} \right)\end{aligned}\quad (31)$$

where

$$\begin{aligned}\frac{\partial V}{\partial Z} &= -2 \left[ K'E(k, \theta) - (K' - E') F(k, \theta) - K' \frac{Z}{r_2} \right] \\ \frac{\partial^2 \chi}{\partial \rho^2} &= \pi - \frac{Zr_2}{\rho^2} E' + \frac{Z(2a^2 + Z^2)}{r_2 \rho^2} K' - \\ &\quad \frac{a^2 + \rho^2}{\rho^2} (K'E(k, \varphi) - (K' - E') F(k, \varphi)) \quad \text{when } \rho < a \\ &= \frac{-\pi a^2}{\rho^2} - \frac{Zr_2}{\rho^2} E' + \frac{Z(2a^2 + Z^2)}{r_2 \rho^2} K' + \\ &\quad \frac{a^2 + \rho^2}{\rho^2} (K'E(k, \theta) - (K' - E') F(k, \theta)) \quad \text{when } \rho > a \\ \frac{\partial^2 V}{\partial \rho^2} &= \frac{(\rho^2 + a^2 + Z^2)(\rho^2 - a^2 - Z^2)}{r_1^2 r_2 \rho^2} E' - \frac{2}{r_2} K' + \frac{r_2}{\rho^2} [(1+k^2)K' - E'] \\ \frac{1}{\rho} \frac{\partial \chi}{\partial \rho} &= \pi + \frac{Zr_2}{\rho^2} E' - \frac{Z(2a^2 + 2\rho^2 + Z^2)}{r_2 \rho^2} K' + \\ &\quad \frac{a^2 - \rho^2}{\rho^2} [K'E(k, \varphi) - (K' - E') F(k, \varphi)] \quad \text{when } \rho < a\end{aligned}\quad (32)$$

$$= \pi \frac{a^2}{\rho^2} + \frac{Zr_2}{\rho^2} E' - \frac{Z(2a^2 + 2\rho^2 + Z^2)}{r_2 \rho^2} K' - \frac{a^2 - \rho^2}{\rho^2} [K' E(k, \theta) - (K' - E') F(k, \theta)] \quad \text{when } \rho > a$$

$$\frac{\partial V}{\partial \rho} = - \frac{r_2}{\rho} \left[ (1+k^2) K' - 2E' \right]$$

$$\frac{\partial^2 V}{\partial Z^2} = \frac{2}{r_2} K' - \left[ \frac{r_2}{\rho^2} + \frac{(\rho^2 + a^2 + Z^2)(\rho^2 - a^2 - Z^2)}{r_1^2 r_2 \rho^2} \right] E'$$

$$\frac{\partial^2 V}{\partial \rho \partial Z} = \frac{Z}{r_2 \rho} \left[ \left(1 + \frac{1}{k^2}\right) E' - 2K' \right]$$

The solution is expressed in terms of elliptic integrals,

$$\begin{aligned} K' &= \int_0^{\pi/2} \frac{d\phi}{(1-k'^2 \sin^2 \phi)^{1/2}} \\ E' &= \int_0^{\pi/2} (1-k'^2 \sin^2 \phi)^{1/2} d\phi \\ E(k, \beta) &= \int_0^{\beta} (1-k^2 \sin^2 \phi)^{1/2} d\phi \\ F(k, \beta) &= \int_0^{\beta} \frac{d\phi}{(1-k^2 \sin^2 \phi)^{1/2}} \end{aligned} \quad (33)$$

where

$$\begin{aligned} k &= \frac{r_1}{r_2} \quad \text{and} \quad k' = (1 - r_1^2/r_2^2)^{1/2} \\ r_1^2 &= (a-\rho)^2 + Z^2 \\ r_2^2 &= (a+\rho)^2 + Z^2 \end{aligned} \quad (34)$$

with  $\phi = \sin^{-1}(\frac{Z}{r_1})$ ,  $\varphi = \pi - \theta$ .

The total load  $P$  in Eq.(19) is related to the distributed pressure over the contact area of radius  $a$  denoted by  $p$  in Eq.(31) by

$$p = \frac{P}{\pi a^2} \quad (35)$$

so the stresses for equivalent loadings can be investigated for the hemispherical and the uniform pressure distributions. As pointed out earlier, the stresses in the elastic half-space will be nearly identical for these two cases except at the periphery of the contact zone when Eq.(35) is satisfied. The equations in (31) are the static analog to Blowers' equations for a uniform pressure over an expanding circular region described by Eq.(2) and (3). The system of equations, Eq.(31) to (35), has been programmed for digital computer computations along with evaluation of the principal normal and shear stresses.

The two principal stress components in addition to  $\sigma_{\theta\theta}$  are determined from

$$\sigma_{1,2} = \frac{1}{2} \left\{ (\sigma_{\rho\rho} + \sigma_{ZZ}) \pm \left[ (\sigma_{\rho\rho} - \sigma_{ZZ})^2 + 4\sigma_{\rho Z}^2 \right]^{1/2} \right\} \quad (36)$$

The angle  $\gamma$  between the normal to the plane on which  $\sigma_1$  acts and the positive  $\rho$  coordinate is given by

$$\tan 2\gamma = \left( \frac{2\sigma_{\rho Z}}{\sigma_{ZZ} - \sigma_{\rho\rho}} \right) \quad (37)$$

Both the magnitude of the principal stress and the angle  $\gamma$  have to be prescribed.

## 2. Comparison of Liquid Drop and Spherical Solid Particle Impacts

The stress distributions for a number of conditions which are of interest in both our solid and liquid particle erosion investigations will be described. The particular cases which will be investigated are for a 290  $\mu\text{m}$  glass bead colliding with a glass surface at 200 fps and for a 1.8 mm water drop impacting a glass surface at 730 fps. The values of the static

and transient stresses can be determined at any point within the half-space for uniform pressure loadings using the solutions provided by Love<sup>(30)</sup> and Blowers.<sup>(23)</sup> Calculations have been made which indicate the relative magnitude of the tensile stress components compared to the magnitude of the localized pressure pulse imparted to the specimen's surface by particle impingement. According to these calculations the duration of a critical stress state at a particular location within the specimen depends on the elastic properties and density of the material. The relevant properties for a number of glasses are summarized in Table 3. The subsequent analysis and experimental observations will be described in terms of the information provided in Table 3.

#### a. Solid Particle Impingement

According to the Hertzian theory of impact, the maximum radius of the loaded circular contact area is  $a_1 = 1.43$  mils ( $36.3\mu\text{m}$ ) and the maximum equivalent static load is  $P=3.56$  lbs. for a  $290\mu\text{m}$  glass sphere impacting a glass plate at 200 fps.<sup>(7)</sup> These values are computed based on the elastic properties of soda lime glass. The magnitude of the corresponding uniform pressure loading, Eq.(35), is  $p = 5.54 \times 10^5$  psi. The radial stress components for static and dynamic loading conditions are compared in Fig. 4. The radial stresses shown in Fig. 4 are evaluated at a depth of 0.17875 mils (or  $0.125a_1$ ) below the surface. When the radius of the expanding contact area for the dynamic case reaches the radius  $a_1$ , the static and dynamic radial stresses are nearly identical for the values of  $\rho$  under the applied load but diverge for  $\rho > a_1$ . The maximum dynamic tensile stress is 35,000 psi while the maximum static value is only 20,000 psi. These differences become greater closer to the surface of the glass plate. The dynamic stress distributions reach higher values of the tensile radial stress component at a much earlier stage of the collision process than the corresponding static stress distributions.



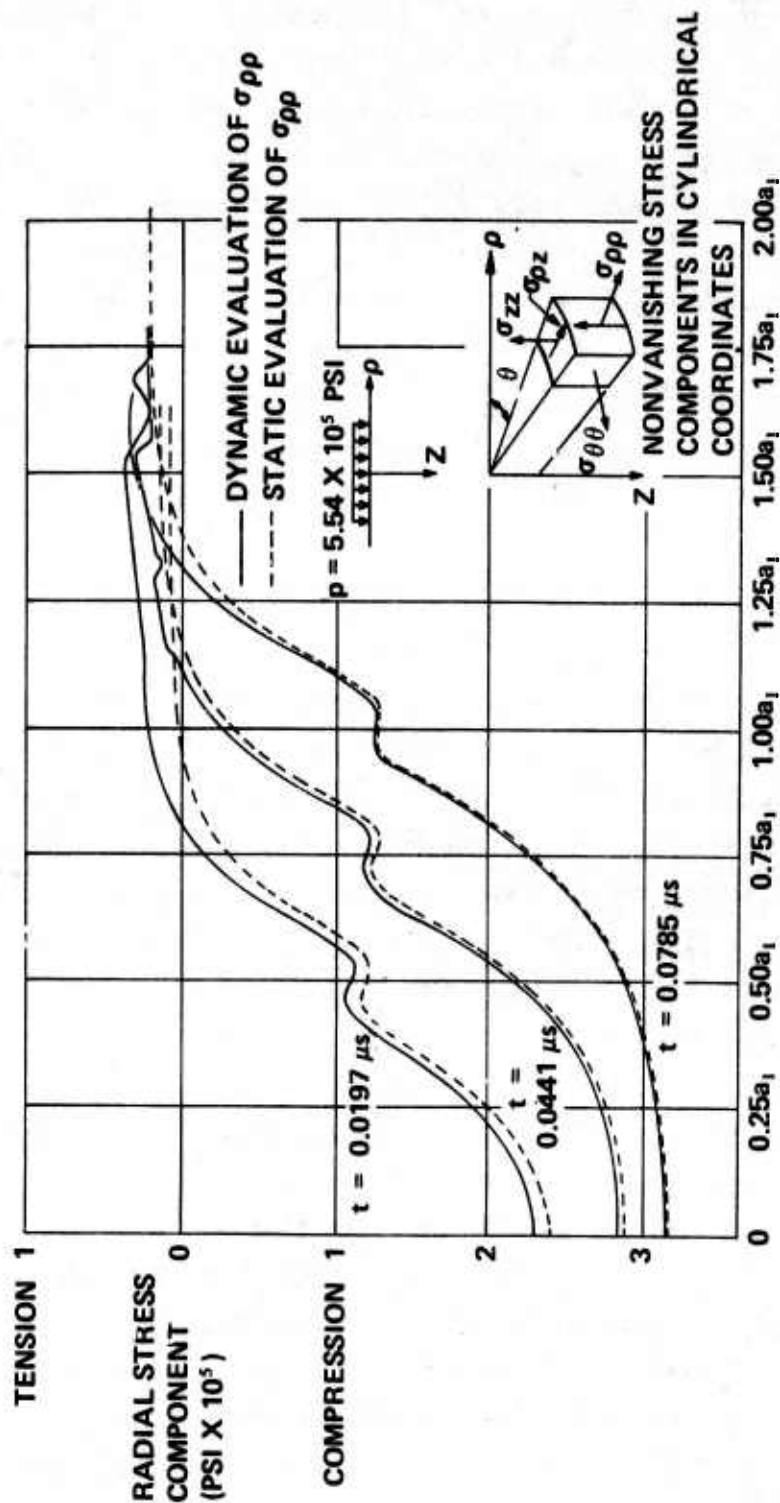


Figure 4. Comparison of Transient and Static Radial Stress Components Evaluated 0.125a, Below the Surface on an Elastic Half-Space Loaded by a Uniform Pressure Over a Circular Domain

The static stresses were computed using both Eq.(19) and Eq.(31) with the equivalent loadings for each case evaluated from Eq. (35). The numerical results confirmed that the form of the loading over the contact circle had relatively little influence on the stress distribution beyond the contact radius.

The time-evolution of the transient radial stresses at a depth of  $0.125a_1$  is displayed in Fig. 5. Comparing Fig. 4 and 5 it is readily seen that the static stress distributions do not even approximate the general form of the radial variation in the dynamic stresses during the very early stages of the collision as would be expected. The initial compressive pulse propagates into the half-space at the dilatational wave velocity in glass of  $2.22 \times 10^5$  in./sec.; so, when the radius of the loaded region reaches the radius  $a_1 = 1.43$  mils, the dilatational wave has reached a distance of almost  $12a_1$  at  $0.079\mu\text{s}$  after the loading begins. In Fig. 5 the location of the boundary of the loaded circular region is denoted by the letter P and the location of the shear front by an S. When the loading reaches a radius of  $0.25a_1$  the dilatational wave has reached a distance of  $0.75a_1$  and the shear front is at  $0.5a_1$ . The radial stress is compressive for all values of  $\rho$ . As the shear wave propagates, tensile radial stresses begin to appear in the vicinity of the shear wave front. The compressive stresses associated with the dilatational wave and the transition to significant tensile stresses can be seen in the plot when the loaded area reaches a radial distance of  $0.375a_1$ . At longer times the tensile radial stresses occur over radial distances just ahead of the shear front to a short distance outside the loading circle.

An additional observation can be made. Essentially two models of particulate impingement have been introduced: one is a perfectly compressible liquid drop striking a rigid plane and the other is a rigid sphere striking an elastic half-space as shown in Fig. 6. Using the Hertzian theory of

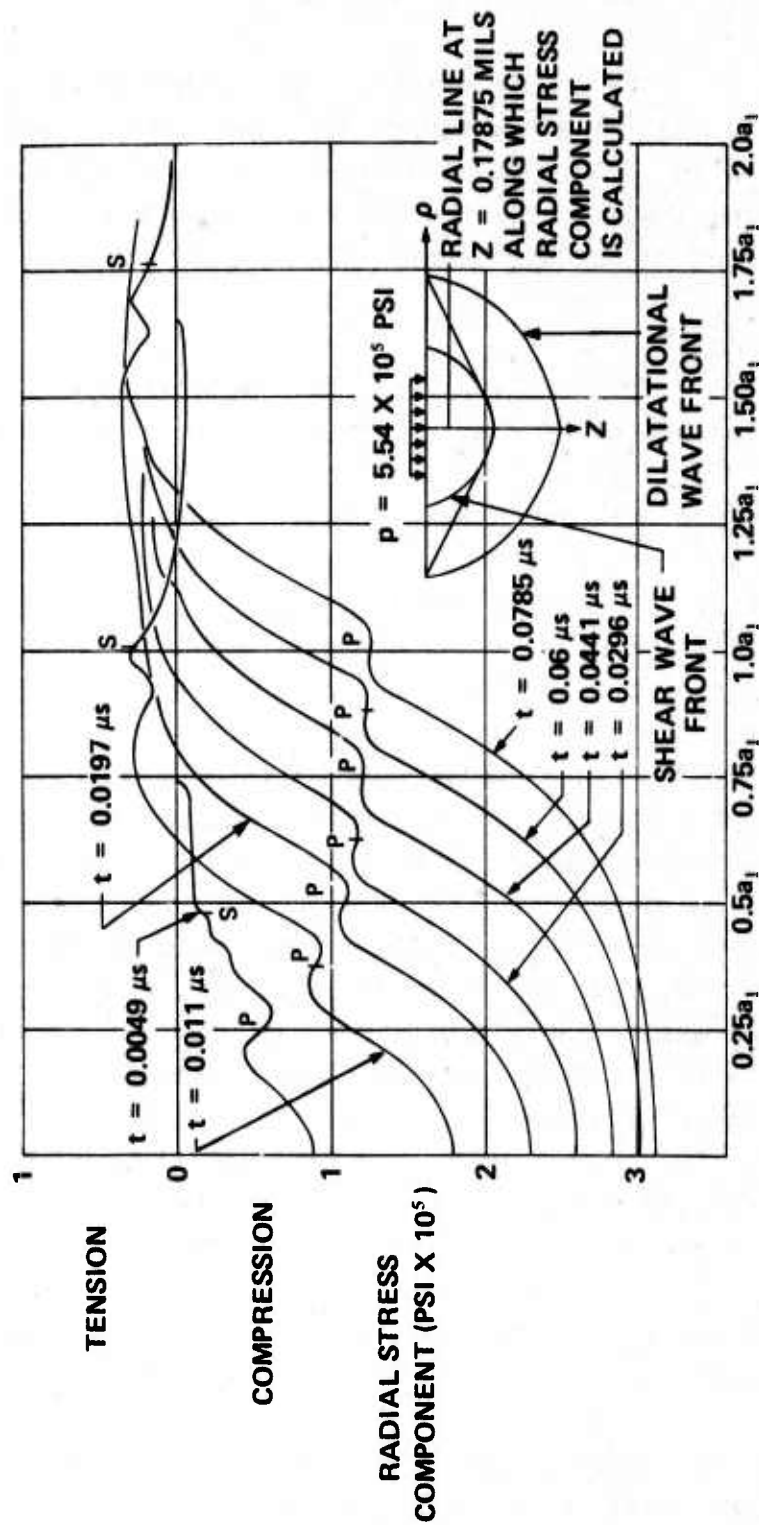


Figure 5. Temporal Development of the Transient Radial Stress Component in an Elastic Half-Space

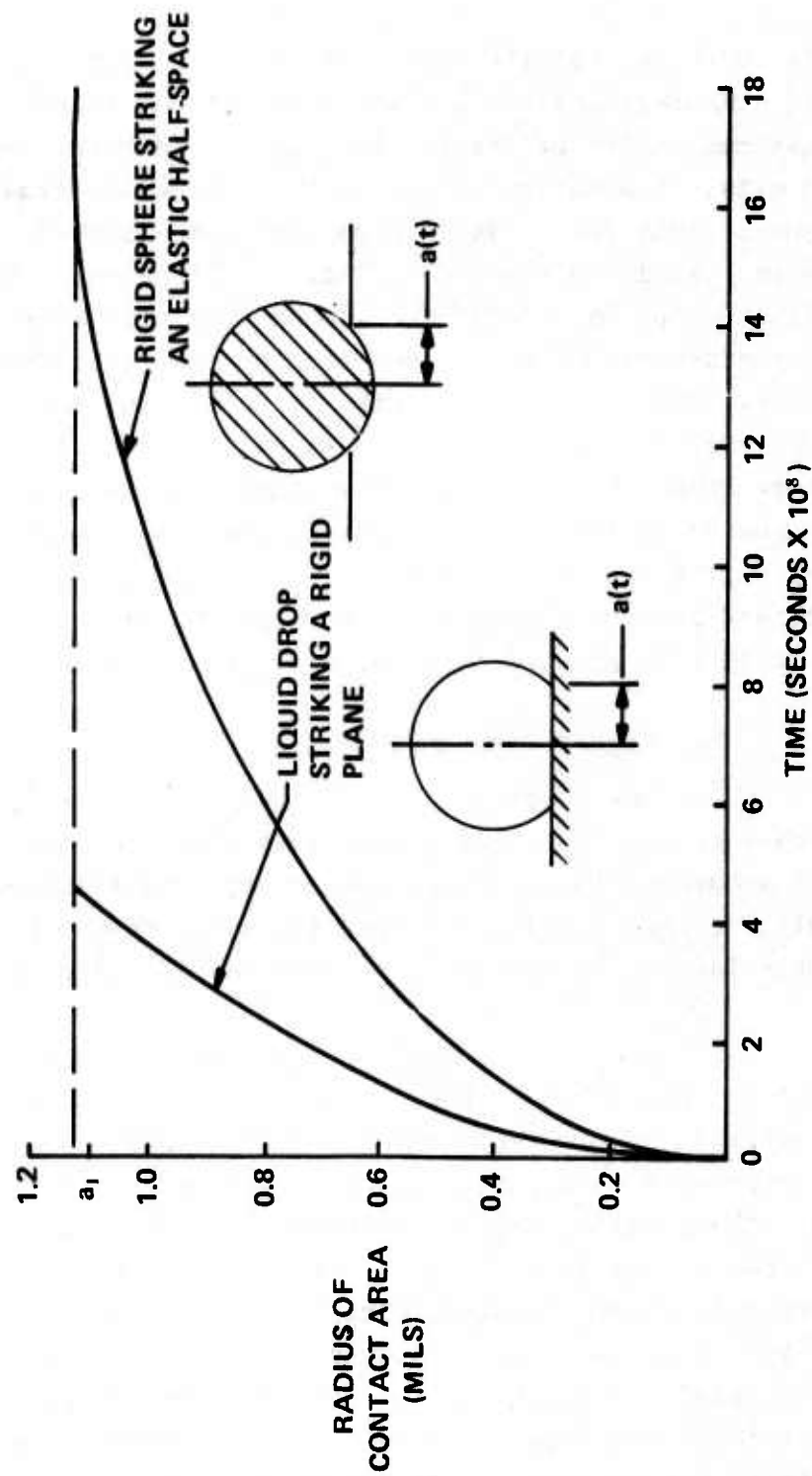


Figure 6. Comparison of Radial Expansion of Contact Area for Liquid Drop and Rigid Sphere Impact Models



impact, the duration for the collision of a rigid sphere, 290 microns in diameter, against a glass plate at 200 fps is  $0.36\mu\text{s}$  and the maximum radius of the boundary of the indented region is  $a_1 = 1.13$  mils. Evaluation of Eq.(1) for the radial expansion of the contact zone for a liquid drop impact and Eq.(29) for the solid sphere, yield the results in Fig. 6. It is seen that for the idealization of the liquid drop impact the time required to reach the contact radius  $a_1$  is much shorter than that for the rigid sphere. The rigid sphere comes to rest at  $a_1$  and is then accelerated away from the elastic surface. The duration of the solid sphere impact will be large for elastic spheres as opposed to rigid spheres as long as they undergo small deformations during the collision. It can also be realized that the magnitude of the contact pressures will be higher for the solid sphere when the density is greater than the density of water.

#### b. Liquid Drop Impingement

Now consider a 1.8 mm water drop striking a glass surface at 730 fps. For a soda lime glass specimen,  $p \approx 38,000$  psi according to Eq.(17). Two contact radii listed in Table 5 will be introduced which span the range over which it is thought that lateral outflow may initiate for liquid drop impacts.

Fig. 7 to 9 show the temporal and spatial development of the radial stress component for  $a_1 = 0.156$  mm for  $\phi = 10^\circ$  in Table 5. It is seen that the dilatational stress wave has only propagated to slightly beyond two times the maximum contact area. The tensile stress levels are sufficient to produce fracture, however the duration of the stress at a particular location is extremely short. The principal radial stress distribution in Fig. 8 indicates that the magnitude of the stress and its duration is increased. The orientation of the planes on which the principal tensile stresses occur requires more study before the most probable orientations of the fracture surface can be determined. As seen already in Fig. 4 and 5 the tensile stresses develop in the vicinity of the shear wave and extend back to the boundary of the loaded region. The short duration of the period before

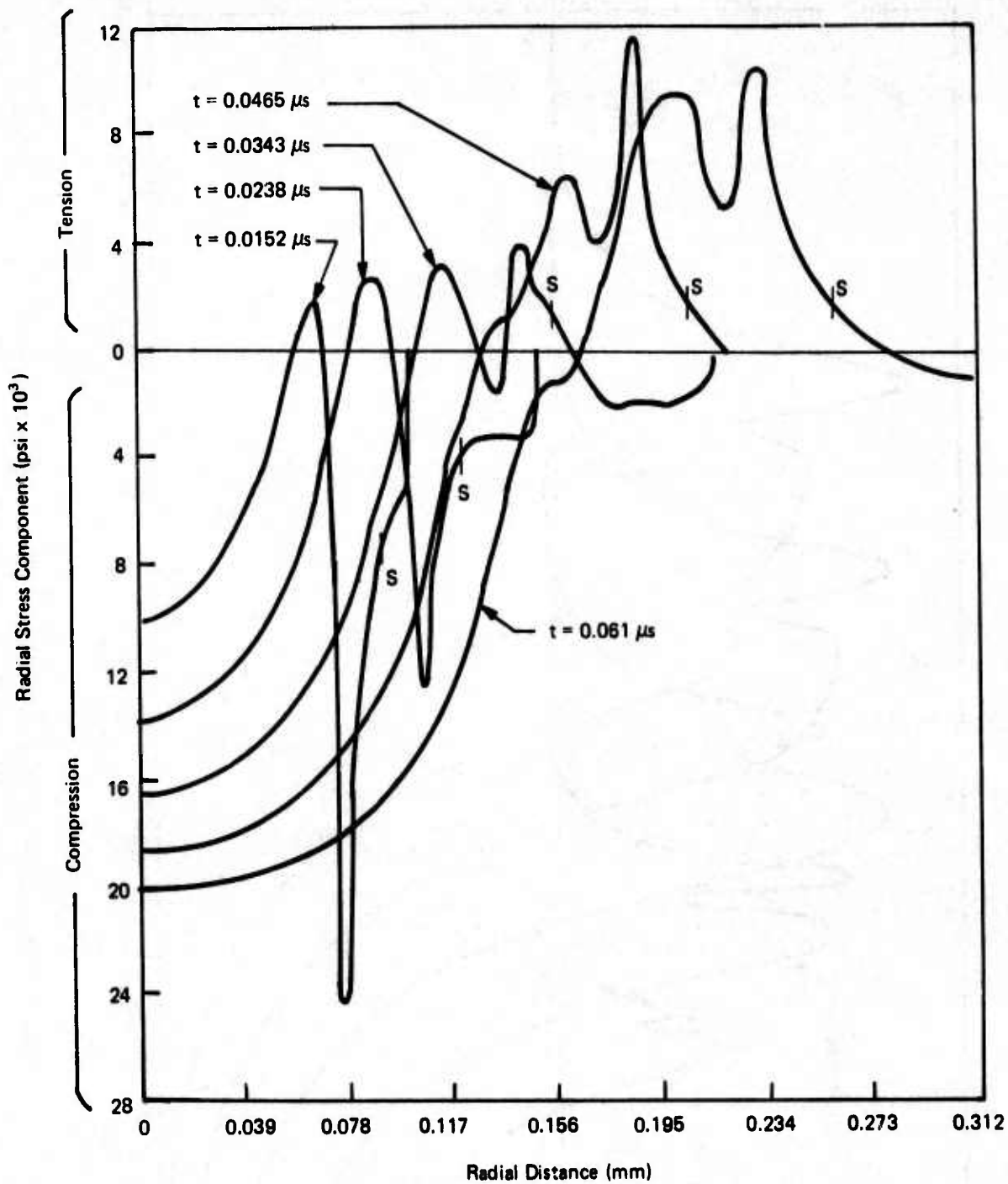


Figure 7. Temporal Development of the Transient Radial Stress Component for  $z = 20 \mu\text{m}$  when  $a_1 = 0.156 \text{ mm}$

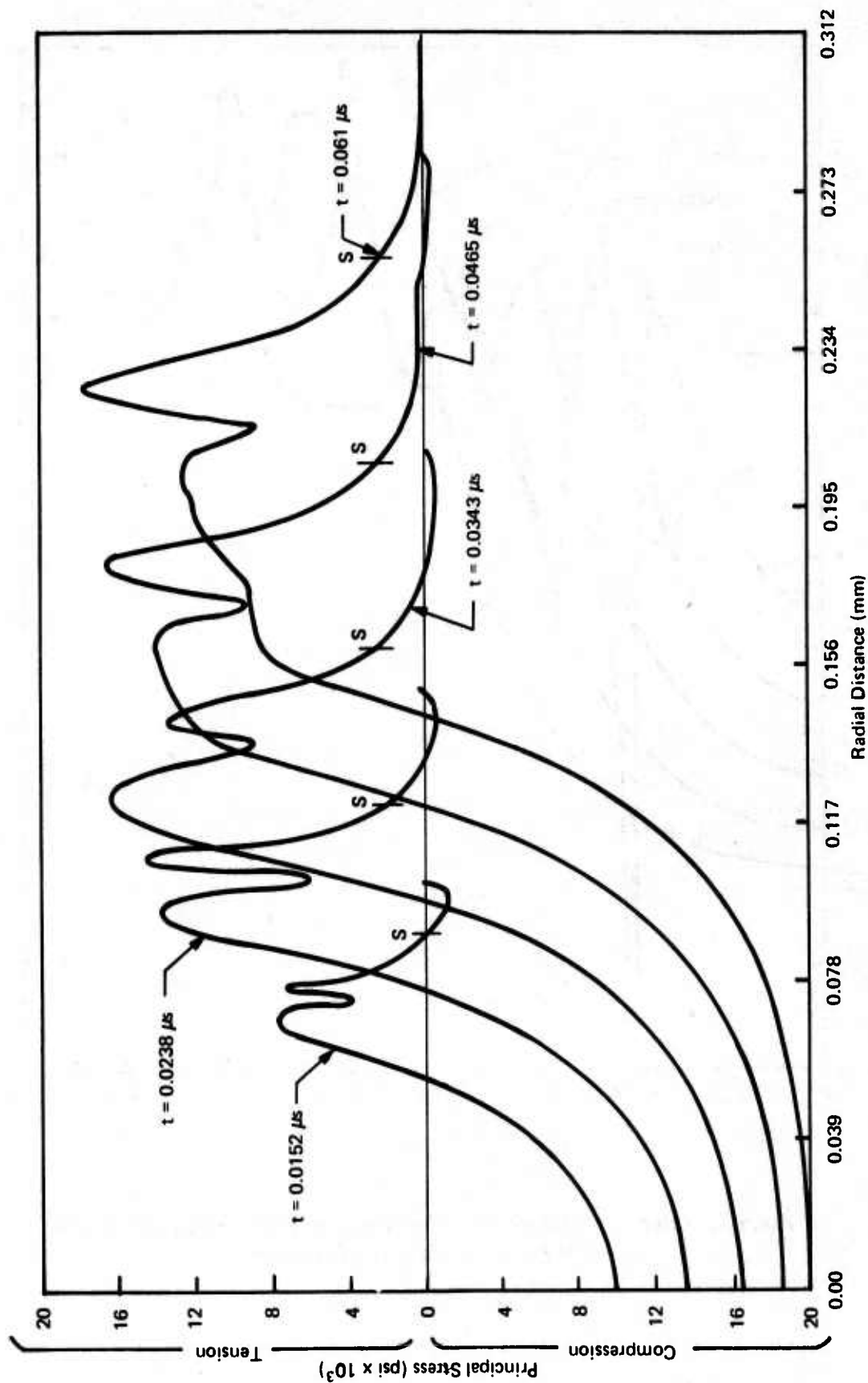


Figure 8. Temporal Development of the Principal Radial Stress Component  
for  $z = 20 \mu m$  when  $a_1 = 0.156 mm$

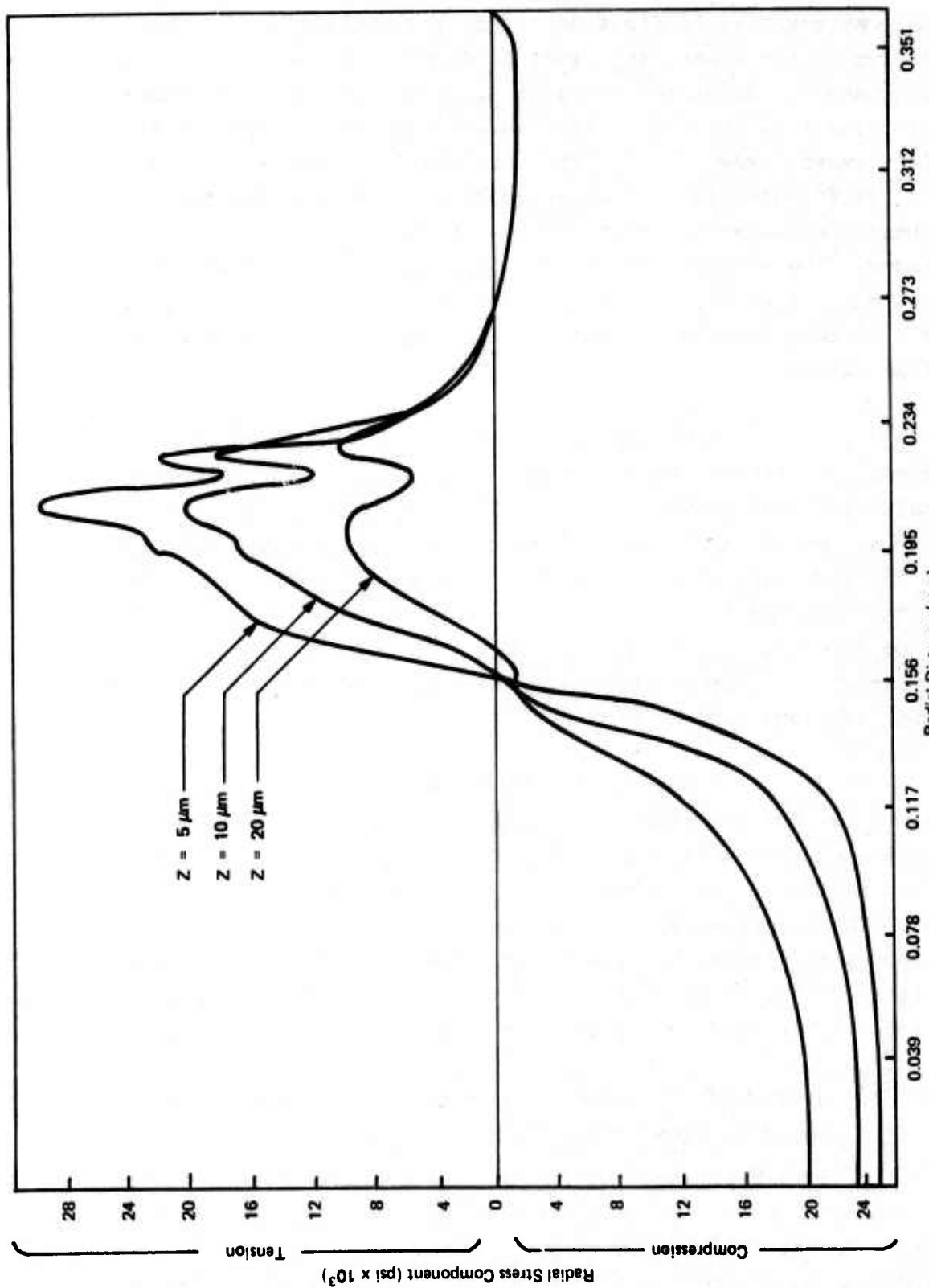


Figure 9. Spatial Distribution of the Transient Radial Stress Component  
when  $a_1 = 0.156 \text{ mm}$



lateral outflow initiates does not allow the shear wave to propagate an appreciable distance beyond the contact zone. The location of the shear wave front is denoted by the letter S in Fig. 6 and 7. Referring to Table 3, it is seen that the shear wave velocities for all of the glasses used in the erosion evaluations except arsenic trisulfide are nearly identical. Only minor differences in the magnitude of the stresses and their propagation characteristics would be anticipated for these glasses. The dynamic and static radial stress distributions are compared in Fig. 10. It is seen that the magnitude of the average transient tensile stresses is much larger than the associated static values.

Similarly plots of the various stress distributions are provided for  $a_1 = 0.380$  mm in Fig. 11 to 14 corresponding to  $\phi = 25^\circ$  in Table 5. For this case the dilatational wave has reached a distance of approximately six times  $a_1$ . The wave patterns are much more developed and moderately high tensile stresses outside the contact area are maintained for almost the entire duration of the impact. The reader can interpret the effects of the impact from the figures provided and on the basis of our previous discussions.

Comparing the plots of the stress distributions for the two contact areas, it is seen that the magnitude and duration of the radial tensile stresses are strongly dependent on the radius of the contact zone before lateral outflow initiates. The experimental observations of the fractures produced in inorganic glasses by liquid drop impacts will be investigated in terms of the computations which can now be made with regard to some of the features of the impact event.

#### C. Ring Fracture Formations on Material Specimens Due to Water Drop Impacts

It was pointed out in the introduction to this section that the damage initiation process in brittle materials at subsonic velocities is a complex phenomenon. At high enough velocities water drops striking brittle materials will produce

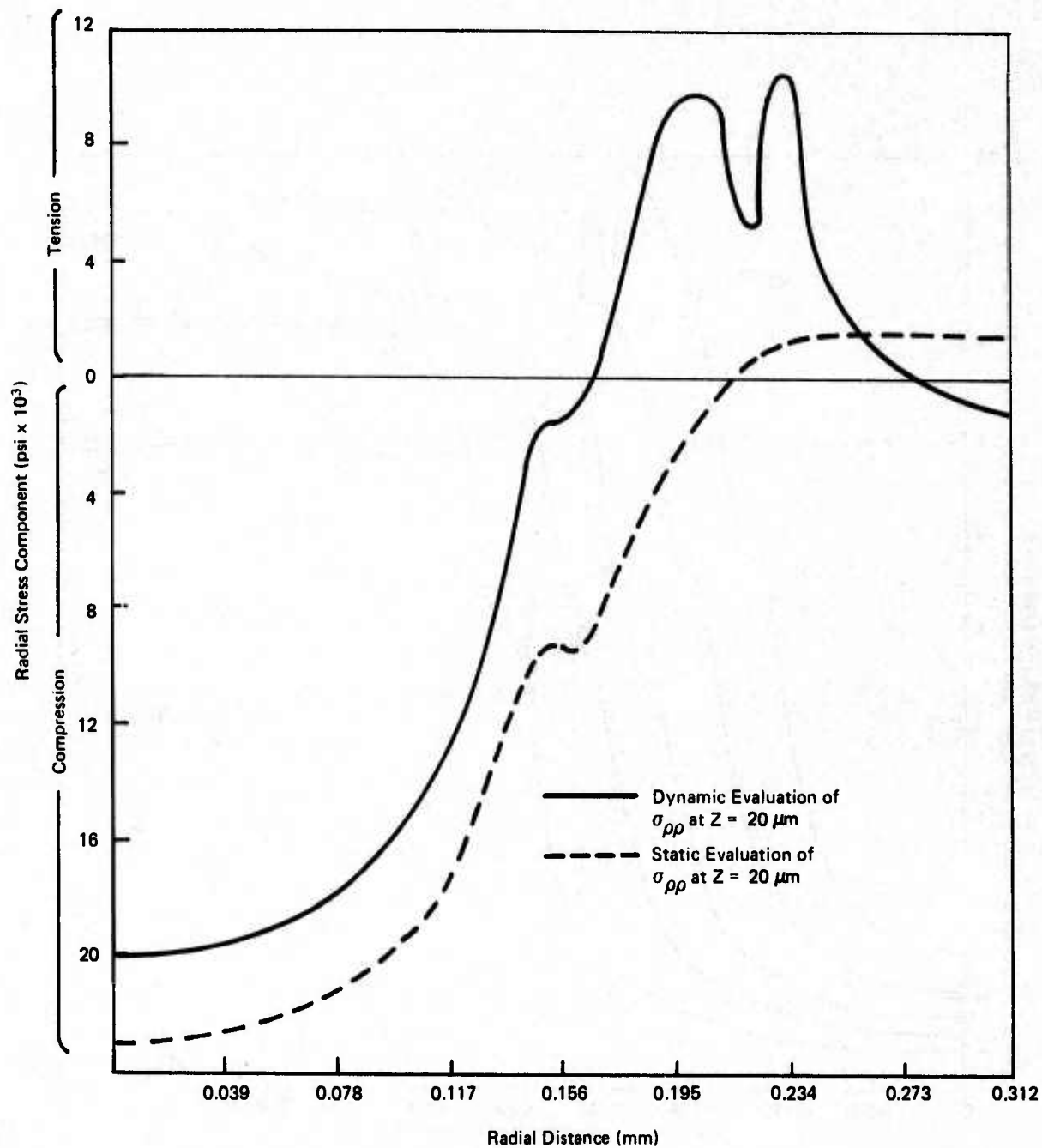


Figure 10. Comparison of Static and Dynamic Radial Stress Components when  $a_1 = 0.156$  mm

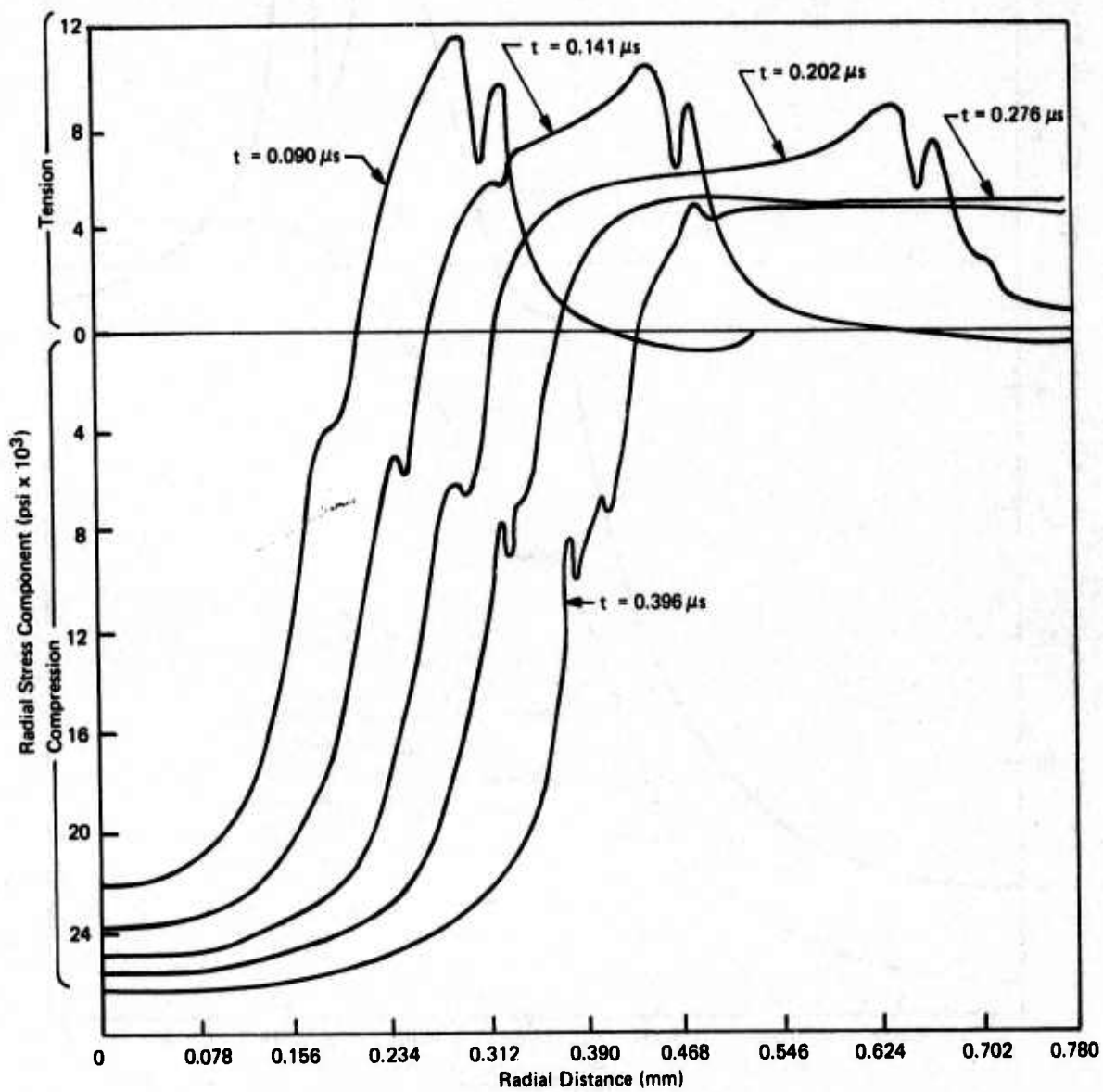


Figure 11. Temporal Development of the Transient Radial Stress Component  
for  $z = 20 \mu\text{m}$  when  $a_1 = 0.380 \text{ mm}$

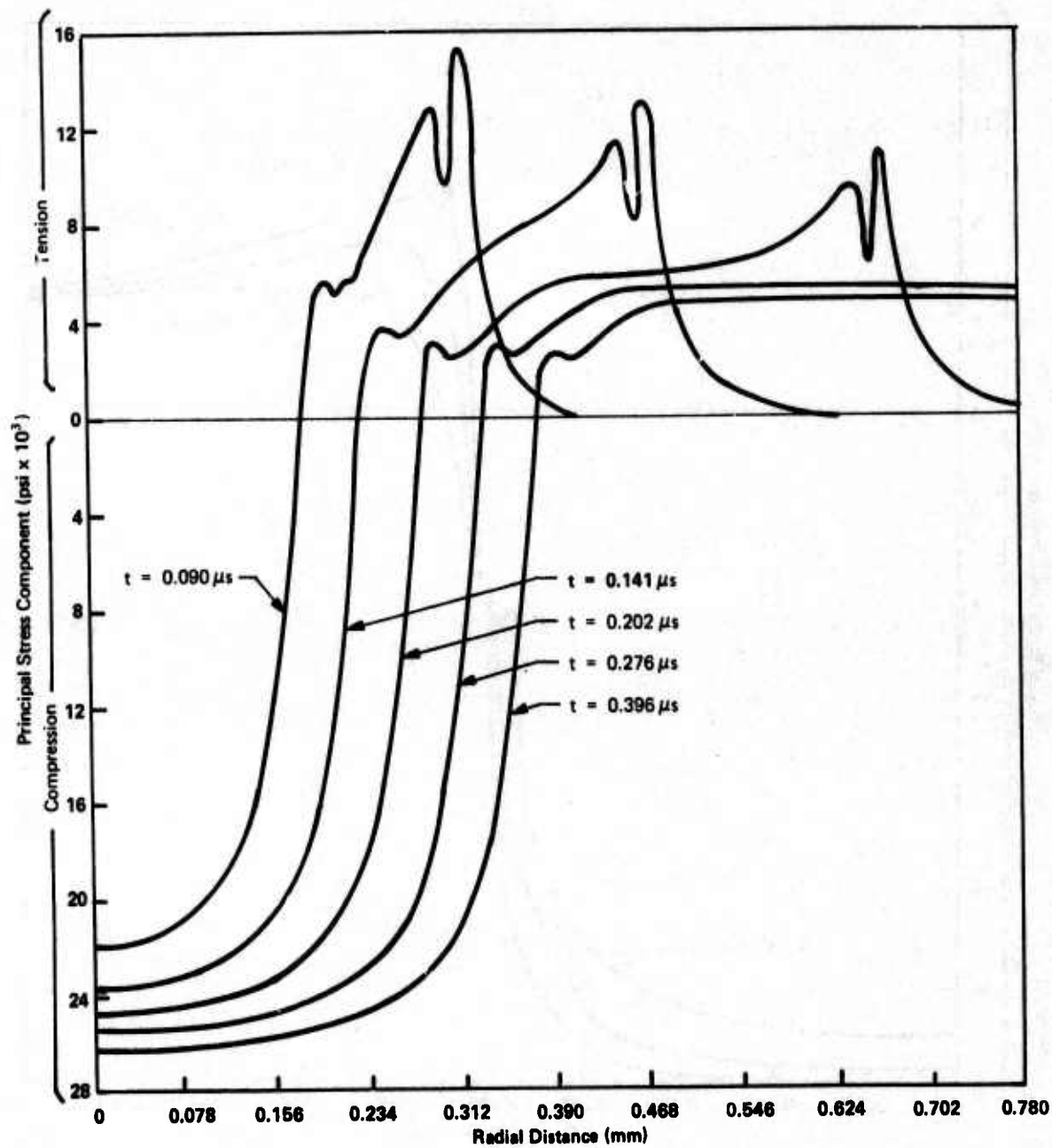


Figure 12. Temporal Development of the Principal Radial Stress Component for  $z = 20 \mu m$  when  $a_1 = 0.380 \text{ mm}$



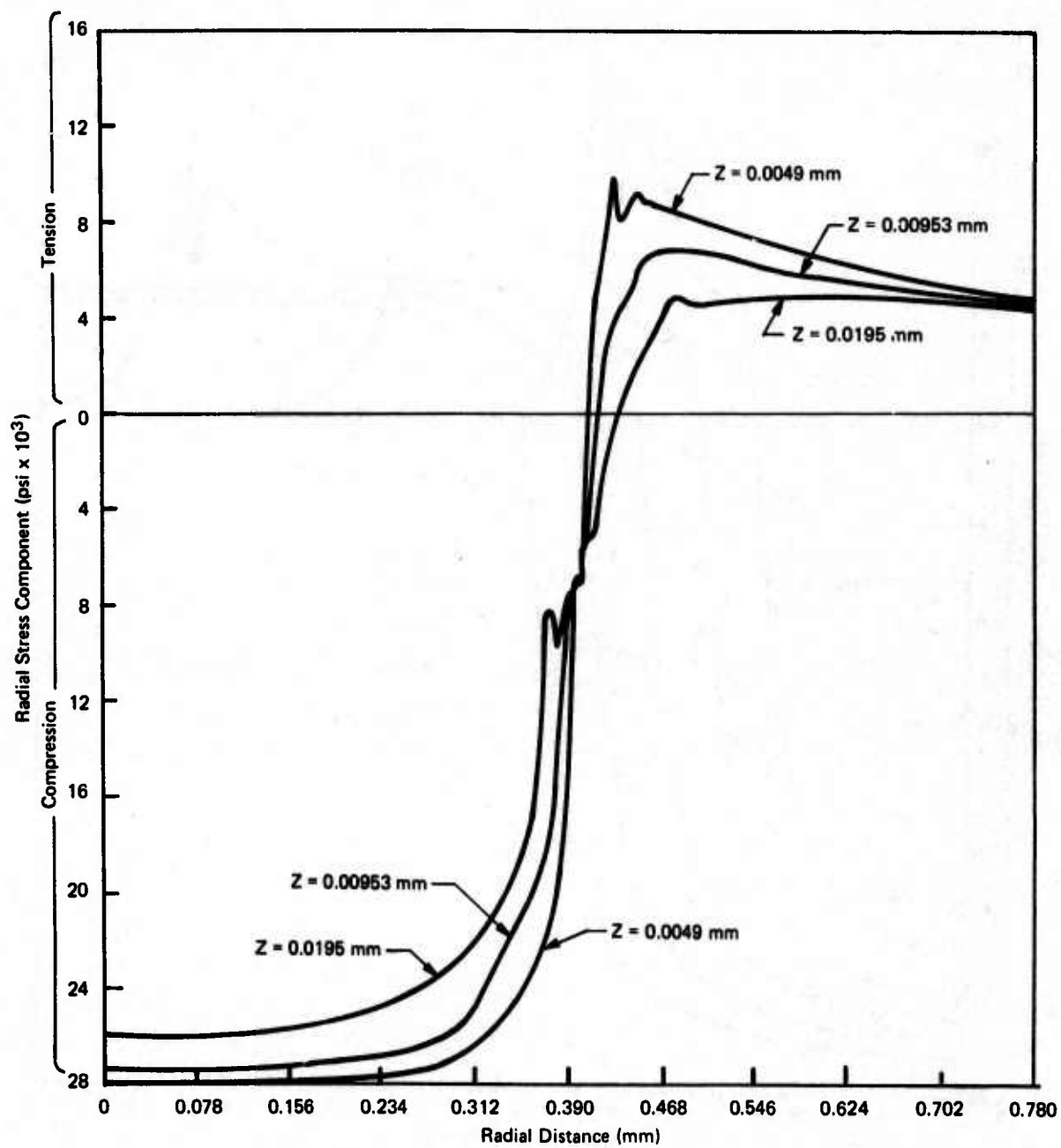


Figure 13. Spatial Distribution of the Transient Radial Stress Component  
when  $a_1 = 0.380 \text{ mm}$

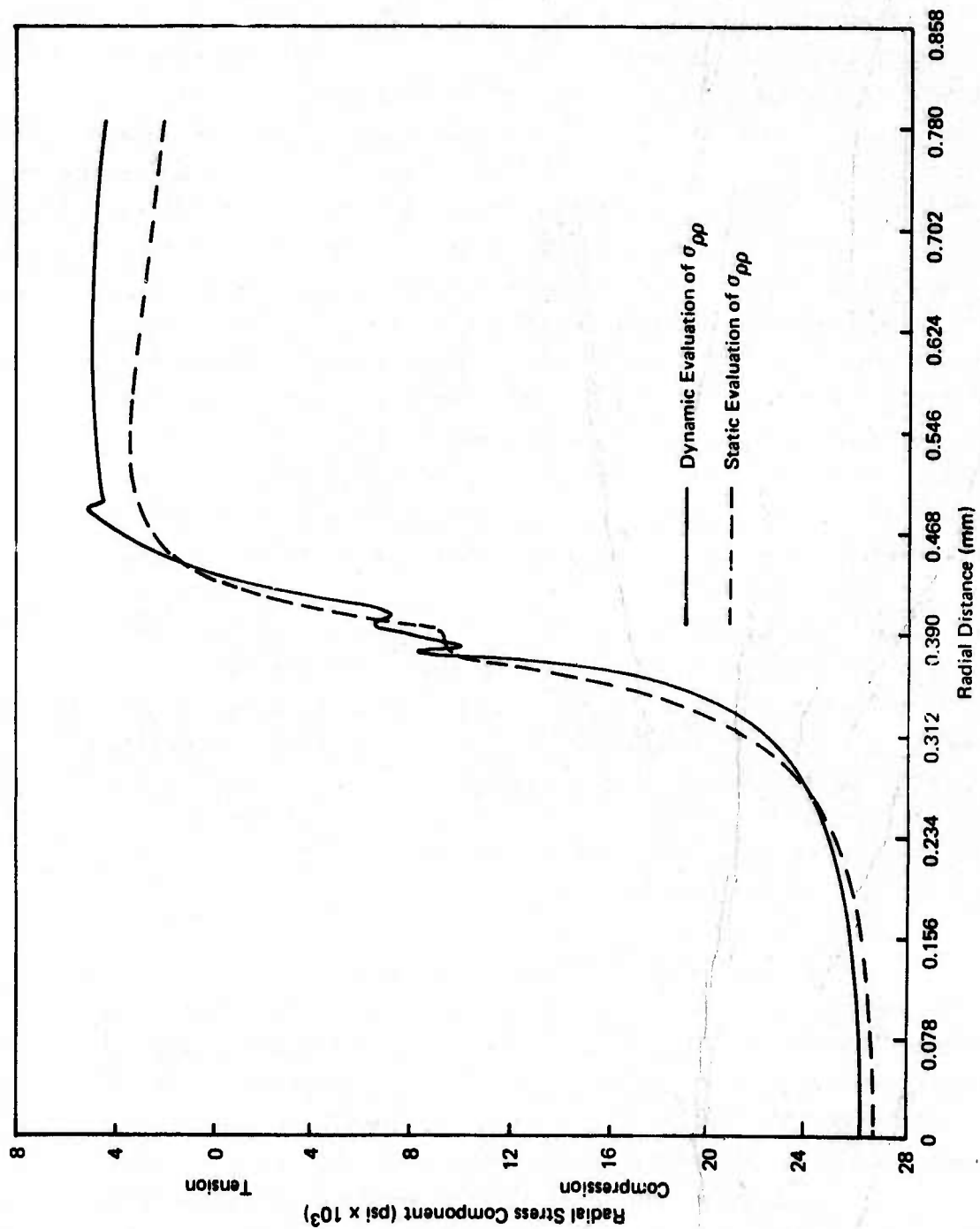
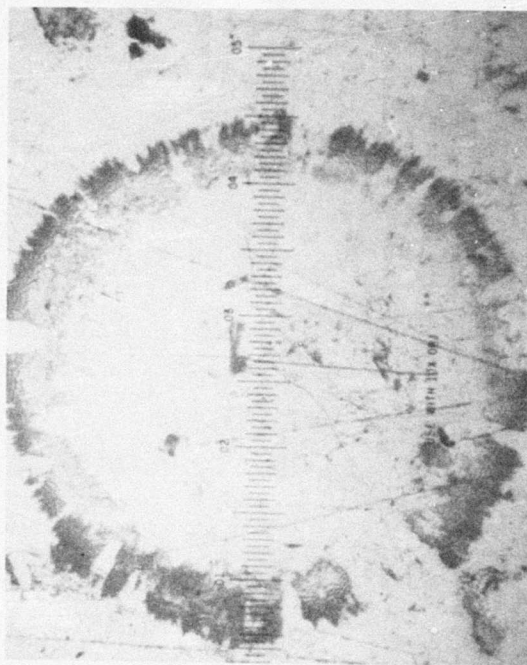


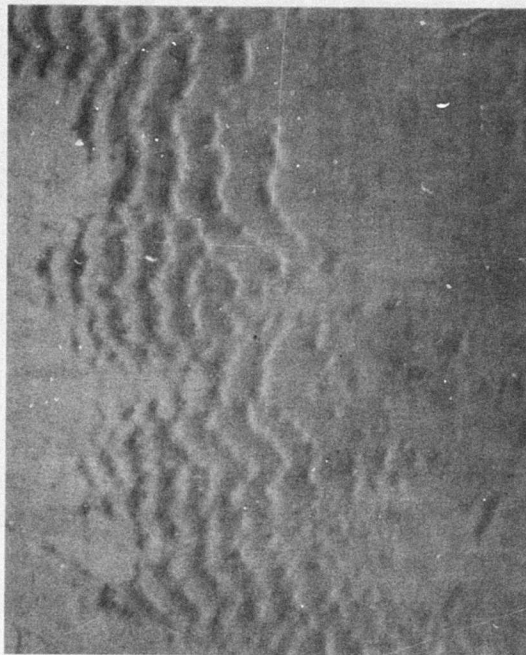
Figure 14. Comparison of Static and Dynamic Radial Stress Components  
when  $a_1 = 0.380$  mm

well-defined ring fractures which form during a single collision and at velocities beyond this range cratering will occur.<sup>(11,12,33)</sup> The impact event is characterizable. On the other hand the sequence of events leading to material removal at subsonic velocities is quite random and complex fracture surfaces are formed after a number of drops strike the same local area on the exposed surface of the specimen. Although the fracture properties measured by standard testing procedures are nearly the same for most of the glasses listed in Table 3, the crack growth behavior due to particulate impingement show considerable variance from the ordering indicated by the measured values of the fracture stress and hardness for the limited test results available. The erosion rate for borosilicate glass is considerably higher than that for soda lime glass (Corning 0080), and the erosion rate for annealed soda lime is considerably higher than that for tempered soda lime glass at a drop impact velocity of 730 fps ( $0.223 \text{ mm}/\mu\text{s}$ ). The erosion rate for fused silica during the early stages of the erosion process for 290 micron glass beads impacting at 200 fps ( $0.061 \text{ mm}/\mu\text{s}$ ) is approximately twice that for borosilicate glass, although this difference decreases as the exposure time increases.<sup>(5,6)</sup> The erosion rate for arsenic trisulfide is extremely rapid consistent with the hardness and fracture stress values recorded in Table 3. The specimen is highly fractured after only a 5-second exposure to the standard rainfield at 500 fps ( $0.153 \text{ mm}/\mu\text{s}$ ).

Individual water drop imprints have been found on some of the materials tested in the AFML/Bell erosion facility. The best examples are shown in Fig. 15 and 16 for polysulfone and polymethylmethacrylate (PMMA) for a 1.8 mm drop diameter at 730 fps. Although the form of the damage surrounding a central undamaged zone is different in the case of polysulfone and PMMA, the general features of the damage correspond to those found by other investigators at higher impact velocities. The central undamaged area for each material is approximately 0.34 to 0.38mm in radius which is only attained at the larger contact angles for the maximum contact radii listed in Table 5. The cause of



(a) Ring Formation on Surface (80X)



(b) Detail of Periphery (800X)

Figure 15. Multiple Ripple Formation on Polysulfone Due to a Single 1.8 mm Water Drop Impacting at 730 fps



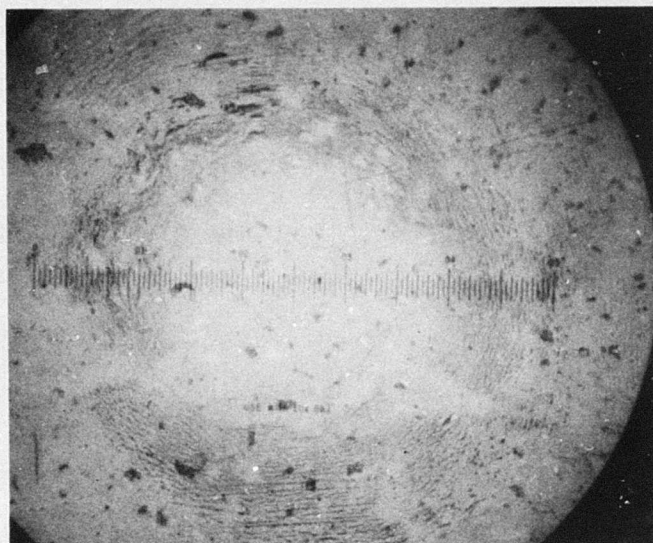
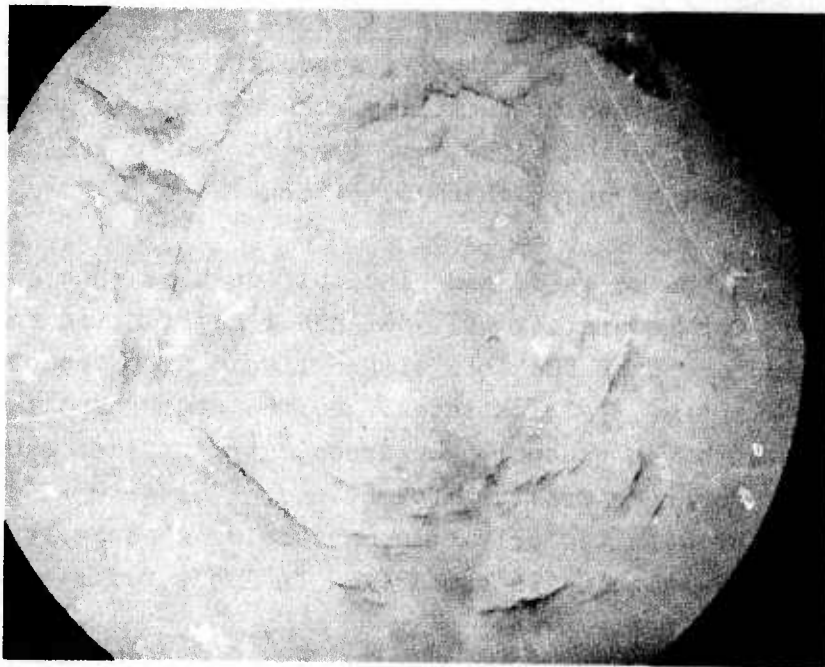


Figure 16. Imprint on the Surface of Polymethylmethacrylate Due to a Single 1.8 mm Water Drop Impacting at 730 fps (60X)

the damage is still a matter of speculation. Polysulfone displays a high degree of ductility when exposed to the strain rates imposed during water drop impacts, while PMMA behaves in a brittle manner under these conditions.

Zinc selenide and zinc sulfide also show a definite tendency for moderately well-defined ring fracture formations which appear to be due to a single liquid drop impact as the example in Fig. 17 illustrates. On the other hand the glasses tested, with the exception of arsenic trisulfide, showed little tendency for ring fracture formations. The general erosive response of selected polymeric materials, glasses, and zinc sulfide and selenide is summarized in Table 6 for water drop impacts at 730 fps.

Borosilicate glass specimens have been exposed to the standard rainfield over a velocity range of from 300 to 730 fps (0.092 to 0.223 mm/ $\mu$ s). The extent of the damage found on the surfaces of these specimens is recorded in Table 7. A negligible amount of damage occurs at 300 fps. As the impact velocity increases the magnitude of the pressure pulse imparted to the specimen's surface increases along with the number of water drop impacts per minute. Gross material removal takes place through a preferential process of erosion pit nucleation and growth as described mathematically in previous reports,<sup>(6,7)</sup> however, the fracture behavior is not coherent but comprises a random array of surface and subsurface fractures. It is not until an impact velocity of 730 fps is reached before coherent ring fractures are observed on the exposed surface. A moderately dense distribution of ring fractures as shown in Fig. 18 can be found over the surface of the specimen after an exposure of 30 sec. which corresponds to roughly 6 or 7 impacts at a particular location. It is interesting to note that the developed ring fractures at 30 sec. appear to be nucleated as a single event, that is, all of the conical fracture surfaces extending into the bulk of the specimen originate at a common origin. However the ring fractures are not observed at an exposure time of 10 sec.



**Figure 17. Ring Crack Formation on Zinc Sulfide due to 1.8 mm Water Drops Impacting at 730 fps (60X)**



TABLE 6  
SUMMARY OF EROSION BEHAVIOR OF TRANSPARENT MATERIALS  
EXPOSED TO STANDARD RAINFIELD AT 730 FPS

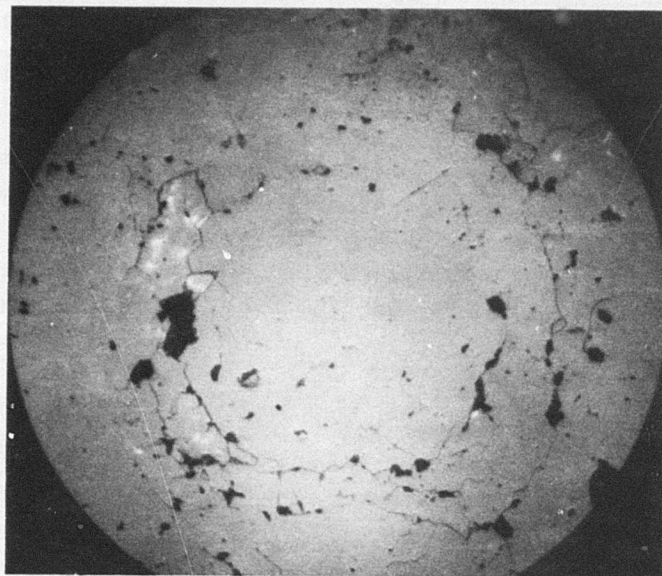
Zinc sulfide, zinc selenide	Initial impacts produce multiple ring fractures. Subsequent impacts extend the fracture surfaces into the interior of the bulk material with minor disruption of the exposed surface of the specimen. Complex patterns of internal fractures develop with relatively little mass loss.
Soda lime glass, borosilicate glass	No coherent ring fractures observed in soda lime glass but some tendency for ring fracture formations displayed in borosilicate glass. Generally random internal fracture surfaces result after numerous water drops have impacted a small region of the exposed surface. Internal fractures once initiated grow and interact to produce highly preferential removal of material from the specimen's surface.
Polymethylmethacrylate	Initial impacts produce multiple ring fractures. These fractures are very shallow in PMMA which behaves in a brittle manner. Fine-scale particle removal occurs shortly thereafter through ring fracture intersection and ring fracture interactions with surface scratches. Fairly uniform rate of material removal takes place over the entire area of the exposed surface as the exposure time increases.
Polysulfone, polycarbonate	Complete and partial multiple ring formations are observed in polysulfone; only short segments of ring formations are seen in polycarbonate. Roughening of the surface layer of the exposed surface occurs after it receives repetitive impacts due to ripple pattern intersections. Pit initiation takes place mainly at surface scratches although it subsequently occurs in highly deformed regions. Material response is ductile with evidence of permanent deformations at the rims of pits. Fracture surfaces originating at scratches penetrate the interior of the specimen and interact at favorably oriented surface scratches. Material removal is initiated by an undermining and upheaval mechanism at these sites.



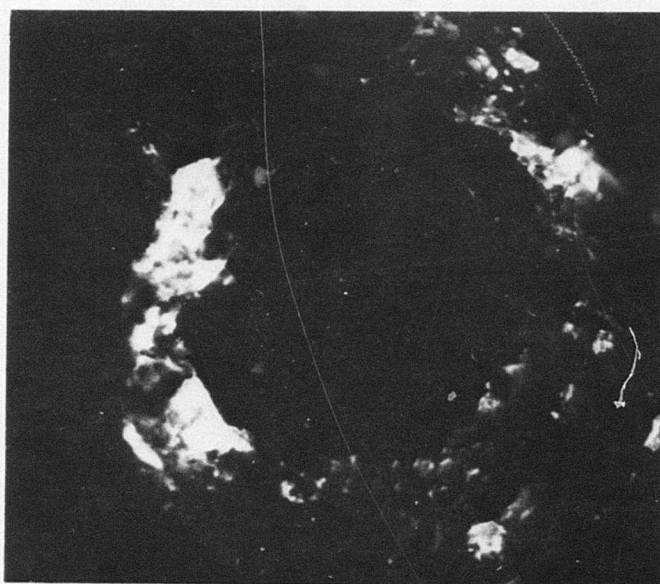
TABLE 7

## RAIN EROSION OF BOROSILICATE GLASS SPECIMENS

Impact Velocity (fps)	Impact Velocity (mm/ $\mu$ s)	Total Exposure (min.)	Impacts per cm <sup>2</sup> min.	Impacts At One Location per min.	Erosion Behavior
300	0.092	40	184	4.68	Insignificant number of subsurface fractures after specimen received 7360 impacts/cm <sup>2</sup> .
400	.122	40	244	6.20	Very isolated internal fractures with shallow penetration into the bulk material. Widely separated pits due to conjoining of subsurface fractures.
500	.153	40	306	7.78	A few very large pits: on the order of several millimeters across. Some radial fractures formed at moderate size pits. Little tendency for coherent ring fractures; uniform distribution of small, random fracture segments. Multiple impact events contributing to growth of internal fracture surfaces can be identified.
600	.183	10	366	9.30	Some tendency for partial ring fracture formations. Uniform distribution of pits formed by intersection of subsurface fractures.
730	.223	2.5	444	11.28	Strong tendency for ring crack formations along with random fracture segments. Rapid removal of material from surface, since each drop impact is capable of producing significant crack growth.



Bright Field (50X)



Polarized Light (50X)

Figure 18. Ring Crack Formations in Borosilicate Glass for 1.8 mm Water Drops Impacting at 730 fps

and are just becoming preceptible at an exposure time of 20 sec. It therefore appears that some precursor of the ring formation must be initiated at an earlier stage of the total exposure time which controls the orientation of subsequent crack growth in the region, since it is not very likely that subsequent drops will impact at the same location to maintain the character of the ring formations seen at the 30 sec. exposures.

The radius of the innermost circular fracture in borosilicate glass ranges from 0.35 to 0.45 mm so the fracture surface is on the order of the larger contact area before lateral outflow occurs considered in Section II.A. The damage observed on soda lime glass is quite distinct from that observed for the borosilicate glass with very little tendency for ring fracture formations, although the general properties for the two glasses recorded in Table 3 are similar.

The observed circular damage formations can be more readily analyzed than the random forms of damage which are a more common occurrence in most of the materials investigated. Conjectures will be made regarding the sequence of events associated with the collision of a water drop with a deformable surface based on the individual drop imprints found on PMMA, polysulfone, and zinc selenide. The transient stresses calculated from Blowers' analytical solution for a compressible drop striking an elastic half-space (described in Section II.B.1) will be used to interpret the origin of the erosion damage observed in PMMA, zinc selenide, and soda lime glass. The material properties required in the computer evaluations of the governing equations are listed in Table 8. The wave velocities are computed from the elastic moduli and densities shown using Eq.(9) and (10) for the long wave length evaluation except for PMMA for which high frequency experimental values are listed. The calculated values for PMMA are significantly different from the experimental values due to the viscoelastic nature of PMMA and the frequency-dependence of the viscoelastic moduli. Excluding polysulfone the other materials listed in Table 8 should behave elastically.

TABLE 8  
DILATATIONAL AND SHEAR WAVE SPEEDS FOR WINDOW MATERIALS

	<u>Polymethylmethacrylate</u>		<u>Poly- sulfone</u>	<u>Zinc Selenide</u>	<u>Zinc Sulfide</u>	<u>Soda Lime Glass</u>
	Quasistatic Values	High Frequency Data			Quasistatic Values	
Specific Gravity	1.19	1.184	1.24	5.27	4.08	2.47
Young's Modulus (psi x 10 <sup>6</sup> )	0.45	1.305	0.36	9.75	10.8	10.0
Poisson's Ratio	0.35	0.325	0.37	0.3	0.3	0.22
Dilatational Wave Speed C <sub>1</sub> (mm/ $\mu$ s)	2.05	2.76	1.885	4.15	4.96	5.71
Shear Wave Speed C <sub>2</sub> (mm/ $\mu$ s)	0.985	1.41	0.855	2.22	2.60	3.23



Zinc selenide, PMMA, and soda lime glass will be subjected to the impact of a single 1.8 mm water drop at 730 fps in order to relate the stress wave computations to the available experimental data. The general observation can be made from the micrographs in Fig. 15 to 18 that the radius of the central undamaged zone corresponds to the larger contact radii listed in Table 5. The radial locations of the shear and dilatational wave fronts are provided in Table 9 when the contact radii reach values corresponding to included angles ranging from 10 to 25 degrees as recorded in Table 5. The nature of the stress distributions in the three materials selected will be investigated for the larger contact angles.

#### 1. Zinc Selenide

The magnitude of the stress components are normalized to unity in all of the plots which will be described. The magnitude of the actual stress component is found by multiplying the value on the graph by the magnitude of the liquid/solid interfacial pressure. Using the calculated dilatational wave velocity for zinc selenide in Table 8, Eq.(15) becomes

$$V_w = \frac{V_o}{1 + \frac{\rho_s C_s}{\rho_w U_w}} \quad (38)$$

For  $V_o = 730$  fps ( $0.2225$  mm/ $\mu$ s),  $V_w = 0.01785$  mm/ $\mu$ s and  $p_w = 3.91$ kbar ( $56,600$  psi) as determined from Eq. (16). The magnitude of the liquid/solid interfacial pressure for an impact velocity of 1100 fps is 6.18 kbar ( $89,500$  psi).

Brittle infrared windows will be susceptible to fracture initiation in domains where tensile stresses of sufficient magnitude occur. Fig. 19 and 20 provide an overview of the regions within the half-space where tensile stresses do exist in zinc selenide substrates at a drop impact velocity of 730 fps. When the critical angle for lateral outflow  $\phi=20^\circ$ , the dominant radial tensile stresses are only found near the surface of the specimen slightly ahead of the shear wave front and extending

TABLE 9  
LOCATION OF SHEAR AND DILATATIONAL WAVE FRONTS (1.8mm DRCP AT 730 FPS)  
ON PLANE Z=0

Material	Maximum Angle for Lateral Flow, $\phi$	Loaded Area (mm)	Shear Wave Front (mm)	Dilatational Wave Front (mm)
PMMA	10°	0.156	0.157	0.204
	15°	.233	.262	.411
	20°	.308	.406	.691
	25°	.380	.721	1.033
Zinc Selenide	10°	0.156	0.181	0.277
	15°	.233	.347	.588
	20°	.308	.572	1.008
	25°	.380	.847	1.522
Soda Lime Glass	10°	0.156	0.238	0.365
	15°	.233	.495	.793
	20°	.308	.842	1.371
	25°	.380	1.267	2.079

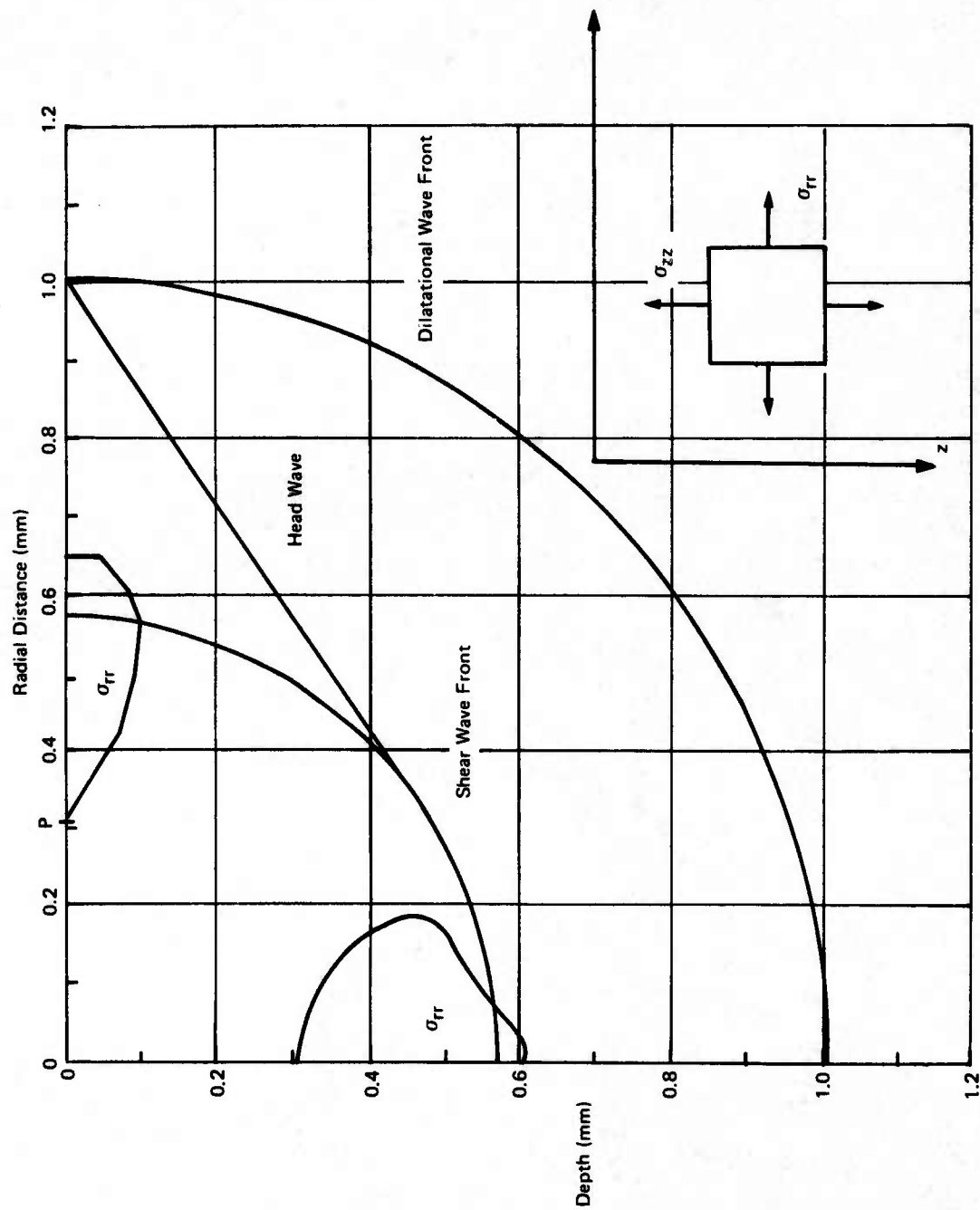


Figure 19. Distribution of Tensile Radial Stresses in Zinc Selenide when  $\varphi = 20^\circ$

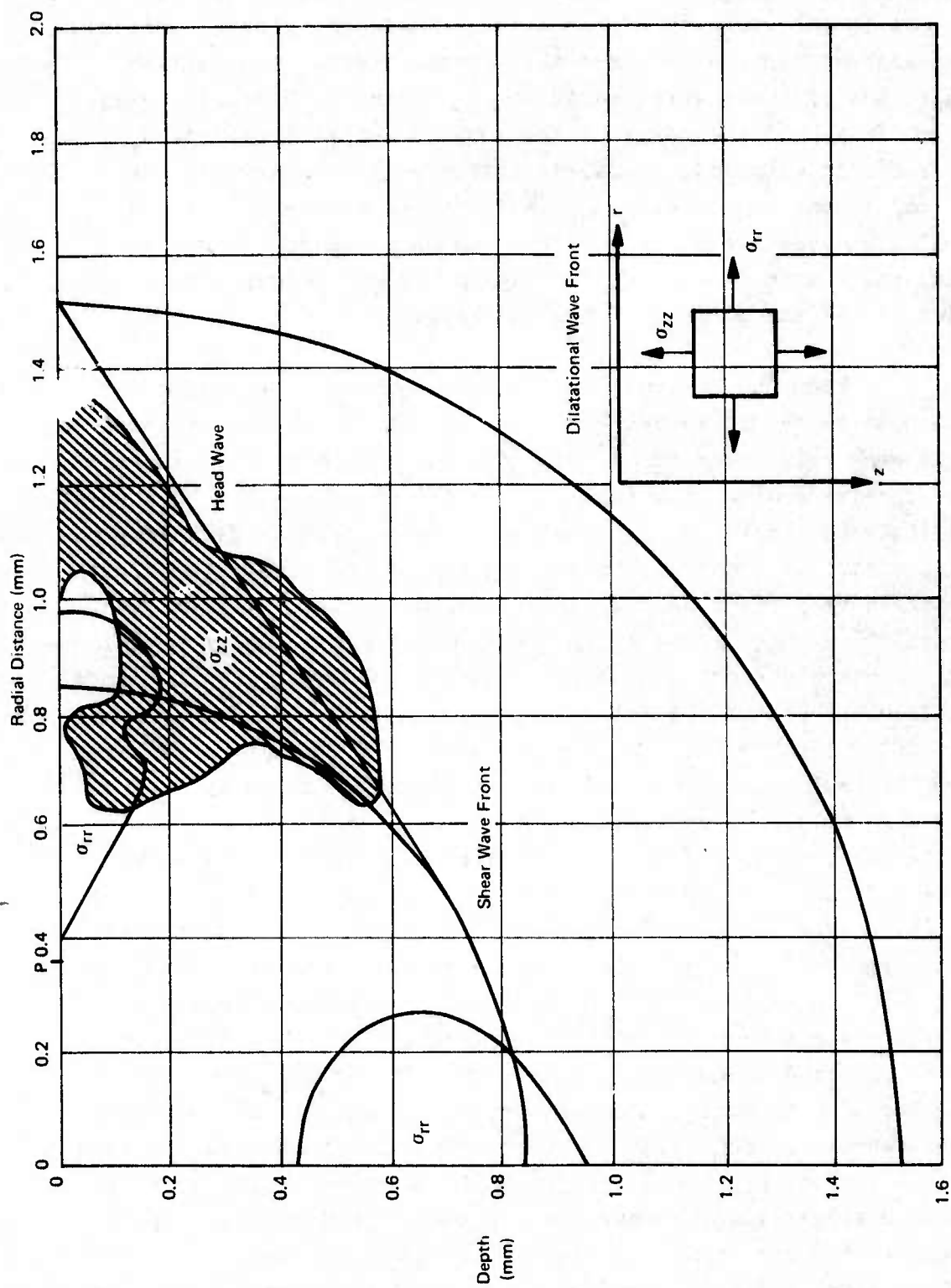


Figure 20. Distribution of Tensile Stresses in Zinc Selenide when  $\varphi = 25^\circ$



back to the loaded area. A region of tensile radial stress exists in the vicinity of the axis through the point of initial contact between the drop and the target, however the maximum magnitude of these stresses is on the order of 1000 psi. For  $\phi=25^\circ$  (Fig. 20) the range of the tensile radial stresses,  $\sigma_{rr}$ , is somewhat extended. A fairly extensive domain wherein the normal stress components,  $\sigma_{zz}$ , are tensile also exists for  $\phi=25^\circ$ , however the distribution of tensile values for  $\sigma_{zz}$  is negligible when  $\phi=20^\circ$ : the tensile values only occur in the vicinity of the surface of the half-space.

From the general maps of the stresses in the zinc selenide target it is concluded that critical tensile stresses will generally occur at and near the surface layer at a radial distance extending from just outside the loaded region to a point slightly beyond the shear wave front. A relatively weak compressive stress is found at the surface beyond the shear wave front which is consistent with the photographic records of the impact event<sup>(11-13)</sup> and is due to the fact that the loading is normal to the plane surface of the half-space. The magnitude of these radial stresses is indicated in Fig. 21 and 22 for a water drop impact of 730 and 1100 fps, respectively. The graphs shown are for one instant of time when the loaded area reaches an included angle of  $\phi=25^\circ$ . The magnitude of the tensile stresses can be compared for 0.5, 1.8 and 2.5 mm drop diameters. It is seen that at this time the duration of the tensile stress for an 0.5 mm water drop is exceedingly short. The direct effects of this size drop at higher velocities would probably be detrimental, but fracture initiation through stress wave interactions with existing flaws does not seem very probable for the short pulse durations imposed on the target. The duration and magnitude of the transient tensile stresses for the 1.8 and 2.5 mm drops do seem capable of producing the circumferential fractures observed on the surface of zinc selenide specimens. The magnitude of the tensile stresses are comparable for the 1.8 and 2.5 mm drops; however, the duration of these stress levels is longer for the 2.5 mm drop, and correspondingly the resulting damage should be

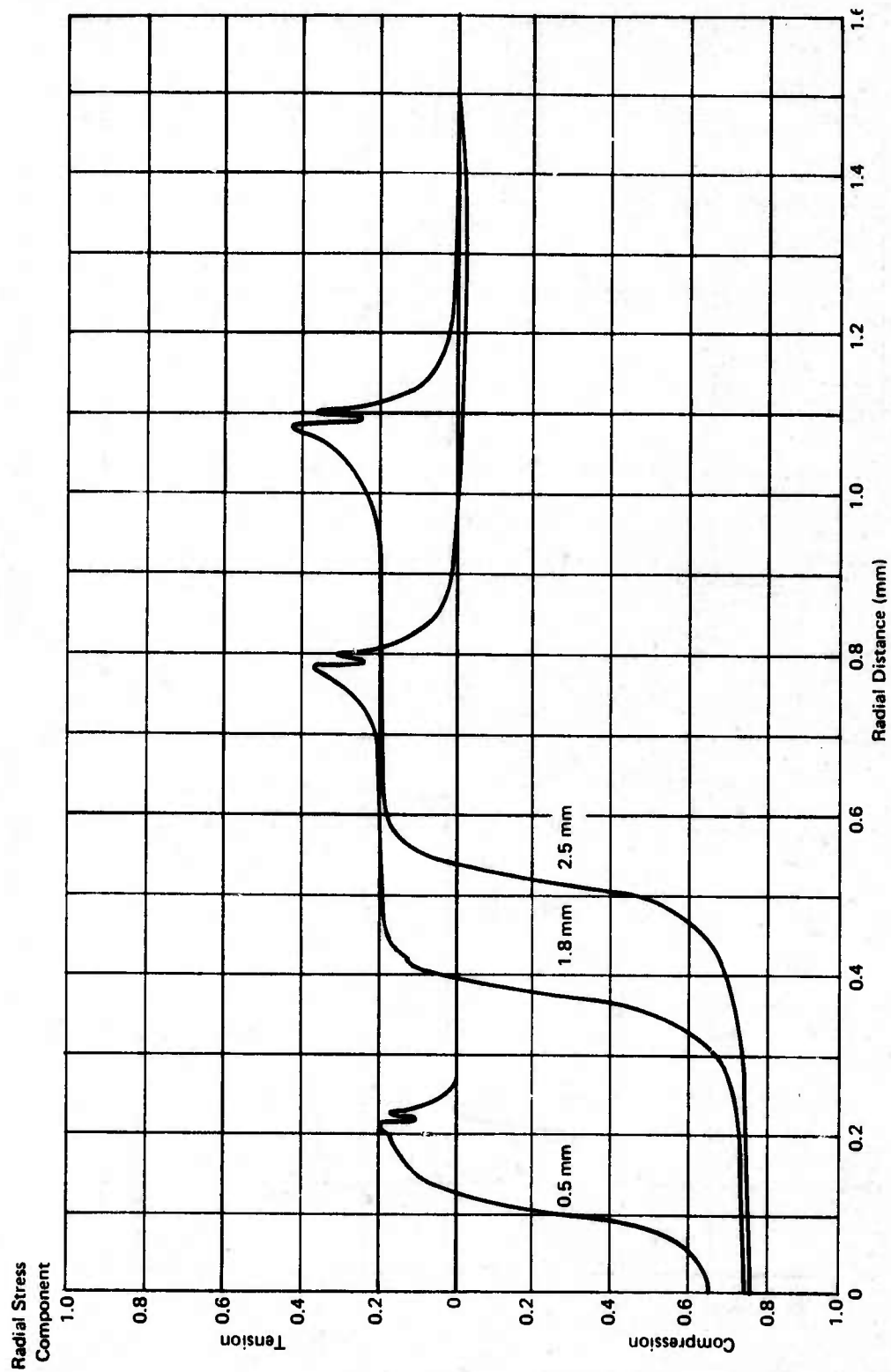


Figure 21. Variation of Radial Stress Component (at  $z = 10 \mu\text{m}$ ) with Drop Diameter for Impacts at 730 fps on ZnSe ( $\phi = 25^\circ$ )

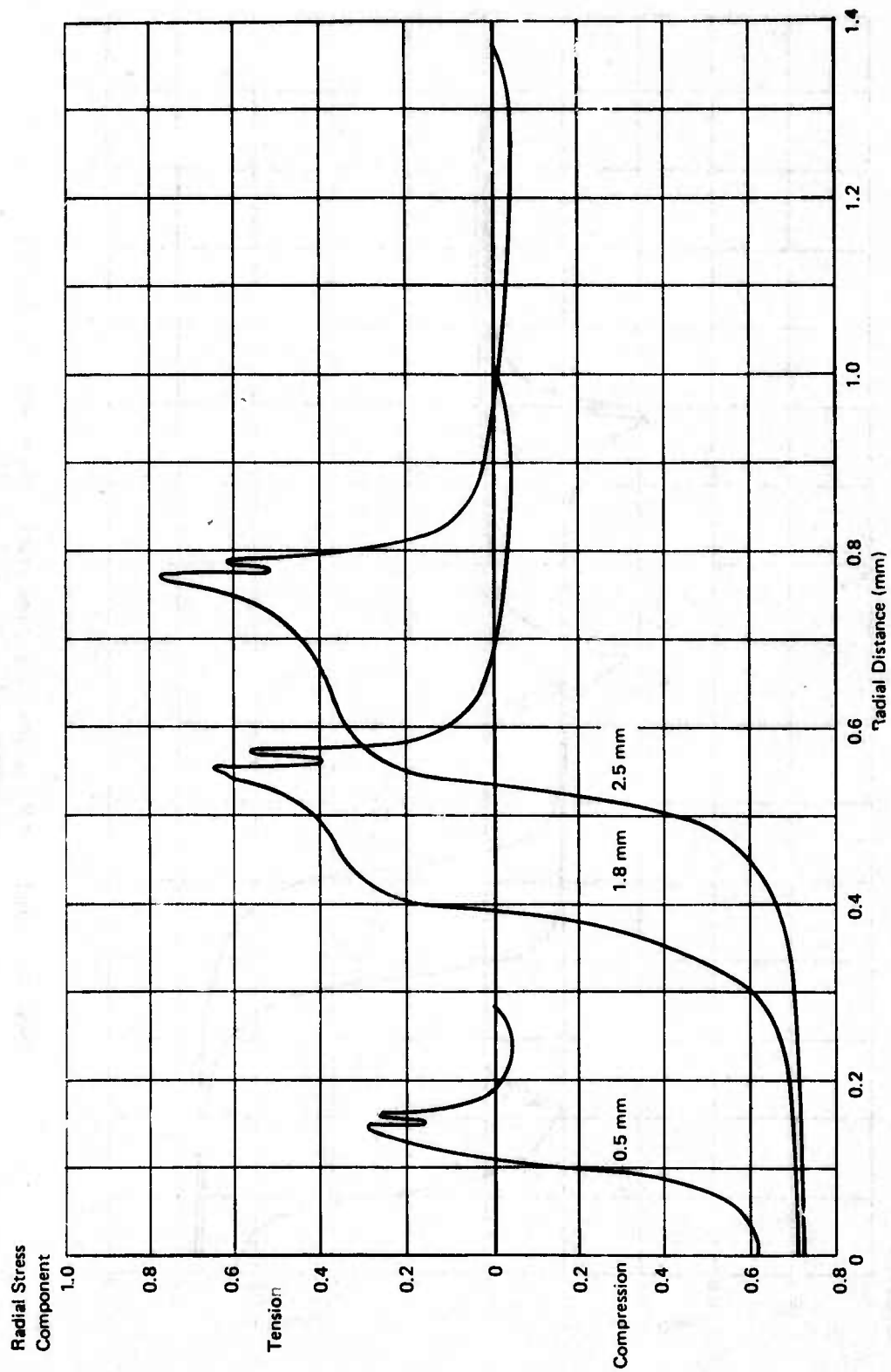


Figure 22. Variation of Radial Stress Component (at  $z = 10 \mu\text{m}$ ) with Drop Diameter for Impacts at 1100 fps on ZnSe

more extensive. From these graphs at  $z=10\mu\text{m}$  the sustained tensile radial stress  $\sigma_{rr} = 11,300$  psi at  $V_0 = 730$  fps. At 1100 fps  $\sigma_{rr}$  is maintained at a value exceeding 27,000 psi for a reasonably long duration with respect to the impact event.

The temporal and spatial development of the principal radial stress distributions for 1.8 and 2.5 mm drops impacting at 730 fps are shown in Fig. 23 to 28 for a range of impact conditions. These graphs are presented to illustrate the nature of the stress distribution within the half-space representing the zinc selenide target. A strong compression pulse is propagated along the axis of symmetry which diminishes in intensity in the radial direction as the included angle between the axis of symmetry and the line drawn from the point of impact to a point in the half-space increases. The magnitude of the normal compressive stress,  $\sigma_{zz}$ , as a function of distance into the target is shown in Fig. 29 along the axis passing through the initial point of contact. In contrast to the one-dimensional shock and plane elastic wave analyses the magnitude of this stress component decreases with distance due to the geometric attenuation of a spherical wave.

The variation in the response of the target when the elastic properties and density are changed will be illustrated for the case of polymethylmethacrylate and soda lime glass. The primary wave speeds for PMMA are considerably lower than those for zinc selenide and higher in the case of soda lime glass. This difference directly affects the development of the transient stress states in these materials.

## 2. Polymethylmethacrylate

The mechanical response of PMMA is more complex than that associated with linearly elastic materials to which Blowers' analysis is applicable. The moduli for polymeric materials are a function of the frequency of the applied loadings, therefore the long wavelength approximation to the acoustic velocities using quasistatic loading conditions are not representative of



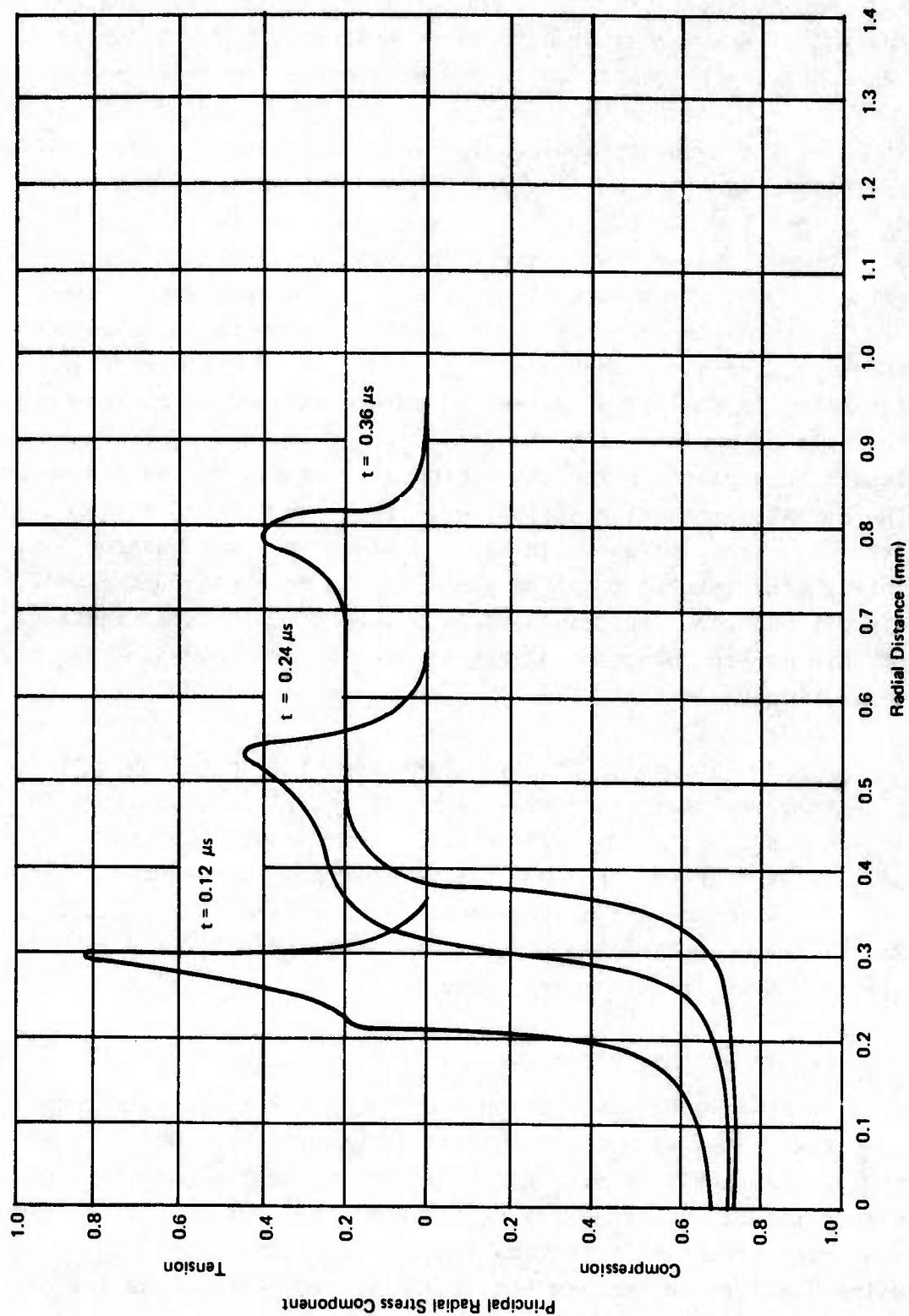


Figure 23. Temporal Development of Principal Radial Stress Component in Zinc Selenide at  $z = 10 \mu\text{m}$  when  $\phi = 25^\circ$  and the Impact Velocity is 730 fps

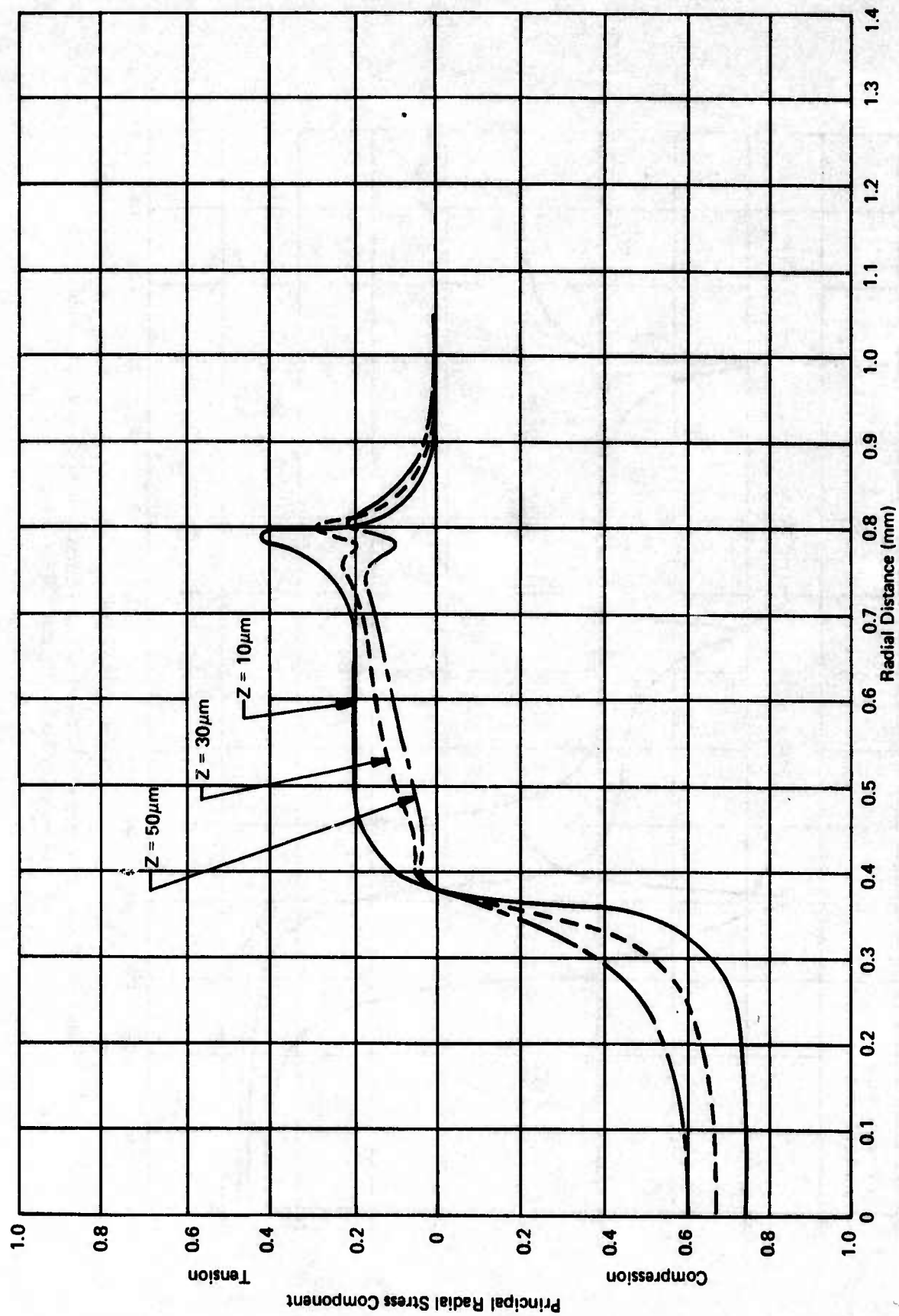


Figure 24. Variation of Principal Radial Stress Component in Zinc Selenide when  $\phi = 25^\circ$

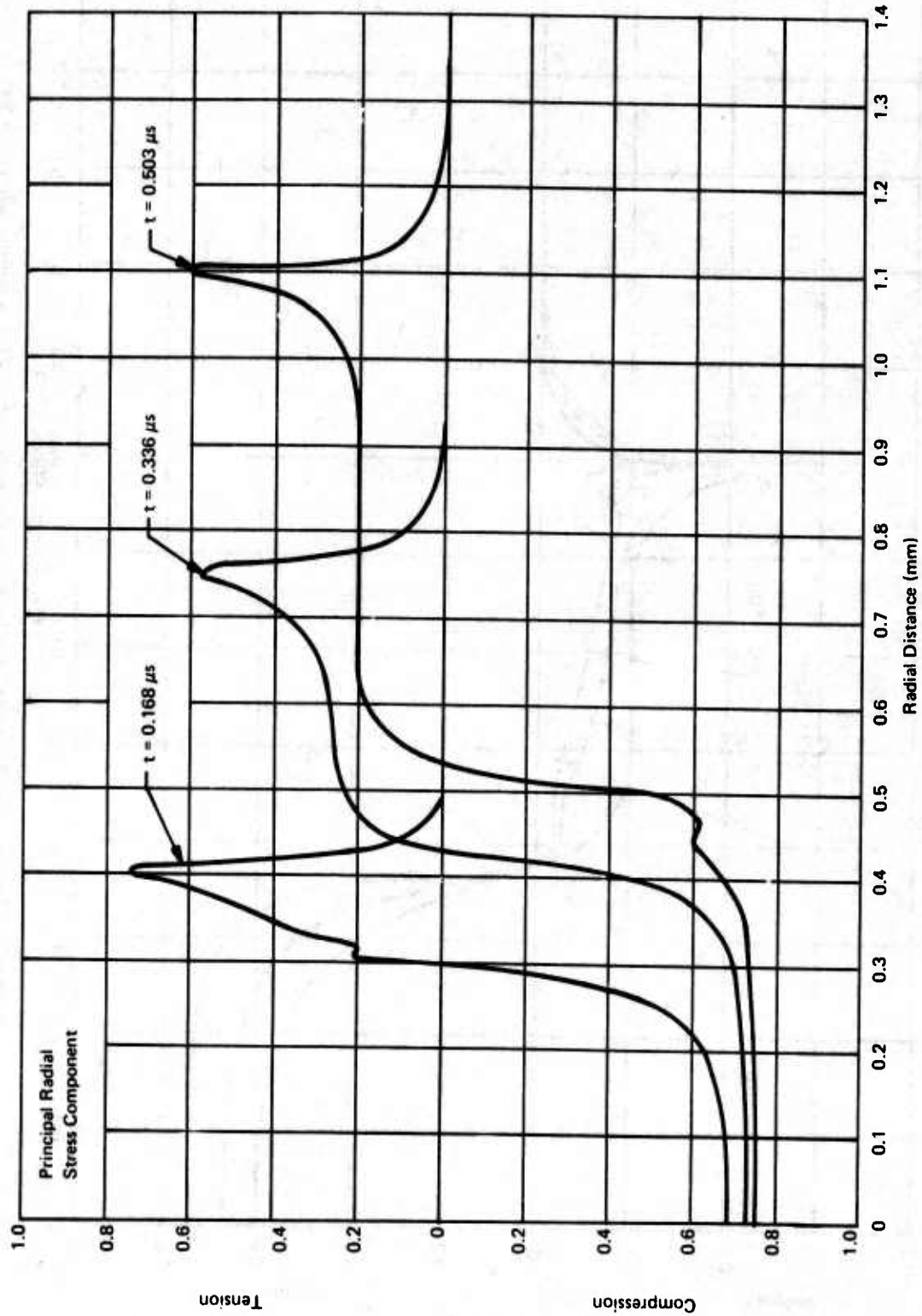


Figure 25. Temporal Development of Principal Radial Stress Component in Zinc Selenide when Impacted by 2.5 mm Drop at 730 fps ( $\phi = 25^\circ$ )

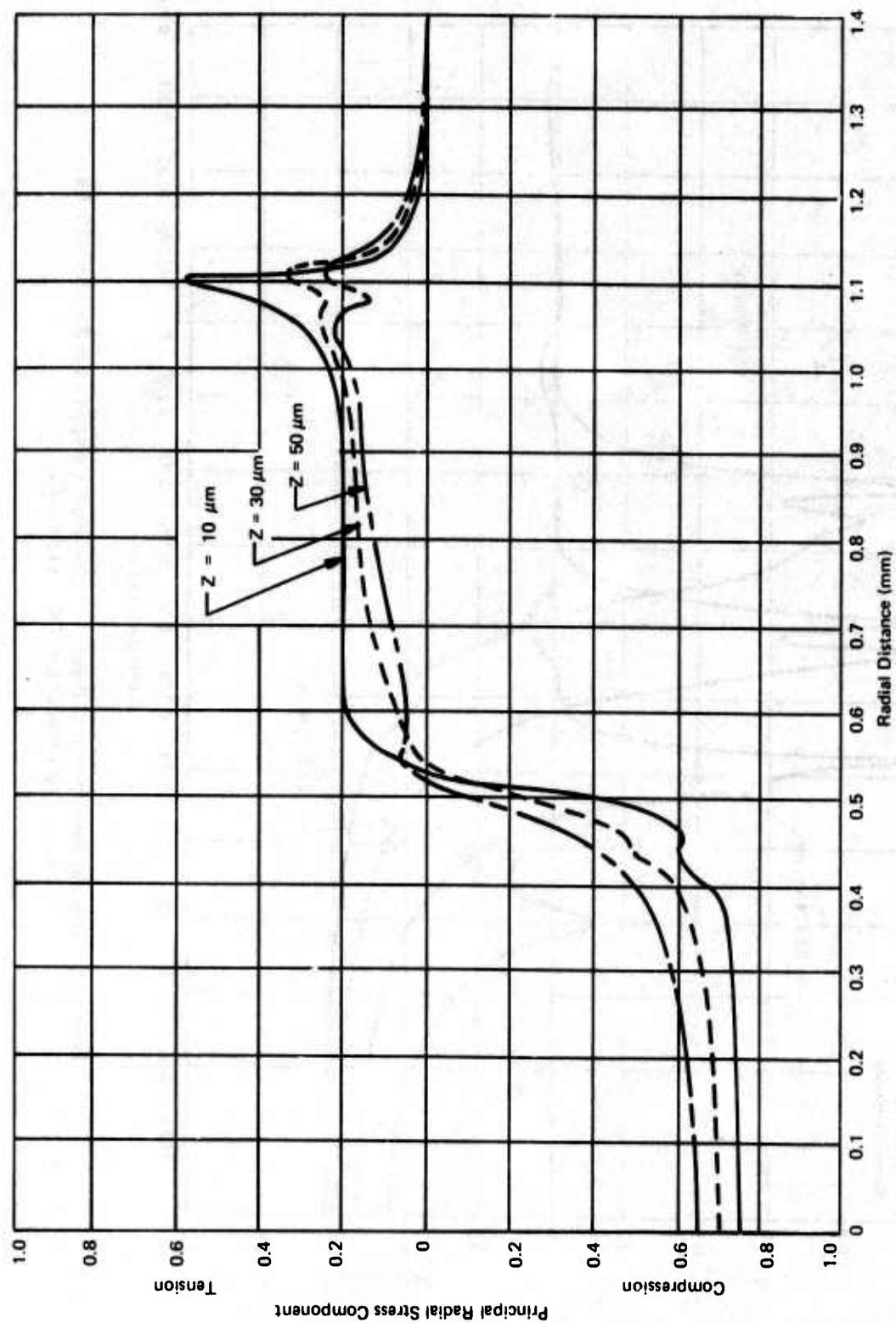


Figure 26. Variation of Principal Radial Stress Component in Zinc Selenide with Depth for 2.5 mm Drop Impacting at 730 fps ( $\varphi = 25^\circ$ )



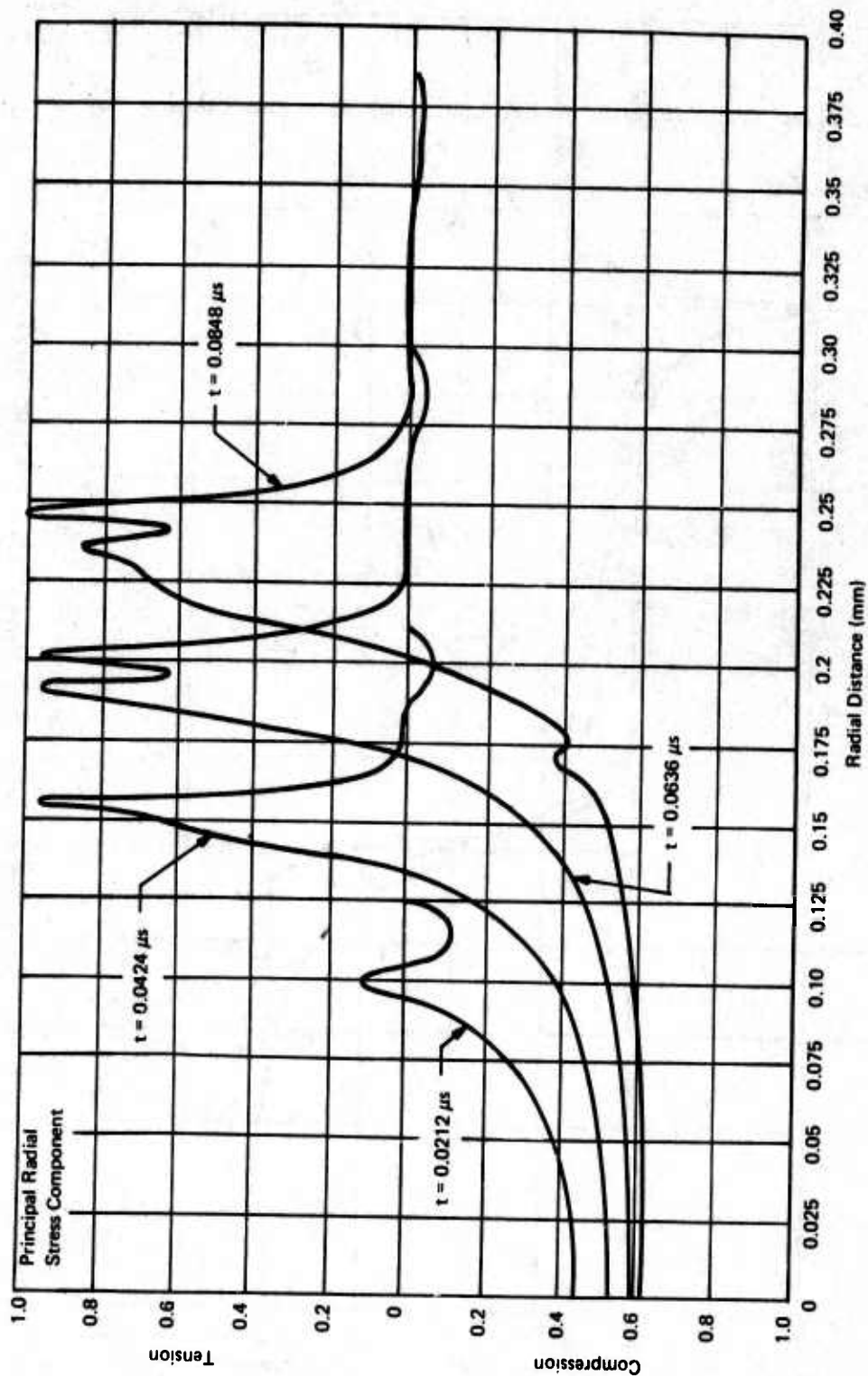


Figure 27. Temporal Development of Principal Radial Stress Component in Zinc Selenide for 2.5 mm Drop Impacting at 730 fps ( $\phi = 10^\circ$ )

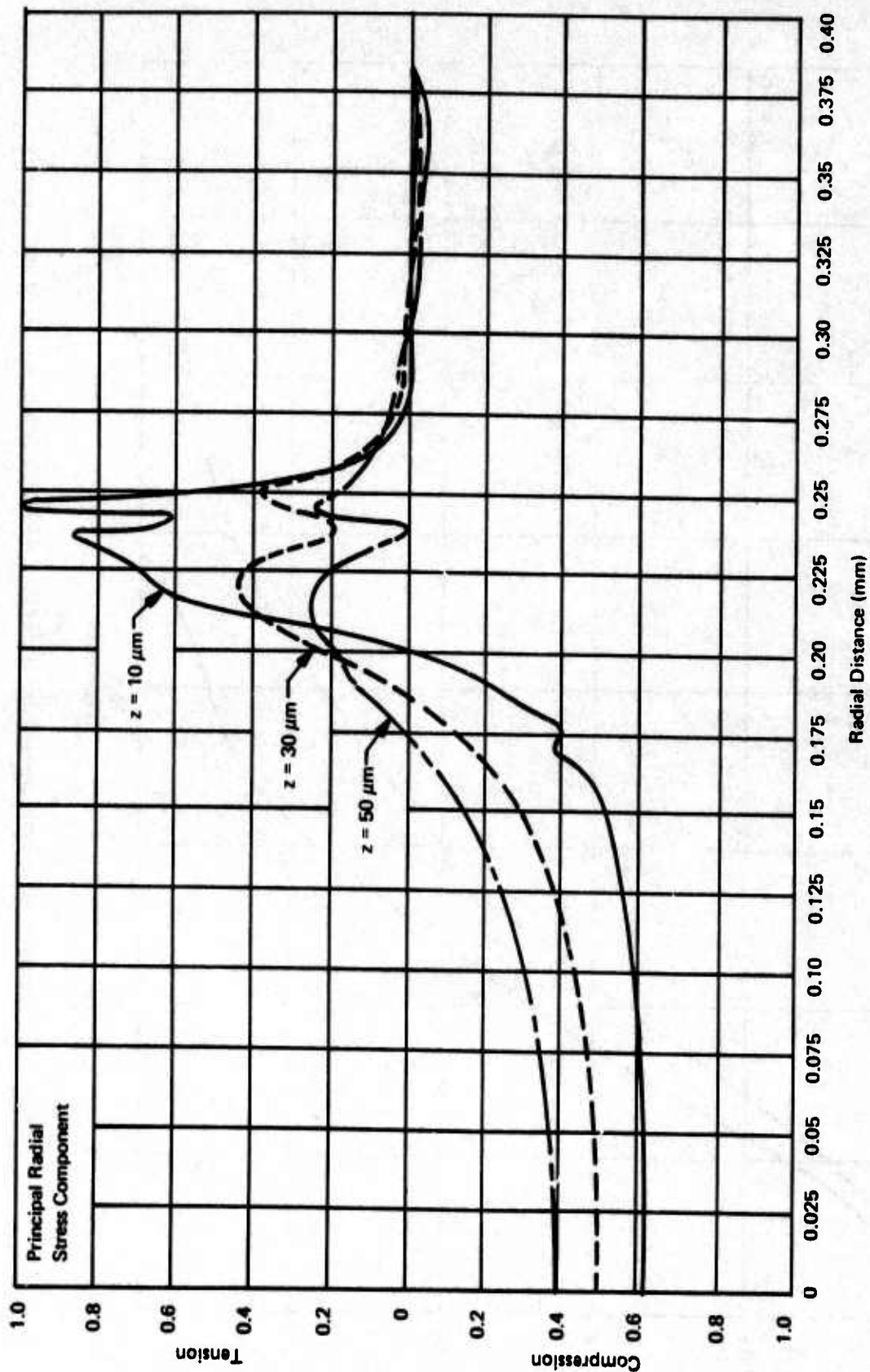


Figure 28. Variation of Principal Radial Stress Component in Zinc Selenide with Depth for 2.5 mm Drop Impacting at 730 fps ( $\phi = 10^\circ$ )

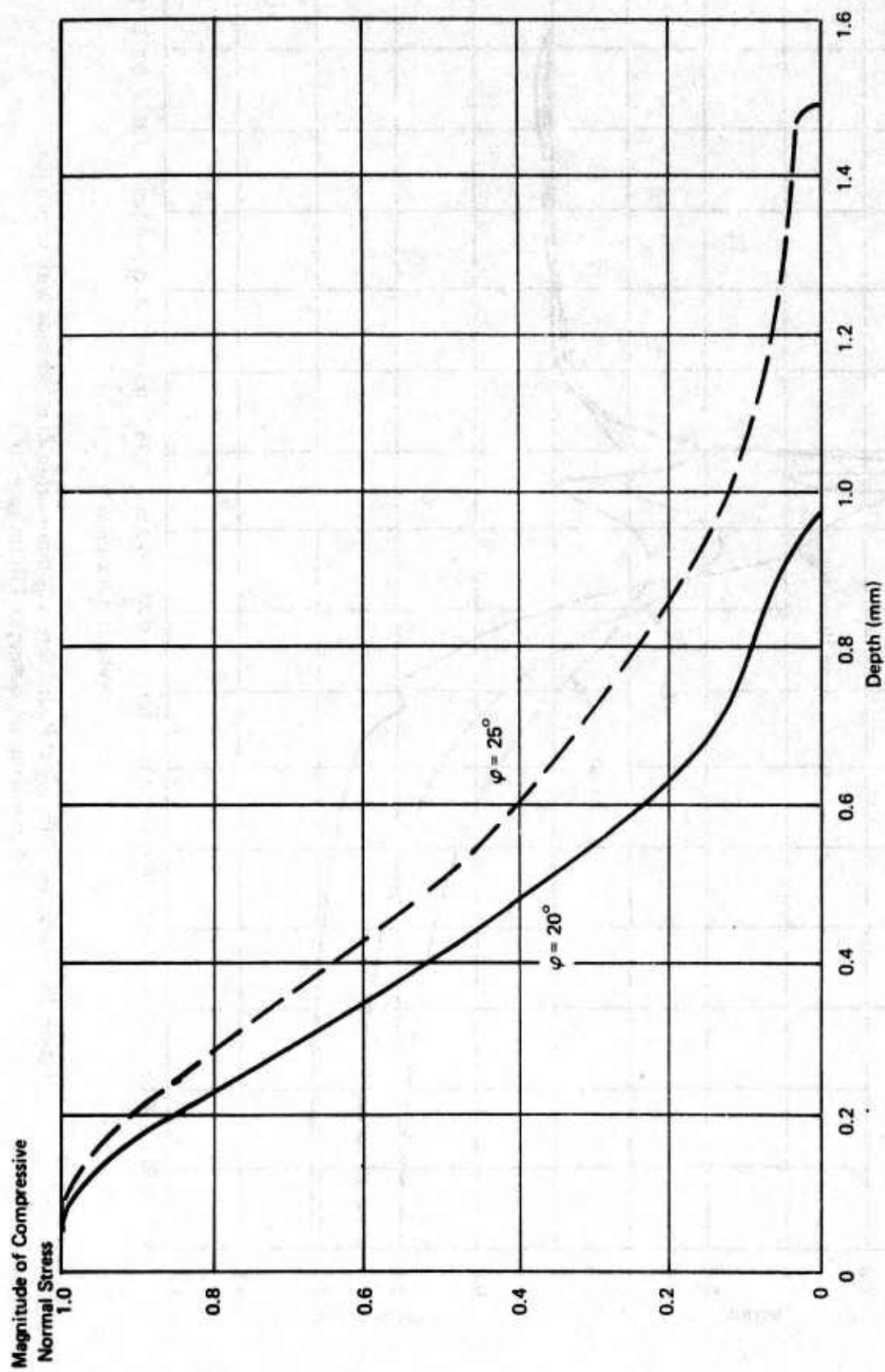


Figure 29. Variation of Normal Stress Component (at  $r = 0$ ) with Depth in Zinc Selenide



the material response for impact loadings. The acoustic velocities for PMMA have been measured in the 6 to 30 MHz frequency range,<sup>(34)</sup> and will be used in the analysis which follows.

Experimental one-dimensional shock wave studies indicate that PMMA behaves as a nonlinear viscoelastic material below a peak stress around 100,000 psi (7kbar).<sup>(35,36)</sup> Plastic deformations may occur at applied pressure above 7kbar. An estimate of the magnitude of the interfacial pressure for a water drop impacting a solid surface at 730 fps (0.2225 mm/ $\mu$ s) can be determined from Eq.(15) and (16), since the shock wave velocity as a function of particle velocity is known for both water and PMMA.<sup>(36)</sup> Eq.(15) can be solved to yield  $V_w = 0.0786$  mm/ $\mu$ s and from Eq.(16)  $p = 2.57$  kbar (37,200 psi). Thus it is seen that plastic deformations are not to be expected under the specified impact conditions.

Although PMMA does not behave as a linear elastic solid, the transient stress distributions due to a liquid drop impact will be evaluated on this basis. The magnitude of the applied pressure will again be normalized to unity, so the actual magnitude of the stresses can be determined by whatever procedure is used to evaluate the pressure at the water/solid interface.

Radial tensile stresses in PMMA only occur in a very shallow layer near the free surface of the target for 1.8 mm drops impacting at 730 fps. The form of the radial stress for a range of values of  $\phi$  is shown in Fig. 30 at a depth of 10 $\mu$ m. The decrease of the magnitude of the radial stress component with depth is indicated in Fig. 31 while the temporal development of the radial stress component is shown in Fig. 32 and 33. The attenuation of the compressive normal pressure pulse with distance into the specimen is shown in Fig. 34.

The level of sustained radial stress for a 1.8 mm water drop striking PMMA at 730 fps when  $\phi=25^\circ$  is approximately 11,500 psi according to Fig. 30. This value of the stress is



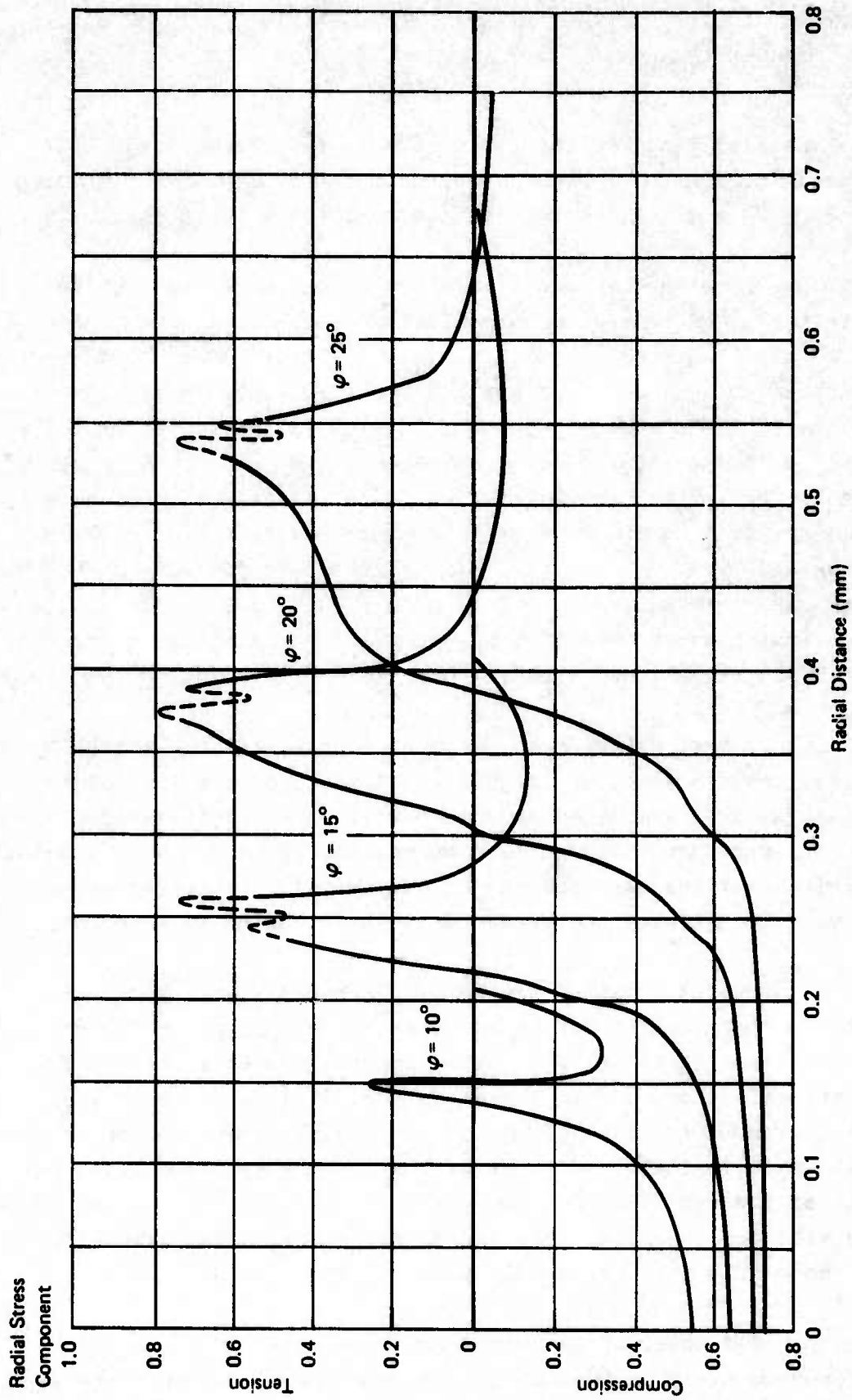


Figure 30. Variation of Radial Stress Component in PMMA with Critical Contact Angle at  $z = 10 \mu\text{m}$

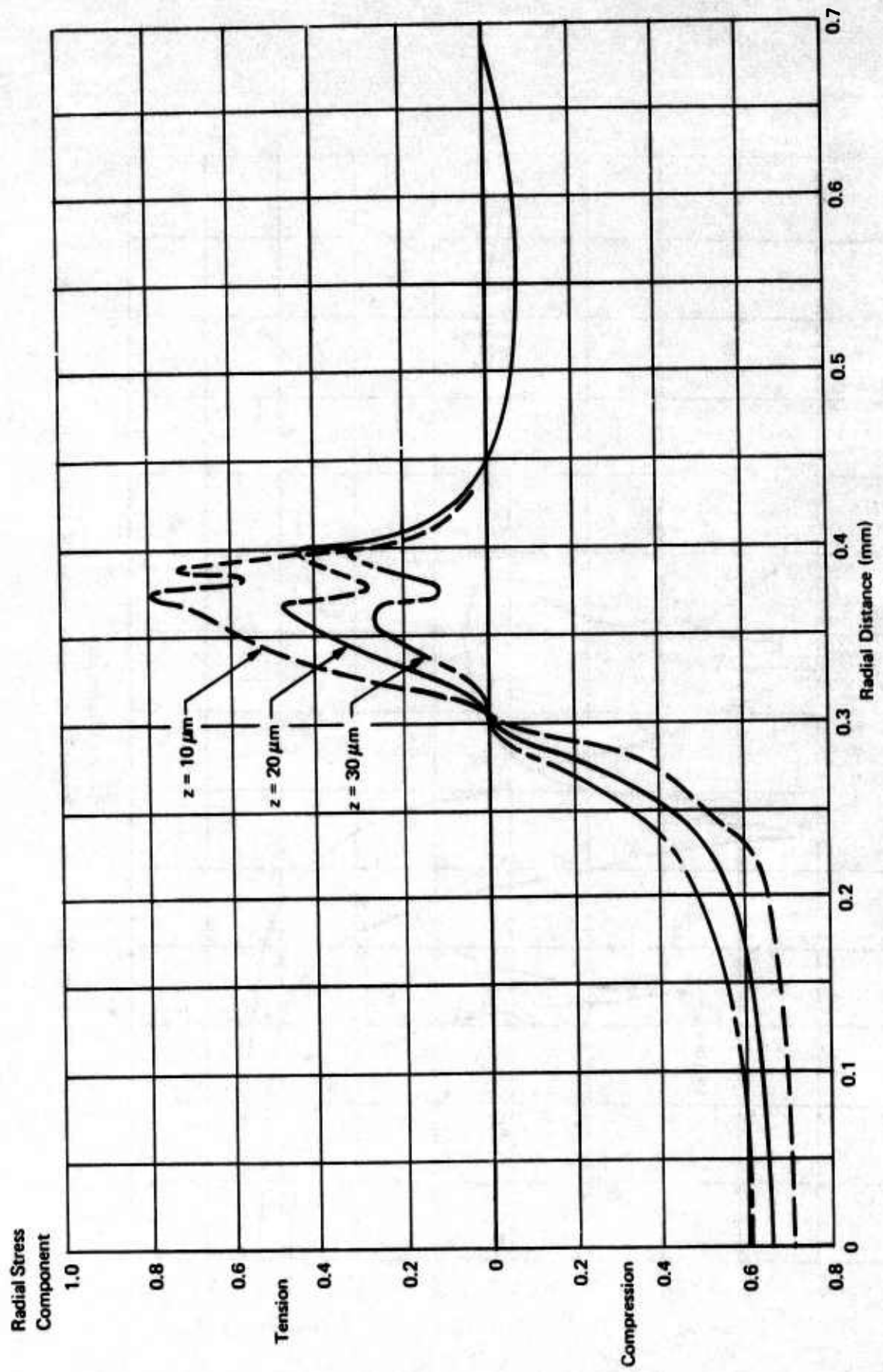


Figure 31. Variation of Radial Stress Component in PMMA with Depth when  $\varphi = 20^\circ$

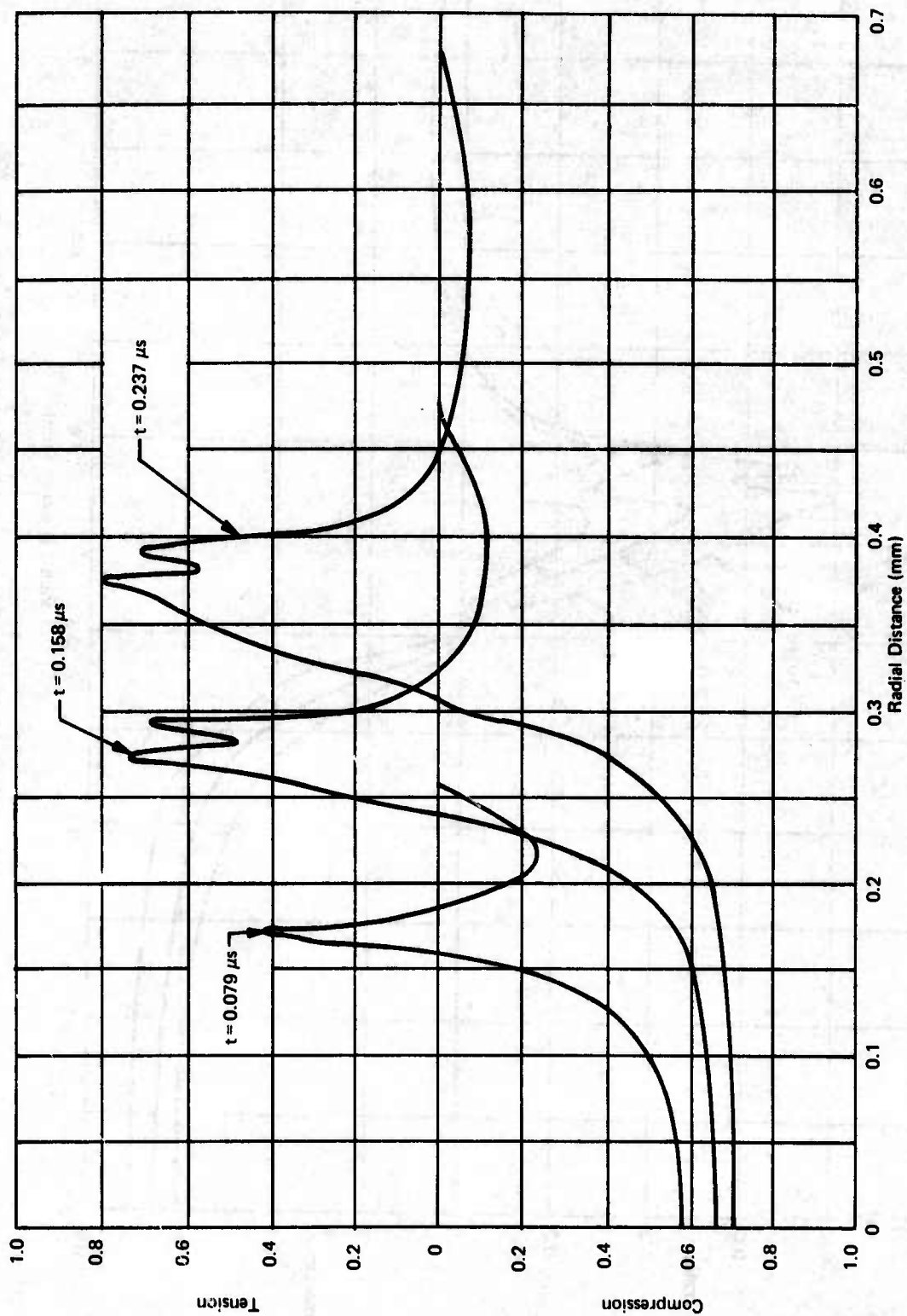


Figure 32. Temporal Development of Radial Stress Component in PMMA at  $z = 10 \mu\text{m}$  when  $\phi = 20^\circ$

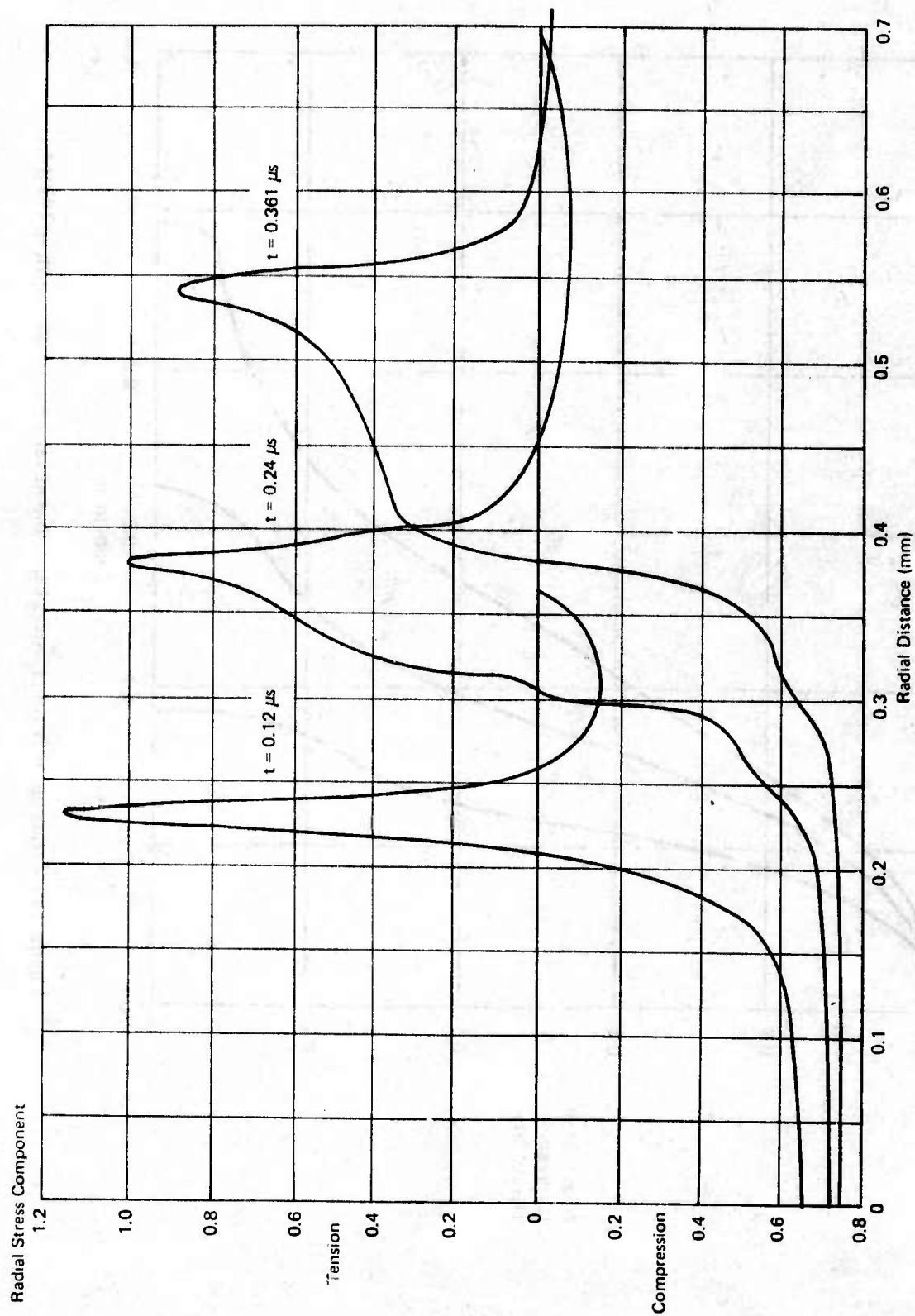


Figure 33. Temporal Development of Radial Stress Component in PMMA at  $z = 5 \mu\text{m}$  when  $\varphi = 25^\circ$



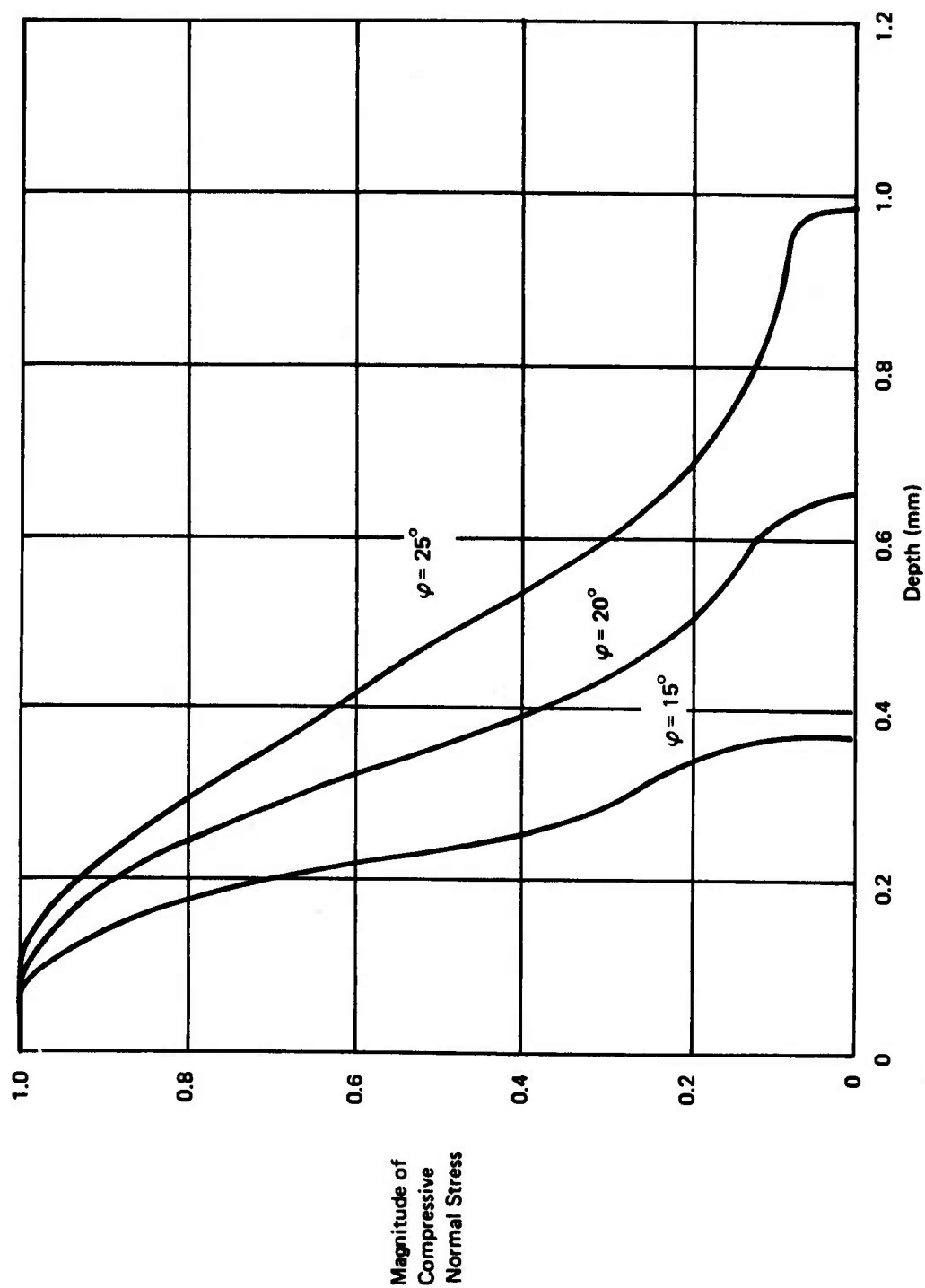


Figure 34. Variation of Normal Stress Component (at  $r = 0$ ) with Depth in PMMA

quite comparable to that for ZnSe for the same impact condition as shown in Fig. 21, however the duration of the tensile stresses at this level is longer in the case of ZnSe.

### 3. Soda Lime Glass

At a water drop impact velocity of 730 fps it is felt that the calculated elastic wave velocities listed in Table 8 are representative of the transient conditions in soda lime glass. Using Eq.(15) and (16) in conjunction with Fig. 3, it is found that  $V_w = 0.0264$  mm/ $\mu$ s and  $p = 3.72$  kbar (53,900 psi). Once again the computed stresses are normalized to unity so all of the values shown have to be multiplied by  $p$  to obtain the actual magnitude of the stresses.

The general distribution of tensile radial and normal stresses when  $\phi = 15^\circ$ ,  $20^\circ$ , and  $25^\circ$  are shown in Fig. 35 to 37 for  $V_0 = 730$  fps. The maximum values of the radial tensile stresses occur in the vicinity of the free surface. The distributions of tensile values of  $\sigma_{rr}$  and  $\sigma_{zz}$  are analogous to those shown in Fig. 19 and 20 for zinc selenide except that the spatial extent of these stresses is expanded due to the higher wave speeds in soda lime glass. The calculated magnitude of the pressure imparted to the specimen is approximately the same for these two materials.

The extent of the radial stress component at  $z = 10\mu$ m for various contact angles before lateral outflow occurs is shown in Fig. 38. The comparison with the corresponding curves for PMMA in Fig. 30 is striking. The magnitude of the tensile stresses for PMMA is somewhat larger than that for soda lime glass, but the radial dimension over which it is applied is about four times less. The time duration over which the tensile stress acts is indicated in Fig. 39 for points in the target  $10\mu$ m below the surface. Fig. 40 illustrates the change in the normal stress component,  $\sigma_{zz}$ , with depth in the soda lime glass specimen.

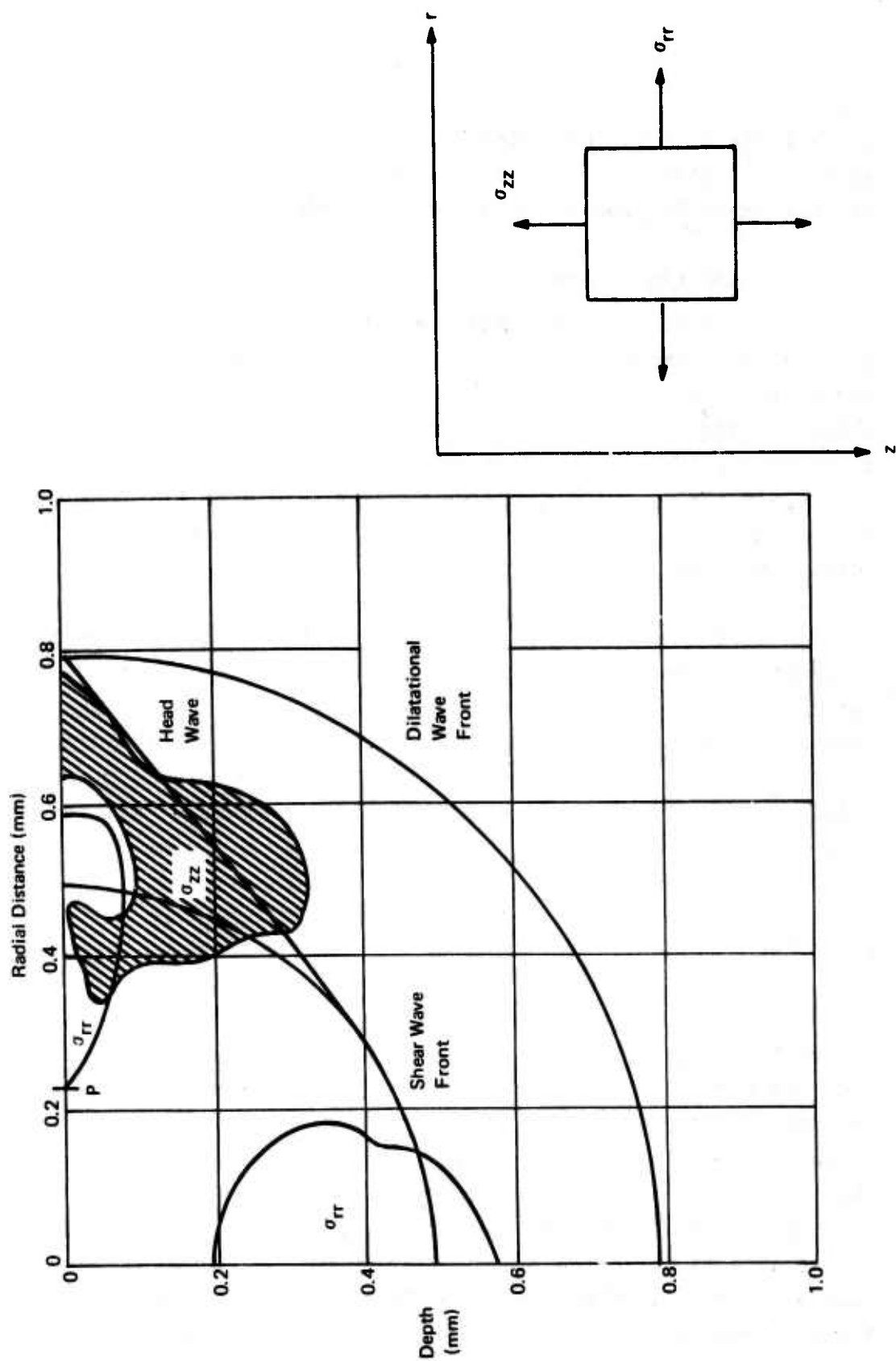


Figure 35. Distribution of Tensile Stresses in Soda Lime Glass when  $\phi = 15^\circ$

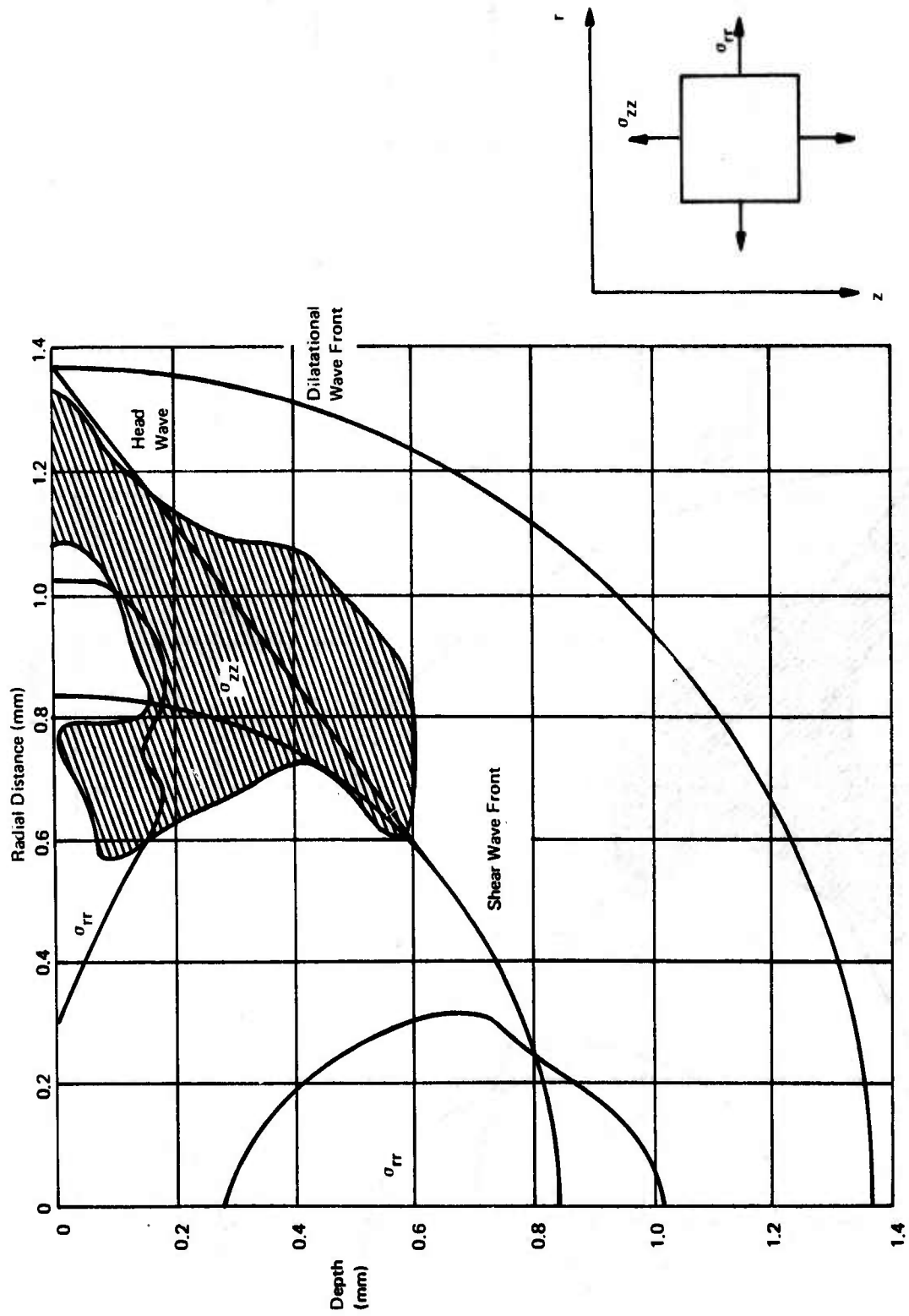


Figure 36. Distribution of Tensile Stresses in Soda Lime Glass when  $\varphi = 20^\circ$



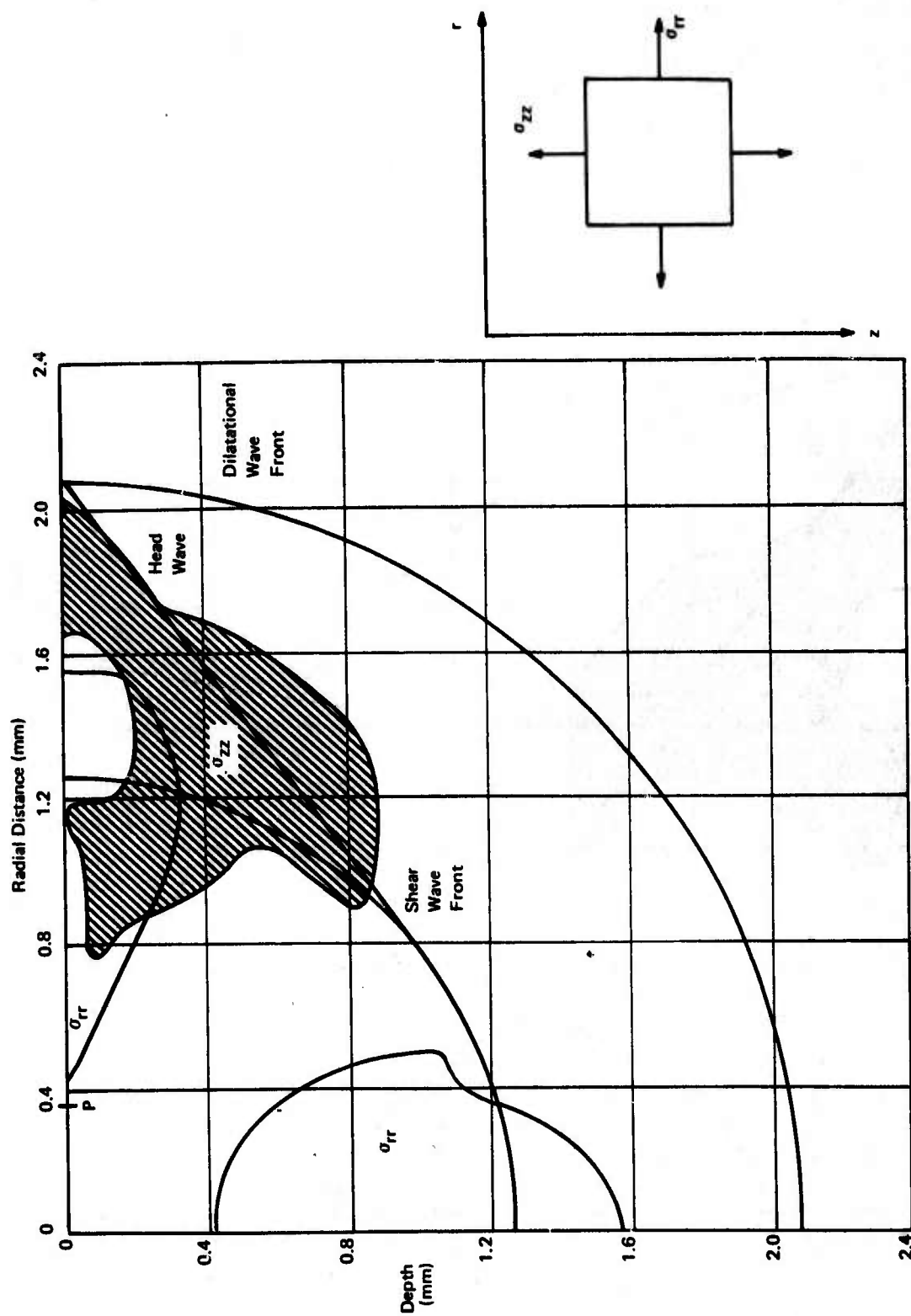


Figure 37. Distribution of Tensile Stresses in Soda Lime Glass when  $\varphi = 25^\circ$

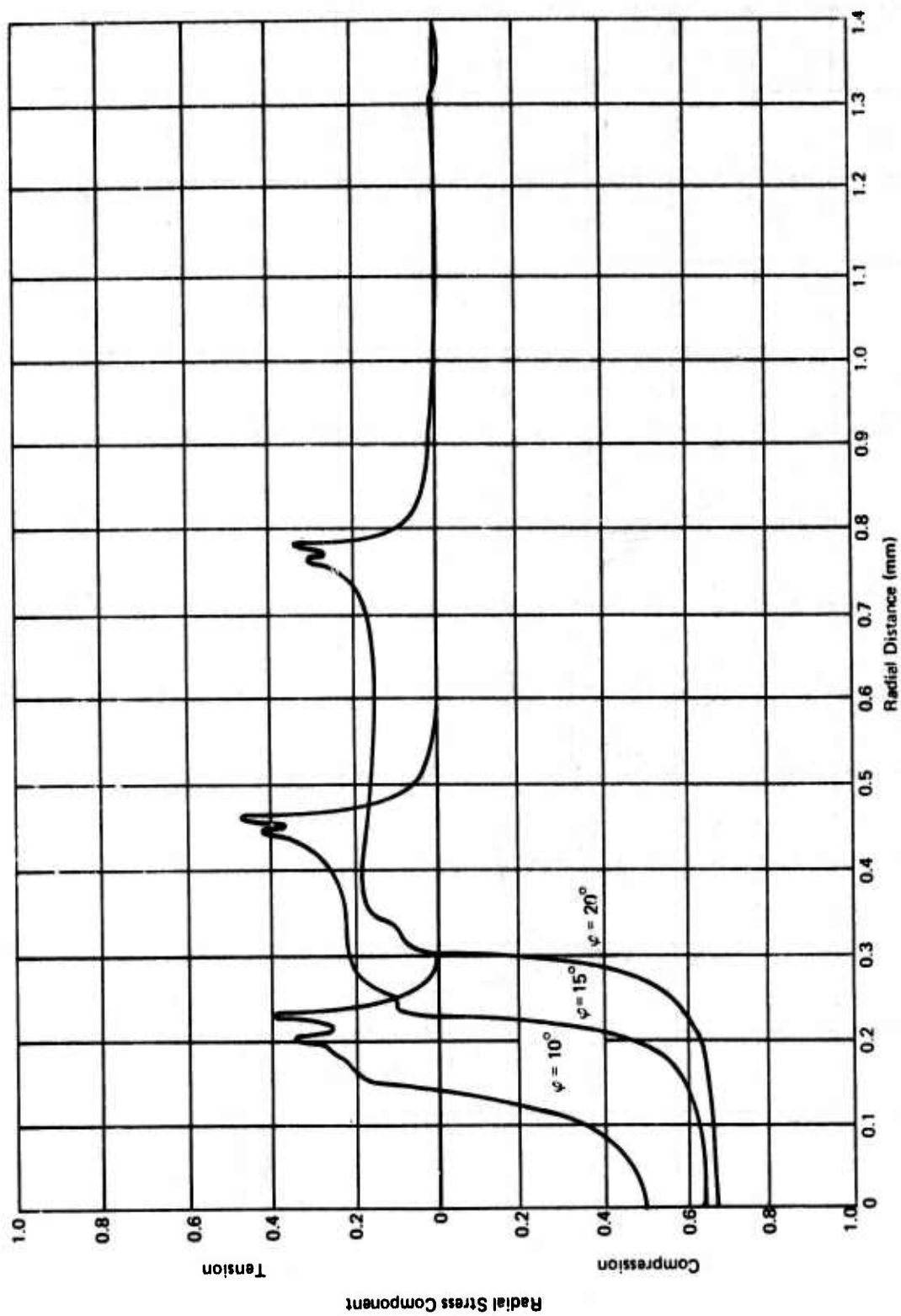


Figure 38. Variation of Radial Stress Component in Soda Lime Glass with Critical Contact Angle at  $z = 10 \mu\text{m}$

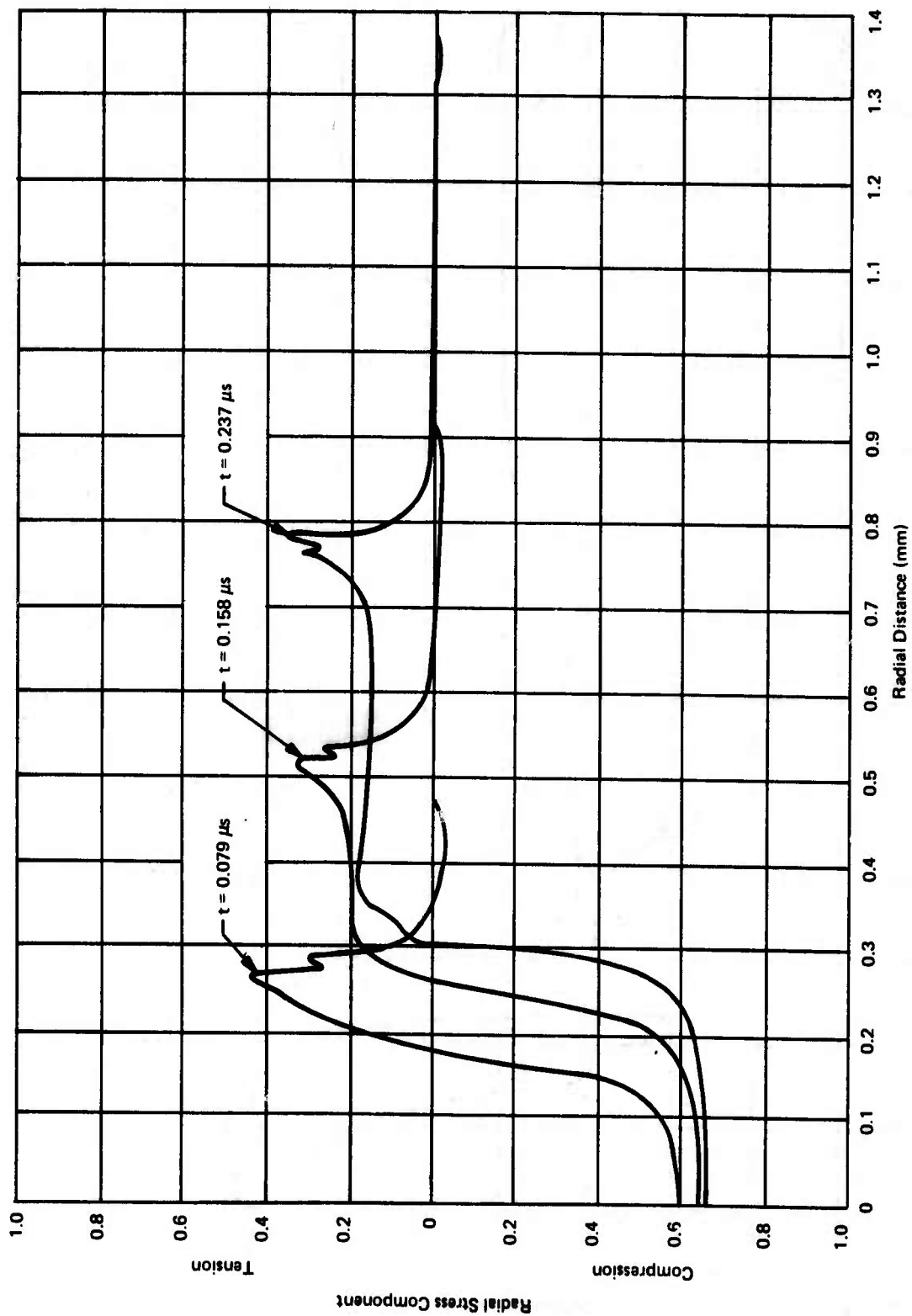


Figure 39. Temporal Development of Radial Stress Component in Soda Lime Glass at  $z = 10 \mu m$  when  $\phi = 20^\circ$

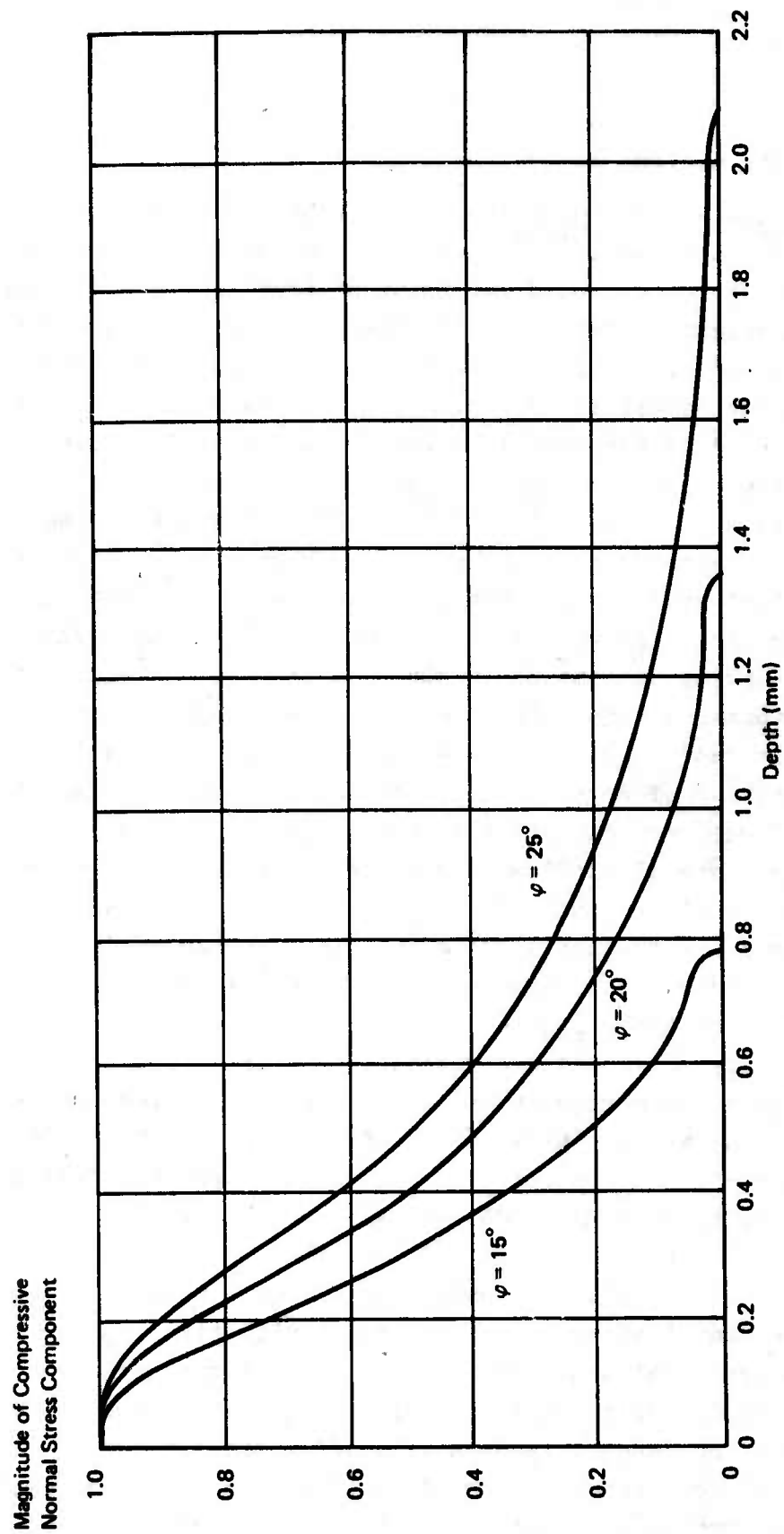


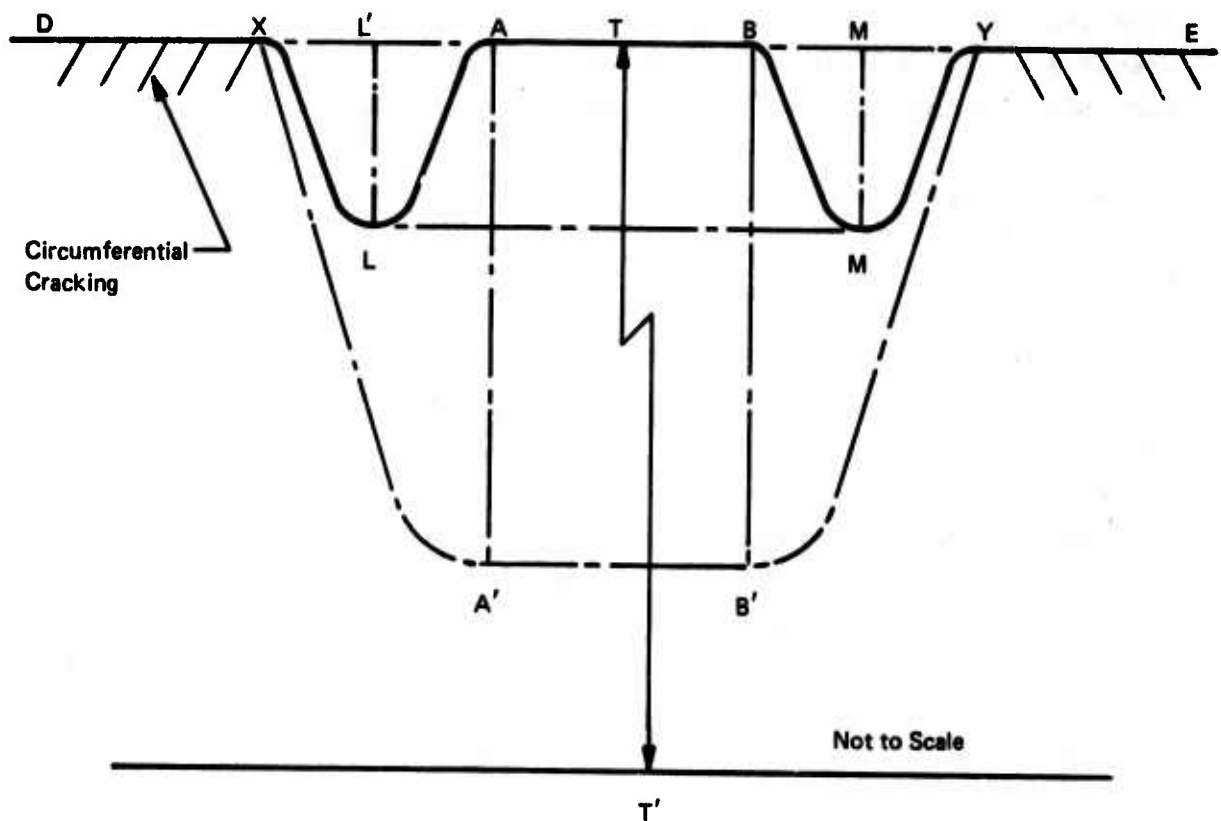
Figure 40. Variation of Normal Stress Component (at  $r = 0$ ) with Depth in Soda Lime Glass



#### 4. Discussion

Single water drop impacts on PMMA have been described by Engel<sup>(37)</sup> and Fyall.<sup>(13)</sup> According to Engel, circumferential cracking forms around the point of impact of an impinging, spherical waterdrop due to the tensile stresses that are produced when the compressive impact stress forms a cup-shaped cavity in the material. A breaking out of material from the surface should be observed as a result of the rapid radial outflow of water over the raised ridges of the fine circumferential cracks that have formed.<sup>(37)</sup> The impact conditions in the experiments reported by Engel are an average 1.9 mm water drop striking PMMA at 730 fps. Fyall's experiments<sup>(13)</sup> were for a 2 mm water drop impinging at 904 to 987 fps. At these velocities a smooth annular depression is observed to occur outside the central undamaged zone with circumferential cracking seen beyond this depressed zone. Fyall provides an explanation similar to that of Engel except that he allows for permanent set in the deformed regions XLA and BMY in Fig. 41. He explains that before lateral outflow occurs the surface AB in Fig. 41 is compressed to A'B'. The sides of the depression XA' and YB' would then be in tension and the tensile stresses would be set up over XD and YE resulting in circumferential cracking. Fyall's measurements of the change of lengths from XA and YB to the deformed state show that any residual tensile strain is very small. The surface returns to AB but the small permanent set induced in XA' and YB' gives the profiles XLA and BMY. The annular depressions are not observed in the imprints studied in our experiments on PMMA at 730 fps as seen in Fig. 16.

Field, et.al.,<sup>(17)</sup> have embarked on a program to demonstrate the quantitative as well as the qualitative similarities between a spherical water drop impact and a liquid jet. At the lower impact velocities in their investigation they show a direct correspondence between a Talysurf trace for one of Fyall's PMMA specimens and the damage due to a water jet collision. The Cambridge investigators<sup>(11,12,17)</sup> have described the



Typical Dimensions (mm)  
 $XY = 1.10$ ;  $AB = 0.39$ ;  $LM = 0.69$   
 $XA = 0.36$ ;  $LL' = 1 \times 10^{-3}$ ;  $TT' = 6.35$

Figure 41. Schematic Profile of Damage Site in PMMA Impacted by a 2 mm Water Drop at 1000 fps (taken from Fyall<sup>(13)</sup>)

damage modes in thin and thick specimens of PMMA subjected to water jet impacts from 290 to 1200 m/s. Fyall's smooth annular depressions surrounding the central undamaged region were observed for impact velocities up to 500 m/s when deep ring cracks would originate within the annular depressed zone. A subsurface damage zone lying on the axis of symmetry developed at velocities in excess of 600 m/s and the central surface area was deformed plastically to produce small but measurable depressions in the undamaged zone. The circumferential cracks outside the annular depressed region were found to be almost perpendicular to the surface but tended to grow parallel to the surface with increasing radial distance from the initial point of impact. The depth of the cracks decreased with radial distance, but the average depth was around  $10\mu\text{m}$ . Using multiple beam interferometry, Bowden and Brunton<sup>(11)</sup> found that at each fracture there is a small step in the surface which is oriented so that the vertical face of the step faces in towards the center of impact. During the impact there will be a radial force acting on the step face due to lateral outflow of the water drop. This interaction is sufficient to chip material out of the surface along the line of fracture as seen in Engel's early micrographs<sup>(37)</sup> and in our observations of the early stages of the erosion process in a variety of materials. As the jet velocity increased in Field's experiments<sup>(13)</sup> the ring crack was found to become wider and deeper until it joined with the axial subsurface fracture at jet velocities around 900 m/s.

According to the preceding discussion one explanation for the circular damage formations in Fig. 15 and 16 would be that the undamaged region is depressed during the period preceding lateral outflow and tensile bending stresses develop outside the depressed region. The material within an annulus surrounding the central region is then stressed beyond the yield point and after the applied pressure subsides localized wrinkling can occur within this annulus. This would account for the ripple pattern shown in Fig. 15 for polysulfone but no large-scale permanent deformations are found within the compressed zone.

The magnitude of the applied pressure has to be such that the compressive stresses which develop within the central undamaged region are not sufficient to yield the material in this region, but the magnitude of the deformations surrounding the central region are sufficient to produce local yielding of the material in tension. The same reasoning can be applied to polymethylmethacrylate. However, due to the semibrittle nature of this material micro-cracks occur in the region surrounding the depressed zone in order to accommodate the tensile field which develops during the drop impact.

An alternative line of reasoning would ascribe the circular damage zones to stress wave phenomena. The computed dilatational wave velocity,  $C_1$ , and shear wave velocity,  $C_2$ , for the polymers as well as the corresponding values for zinc selenide, zinc sulfide and soda lime glass are listed in Table 8. The stress wave computations indicated that the critical tensile stresses occur after the shear wave has propagated outward from the contact area. The location of the shear wave fronts for the contact radii considered in the numerical computations are listed in Table 9. The actual radial stress distributions for PMMA, zinc selenide, and soda lime glass are shown in Fig. 42 when  $\phi=20^\circ$ . The comparison indicates that although the intensity of the applied pressure is the least for PMMA the radial stresses at this instant of time are more confined and more intense than for the other two materials. The depression mechanism described earlier therefore seems to be supported by these calculations in the case of polymethylmethacrylate and polysulfone. On the other hand, the composition of the transient waves will be fully established in the annular region around the impact zone for zinc selenide, zinc sulfide, and soda lime glass when  $\phi=20^\circ$  and the primary wavefronts are detached from the contact area. Critical stress conditions result in the annular region around the impact zone to which each material responds in its own way. The magnitude of the tensile stress decreases more rapidly in soda lime glass as compared to zinc selenide due to the higher wave speeds in soda lime glass.



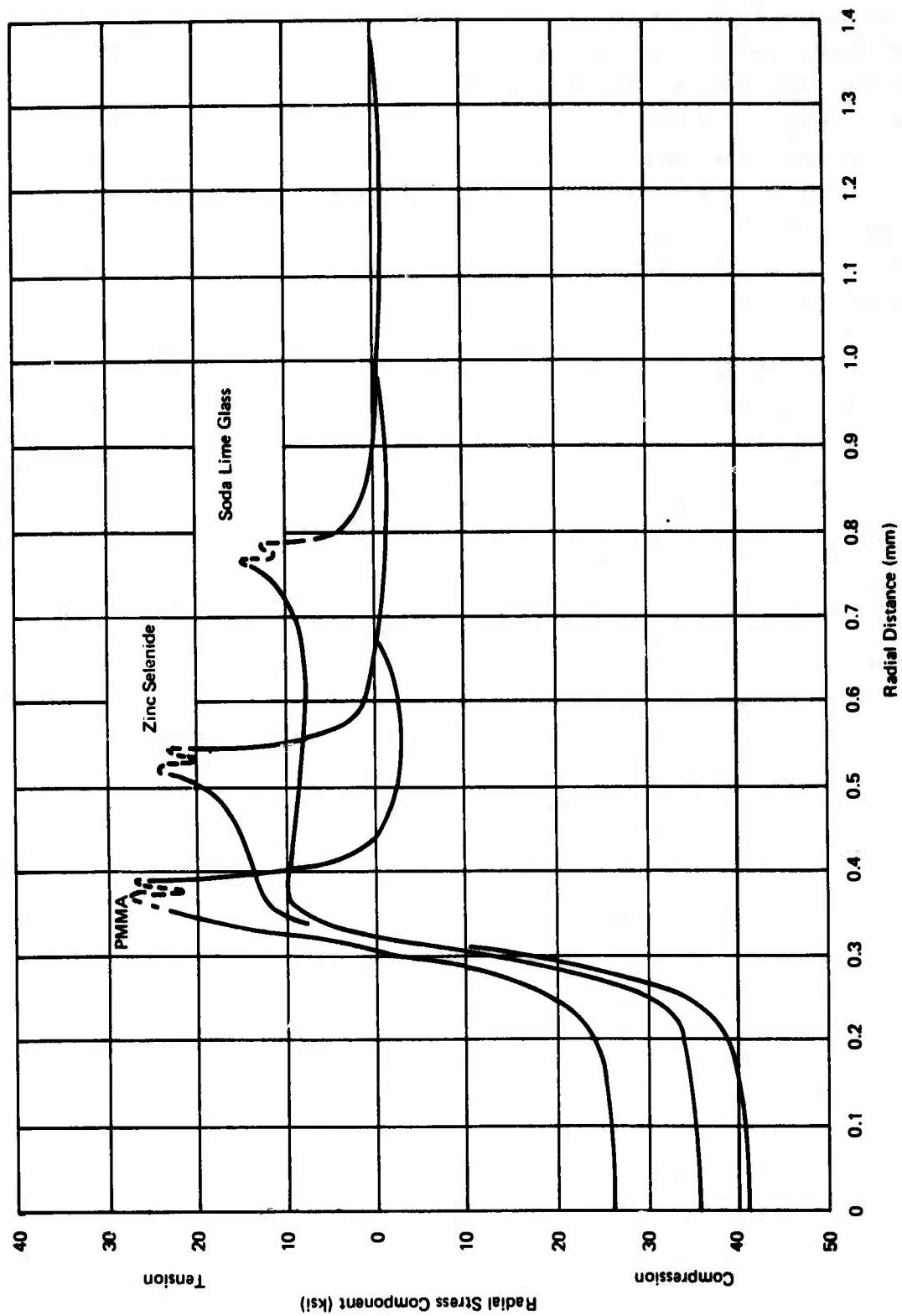


Figure 42. Variation of Radial Stress Component at  $z = 10 \mu\text{m}$  for 1.8 mm Water Drop Impacting Various Materials at 730 fps ( $\phi = 20^\circ$ )

The actual magnitudes of the normal stress component as a function of depth into the target are shown in Fig. 43 for PMMA, zinc selenide, and soda lime glass. For the normal stress component the higher wave velocity for soda lime glass tends to maintain the magnitude of the stress at a higher level to a greater depth than for the other materials represented.

The comparison between the computed and experimental results appear to be consistent: the magnitude and duration of the transient tensile stresses at and near the surface must be sufficient to initiate crack growth at a number of locations around the central point of contact. The interaction of subsequent drop impacts with a system of small fractures on the surface is still not completely evident. Once a series of small cracks are present on the surface it is difficult to isolate the stress wave effects generated by a drop impact in the vicinity of these flaws and crack propagation which takes place due to the direct pressure applied to a pre-existing crack. Details of the microscopic observations of the fracture behavior of transparent materials are described in Section III, however much remains to be learned about the correlation of fracture data with the transient stress distributions in the target material.

The deformation of a spherical water drop striking rigid and elastically deformable surfaces have been computed by a few investigators.<sup>(22,24)</sup> It is interesting to compare the results from these numerical computations with the idealized model the impact event used for the stress wave computations. Hwang's computations<sup>(22)</sup> are based on an inviscid compressible liquid. The shape of a 2 mm drop striking a rigid surface at 980 fps is shown in Fig. 44a: the dashed lines indicate the shape corresponding to a perfectly compressible drop impacting a rigid surface. Kreyenhagen's numerical solution<sup>(24)</sup> employs the Walker-Sternberg equation of state for water.<sup>(38)</sup> The shape profiles for a 1 mm drop impacting at 675 fps are shown in Fig. 44b and again the corresponding profiles for a perfectly compressible drop are indicated by the dashed curves. The

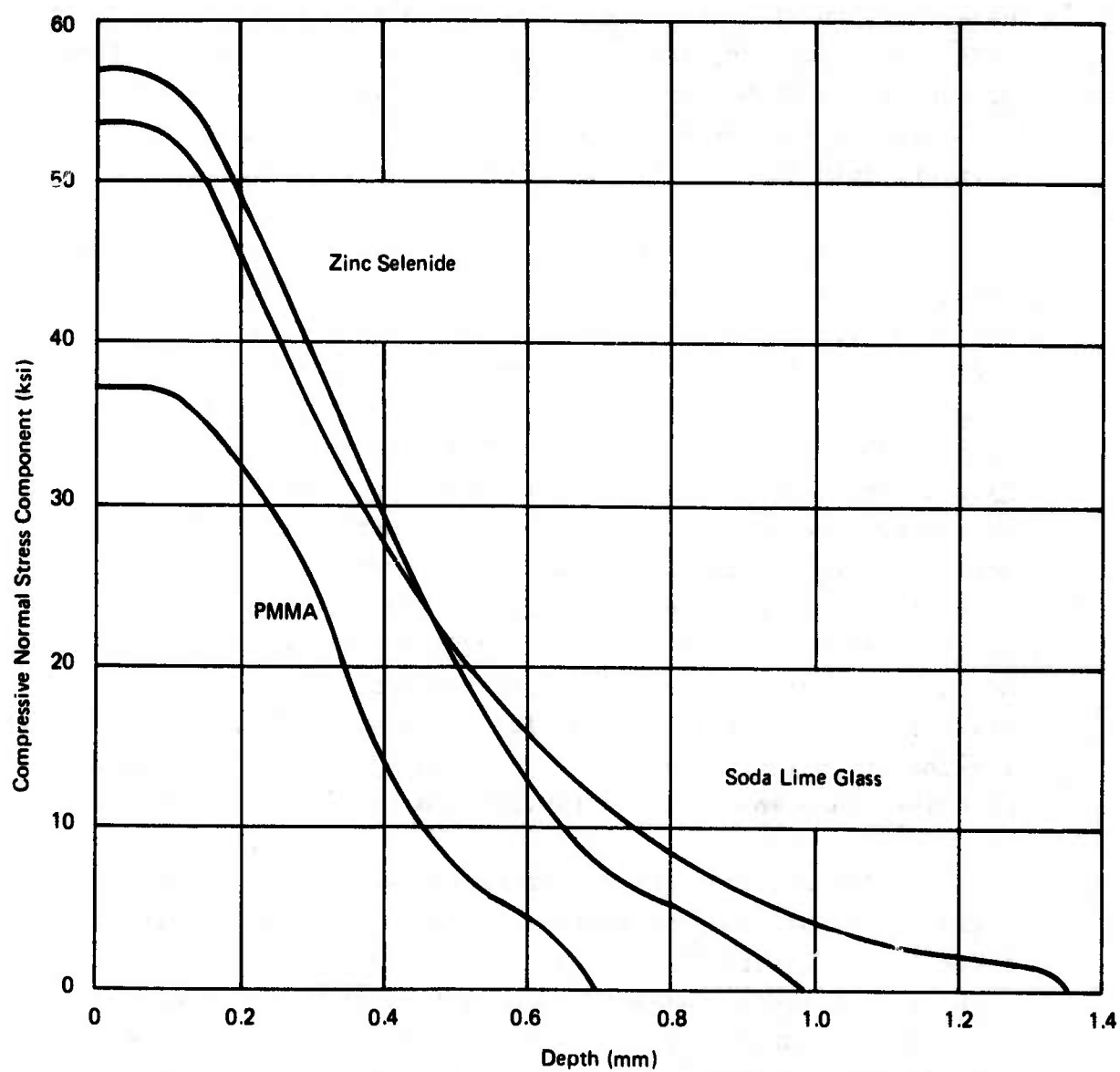
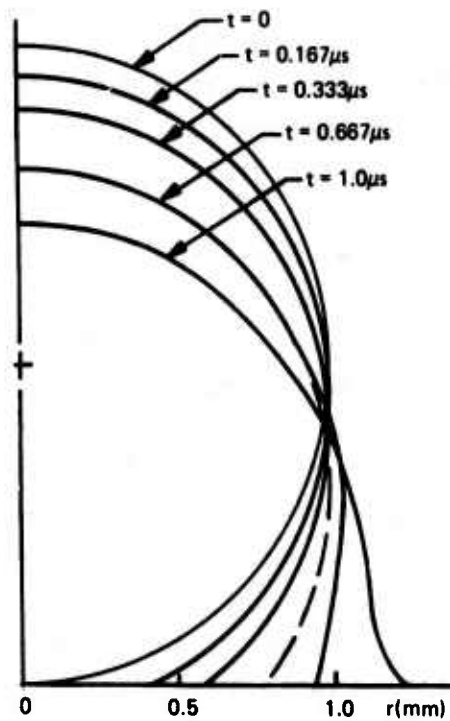
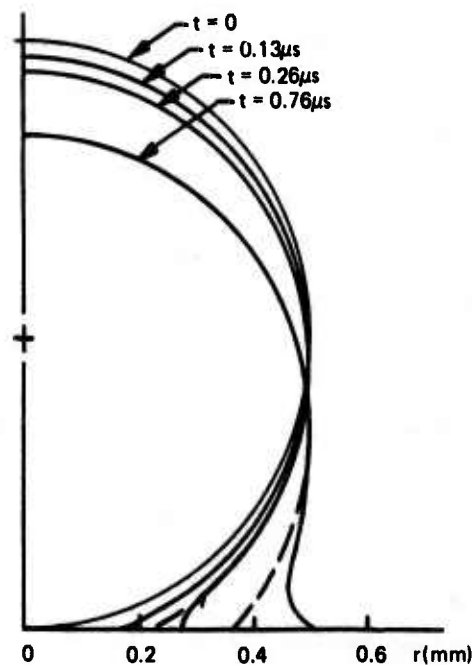


Figure 43. Variation of Normal Stress Component (at  $r = 0$ ) with Depth for 1.8 mm Water Drop Impacting Various Materials at 730 fps ( $\varphi = 20^\circ$ )



(a) 2mm Water Drop Impacting at 980 fps



(b) 1mm Water Drop Impacting at 675 fps

Figure 44. Computed Temporal Profiles of Water Drops Striking a Rigid Plane



comparison with both numerical procedures suggest that incompressibility effects are not significant for the range of  $a/R$  values used in our stress wave computations, so the transient stress distributions reported here should be indicative of the very early stages of the water drop collision.

Hwang and Kreyenhagen evaluated the liquid/solid interfacial pressures. Hwang finds that this pressure rapidly rises to a value of  $0.7\rho_0 C_0 V_0$ . The pressure distribution is spatially uniform with the peak pressure occurring along the axis of symmetry of the drop impact. As the contact radius increases the location of the maximum pressure moves to the perimeter of the contact zone and the value of the pressure along the axis of symmetry decreases. The peak pressure is found to be  $1.06\rho_0 C_0 V_0$  and occurs at a contact radius of  $0.6R$ , although the results from the numerical computations for contact radii ranging from  $0.5$  to  $0.8R$  show a sizeable degree of scatter. It does not appear that the form of the pressure distribution stipulated by Hwang can be unequivocally supported on the basis of the numerical results he presents. Hwang also investigated the impact of a spherical drop on an aluminum and PMMA half-space. He finds for PMMA that due to the small deformations calculated at the liquid/solid interface there is no appreciable difference between the drop shape profiles for a spherical drop striking the elastic half-space and the collision with a rigid surface. Hwang also found for the same impact conditions the liquid/solid interfacial pressure on elastically deformable materials was lower and more uniform than for a rigid body. Both of these factors would tend to support the simplified modeling approach reported in the previous sections.

Based on the limited time steps reported by Kreyenhagen<sup>(22)</sup> the interfacial pressure has a maximum value at the perimeter of the contact zone in the very early stages of the collision and becomes more uniform toward the later stages of the impact: after lateral outflow is initiated. The shape history for the drop impact shown in Fig. 44 seems to indicate a more rapid

expansion of the contact area than that corresponding to Hwang's computations or the idealized model. The relative magnitude of the liquid/solid interfacial pressure during the initial stages of the impact is also found to be considerably lower than the values reported by Hwang.

On the basis of both the experimental and numerical results it would seem that the analytical approach developed here is a viable approach for understanding the transient stresses generated in an elastic body during the period when the direct pressure applied to the surface by the impacting drop dominates the collision. While some difficulties are encountered in evaluating the stresses at the plane surface of the half-space in the analytical approach, the stress values can be prescribed throughout the half-space and show a consistent variation from point to point. The finite difference schemes, on the other hand, display a fairly high level of irregularity in the results presented to date due to the requirement that a reasonable grid size be used in order to maintain economical computer times. However for the purpose which it serves the analytical approach is sufficient to get a handle on the mechanics of the water drop impact on deformable materials. It is important to note that consideration of the elastic properties alone are not sufficient to differentiate the range of the response displayed by materials under dynamic loadings. Additional material characterization is required if a correlation between the material properties and erosion damage is to be developed as will become evident in Section III.

Furthermore the mathematical description of a single drop impact is only a small part of the overall erosion process even in the case of brittle infrared window materials. The significant damage observed in all of the materials tested in the subsonic range is not due to a single impact but is due to nearly overlapping but non-concentric multiple drop impacts. It is the manner in which the initial fracture surfaces grow and interact with other fracture surfaces which contributes to

the loss of optical clarity and infrared transmittance. The experimental observations of the fracture behavior and pit nucleation for the transparent materials listed in Table 1 are described in Section III.

### III. MICROSCOPIC EXAMINATION OF PROGRESSIVELY ERODED SPECIMENS

The results of microscopic examination of the erosion damage which develops on the surfaces of the polymeric materials, infrared transmitting materials, and oxide-based glasses listed in Table 1 will be described. All of the specimens tested in the AFML-Bell erosion facility were exposed to the standard rainfield (1 in./hr. rainfall of 1.8 mm drops) at an impact velocity of 730 fps.

#### A. TRANSPARENT POLYMERS

In the very early stages of the erosion process all of the polymers considered displayed some tendency toward damage in the form of multiple ring formations which will be described for each material. However the predominant characteristic of the multiple ring formations is that they have an interior zone which is devoid of damage and a concentric band of damage whose maximum diameter is always less than that of the impacting drop. In order to obtain some perspective on the conditions each location on the specimen's surface may experience when subjected to the standard rainfield at 730 fps, an estimate was made of the number of drops required to cover a unit area of the specimen's surface with non-overlapping ring formations. Using a maximum diameter of 1.5 mm, 330 rings would be required if distributed in a hexagonal array; while 745 rings would be required if the maximum diameter was only 1.0 mm. It is estimated that an exposure time from 6 to 14 sec. in the standard rainfield is necessary for the entire exposed surface of the specimen to show evidence of water drop collisions in accordance with the assumed damage configuration.

##### 1. Polysulfone

The initial damage on the surface of polysulfone at an exposure time of 10 sec. appears in the form of rippling of the surface. Most of the damage occurs in fragmentary arc sections, however numerous well-formed complete ring patterns are observed



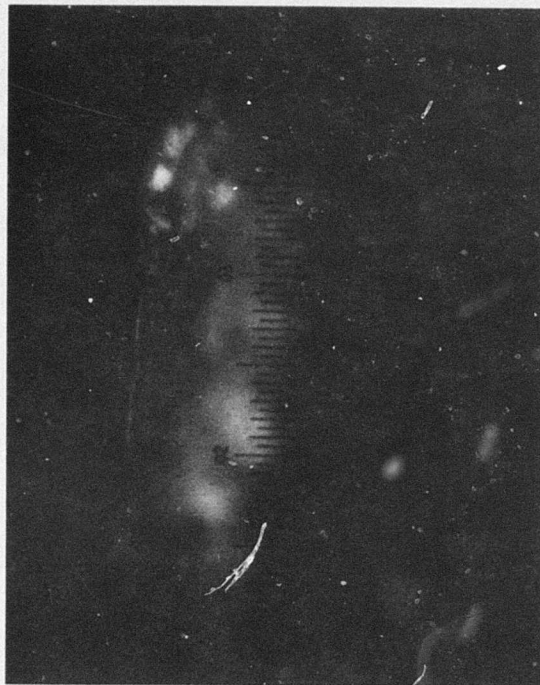
as shown in Fig. 15. The rippled domains are confined to a region ranging from 40 to 60 percent of the radius of the 1.8 mm water drop. The radial dimension of the rippled zone is confined to roughly 100 microns. As the exposure time increases, the rippled domains begin to overlap with fairly uniform coverage on the surface of the specimen at an exposure time of 2 min. The polysulfone displays a high degree of ductility with very little tendency for material removal. It is the ductile nature of the material when subjected to the moderately high strain rates imposed by liquid particle impingement which contributes to the loss of optical transmission before detectable mass loss has taken place.

Surface scratches provide sites for the development of internal fractures. The cracks penetrate the bulk material along essentially plane surfaces inclined to the perpendicular to the surface of the specimen. The variation in the angle of inclination of these cracks has not been determined. The boundaries of the cracks are roughly semi-elliptical as is shown to some extent in Fig. 45. Additional drop impacts produce large and highly localized deformations along the pre-existing cracks along the surface scratches as shown in Fig. 46; the ductility of the polysulfone specimens is easily observed in the permanent deformation of the material surrounding the pits.

The SEM micrograph in Fig. 47 shows a piece of material on the order of 40 microns being uplifted from the surface which may represent the initiation of material removal from a highly deformed region on the surface. The general condition of the eroded surface after an exposure time of 4 min. is shown in Fig. 48 where it can be seen that a range of particle sizes are being removed from the surface. Larger fragments are removed through the continued growth of the pits nucleated in deformed regions as shown in Fig. 47 or by the intersection of cracks with concomitant cleavage of the material below the surface and subsequent tearing of the undermined material by additional drop impacts. Intermediate stages in this process are shown in Fig. 49 where



(a) Focused at Surface Elevation



(b) Focused 180 microns below Specimen's Surface

Figure 45. Internal Fracture Originating at Scratch on Surface of Polysulfone Specimen  
After a 2-Minute Exposure to Standard Rainfield (110X)



Figure 46. Ductile Nature of Polysulfone in Vicinity of Pits  
Formed Along Surface Scratches (100X)





Figure 47. Initial Stage of Pit Nucleation in Polysulfone (1300X)



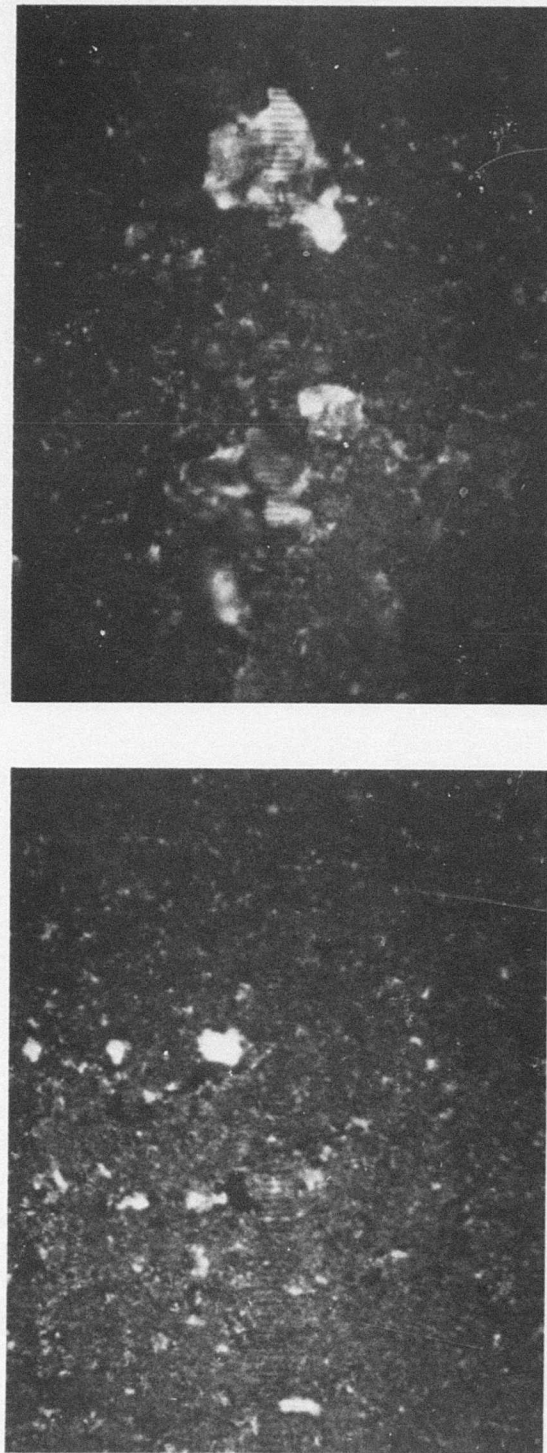
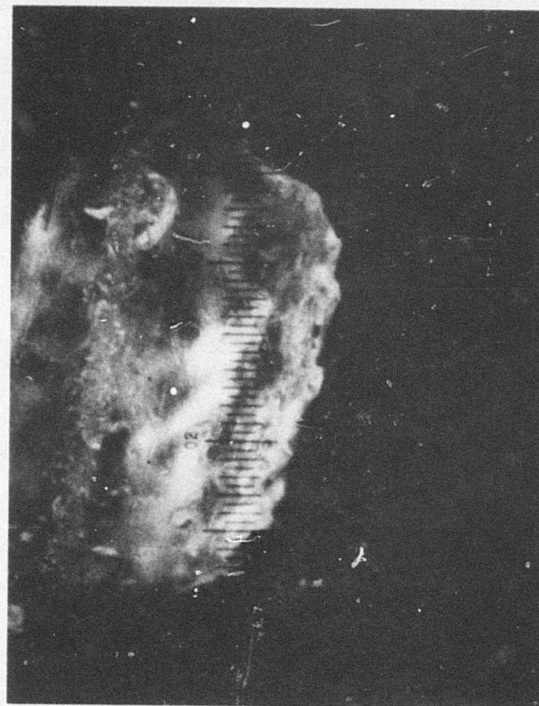


Figure 48. General Surface Condition of Polysulfone Specimen After 4-Minute Exposure to Standard Rainfield (80X)



(a) Crack Intersection (80X)



(b) Pit Growth (100X)

Figure 49. Particle Removal from Surface of Polysulfone Specimen

material removal is originating at the intersection of two cracks (Fig. 49a) and possibly within a small pitted region (Fig. 49b). The pieces of material being removed have lateral dimensions of approximately 700 microns. At this point the polysulfone is becoming quite opaque and at an exposure time of less than 4 min. the transmission of light through the specimen is essentially zero (refer to Section IV).

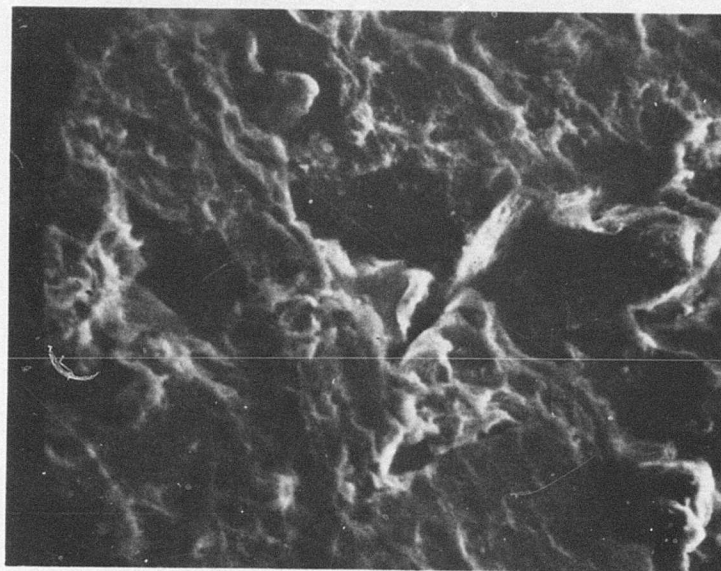
After an exposure of 6 min. the surface is highly distorted and contains numerous crevices and pitted regions as shown in Fig. 50a. The microscopic details of the cleavage surface inside a typical erosion pit can be seen in Fig. 50b.

## 2. Polycarbonate

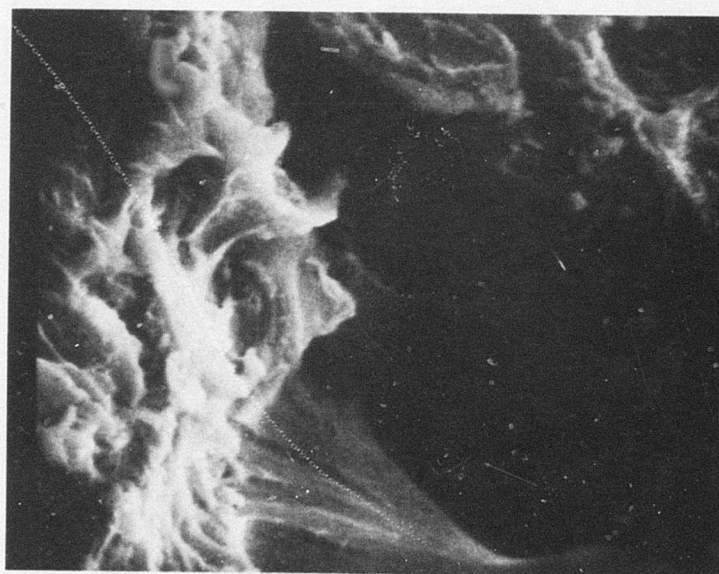
An uncoated and a melamine coated polycarbonate were tested. On the basis of the mass-loss data and general optical characteristics the uncoated polycarbonate was slightly superior to the melamine coated material. The details of the microscopic observations for the uncoated polycarbonate will be described first.

At short exposure times patches of shallow ripples several microns deep are randomly distributed over the surface of the uncoated polycarbonate analogous to those observed on polysulfone. The general condition of the surface at an exposure of 2 min. is shown in Fig. 51. It is interesting to note that no complete ring patterns could be found. Instead, ripple formations occur as very small circular arcs. At equivalent exposure times the surface of the polycarbonate specimens is considerably less distorted than the polysulfone, since each drop impact is much less damaging than in the case of polysulfone. Consequently, the optical transmittance of the polycarbonate is not impaired to the same extent as the polysulfone. The polycarbonate maintains a high level of ductility at the strain rates imposed by the impacting drops, however initially very isolated domains within the drop impact zone are susceptible to ductile





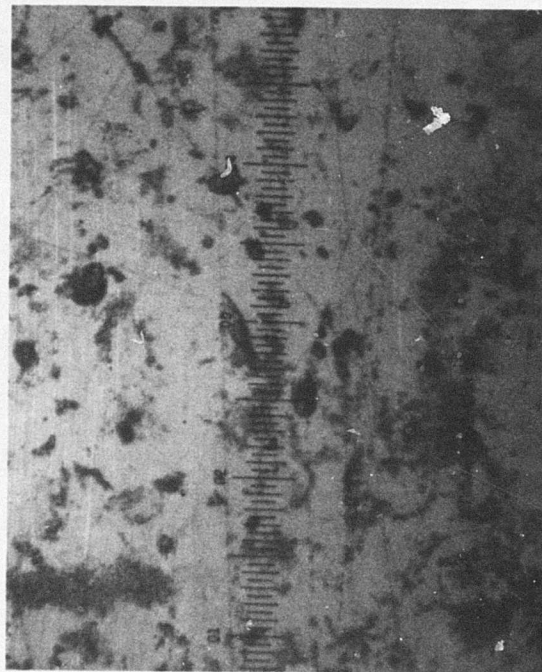
(a) General Surface Features (680X)



(b) Detail of Erosion Pit (2940X)

Figure 50. General Character of Eroded Surface of Polysulfone after a 6-Minute Exposure





General Surface Condition (80X)

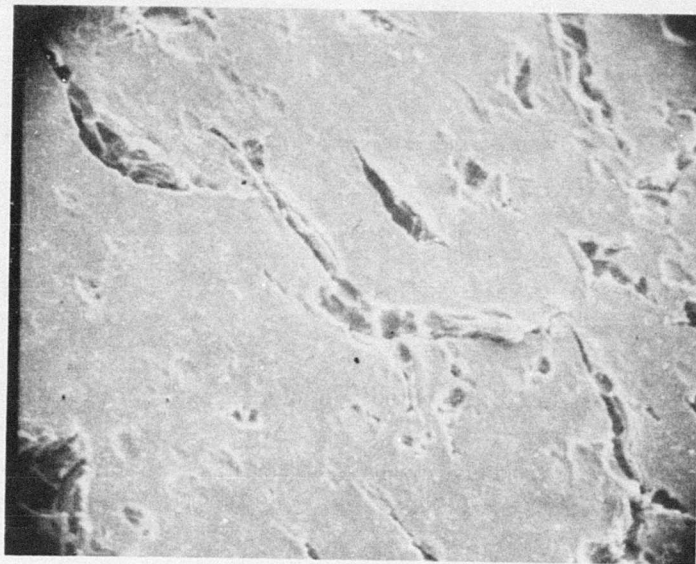


(b) Detail of Surface Feature (560X)

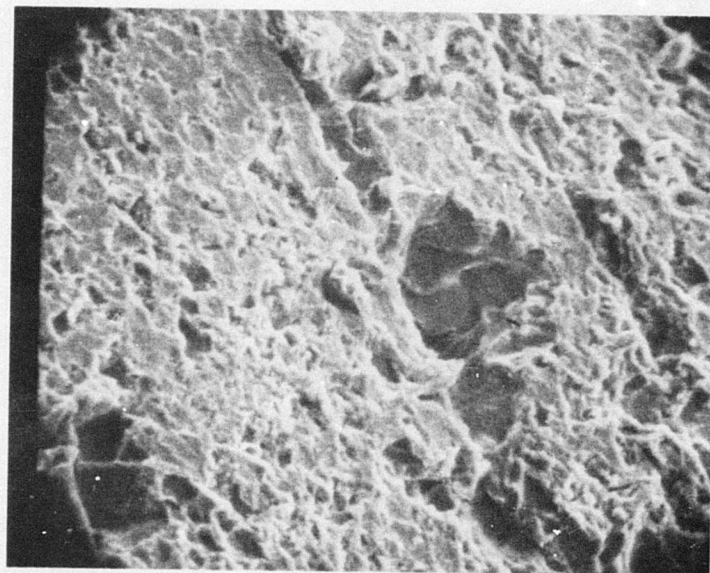
Figure 51. Polycarbonate after 2-Minute Exposure to Standard Rainfield

formations. While these deformations cause deterioration of transmission in the visible range, they do not in themselves produce mass loss.

The condition of the surface after a 6 min. exposure to the standard rainfield is shown in Fig. 52 and compared with polysulfone under the same conditions. The extent and nature of the damage is seen to differ. The erosion process in polycarbonate does not exhibit the dependence on surface scratches which is observed to be the case for polysulfone and nylon. Internal fractures develop in the polycarbonate in conjunction with the highly-deformed regions produced by overlapping ripple patterns. The deformation patterns associated with relatively small indentations on the surface can be seen in Fig. 53. Fine cracks are beginning to develop within the deformed areas. It is conjectured that the localized cracking within the deformed areas serve as nucleation sites for larger scale material removal. The relative influence on light scattering of the internal fracture surfaces and surface deformations is illustrated in Fig. 54. Fig. 54a was photographed under illumination which emphasized the scattering due to the ductile deformations, while Fig. 54b was photographed under illumination which suppressed the scattering due to the ductile deformations and emphasized the associated crack distribution. The narrow crevices seen in Fig. 52a and 54b are formed in a rather unusual way. Each crevice was found to originate from an erosion pit. A crack appears to be formed by penetration of the material below the surface and the overlying material is torn apart by the water escaping from the interior of the material. Stereo microscopy indicates that segments along the crevice have one very sharp edge but a flap of material can be seen along the opposing edge of the crevice. These edge conditions alternate several times from one edge to the other along the length of the crevice. Once a crevice is formed it contributes to the growth of erosion pits in much the same way as surface scratches provide additional pit nucleation sites in polysulfone. Further exposure to water drop impacts



(a) Polycarbonate



(b) Polysulfone

Figure 52. Comparison of Polycarbonate and Polysulfone  
Surface after 6-Minute Exposure (163X)



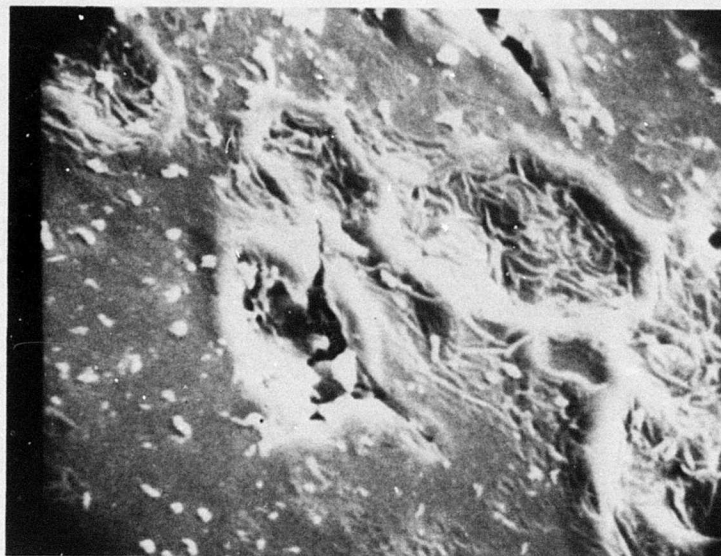
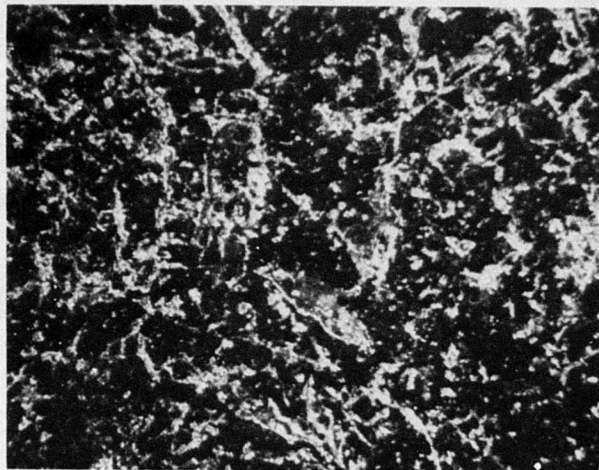
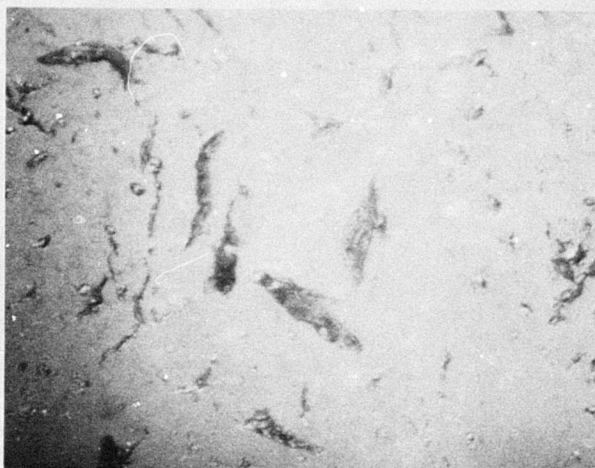


Figure 53. Crack Formation within Locally Deformed Regions  
on the Surface of Polycarbonate Specimen (1300X)





(a) Dark Field Illumination



(b) Bright Field Illumination

Figure 54. Crevice Distribution Associated with Ductile Deformations of Polycarbonate (30X)

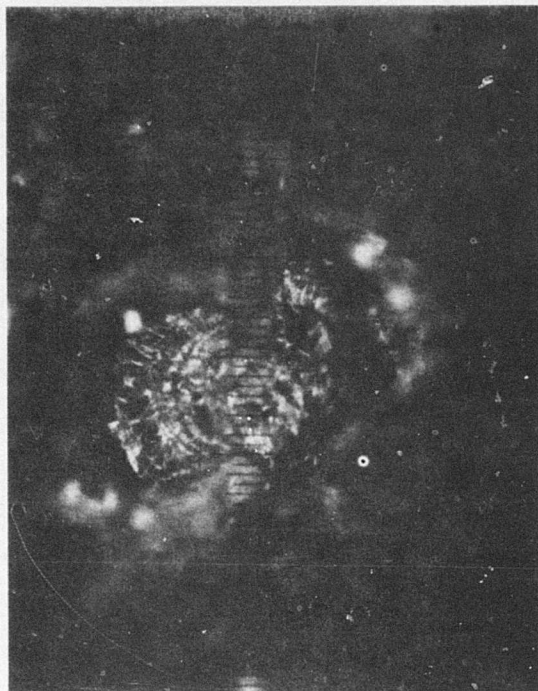
results in a small increase in surface wrinkling, but a steadily increasing number of larger cracks and crevices develop.

Larger erosion pits are created by the intense hydraulic pressure developed when a water drop impacts upon an existing crack in the surface. The water penetrating the crack separates small fragments of material from the bulk specimen by cleavage fractures as shown in Fig. 55 and 56. A number of erosion pits with a variety of orientations can be found along the cracks in the surface indicating that a number of water drop impacts have taken place to produce the highly localized pitted regions. This process continues to provide an abundance of sites for material removal as shown in Fig. 57 by the number of material fragments being freed from the surface after an exposure time of 10 min.

The general character of the material removal mechanisms in the later stages of the erosion process are the same in polysulfone and polycarbonate. Differences in the erosion behavior of the two materials during the incubation period are attributed to the greater susceptibility of polysulfone to rippling of the surface due to individual water drop impacts and the influence of surface scratches on the nucleation of erosion pits. It is the severe rippling of the surface in polysulfone which produces the significant difference in visibility when compared with polycarbonate. In the early stages of the erosion process in polycarbonate surface wrinkling is quite localized so visibility is maintained for a longer duration. Although the mass loss data in Fig. 134 is not conclusive, it appears that crevice formation within the locally deformed regions in polycarbonate during the incubation period is more effective in removing material than the material removal mechanisms operative in polysulfone during this period. The greater number of erosion sites available in polysulfone is probably responsible for the higher mass loss at the intermediate stage of the erosion process, however it is seen in Fig. 134 that the rate of material removal is comparable for polysulfone and polycarbonate in the



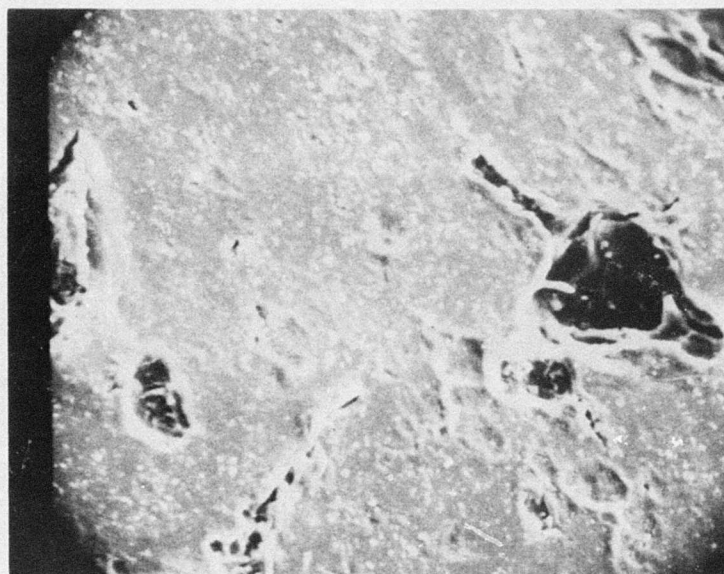
(a) Focused at Original Surface Elevation



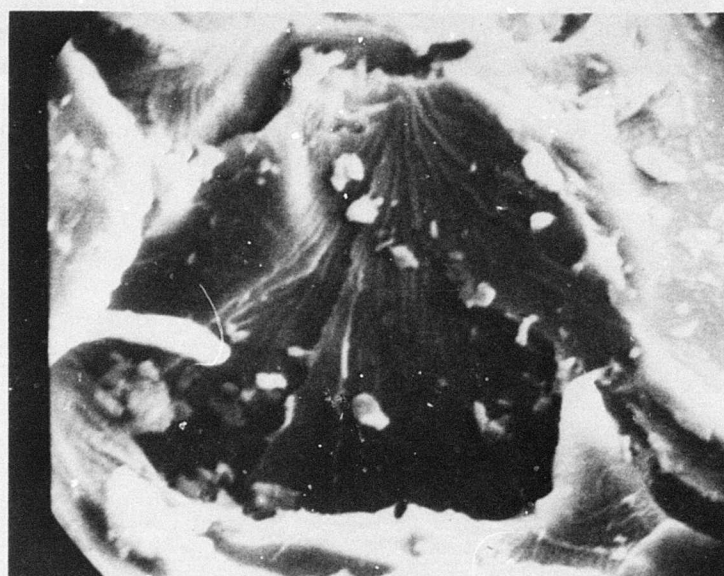
(b) Focused 65 microns below Surface Elevation to show Details of Fracture Surface

Figure 55. Pit Formation on Surface of Polycarbonate Specimen After 6-Minute Exposure to Standard Rainfield (110X)





(a) General Surface Condition (650X)



(b) Detail of Erosion Pit (1300X)

Figure 56. Characteristic Erosion Pits on Polycarbonate Specimen after 6-Minute Exposure



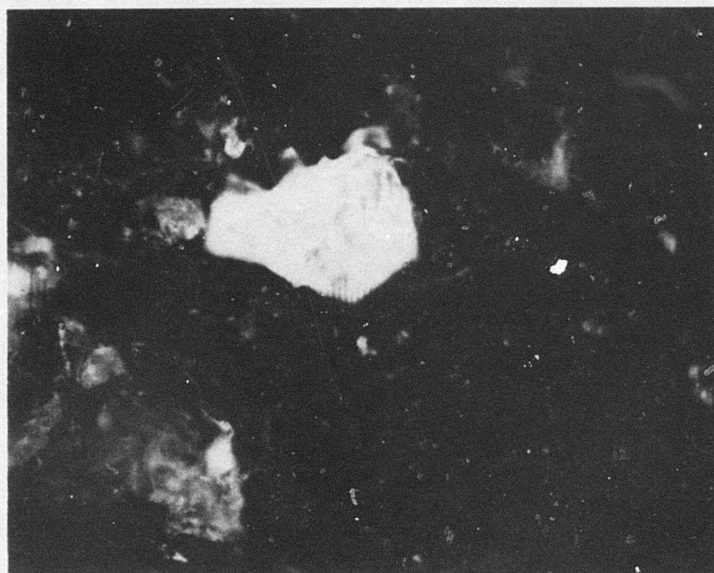


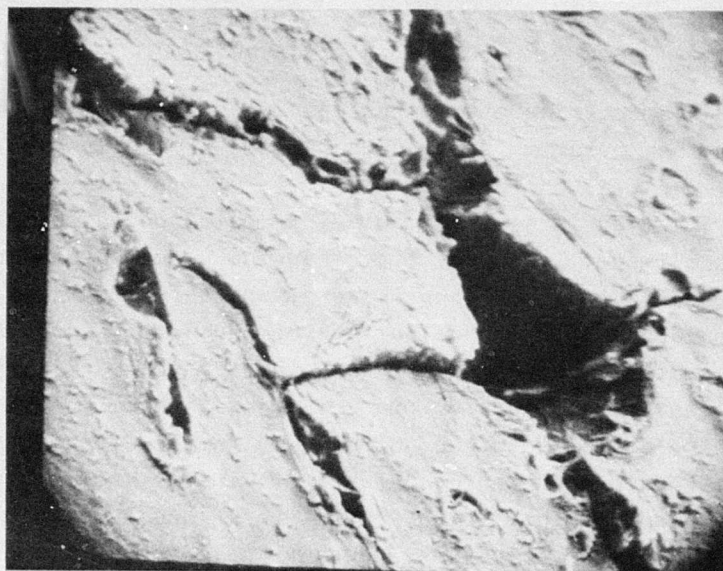
Figure 57. Particle Removal from Surface of Polycarbonate Specimen  
After 10-Minute Exposure to Standard Rainfield  
(70X)

advanced stage of the erosion process when the initial differences in the operative erosion mechanisms are no longer important.

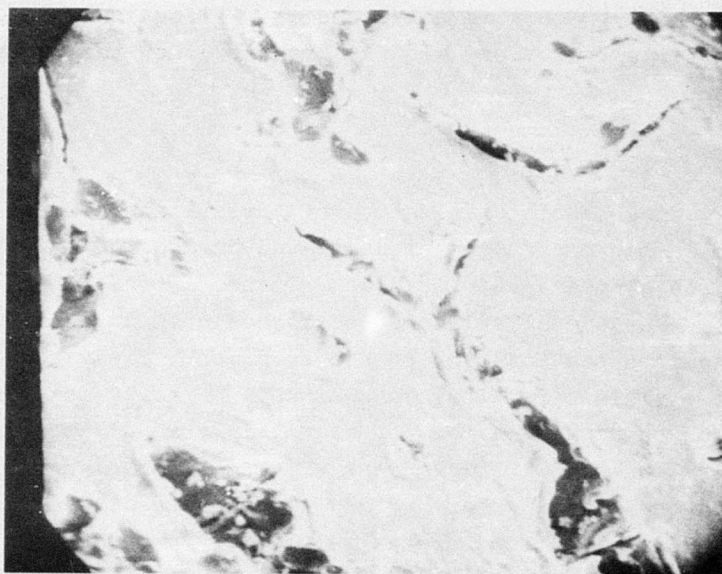
The surface of the melamine coated polycarbonate exhibits slightly less ductility than the uncoated specimens when subjected to water drop impacts, and very few ripple patterns could be found on the surface compared to the uncoated polycarbonate. The coated polycarbonate displays crevices which have a greater tendency for branching and generally have larger bifurcation angles than the uncoated polycarbonate as seen in Fig. 58. Again the crevice network originates from pitted regions. The markings in the interiors of the pits show material was removed by cleavage, however the edges of the pits seen in Fig. 59 show considerably less ductility than shown in Fig. 56 for the uncoated material. Except for these minor differences in the initial behavior of the type of specimens, the erosion mechanisms for the coated polycarbonate differ only in quantitative details from those already described for the uncoated specimens.

### 3. Nylon

Microscopic examination of the nylon specimens revealed that two damage mechanisms predominated during the initial exposure to the standard rainfield at 730 fps. First, the drops which struck residual polishing scratches opened linear cracks extending into the interior of the specimen. Cleavage occurs before the yield stress of the surrounding matrix is exceeded so the surrounding material is relatively free of deformation. Generally both crack walls appear wrinkled from plastic deformation produced by the water jet as it penetrates the cleavage crack. Additional drop impacts selectively extend these cracks deeper into the interior of the specimen. At sites of crack or scratch intersection, the water drops appear to penetrate beneath the surface layer of the nylon and push out small fragments of material as seen in Fig. 60. Consequently, material located within the acute angle of intersecting cracks, whether impacted



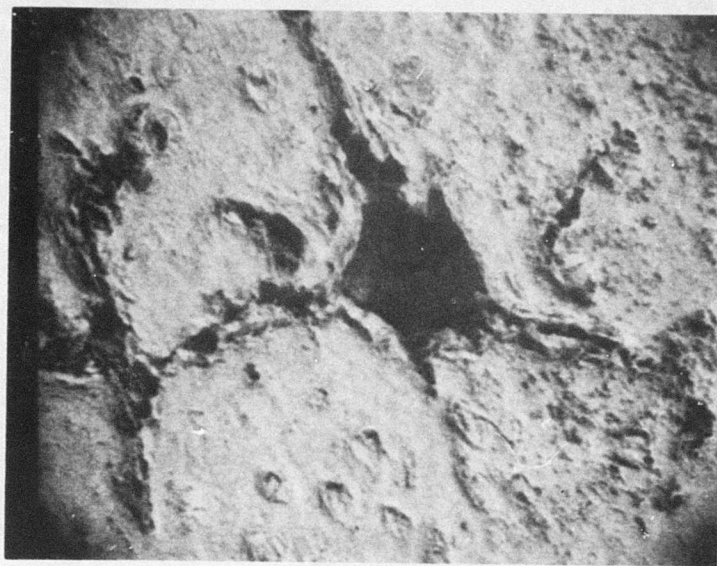
(a) Coated Polycarbonate



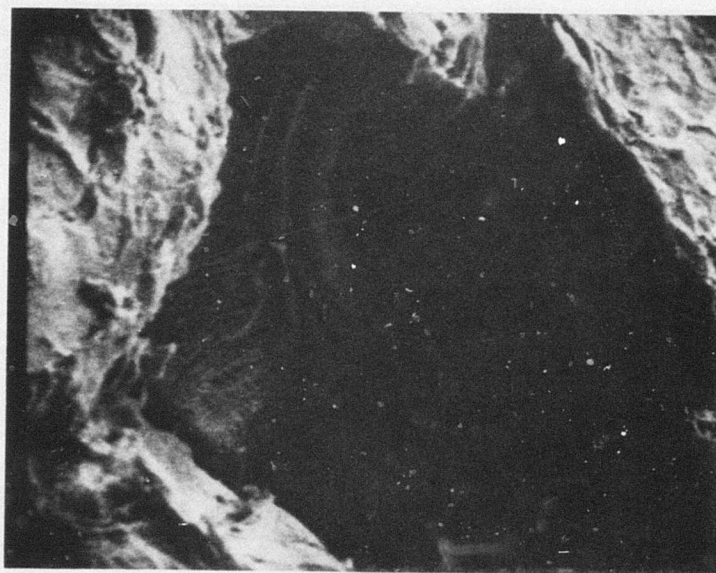
(b) Uncoated Polycarbonate

Figure 58. Comparison of Surface Features for Coated and Uncoated Polycarbonate After 6-Minute Exposure (325X)





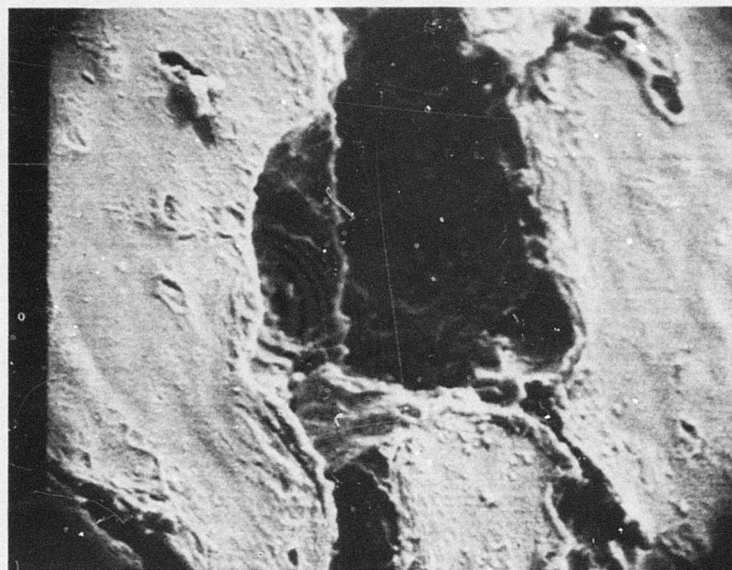
(a) 230X



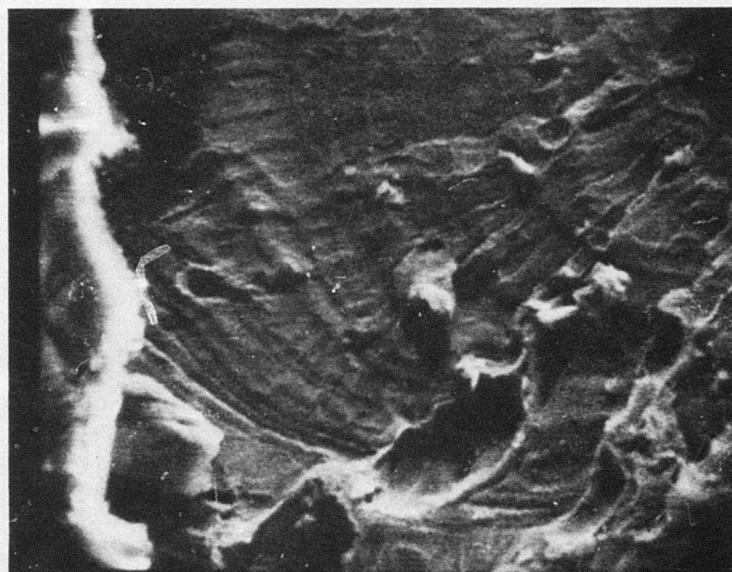
(b) Detail of Pit in (a) (920X)

Figure 59. General Character of Erosion Pits on Surface of Coated Polycarbonate Specimen



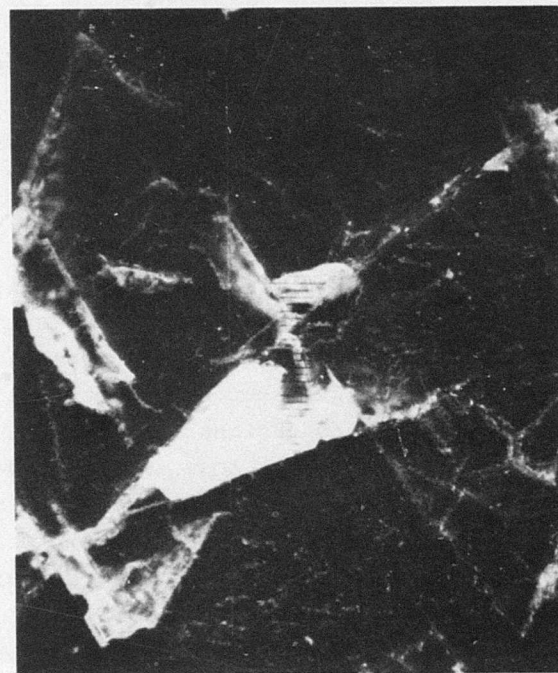


(c) 325X

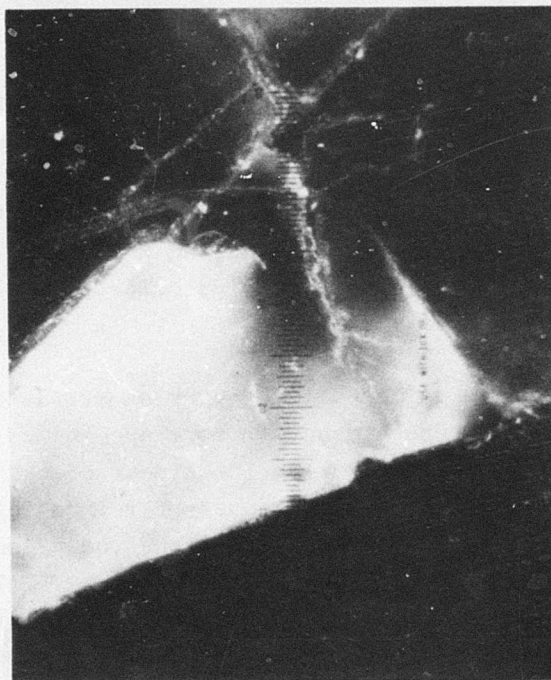


(d) Detail of Pit in (c) (4400X)

Figure 59. (continued)



(80X)



(240X)

Figure 60. Material Removal through Intersection of Fracture Surfaces

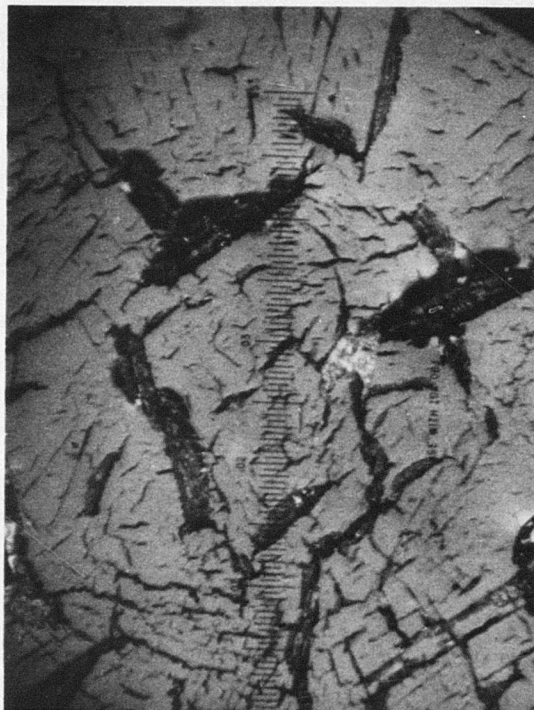
in the initial impact or subsequent impacts, is vulnerable to being torn free from the specimen's surface. This mechanism is primarily responsible for the observed form of the mass loss data. The mass loss data in Fig. 134 indicates an incubation period of several minutes is required during which the requisite network of cracks is produced. The optical micrographs in Fig. 61 illustrate impacted scratches.

The second damage mechanism occurs on surfaces free from defects which yield upon impact to form arc-shaped zones of damage. Cleavage cracks similar to the linear cracks are readily initiated but do not penetrate very far into the interior of the specimens. Under these conditions the nylon does not form cracks which propagate by brittle fracture. Although the cracks tend to propagate along linear paths, the material is noncrystalline and no preferential path orientations are observed. In addition to the larger cracks, a pattern of very fine microcracks and crevices develop as shown in Fig. 62.

A tendency toward a circular damage pattern can be observed in Fig. 61. Toward the droplet impact perimeters the induced radial stresses open cracks creating the damage zones. This zone lies within the original drop impact diameter.

During the initial stages (first several minutes) the optical transmission properties degrade due to scattering from microscopic crack patterns. Concurrently, a macroscopic network of linear cracks is gradually produced which run along pre-existing scratches and the longer impact cracks. This crack network causes the onset of rapid mass loss and subsequent destruction of the specimen's surface. The primary crack network penetrates more deeply into the interior of the bulk material and is more sparsely distributed than in the case of polysulfone and polycarbonate. The form of the cleavage surfaces found within larger pitted regions is shown in Fig. 63. In general, the nylon specimens display much less ductility than observed

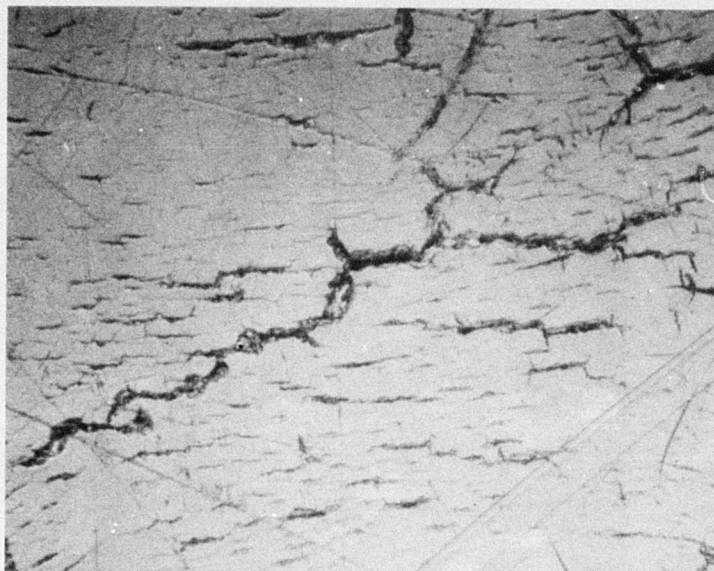




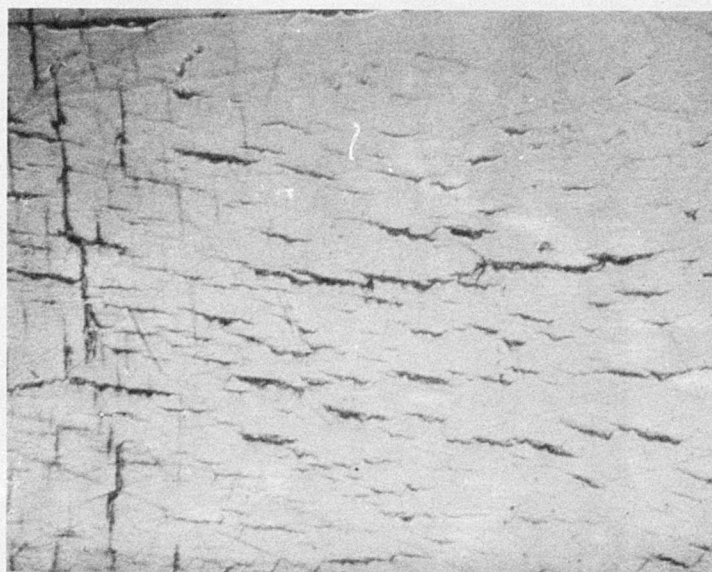
Polarized Light (70X)

Figure 61. Surface Condition of Nylon Specimen after 3-Minute Exposure to Standard Rainfall





(a) 320X

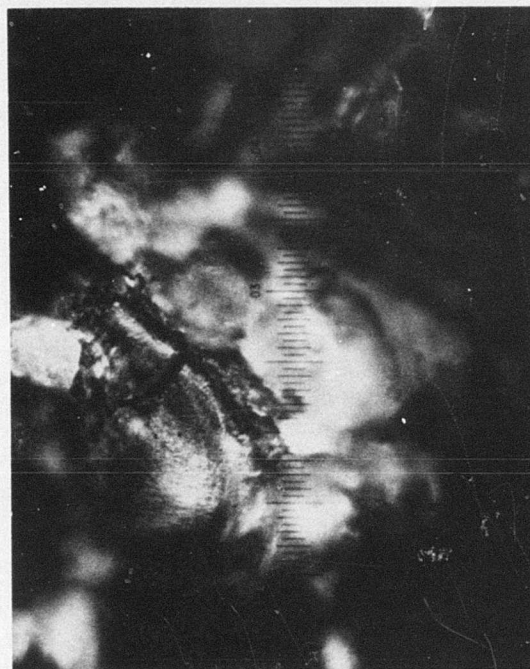


(b) 600X

Figure 62. Fine-scale Damage on Nylon After 2-Minute Exposure to Standard Rainfield



(a) Pitted Region on Surface of Specimen (80X)



(b) Detail of Fracture Surface within Pitted Region (80X)

Figure 63. Intermediate Stage of Material Removal Process

for polysulfone and polycarbonate at the strain rates imposed by water drop impacts, although the quasistatic elongation is the highest value recorded in Table II for the polymers tested.

#### 4. Polymethylmethacrylate

In contrast to the other polymers tested, PMMA responded in a brittle manner when exposed to the rain environment. The initial damage appeared in the form of multiple ring fractures (or ring crack patterns) as shown in Fig. 16 whose maximum diameter was always less than the diameter of the impacting drop. Apparently each impacting drop onto a previously undamaged surface produced a ring crack pattern. The interior zone of the ring pattern was initially free of damage and resisted the introduction of damage by subsequent drop impacts. However, this resistance was not as effective as that observed in the ring crack patterns formed in brittle inorganic transmitters which could exclude early stage fracture. The ring crack diameter typically extended from 1.0 mm to 1.5 mm. When possible, the perimeter cracks tended to align along the straight line paths of polishing scratches. This preferential attack mechanism was particularly effective in PMMA, since Nomarski interference contrast was required for scratch detection at sites free of impact damage. Even for the first impact event, these cracks tended to have an optically resolvable width (perhaps  $.3 \mu\text{m}$ ) and some showed pitting on the exterior edge together with a straight, undamaged interior edge. Consequently, the impacting drop enlarged residual scratches and established surface fractures at the perimeter during the early period of the drop impact, producing raised edges and surface discontinuities. As evident in Fig. 44 a high velocity water jet emerges tangential to the surface during the early stages of drop collapse. The observed edge pitting results from the impact of the lateral jet against the raised exterior edges of the circumferential fractures as described on page 88.

In the absence of residual scratches, the drop impact produced very short and discontinuous perimeter cracks which in the aggregate formed a band which encircled the central impact



zone. These initial perimeter cracks all tended to be very shallow (no appreciable interaction with transmitted light) but possessed optically resolvable widths and height differences suggesting limited microplasticity. Consequently, the initial crack structures were vulnerable to direct attack by hydraulic penetration and lateral outflow during subsequent rain exposure. The fracture surfaces generally did not suggest conchoidal structure as illustrated in Fig. 55 and 59 (although a rough river structure could be discerned) but instead contained a fine, non-reflective microstructure which could not be optically resolved. The density and dimension of the individual perimeter cracks tended to be greatest at approximately the center of the annulus and then decreased as the outer limit of the annulus was approached.

The perimeter crack annulus is particularly important in PMMA because the course of subsequent erosion is based primarily upon the interaction of the initial crack annulus with subsequent impacts. The impact of a second drop whose center would be located perhaps two-thirds of the perimeter diameter from the center of the initial drop reveals the relevant stages. Two zones of interest were produced during this sequence. Midway along the axis connecting the impact sites, scratches and larger cracks were greatly enlarged. Whereas the largest scratch width at noninteracting perimeter sites was less than  $1\mu\text{m}$ , the scratch widths in this zone were  $1\text{--}3\mu\text{m}$  and the depths of damage correspondingly deeper. These scratches had pitted edges on both sides where successive lateral outflow jets had chipped material free. As the scratches were traced around the perimeters away from the axis, the outflow orientation of the closer drop became more important and ultimately predominating as described for the initial impact (straight interior edge and a pitted exterior edge). Often a weak fracture annulus could be detected within the central zone of the first drop but greatly diminished in comparison with the crack annuli of both drops at noninteracting sites. At the sites of crack annuli overlap above and below the axis strong damage enhancement and a dense



crack pattern resulted although not quite as severe as that at the axis. The lateral outflow pitting and crack enlargement were particularly pronounced. The two sets of perimeter fracture structures seemed to propagate through one another without interference yielding a criss-crossed array of scratches. These scratch patterns were more important than their dimensions would indicate since scratch intersections are preferential sites for pit formation and the resulting surface discontinuities increased the number of orientations from which lateral outflow jets could produce edge pitting. Observation of the perimeter fracture structures in transmitted illumination clearly indicated the pronounced enhancement of the damage at the overlap sites.

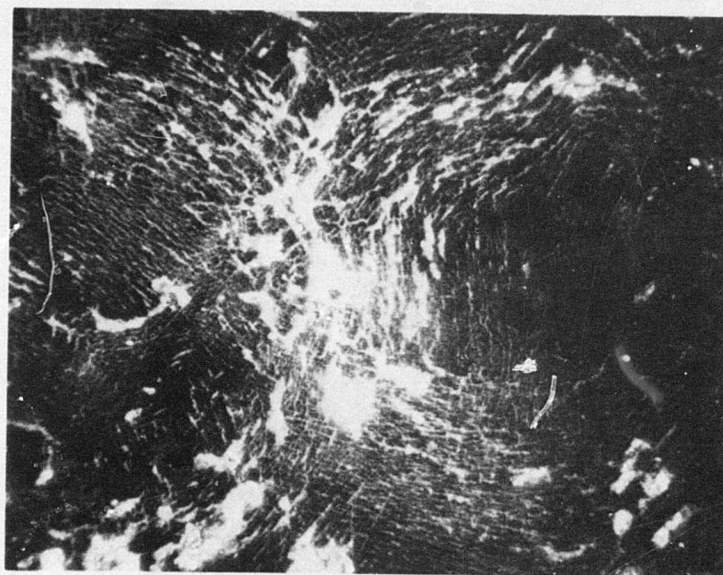
Continued exposure of the overlapping impact sites to rainfield gradually eliminated the structure of the original impacts. The density of pitting due to the lateral outflow during the collapse of subsequent drop impacts increased rapidly at the sites of ring crack overlap. The crack density also increased rapidly and the surface appeared wrinkled, although the originating impact sites could still be traced for up to four overlapping impacts. However, the most important damage resulted from hydraulic penetration so that a third drop impact could open the cracks in the interaction zones to widths up to  $15\text{ }\mu\text{m}$  (and possibly greater) concurrently penetrating far more deeply into the interior. In this earlier stage, the crevices often moved from one circumferential crack to another via the circumferential cracks of another impact resembling the cross-slip mechanism observed in crystallographic materials. As the crevice edges were plastically deformed and displacements were introduced along the path, reconstruction of the damage sequence became more difficult and the crevices began to resemble those shown in Fig. 34b for polycarbonate (typical widths perhaps  $3\text{-}6\text{ }\mu\text{m}$ ). The central sites of initial impacts were able to resist the subsequent introduction of damage at least up to this stage of 3-4 sequential impacts.

Sites influenced by four or more impacts resulted in a dense maze of fine cracks and pits together with a distribution of these randomly oriented crevices. An increasing proportion of randomly oriented cavities of irregular shaped cavities appeared whose structures bore no apparent relationship to the surrounding microstructure. The straight lines of initially damaged cracks were able at this stage to serve as initiating sites for subsurface fracture formation analogous to those shown in Fig. 61 (although at a much lower frequency). Subsequently, hydraulic penetration into the crack opening dislodged the overlying material analogous to the glass fracture shown in Fig. 109a. These observations suggest that a network of microcracks and a degree of micro-yielding embrittled the surface layer to allow the formation of these deformation modes observed only in the advanced erosion stages. Isolated cavities and crevices began to enlarge very rapidly with respect to the surrounding microstructure suggesting these structures trapped ever increasing volume fractions of the impacting drop. Intersections of enlarged scratches were also particularly effective sites for the preferential formation of cavities. Cavities at some sites ranged as large as 15 mils length by 5 mils width in this advanced erosion stage (perhaps 60 drop impacts per square centimeter). Surprisingly, the random spatial distribution of impacts permitted a number of enlarged scratches and damage resistant central zones from the initial stage of erosion to be identified on this specimen.

The preceding discussion was based upon short duration exposures in the AFML facility to the standard rainfall at 730 fps/sec. Exposures corresponding to a greater density of drop impacts were carried out in the AFML/Bell facility for the same nominal rainfall and velocity. Fig. 16 illustrates a single drop impact at a previously undamaged site on the PMMA surface. Although the contrast is poor (partially the result of the very shallow fracture penetration) examples of lateral outflow pitting appear at the top of the figure for scratch initiation and at the bottom for ring fracture initiation. Note the absence

of damage in the central zone. Fig. 64 illustrates the damage introduced by two overlapping perimeter crack annuli as enhanced by subsequent drop impacts (and also photographic over-exposure). Note, however, the increase in damage intensity at the interaction site, the large cavities vulnerable to hydraulic penetration, the important contribution of the lateral outflow jets to pit initiation, and the low density of damage in the central zones. In the center the dense, cross-checked pattern of the fine circumferential cracks can be distinguished between the large cavities. At perimeter sites distant from the overlap interaction, the arc-shaped fracture annuli illustrate the information sources from which the damage sequence can be reconstructed. Fig. 64 and 65 do illustrate the primary contribution of the lateral outflow mechanism and the overlap of perimeter crack zones to the initiation of pit removal and the perimeter overlap to the initial optical degradation. Obviously, the greatest importance of these mechanisms is that they render the sites vulnerable to subsequent hydraulic penetration which is far more damaging in the advanced stages of the erosion process. Evidence of how effective this mechanism was is shown for specimen PM 1 (refer to Section IV.A) which lost 4 mg mass and approximately 25% transmittance for a 30 sec. exposure (estimated to be two impacts per arbitrarily located site) in comparison to specimen PM 2 which lost 16 mg mass and over 90% of its transmittance for a 60 sec. exposure (estimated to be four impacts per site). Optical micrographs illustrating this degradation in optical properties and subsequent mass are shown in Fig. 65 and 66. Although these micrographs show the influence of lateral outflow mechanisms in Fig. 45 and the accelerated growth of cavities in Fig. 66, the deep scratch-initiated fractures are more clearly observed in Fig. 41. It is assumed these produce the extensive subsurface fracture networks shown in Fig. 67 by a mechanism similar to those observed in the less resistant glass systems. Further exposure to the rainfield caused the mass loss to approximately double with each additional 30 sec. exposure as the undercut surfaces cause larger size particle removal.

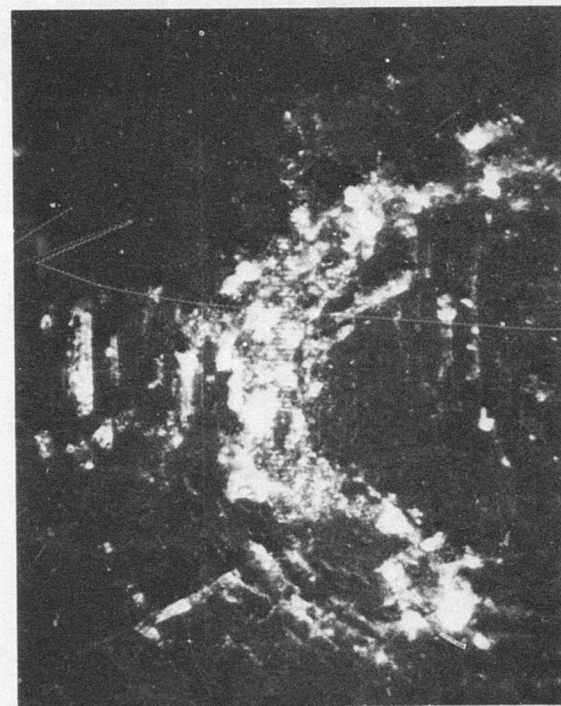




(80X)

Figure 64. Intersection of Droplet Impacts Initiating Material Removal on Surface of Polymethylmethacrylate





20 -Second Exposure (60X)



45-Second Exposure (80X)

Figure 65. Fracture Sites Initiated at Surface Scratches on Surface of Polymethylmethacrylate Specimen

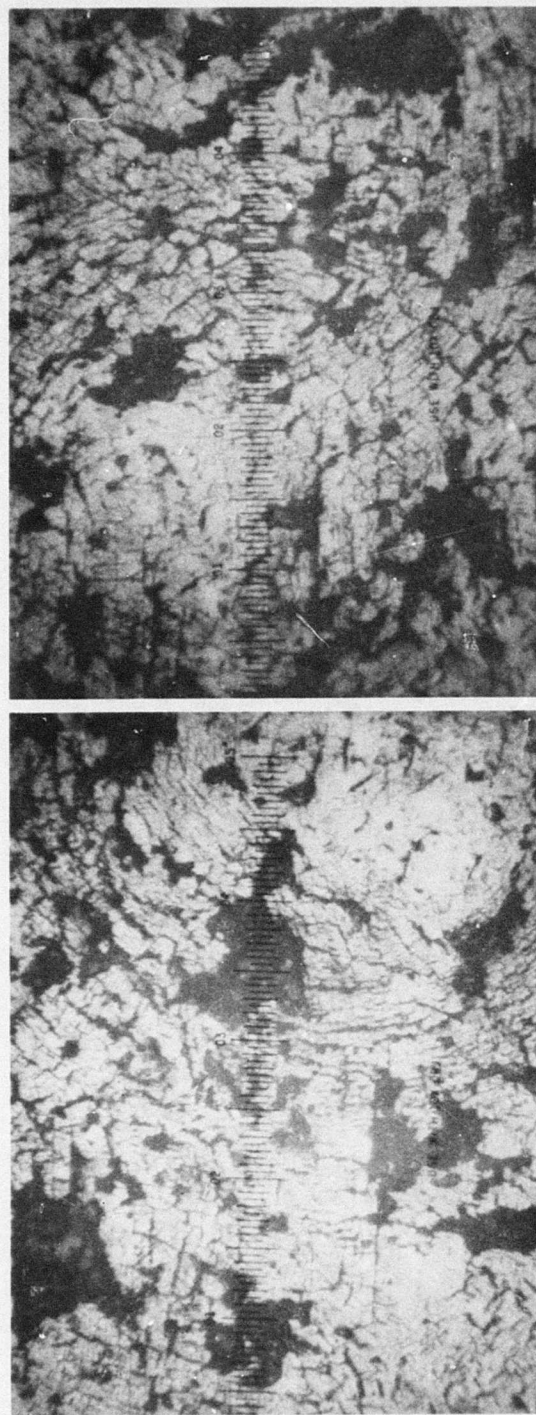
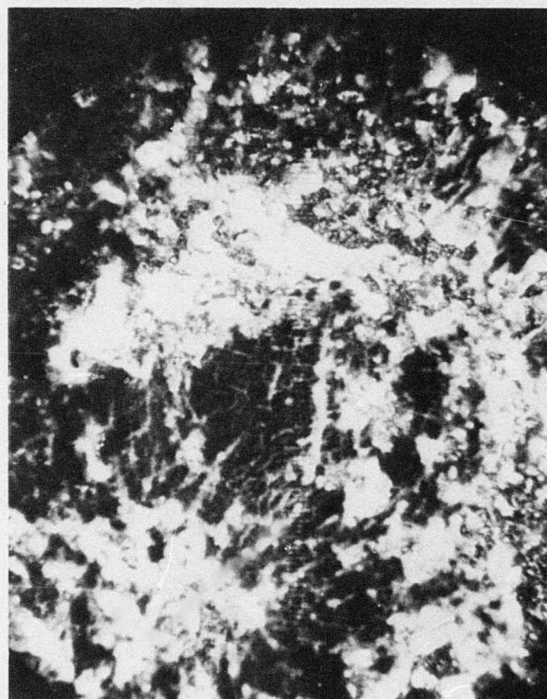


Figure 66. General Pattern of Material Removed from the Surface of a Polymethylmethacrylate Specimen after a 45-Second Exposure to the Standard Rainfield (80X)





Dark Field (60X)



Polarized Light (60X)

Figure 67. Condition of Surface of Polymethylmethacrylate after 75-Second Exposure to Standard Rainfall

## B. INFRARED TRANSMITTING MATERIALS

The leading candidate materials for infrared window applications include the covalently-bonded semiconductors germanium and silicon; binary semiconductors with a high covalent bond content such as cadmium telluride, gallium arsenide, zinc selenide, and zinc sulfide; binary salts with primarily ionic bond character such as potassium chloride and strontium fluoride; semiconductor glasses such as arsenic trisulfide; and oxides of high covalent bond strength such as magnesium oxide and sapphire. These substances are carefully purified and then fabricated by single crystal growth from the melt or as a polycrystalline aggregate by such techniques as chemical vapor deposition, crystal growth from the melt, fusion casting, hot-pressing, and physical chemical deposition. With the exception of sapphire, these substances are generally prepared as polycrystalline substances both to reduce cost and to increase mechanical strength and toughness. Obviously, the final optical and mechanical properties will be sensitive functions of these processing techniques. For the lower strength materials such as the halide salts and the binary semiconductors the processing techniques become critical so that the grain and subgrain structures must be introduced by press forging or fusion casting the single crystal (e.g. potassium chloride); alternatively binary alloy systems have been explored (e.g. potassium bromide-potassium chloride and zinc sulfo-selenide) to attain the necessary mechanical properties. Materials parameters such as composition, crystal orientation, crystal structure, grain boundary properties, grain size, impurity distribution, residual stresses and surface finish will all influence the rain erosion rates.

Exposure to water drop impacts such as would be encountered during subsonic flight through rainfields produces mechanical and optical degradation in infrared window materials. Since these materials are brittle, damage primarily consists of conchoidal fracture, cleavage crack formation and cavity formation (initially microscopic but ultimately macroscopic). However, the dependence of the extent of drop impact damage, the interaction of drop



impaction with pre-existing damage, and the rate of macroscopic damage upon the material properties and the fabrication processes are still not understood. In general, the IR transmission through these materials is greatly reduced before a measurable weight loss is recorded, and it is obvious that the interaction between the infrared beam and the evolving network of internal fracture surfaces contributes significantly to this reduction.

#### 1. Zinc Selenide and Zinc Sulfide

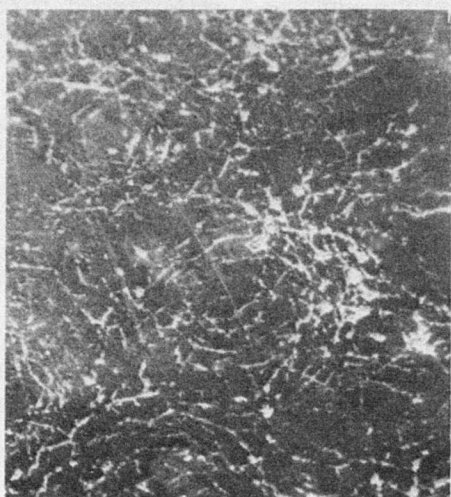
These materials are primarily covalently bonded semiconductors and therefore tend to be more brittle than materials with ionic or metallic bonding. The fact that they do have some ionic contribution to their bonding (e.g., ZnSe is thought to be 20% ionic<sup>(39)</sup>), may enable dislocation motion to occur more readily than would be possible in a purely covalently bonded structure. In the absence of any significant heating of the compounds during exposure to rain erosion, the impact energy will probably be initially absorbed by elastic deformation, plastic deformation and fracture propagation. Fracture can initiate in the compound semiconductors by both cleavage along {110} planes<sup>(40)</sup> and also by grain boundary separation.

Zinc selenide and zinc sulfide are primarily fabricated by four techniques: chemical vapor deposition, hot-pressing, physical vapor deposition, and crystals grown from the melt. Commercial polycrystalline samples fabricated by the first two techniques were examined in this work. Eroded specimens of chemically vapor-deposited material were examined after exposure to the rain environment in the AFML rotating arm facility at an impact velocity of 690 ft/sec. This material is fabricated by the chemical reaction of zinc vapor with hydrogen selenide and hydrogen at a graphite mandrel to form the binary compound at the surface.<sup>(41)</sup> The fabrication of large pieces (2 ft. x 1 ft.) with good optical and mechanical properties has been demonstrated for satisfactory deposition rates with both zinc selenide and zinc sulfide. Quality control is excellent, yielding very low

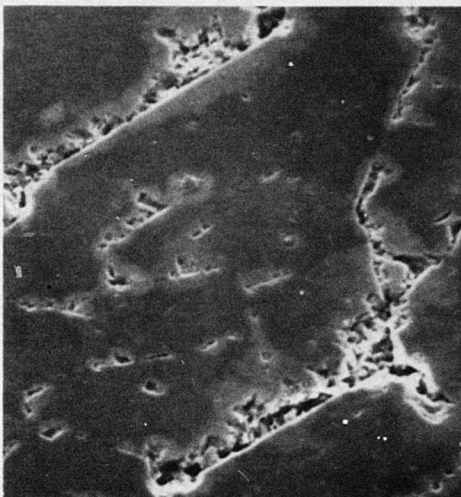
porosity, very low impurity content, uniform grain size, and uniform material properties. Previous work has established that under bend bar loading quasistatic fracture in these materials tends to initiate at surface sites of machining flaws and at volume sites such as porosity and defects in large grains.<sup>(42)</sup> Consequently, the surface finishing quality would be anticipated to be a critical parameter in determining the rain erosion rates.

Macroscopic inspection of the zinc selenide specimen after an exposure of 10 minutes and the zinc sulfide specimen after an exposure of 20 minutes in the AFML erosion facility under transmitted illumination revealed both specimens contained extensive internal fracture networks. Although such an examination could suggest that these networks were initiated at volume sites, microscopic examination under several illumination modes revealed fracture continuity between many surface cracks and the interior propagation cracks whose surfaces roughly approximated segments of expanding cones (analogous to the Hertzian ring crack structures formed in glass). It additionally indicated that the observed reductions in infrared transmittances arose primarily from reflections at the internal fracture facets. Repeated surface impacts enlarged the crack wall separations producing the high internal reflectances and extended the crack propagation depths until one-third of the sample thickness had been penetrated at some sites.

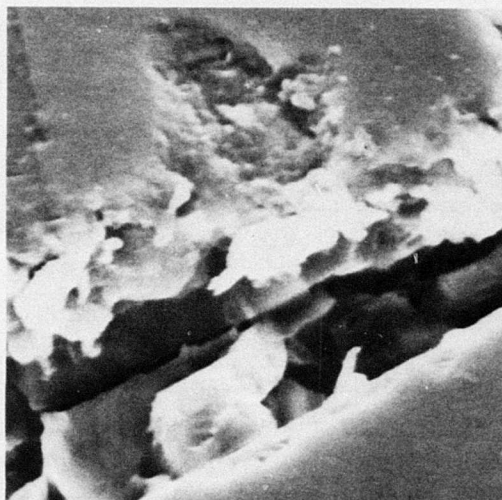
Fig. 68a shows a typical low magnification field of view at this stage of erosion. The damage consisted of overlapping arrays of eroded cracks whose jogged structures appeared to approximate concentric circular segments (with some misregistration) together with eroded cracks of random orientation and cavitites of various dimensions. The optical micrograph shown in Fig. 69 emphasizes both the circular appearance of the cracks and the presence of cavities. The scanning electron micrograph contained in Fig. 68b shows the straight edges characteristic of many of the surface cracks. These cracks were primarily formed by transgranular cleavage (consistent with the fracture study cited above)<sup>(42)</sup> and ranged from a few microns to several



(a) 36X



(b) 720X



(c) 7200X

Figure 68. Scanning Electron Micrographs of Arc and Ring Fractures in CVD Zinc Selenide after 10 min Exposure to 1 in/hr Rainfall at 690 fps in AFML Facility



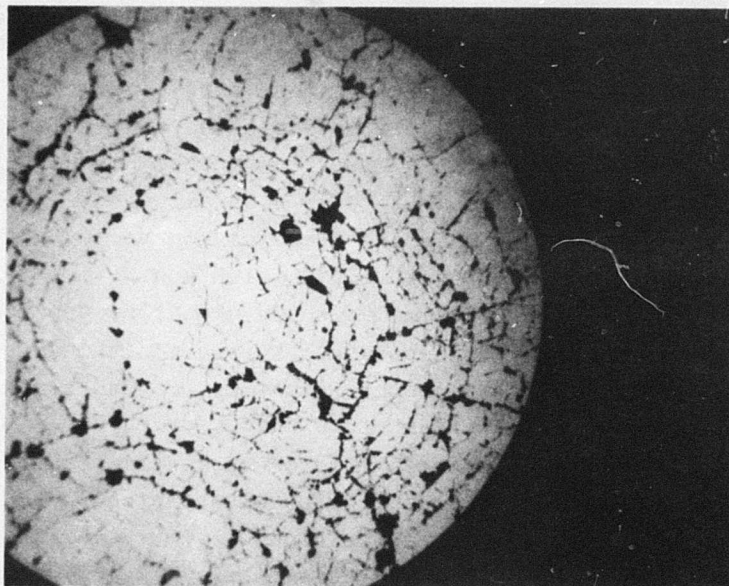


Figure 69. Optical Micrograph in Bright Field Reflected Light of CVD Zinc Selenide after 10 min.  
Exposure to 1 in/hr Rainfall at 690 fps in AFML Facility (50X)



hundred microns in length. It is believed the longer traces could have arisen in several adjacent grains with closely similar orientation. Such propagation has been observed on bulk fracture specimens and chemical vapor deposited zinc selenide has been demonstrated to contain significant residual texture which would increase the probability of such alignments.<sup>(43)</sup> Detailed examination using scanning electron microscopy and optical microscopy, with oblique illumination and Nomarski interference contrast (illumination modes which emphasize topological differences) established that residual surface finishing scratches exert a negligible influence on the formation of such cracks. Preferential initiation at sites of twin boundaries could not be evaluated. The advanced state of erosion restricted fracture analysis, since the high flaw density precluded etching and the severe edge pitting obscured the original fracture markings. However, possible grain structures consistent with the grain size listed in Table 4 can be identified along some of the fractures shown in Fig. 68b suggesting a significant contribution along intergranular paths. Any evidence of severe subsurface flaws (comparable to chatter marks in glass) arising from residual grinding damage would have been removed during the early stages of erosion and the importance of this initiation mechanism which was found to be important in the fracture study cited above<sup>(42)</sup> is impossible to assess.

Further evidence for the transgranular mechanism is provided by viewing the specimen under the metallograph with polarized illumination which suppresses the direct surface reflection from the specimen. Within large grains which contained the long straight surface cracks, associated large transgranular surfaces containing prominent cleavage river markings could be traced along the entire length of the surface cracks. In general, the surface crack walls were surprisingly straight suggesting that these {110} surfaces must have been aligned approximately orthogonal to the perimeter of the advancing impact stress since little or no evidence of large cleavage steps could be detected. The {110} surfaces in grains which were not favorably oriented for fracture propagation either resisted crack formation or yielded jogged cleavage cracks which were more susceptible to

subsequent edge attack. Fig. 68b illustrates the chipping and pitting which occurred preferentially along only one edge in many materials. It is believed this attacked edge was on the exterior side of the initiating impact event. In view of the large grain size, the substructure within the cracks must result from transgranular fracture propagated by the hydraulic mechanism during subsequent impacts as illustrated in Fig. 68b and 68c.

Examination of the cracks at higher magnifications revealed that curved cracks were very unusual (e.g. Fig. 68b) indicating conchoidal fracture formation is not an important mechanism in this system. A similar preferential formation of transgranular fracture was observed in eroded specimens of single crystal gallium arsenide in which the surfaces of shallow pits were composed of rectilinear cleavage faces which approximate the curved conchoidal shapes observed in germanium and the glasses.<sup>(42)</sup> Both the zinc chalcogenide compounds and gallium arsenide<sup>(44)</sup> have the zinc blende crystal structure and the preferential formation of cleavage cracks dominated erosion of the gallium arsenide surfaces during the incubation period before measurable optical degradation. The absence of conchoidal fracture in these zinc blende structures is attributed to the low energy of {110} cleavage ( $.6-.7 \text{ J/sq.m}^2$ ) in zinc selenide.<sup>(42)</sup> Cleavage along {111} planes required unattainable energies since oppositely charged {111} surfaces must be separated. At high magnifications, the formation of very small cleavage traces on otherwise undamaged zinc selenide surfaces could be readily discerned by optical metallography with topologically sensitive illumination - such traces show parallel alignment and constant angles of intersection. Although smaller and sparser than the cleavage traces observed on eroded surfaces of germanium and gallium arsenide, this difference probably results from the much smaller grain size as well as the dissipation of a greater fraction of the impact energy within the specimen bulk (extending the fracture by the hydraulic penetration mechanism). Although a few large cavities were observed (greater than 0.5 mm in diameter), most were small as shown in Fig. 69. Both optical microscopy and scanning electron

microscopy observations indicate that the pit walls also are formed predominantly by transgranular cleavage as shown in Fig. 70.

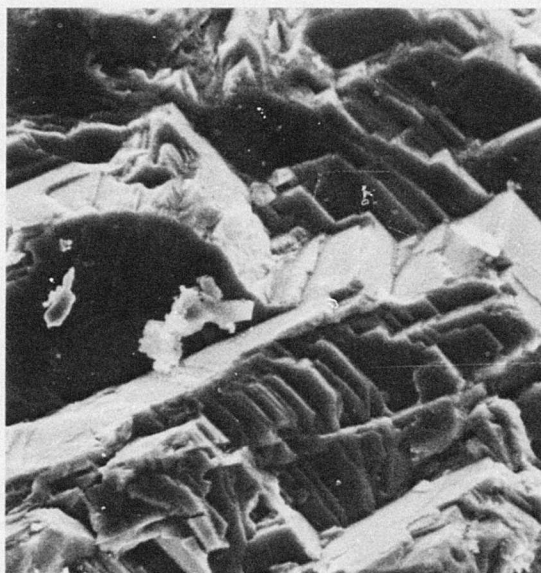
Optical microscopy revealed large cleavage surfaces frequently occurred within the larger pits in which one or more grains had undergone transgranular fracture. These cleaved grains closely resembled those observed on the bulk fracture surfaces (which were virtually flat with the exception of a few cleavage traces).<sup>(42)</sup> At higher magnifications (40X objective) and polarized illumination, such cleaved grains spanning 50  $\mu\text{m}$  or more were observed to lay beneath 20% or more of the intact specimen surface. These strongly reflected light (visible wavelengths) as noted earlier and suggested the bulk material to have been heavily damaged in comparison to the surface. A high magnification view of the fracture surface of a bend test specimen is provided in Fig. 71a; more representative micrographs have been published.<sup>(42)</sup>

As noted earlier, the advanced state of damage prevented a precise determination of the early erosion stages. It is believed the first drop impact to strike a surface site either resulted in the initial formation of a partial ring crack structure or the first drop impact established a precursor form of damage which interacted with subsequent drop impacts to produce partial ring crack structures. Such a precursor state could arise from stress concentrations introduced by plastic flow or the subcritical extension of fracture initiating flaws (e.g. microcracks, pores, inclusions, etc.). It is believed that the early damage was dominated by the formation of ring perimeter segments composed of fine transgranular cracks. It is probable that some subsurface damage is associated with these early cracks since ring structures are clearly evident in optical macrographs employing transmitted illumination of a zinc selenide specimen exposed to the same erosion environment for only 30 seconds.<sup>(45)</sup> Some pitting of the exterior edges of the outer perimeter cracks was observed at this early stage of damage. Continued exposure then produced the extensive damage described above for 10 min. exposure.





(a) 180X



(b) 1800X

Figure 70. Scanning Electron Micrograph of Erosion Pit in CVD Zinc Selenide after 10 min.  
Exposure to 1 in/hr Rainfall at 690 fps (AFML Facility)



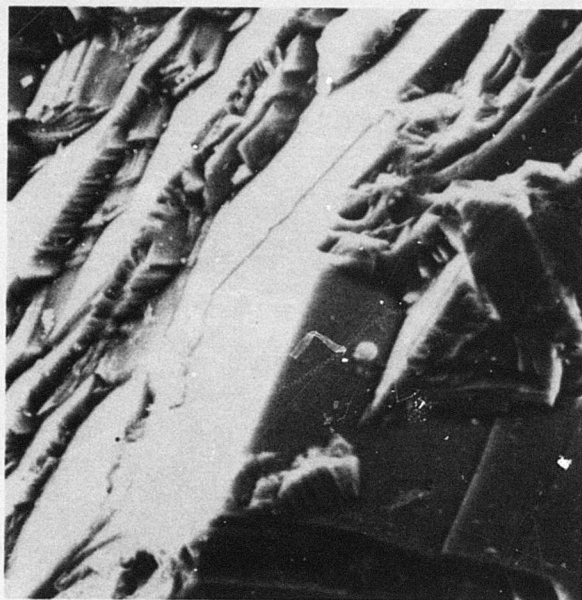


Figure 71. Scanning Electron Micrograph of Bend Bar Fracture of CVD Zinc Selenide (1500X)

Correlation of the grain size at the fracture origin with the observed fracture strengths observed under bend bar loading showed the fracture strengths depended upon the inverse square-root of the grain size.<sup>(42)</sup> Such a relationship has been previously demonstrated for a number of polycrystalline ceramics.<sup>(46)</sup> In addition, continued propagation of a crystallographic crack through a polycrystalline material requires both directional changes at the grain boundary and grain boundary rupture. Consequently, although the previous rain erosion literature does not clearly define the relationship between grain size and erosion rate; the above information, cavitation studies on nickel, and ballistic impact studies on alumina ceramic all indicate that decreased grain size should increase rain erosion resistance.<sup>(47-49)</sup>

Although the chemical vapor deposited zinc sulfide specimen was exposed in the AFML erosion facility for 20 min., twice the exposure period for the zinc selenide specimen, the apparent surface damage observed under optical microscopy was minimal in comparison as illustrated in Fig. 72. Note particularly the absence of the long straight line segments characteristics of the zinc selenide erosion surface. The absence of these cleavage cracks (and also the large subsurface cleavage facets) could result from the much greater fracture strength of zinc sulfide (16,000 psi vs. 7,500 psi)<sup>(50)</sup> exceeding the perimeter tensile stresses induced by drop impact and/or the very small grain size 2-10 $\mu$ m determined by metallographic measurement after a hydrochloric acid etch.

Instead the apparent surface damage under bright field examination consisted of a sparse distribution of fine circumferential cracks some of which appeared to comprise incomplete sectors of the original impact. Polarized reflected illumination or transmitted illumination permitted the fracture propagation path to be traced from these cracks into the interior. These interior surfaces generally involved a smaller angular sector which penetrated less deeply than those of zinc selenide suggesting the greater fracture strength of the zinc sulfide

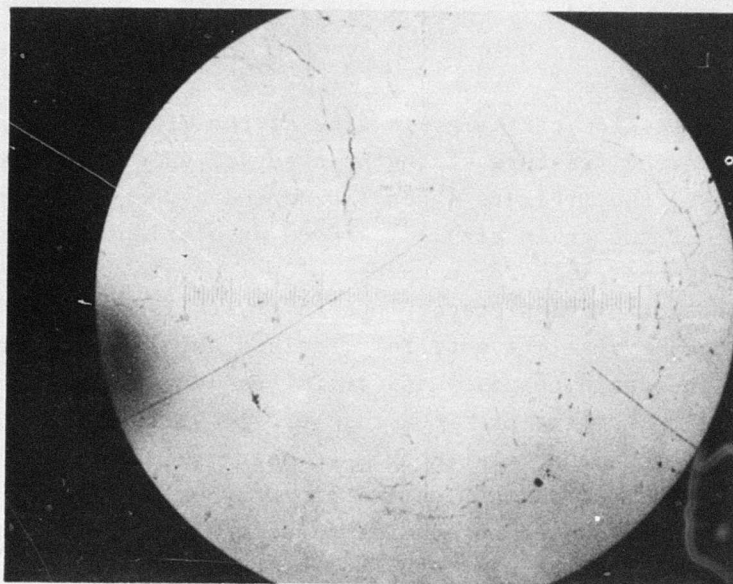


Figure 72. Optical Micrograph in Bright Field Reflected Light of CVD Zinc Sulfide after 20 min.  
Exposure to 1 in/hr Rainfall at 690 fps in AFML Facility (50X)

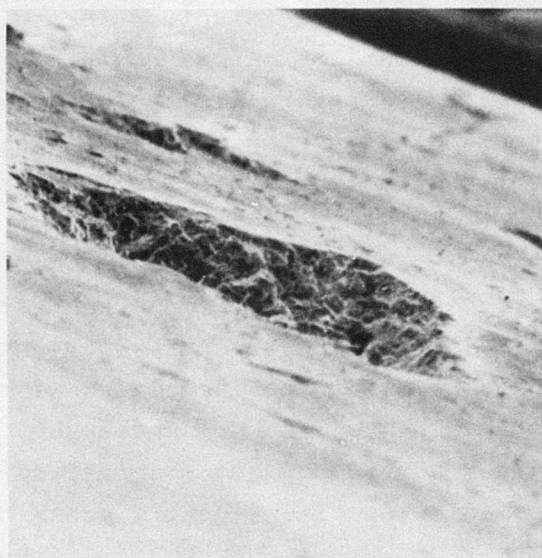


restricted surface fracture extension as well as surface crack enlargement. Instead, higher magnification resolved only that the surface cracks generally consisted of connected lines of fine pits without revealing whether the path structure arose from intergranular fracture or transgranular fracture conforming to the interaction between the advancing tensile stress wave front and the flaw distribution within the zinc sulfide surface.

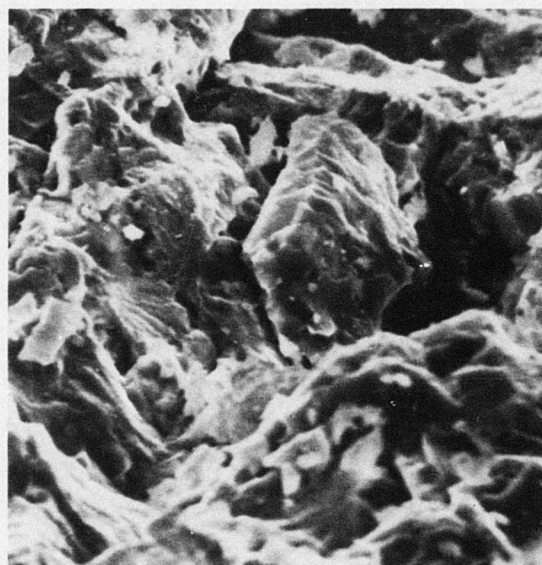
Subsurface fractures were more easily identified and frequently could be traced back to surface crack structures. At some surface sites, the subsurface fractures were shown by Nomarski interference contrast to be associated with slight surface bulges rather than surface cracks. These very small bulges were analogous to larger surface bulges observed during compression tests of zinc selenide specimens before gross failure occurred. (approximately 5,000 - 6,000 psi).<sup>(51)</sup> However, many of the smaller subsurface fractures could not be traced to surface cracks or flaws under oblique illumination (which was usually a very effective technique) and the more sensitive Nomarski interference contrast established that some subsurface fractures were not associated with surface flaws. Such damage could have arisen either at sites of subsurface machining damage or volume distributed flaw sites; however, residual polishing scratches and submicroscopic surface flaws are excluded as origin sites. Such subsurface initiation was probably more frequent than indicated at this stage of erosion and the subsurface damage propagated back to the surface during the erosion exposure. The surface above such suspected subsurface initiated fractures consisted of shallow cleavage traces or irregular surface mounds.

The subsurface fracture surfaces were covered with tiny facets and the nature of their structure could not be optically resolved. However, examination of some larger surface cavities at high magnification with the scanning electron microscope as shown in Fig. 73 established their walls to have been formed by transgranular cleavage; it is believed this mechanism





(a) 180X



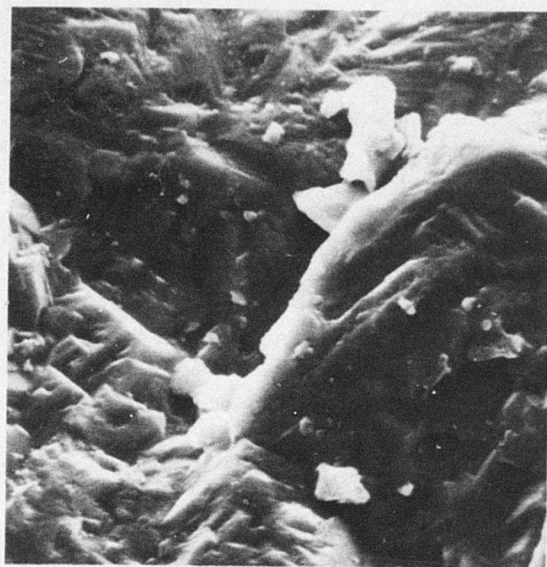
(b) 1800X

Figure 73. Scanning Electron Micrograph of Erosion Pit in CVD Zinc Sulfide after 20 min.  
Exposure to 1 in/hr Rainfall at 690 fps in AFML Facility

dominated the fracture propagation. Again, the fracture mechanisms observed on both the bend bar surfaces and the rain erosion surfaces were transgranular cleavage (illustrated in Fig. 74). The smaller scale of facets on the bend bar surfaces of zinc sulfide is primarily attributed to the smaller grain size; the facet dimensions on the eroded surfaces may also have been reduced by the requirement for a large number of randomly located rain impacts to propagate the fractures a significant distance along the surface.

Rain erosion tests of a hot-pressed zinc sulfide material were initiated on the AFML/Bell erosion facility at 730 fps. Due to the large difference in the droplet encounter densities for the same specified rainfall rate for the erosion facilities at AFML and Bell, these tests do not allow a direct comparison of the relative erosion resistances of the two materials based upon exposure periods. Note also that the as-polished (by the vendor) hot-pressed specimens contained a relatively high density of surface pits, perhaps several million per centimeter squared primarily ranging from 1-5 $\mu$ m in size. Although their structure could not be resolved under optical microscopy, a probable origin would be grain pull-out during polishing. The grain diameter determined by optical etching corresponds to the smaller pits and the larger pits could result from loss by small aggregate. After 20 and 40 second exposures (independent tests) on the AFML/Bell facility, fine ring cracks were observed on both specimens.

After the 20 second exposure, two principal damage modes become apparent as illustrated in Fig. 75 and 76. First, surface ring crack patterns form whose perimeters consist of concentric jogged cracks. Fig. 77, photographed after an additional minute of exposure on the AFML erosion facility, illustrates that many of the surface cracks are nearly invisible under bright field observation. However, reflected polarization illumination of the same field of view reveals that significant cone crack penetration into the substrate occurred together with the onset of optical



(a) 1800X



(b) 7200X

Figure 74. Scanning Electron Micrograph of Bend Bar Fracture in CVD Zinc Sulfide



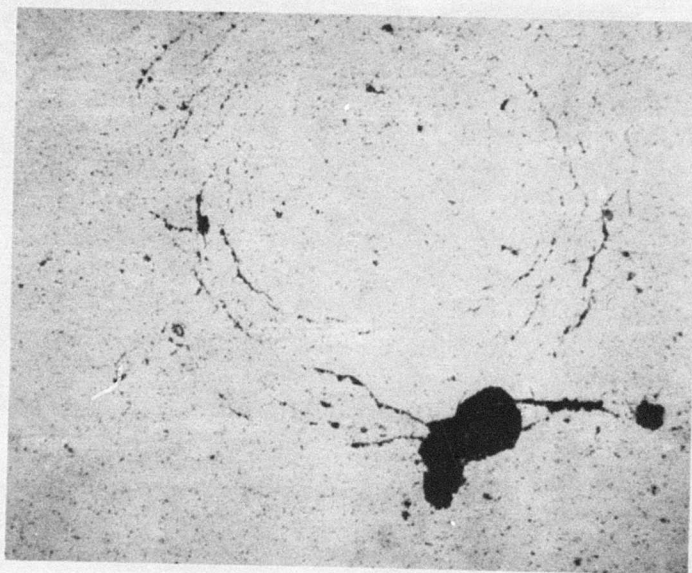


Figure 75. Optical Micrograph in Bright Field Reflected Light of Ring Crack Pattern and Associated Cavity in Hot-Pressed Zinc Sulfide after 40 sec Exposure to Standard Rainfield (80X)

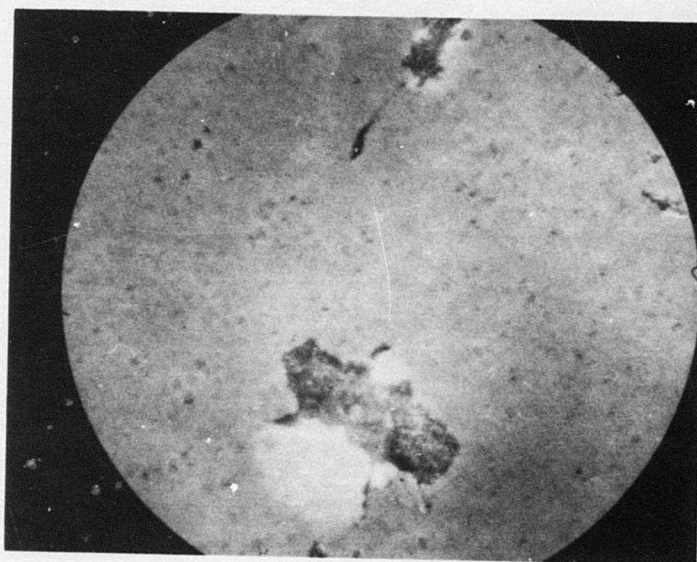
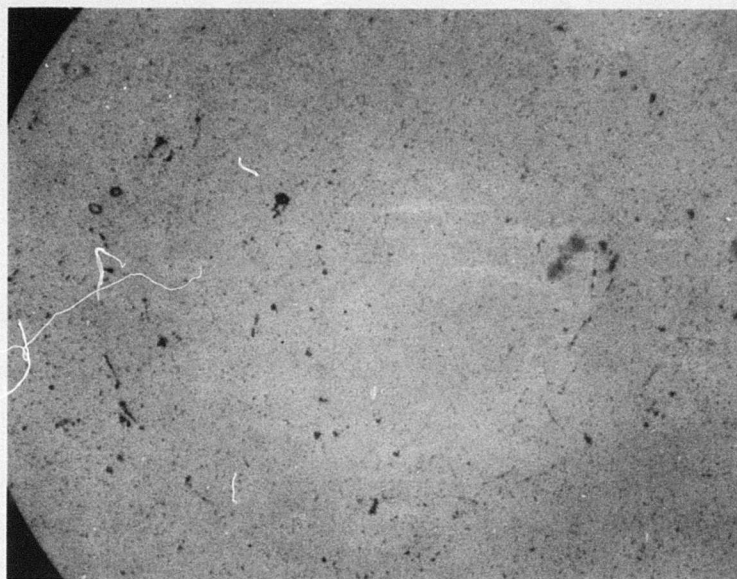
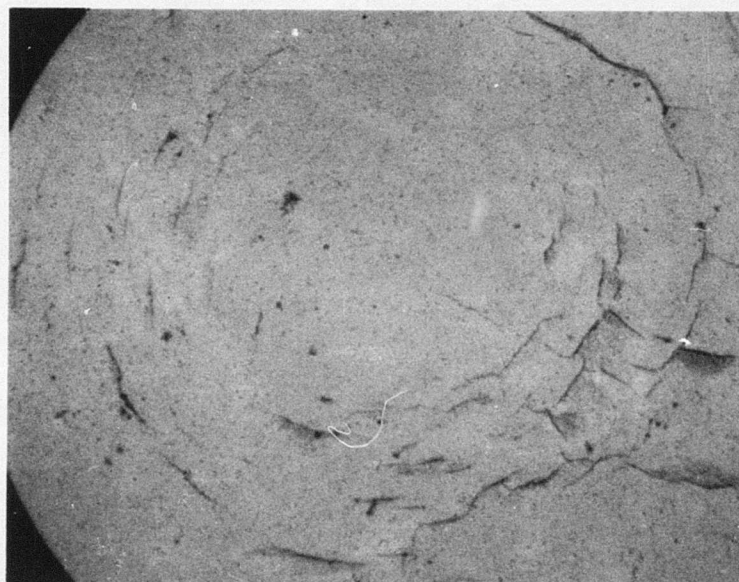


Figure 76. Optical Micrograph in Bright Field Reflected Light of Erosion Cavities in Hot-Pressed Zinc Sulfide after 20 sec Exposure to Standard Rainfield (200X)





(a) Bright Field Reflected Light



(b) Polarized Reflected Light

Figure 77. Optical Micrographs of Ring Crack Pattern in Hot-Pressed Zinc Sulfide after 20 sec Exposure to Standard Rainfield (70X)

transmittance degradation. Optical microscopy employing Nomarski interference contrast and transmitted illumination indicated similarities between the initiation of damage in the chemical vapor deposited and the hot-pressed zinc sulfide specimens. In this system, a small fraction (but larger than that for the chemical vapor deposition product) of the subsurface fractures could not be associated with surface topography variations. Although the relative contributions from subsurface grinding damage and from volume distributed flaws could not be isolated, such flaws initiated a significant fraction of the erosion damage. Early stage fracture initiation and propagation definitely proceeded by an intergranular mechanism. Surprisingly, the size of the surface displacements above small to moderate subsurface fractures did not simply correlate with size and intensity of the subsurface damage suggesting also that competition occurred between surface and subsurface fracture initiation. As the extent of the subsurface damage progressed further, grain ejection systematically occurred at the surface crack above the damage in approximate proportion to the intensity of subsurface damage. Ultimately, the severely damaged areas showed enlarged crack widths (analogous to those shown in Fig. 68 but resulting from intergranular fracture).

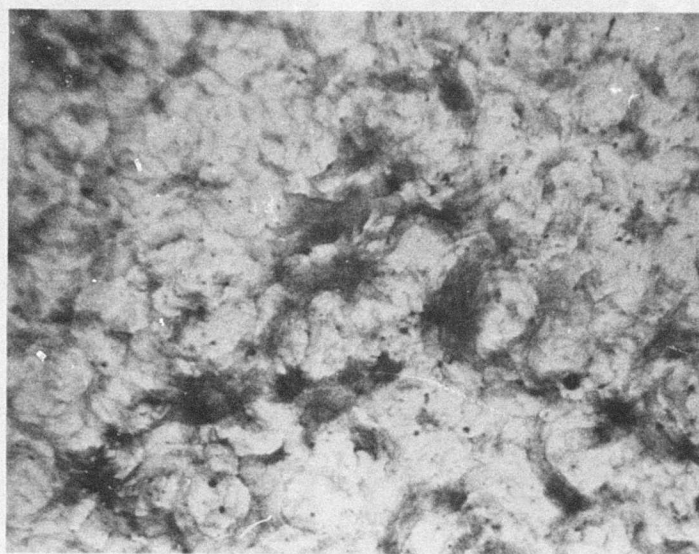
The other major damage mode shown in Fig. 76 is the formation of large cavities together with associated subsurface structures. Unlike the conical subsurface fracture structures which measurably influence the infrared transmittances data only, the cavities influence both the infrared transmittance and the mass loss data. However, to this stage of damage the conical subsurface fracture structures are the more important source of transmittance loss. Progressive degradation of the optical and mechanical properties occurred during the 20 sec. exposure as subsequent drop impacts extended and enlarged these damage modes. The cavities enlarged by extension of subsurface fractures originating at flaw sites along the interior surfaces. An undercut surface is clearly evident as the bright area adjacent to the cavity in Fig. 76; this surface is probably slightly uplifted

since its lateral boundaries are marked by surface cracks. Subsequent drop penetration would cause mass removal by the hydraulic penetration mechanism. Although cavities were often associated with surface cracks, their initiation did not appear to require a mechanism based on the ring crack patterns or the intersection of the cone fractures of two adjacent ring crack patterns. Instead the surface damage associated with the ring patterns only tended to enlarge the crack widths and extend the fracture surfaces deeper into the substrate as described above.

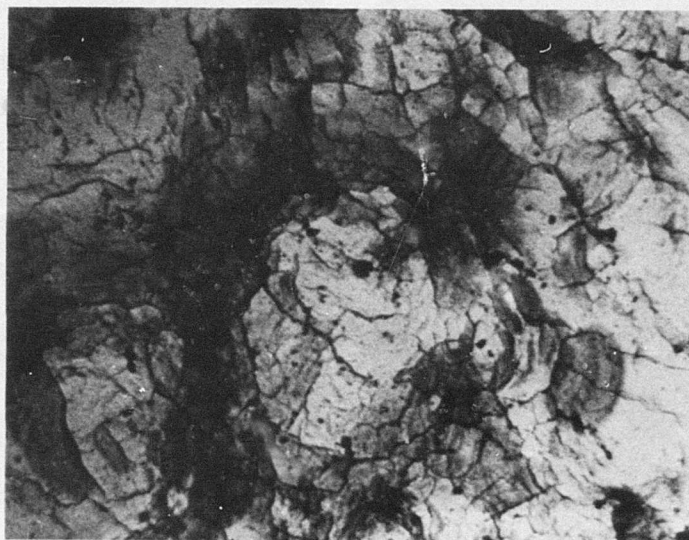
After 40 seconds exposure in the AFML/Bell erosion facility, the specimen surface was covered with a dense array of ring patterns whose subsurface cone fractures interacted strongly with the incident light as shown in Fig. 78. With continued exposure, surface cracks perpendicular to the ring perimeter, within the ring pattern, and at isolated sites also appeared. These surface cracks appeared to be less important to specimen degradation than those associated with the subsurface conical fracture extensions and the cavity enlargements.

A study of the cavity walls employing scanning electron microscopy confirmed that fracture propagation in the hot pressed zinc sulfide is dominated by the intergranular mechanism as shown in Fig. 79. It is possible that this material was not prepared under conditions suitable for optimal grain boundary strength. Surprisingly, for similar grain size material, both the chemically vapor-deposited material and the hot-pressed material yielded similar microhardness values indicating that microplasticity is probably not the critical parameter in determining the rain erosion resistance.<sup>(52)</sup> Consequently, although the macroscopic damage modes observed in zinc sulfide fabricated by the chemical vapor deposition and hot-pressing processes were similar, fracture in the latter material proceeded by an intergranular mechanism; the grain boundaries separated before the critical resolved cleavage stress on the {110} plane could be attained. Although direct comparisons of the erosion resistances between the two fabrication techniques were not possible, this data





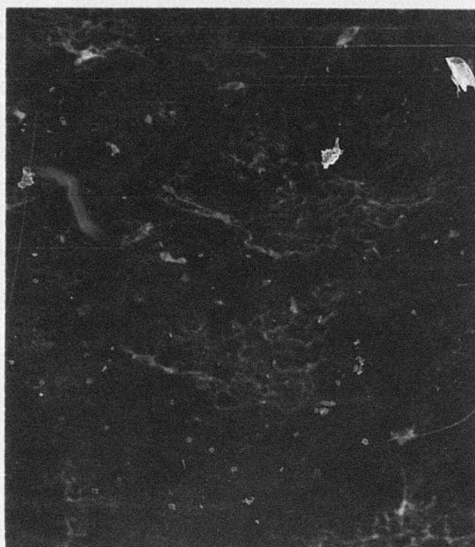
(a) 51X



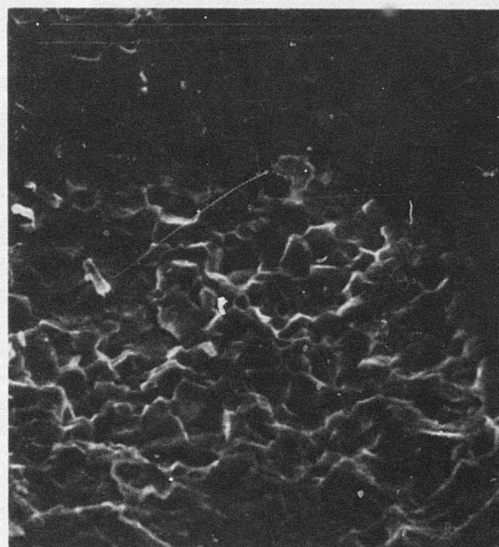
(b) 128X

Figure 78. Optical Micrographs in Transmitted Light of Hot-Pressed Zinc Sulfide after 40 sec Exposure to Standard Rainfield

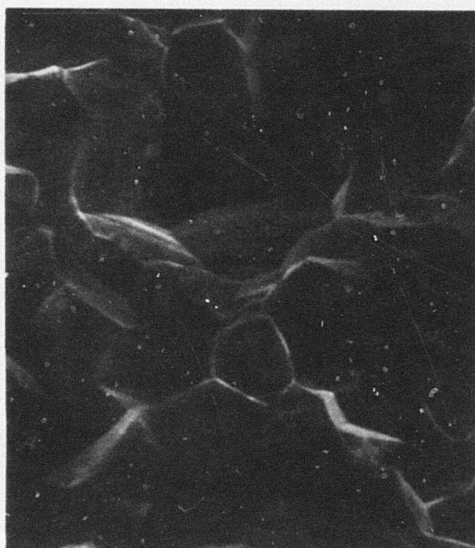




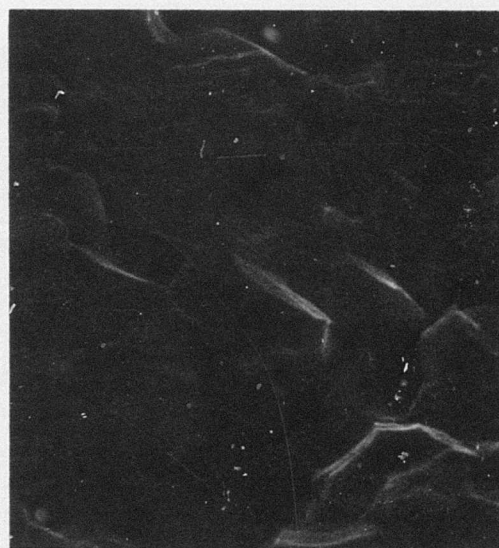
(a) 600X



(b) 1200X



(c) 6000X



(d) 6000X

Figure 79. Scanning Electron Micrograph of Hot-Pressed Zinc Sulfide after 40 sec Exposure to Standard Rainfield

suggests the hot-pressed zinc sulfide would undergo degradation at a more rapid rate both before and during the weight loss regime.

## 2. Arsenic Trisulfide

Amorphous arsenic trisulfide ( $\text{As}_2\text{S}_3$ ) is an important candidate for antireflective coatings at 10.6 microns. The material may be obtained in bulk as a glass and its fracture properties have been characterized (see Table III).<sup>(42,53)</sup> In bend bar tests, fracture initiation occurs at surface flaw sites and the fractography structure is typical of such fractures in glasses. The fracture parameters, modulus of elasticity, and hardness range from 25 to 50% of the values for the common oxide-based glasses. Consistent with these smaller mechanical parameters, the bulk arsenide trisulfide specimen demonstrated a low resistance to rain erosion as described below.

The initial evaluation of the rate of erosion for arsenic trisulfide in the AFML/Bell erosion facility resulted in destruction of the specimen after a 20 second exposure to the standard rainfield at 730 fps. An average depth of 2-3 mm of material was removed from the exposed surface yielding an opaque specimen covered with a macroscopically rough surface. At some sites, the fracture surfaces penetrated about two-thirds of the way through the specimen although the specimen remained intact to completion of the test run on the rotating arm. However, a hairline crack could be seen on the back face of the specimen which ran diagonally across the specimen and the specimen was later manually fractured along this line without difficulty. Consequently, testing at 730 fps was discontinued and instead lower velocities were employed in subsequent erosion exposures.

A second specimen was run for 5 seconds at 500 fps in the AFML/Bell erosion facility to further investigate the damage mechanisms. Although the extent of bulk damage was greatly reduced, it was still more severe than that sustained by the other brittle transparent materials evaluated in this study. Note, however, that the intended application for this material

is as a component in infrared coatings rather than as a substrate. Light transmission through the specimen revealed the extensive damage which occurred in the bulk of the specimen as illustrated in the macrograph (Fig. 80). The opacity was produced by very extensive and complex subsurface fracture networks which reflected and scattered visible light too effectively to permit microscopic study with transmitted illumination. Although continuity between the surface cracks and subsurface fractures which indicated surface initiation could be established by optical microscopy, a disproportionately great fraction of damage occurred below the surface (in comparison to other materials reported herein). Similar to the early exposure of the hot-pressed zinc sulfide, the intensity of surface damage did not simply correlate with the intensity of subsurface damage. For such erosion systems, the measurement of weight loss curves is of limited value and optical transmittance provides a more realistic assessment of both mechanical and optical degradation.

The intensity of subsurface fracture damage varied considerably over the sample surface. The substructures at the opaque regions were very complex, consisting of intersecting layers and networks or large conchoidal fracture surfaces. Examples of such subsurface facets are shown in the micrograph contained in Fig. 81. At some sites where the fracture surface penetrated along a single plane without branching, successive hackle and rib markings indicated macroscopic penetration depths produced by a single drop impact. Although not so apparent as the complex subsurface fracture systems and the conical subsurface fracture sectors, these large planar cracks are the damage mode which limits mechanical integrity in this system.

Inspection of the eroded surface established that the surface damage primarily consisted of a distribution of individual raindrop imprints together with a random array of disjointed cracks. Under bright field microscopy, the surface seemed to be moderately damaged and a significant fraction of the surface was free of cracks and pits. A typical ring pattern is shown



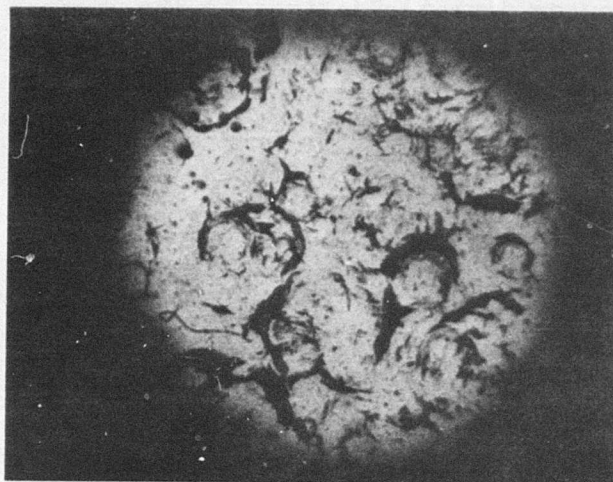


Figure 80. Optical Macrograph in Transmitted Light of Arc and Ring Crack Patterns in Arsenic Trisulfide Glass after 5 sec Exposure to Standard Rainfield at 500 fps (8X)

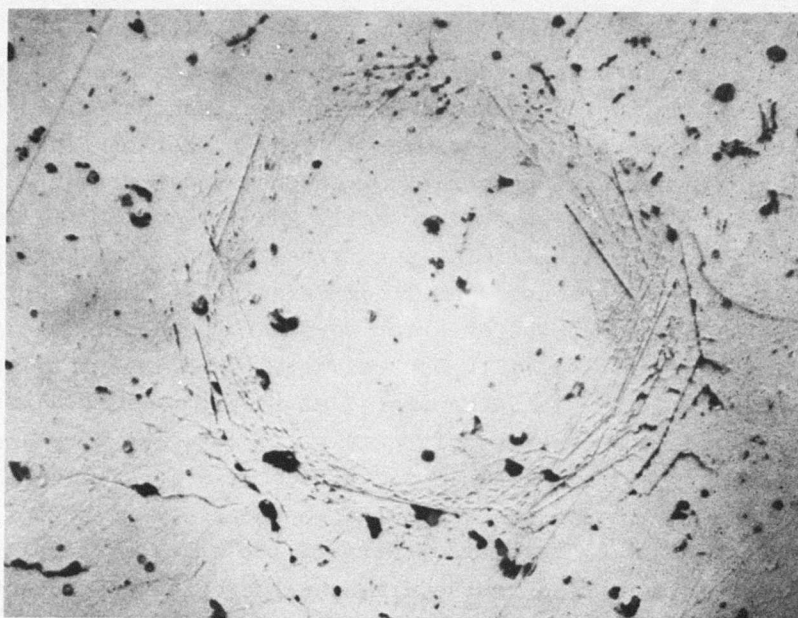


Figure 81. Optical Micrograph in Dark Field Reflected Light of Subsurface Conchoidal Fractures in Arsenic Trisulfide Glass after 5 sec Exposure to Standard Rainfield at 500 fps (80X)

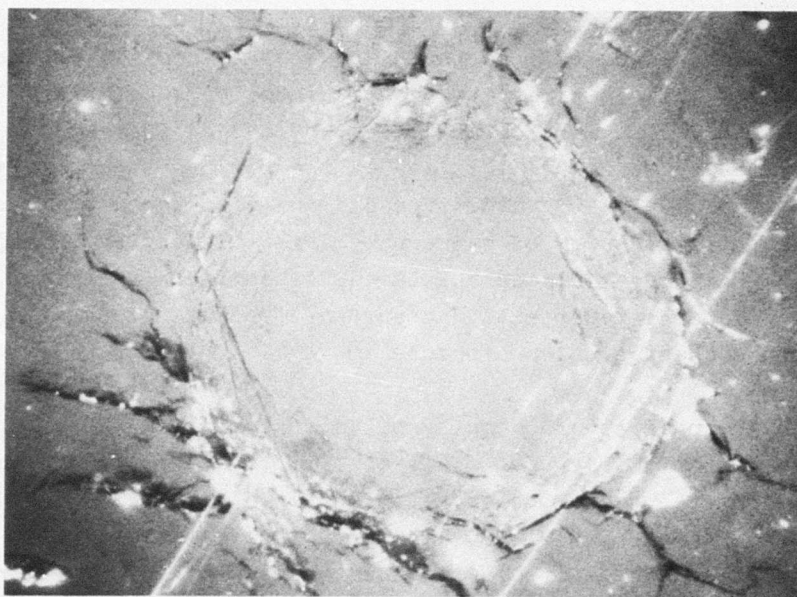


in Fig. 82 under oblique reflected and polarized reflected illuminations. The central diameter of undamaged material spanned .50 mm. and the outer diameter defined by the surface cracks ranged from 0.75 - .90 mm. These dimensions are approximately 70% of the corresponding dimensions observed for polymethylmethacrylate exposed in the AFML/Bell erosion facility (1.8 mm nominal drop diameter). The perimeter walls preferentially formed along residual polishing scratches oriented tangentially along the perimeter consistent with the observations of surface flaw initiation in bend bar specimens. These flaws penetrated substantially into the specimen interior at angles close to 90° similar to the very deep line fractures cited earlier. However, the ring fractures are propagated less deeply since the drop impact interacts with a greater number of cracks. The higher magnification views of Fig. 82 (also under oblique illumination) show that the polishing scratch widths are enlarged where the impact stress wave exceeded the fracture stress and that a shallow fracture was initially created. The optically resolvable width of these cracks suggests the hydraulic mechanism could make a significant contribution to subsurface propagation during subsequent rainfield exposure. The subsidiary cracks which connected from one residual scratch to another were not associated with a depth of subsurface damage comparable to that associated with the enlarged residual scratches. In the areas where the residual surface scratches were not enlarged by the drop impacts, topologically sensitive illumination was required for their detection and no subsurface damage could be associated with them.

In the absence of appropriately oriented residual scratches, the perimeter tensile forces produced a ring pattern comprised of a dense distribution of fine discontinuous cracks as shown in Fig. 82b. These secondary crack systems suggest that the impact tensile stresses at the interior diameter were comparable to those required for propagation of the typical surface flaw so that concentric arrays of flaws were briefly propagated as the impact stress wave expanded. These cracks do not



(a) Oblique Reflected Light



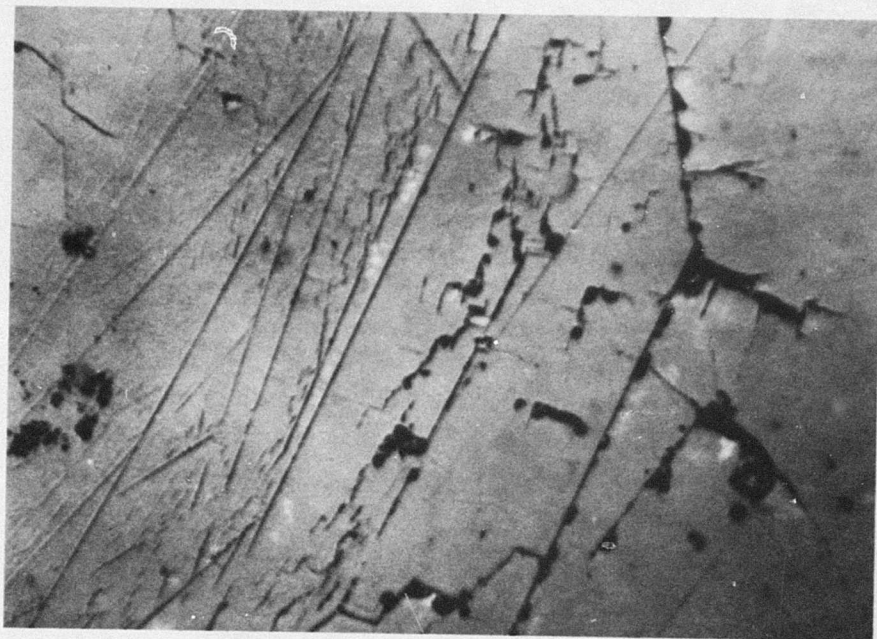
(b) Polarized Reflected Light

Figure 82. Optical Micrographs of Ring Crack Pattern Formed in Arsenic Trisulfide after 5 sec Exposure to Standard Rainfield (80X)

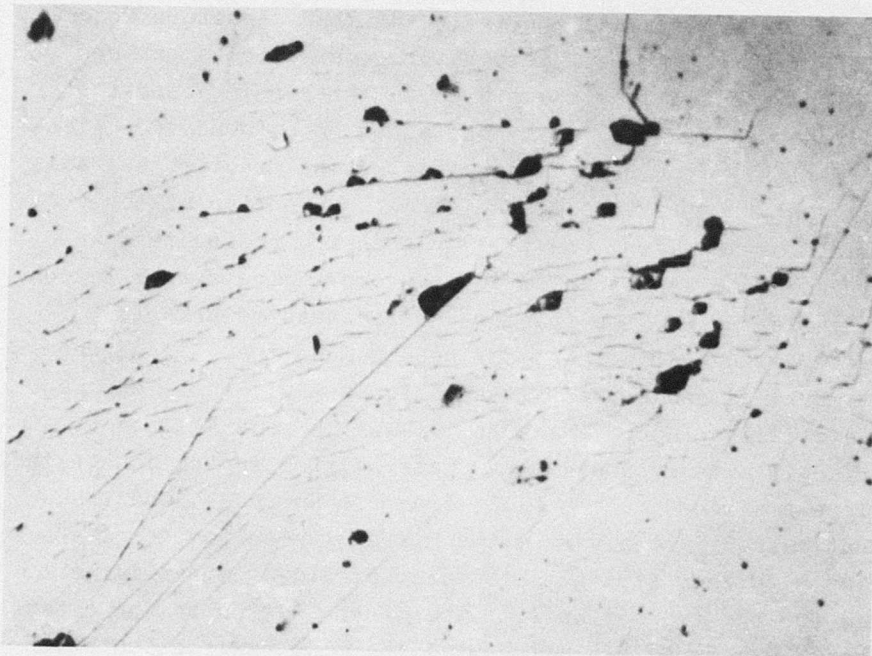
appear to be an important source of degradation and may protect the surface from the more damaging scratch extension (similarly dissipating the droplet impact over a large number of flaws). No appreciable depth of penetration was observed for such surface crack formations. Likewise, the small, shallow, discontinuous pits and cavities which form at such sites are not believed to be important. In contrast, the linear cracks and irregular cracks which formed at the exterior were large and more damaging. In Fig. 83b the pitting, although relatively small at this site as shown in Fig. 82b, is concentrated at the outer ring diameters. At other sites, both macroscopic cracks and cavities were located at the outer ring diameters. The cavities were located on the exterior side of the cracks analogous to those observed in the zinc chalcogenides. The crack widths of the enlarged scratches became increasingly wide as the diameter increased and subsurface penetration increased also. Comparison of Fig. 82b and 83a indicates one of the larger perimeter subsurface networks originated at the surface. Most of the surface overlying this site was apparently undamaged. Adjacent to and just beyond the perimeter, subsurface fractures penetrated deeply into the substrate as shown in Fig. 82b. Inspection of Fig. 82 and 83 indicates that these fractures tended to initiate at the peripheral cracks and that the surface scratch dimension did not simply correlate with the extent or intensity of subsurface damage. This again suggests that although surface initiated, subsurface fracture propagation was more important than surface fracture propagation during subsequent erosion exposure.

A ring fracture density of approximately 15 rings/cm<sup>2</sup> was observed at this stage. This density is a large fraction of the estimated number of impacts consistent with the observation that the majority of circular arcs were fragmentary rather than complete. In general, ring location was disjoint from or adjacent to rather than overlapping suggesting that the initial ring crack interacted with overlapping drop impacts to propagate damage by subsurface crack propagation and extension of subsurface cone fractures at the drop periphery. As noted earlier,





(a)



(b)

Figure 83. Optical Micrographs in Oblique Reflected Light of Perimeter Sectors (Contained in Figure 82) in Arsenic Trisulfide after 5 sec Exposure to Standard Rainfield (400X)



the structural integrity of the sample was most threatened by isolated surface fractures which could penetrate deeply into the substrate whereas the optical degradation arose primarily from the formation of complex subsurface fracture systems whose interactions limited individual crack penetration. In general, superimposed drop impacts did not leave a clear record of the subsequent impact events on the initial fracture site. Instead the central area remained free of surface and subsurface damage and the outer perimeter cracks initiated conical subsurface fractures which penetrated deeper into the substrate with continued exposure. Of the rain-eroded systems studied here, this most closely resembled the erosion behavior observed for glass bead erosion of glass surfaces.

### 3. Germanium

Germanium crystallizes in the diamond structure which has cubic symmetry. At room temperature, germanium specimens aligned along the  $\langle 111 \rangle$  axis ruptured in three-point bend tests to yield fracture surfaces which contained no evidence for plastic deformation.<sup>(54)</sup> Instead, analysis of the fracture surfaces indicated that the fracture mechanism in the tensile stress region was cleavage along the  $\{111\}$  planes and passed into an irregular and complex mechanism in the compressive stress region. In the tensile region, the fracture surface was remarkably planar with height variations confined to less than 50A between cleavage markings and surface layer alignment within  $1^\circ$  of the appropriate  $\{111\}$  plane. Fracture initiation generally occurred at a surface flaw surrounded by a glassy mirror region constrained to be closely aligned to the  $\{111\}$  fracture surface. The fracture front passed directly from the mirror region to the cleavage region with long straight rib marks providing a realignment mechanism for the transition from the mirror region to the cleavage planes. Fracture initiation with the  $\langle 100 \rangle$  axis orientation to minimize the resolved tensile stresses across the  $\{111\}$  cleavage planes yielded very rough surfaces which did not orient along a crystallographic face.<sup>(55)</sup> Further evidence for orientation

preference in fracture propagation has been observed for quasi-static Hertzian ball indentations on {111} surfaces at high stress levels.<sup>(56)</sup> Those sectors of the ring crack which lay along the three traces of the intersecting {111} planes penetrated deeper into the substrate than the remaining arc sectors. In summary, germanium behaves as a classic brittle crystal with fracture initiating at surface flaws and the magnitude of the initiating stresses proportional to the square root of the abrasion depth.

The rain erosion resistance of germanium has been reported for 1.2 mm drop diameter at 400 m/sec velocities.<sup>(52)</sup> This report does not indicate the structure of the germanium, focusing primarily upon both the transmittance loss as a function of exposure duration and the incubation period for weight loss. For these conditions, the authors found that a period of perhaps 12 seconds was required for the onset of weight loss and ranked it comparable to some calcium aluminate glasses. This erosion ranking cannot be directly compared to the data reported herein since this glass was not tested.

The substructure of polycrystalline germanium used in the initial erosion studies was characterized by etching: 20 sec. immersion at 100°C in an etchant prepared by dissolving 8g  $K_3Fe(CN)_6$  and 12g KOH in 100 ml water just before etching. Although this etchant is a demonstrated dislocation etchant, application to the as-polished surface (vendor supplied) yielded only chemical polishing indicating the surface layer to be relatively free of dislocations and microcracks. To sensitize the surface to reveal damage and orientation, metallographic cross-section specimens were prepared with a terminal polishing by 0.3 micron  $\alpha$ -alumina on a napped cloth. Fig. 84 and 85 illustrate the macroscopic zones within the specimen and also the etch pits observed on the central section which appeared to be near the {111} orientation. A survey of the etched cross-section indicated that clusters of similarly oriented grains occurred frequently within the zones and major orientation changes occurred

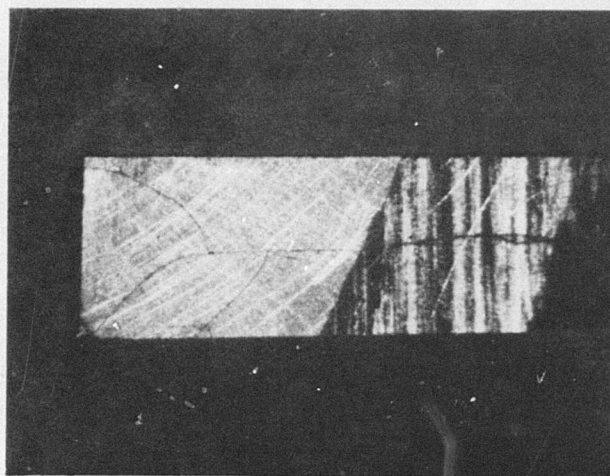


Figure 84. Optical Macrograph in Bright Field Reflected Light of Zones in Polycrystalline Germanium after Etching (7X)

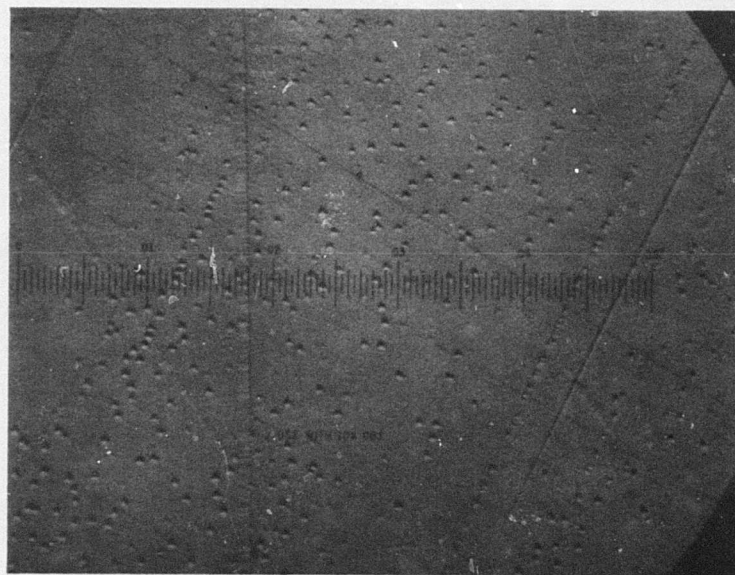


Figure 85. Optical Micrograph in Oblique Reflected Light of Etch Pits in Polycrystalline Germanium near  $\langle 111 \rangle$  Orientation after Etching (560X)

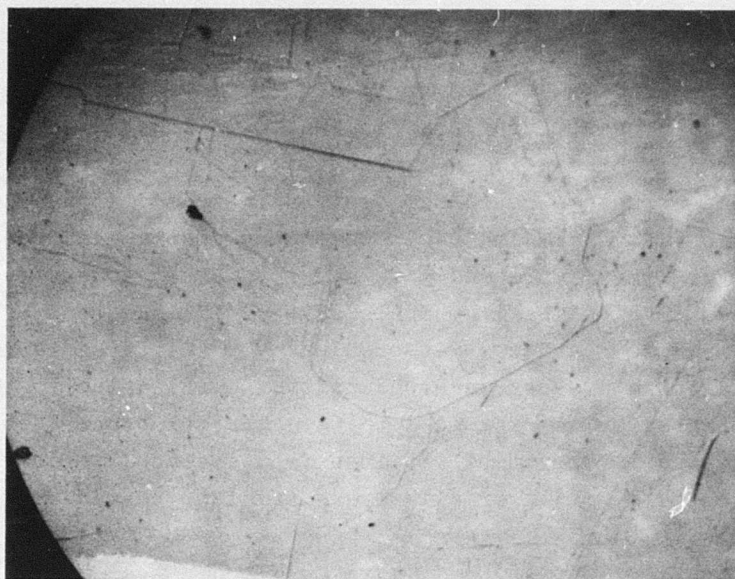


across zone boundaries. The grain structure was quite complex as indicated by the micrographs in Fig. 86 so that a simple grain size did not provide a representative description (additional fine structure could be observed in some fields as the magnification was increased). Grain dimensions ranged from perhaps  $10\mu\text{m}$  to  $1\text{mm}$  or more and growth twins were frequently observed during the metallographic survey. Measurement of a well-defined microhardness was precluded by the large variations in orientation and substructure density. Qualitatively, this germanium appeared to be inferior in mechanical properties to those observed in specimens obtained from a second vendor; the forces exerted by a fingernail were sufficient to manually split off a chunk.

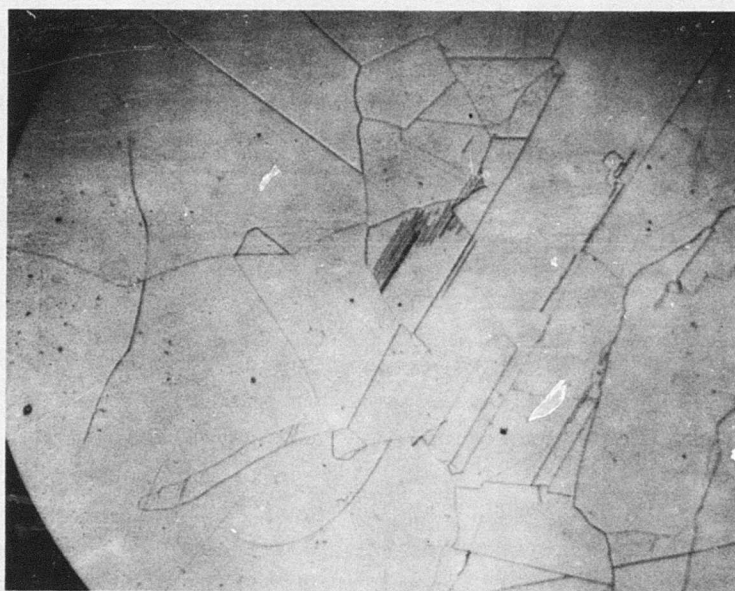
Initially, two germanium specimens were exposed to the standard rainfield at 730 ft/sec in the AFML/Bell erosion facility for periods of 20 and 40 seconds, respectively. Microscopic inspection of both samples indicated both erosion exposures had produced relatively uniform distributions of damage over the specimen surfaces. Fracture occurred via several competitive mechanisms consistent with fractography studies of bend test specimens cited earlier.<sup>(45,55)</sup> As illustrated in Fig. 87-92, these damage modes included crystallographic cleavage, conchoidal fracture, cavity formation, small, dense arrays of fine cracks, and crushed fracture cores (Fig. 91-92).

After the 20 second exposure, the fracture patterns formed by  $\{111\}$  plane cleavage were the most striking feature (particularly under topologically sensitive illumination). In some microscopic fields of view, extrapolation of the cleavage lines yielded equilateral triangles whose angles were measured to be  $60 \pm 2^\circ$  (protractor uncertainty) indicating those fields to be very close to the  $\{111\}$  orientation. This is consistent with the microstructure observed by etching the shielded areas on the erosion face and the specimen cross-section. However, no evidence was observed in this survey for a correlation between the density and partitioning of damage modes with the intersection angles





(a)



(b)

Figure 86. Optical Micrographs in Oblique Reflected Light of Typical Grain Structures in Polycrystalline Germanium (70X)

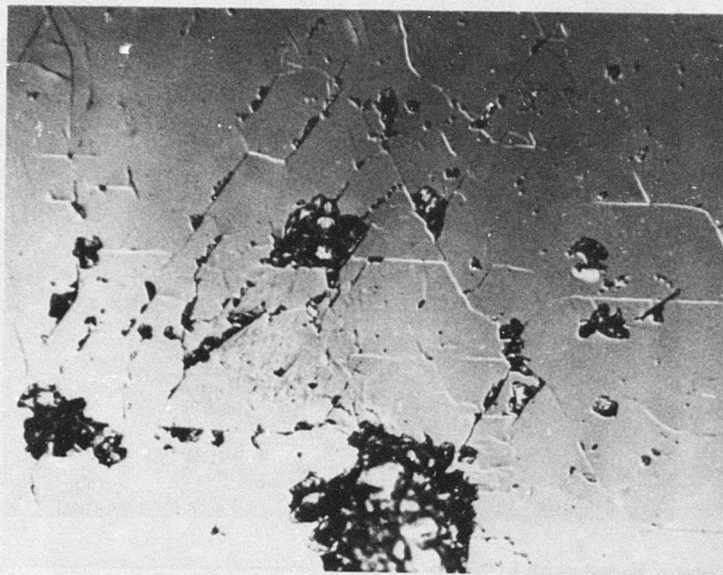


Figure 87. Optical Micrograph in Nomarski Interference Contrast of Crystallographic Slip and Conchoidal Fracture of Polycrystalline Germanium after 40 sec Exposure to Standard Rainfield (120X)

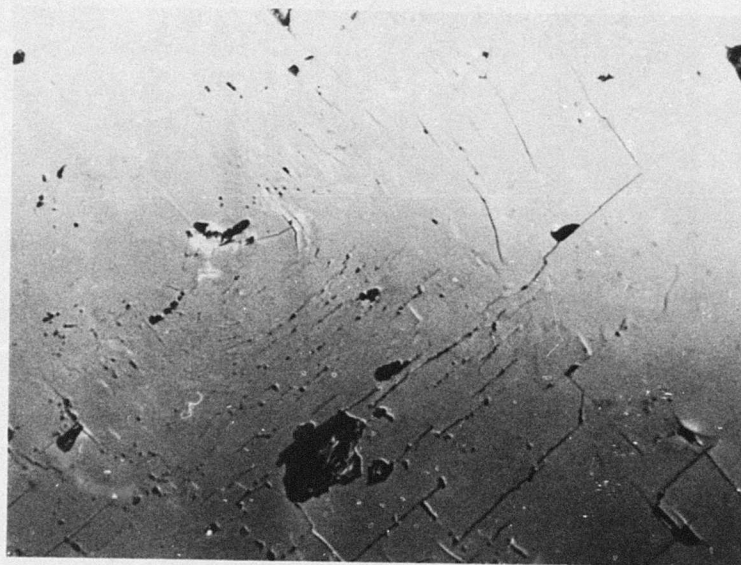


Figure 88. Optical Micrograph in Nomarski Interference Contrast of Possible Ring Crack Pattern in Polycrystalline Germanium after 20 sec Exposure to Standard Rainfield (120X)



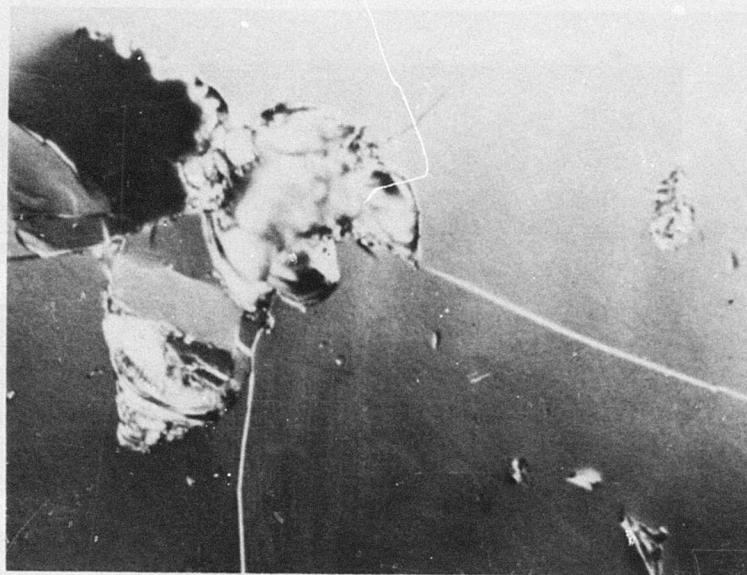


Figure 89. Optical Micrograph in Nomarski Interference Contrast of Conchoidal Fracture and Surface Removal in Polycrystalline Germanium after 20 sec Exposure to Standard Rainfield (800X)

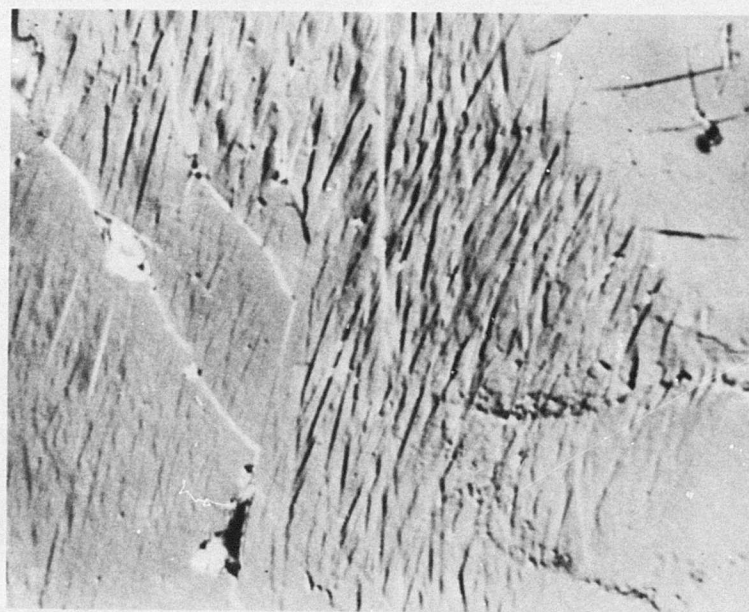


Figure 90. Optical Micrograph in Nomarski Interference Contrast of a Compact Fracture Site in Polycrystalline Germanium after 40 sec Exposure to Standard Rainfield (620X)



Figure 91. Optical Micrograph in Nomarski Interference Contrast of Erosion Pit Formed by Crushing in Polycrystalline Germanium after 40 sec Exposure to Standard Rainfield (950X)

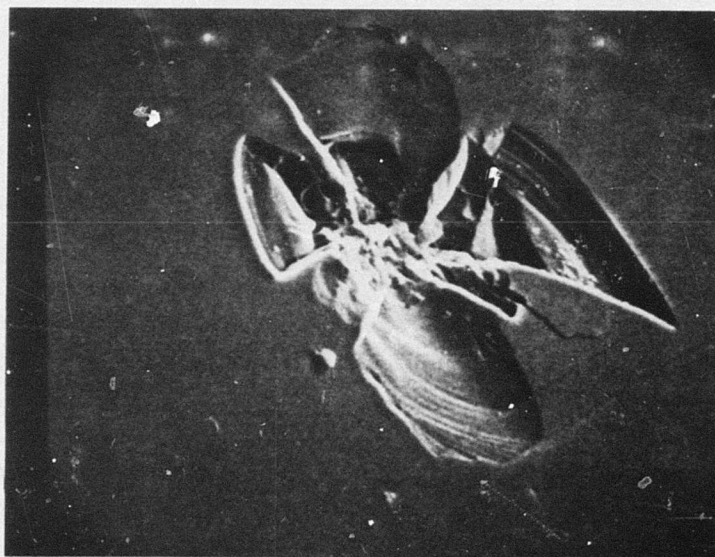


Figure 92. Scanning Electron Micrograph of Surface Relief Fractures Originating at a Microhardness Indentation in Polycrystalline Germanium (650X)



formed by the cleavage traces (and so grain orientation). Cleavage predominated when the fracture formed at large angles with respect to the specimen surface. As the fracture angle decreased, conchoidal fracture became increasingly important and was generally associated with cavity formation and surface relief fractures as illustrated in Fig. 87 and 88. Fig. 88 also illustrates how cavity walls preferentially formed along one side of the cleavage fracture; probably the exterior wall as observed in the brittle materials which underwent ring crack formation. Subsequent erosion exposure of these cavities led to enlargement on both sides of the cleavage fracture until the initiating cleavage fracture source was obscured. Small cavities also formed preferentially at small angle intersections of cleavage fractures (illustrated in Fig. 110b for analogous erosion at surface scratches on glass). Possibly because of the low mechanical strength of the polycrystalline germanium, the cleavage traces generally conformed very closely to the preferred crystallographic orientation; greater deviations in angle and straightness were observed in the harder  $\langle 111 \rangle$  orientation germanium specimens tested here and in gallium arsenide samples tested in the AFML rain erosion facility.

As noted earlier, pits and cavities formed an important damage mechanism which would be the primary cause for both optical degradation and mass loss. The larger cavities strikingly resembled the classic conchoidal cavities formed in glass and their surfaces contained pronounced microhackle and rib markings. Similar surface relief fractures were observed surrounding Vicker's microhardness indentations produced with excessive loads again suggesting similarities in the response of germanium to the drop impact and to quasistatic fracture initiation. Although the most frequently observed nucleation site was the cleavage fracture, cavity formation also nucleated at sites of surface flaws, fracture cores, and surface nicks (illustrated in Fig. 121a for calcium alumino-silicate glass). Cavity enlargement would be expected to occur by the same mechanisms which were observed for the zinc sulfide and glass specimens.

Less important microscopic damage modes included the compact crack patterns, surface nicks, pits, and the crushed fracture cores. These features were small, did not propagate rapidly, and probably did not influence the macroscopic specimen properties (except possibly as nucleation sites for other forms of damage). Similar microscopic features were observed in the oxide based glasses.

Comparison of the 20 sec. specimen with the 40 sec. specimen emphasized the increasing importance of cavity formation with continued rainfield exposure. This rapid increase in cavity volume resulted from increases in both the density and dimension of the cavities. The larger cavities would be the primary cause of subsequent optical degradation and mass loss; a significant optical degradation was observed after 40 sec. as shown in Table 10.

To clarify the early stages of germanium erosion, a polycrystalline specimen and a  $\langle 111 \rangle$  oriented single crystal specimen (the latter grown by a different vendor) were initially exposed to the rainfield in the AFML erosion facility for a period of approximately 6 seconds. The quality of surface finish was inferior to that of the specimens tested earlier since only a brief manual polishing sequence was permitted by a late change in the testing schedule. This polishing procedure left a residual pattern of fine scratches. It is estimated that approximately 40-60 drops struck the 1.0 cm x 3.5 cm exposed areas (11-17 drops/cm<sup>2</sup>) based on a study of polymethacrylate samples exposed in the AFML erosion facility for periods of 6 and 12 sec. For these exposure periods, the plexiglass preserved an accurate impression record of each impact event. The study also indicated that imprints were generally isolated so that very few sites would receive two impacts and probably no site would receive three impacts.

Microscopic inspection of the samples under oblique illumination indicated that each sample had one detectable region

TABLE 10

## TRANSMITTANCE DEGRADATION AFTER 40 SEC. EXPOSURE TO STANDARD RAINFIELD

	Wavelength (microns)				
	<u>2.5</u>	<u>4.0</u>	<u>8.0</u>	<u>9.5</u>	<u>11.0</u>
Hot Pressed Zinc Sulfide (percent transmittance)					
Before Exposure	75.2	78.0	79.7	79.0	65.4
After Exposure	65.6	69.0	-	71.8	59.9
Transmittance Difference	9.6	9.0	-	7.2	6.5
Polycrystalline Germanium (percent transmittance)					
Before Exposure	53.5	53.8	54.5	53.7	52.1
After Exposure	39.4	40.9	43.3	43.4	42.3
Transmittance Difference	14.1	12.9	11.2	10.3	9.8

of apparent cleavage and closely spaced cracks. In each case, the dimension spanned by the damage on each specimen appeared to be approximately 1-2 mm. The damage primarily consisted of crystallographic traces ranging from 10 to 100 $\mu$ m as illustrated for the polycrystalline sample in Fig. 93 (the circular blotches are mineral salt deposits from the test water and the pits resulted from an etch and subsequent polish cycle required to select crystallographic sites for monitoring). Note that there is no evidence for a ring pattern of cracks as observed in the zinc chalcogenides and the weaker glasses. However, both specimens contained a compact array of very faint cracks indicating that such crack arrays together with the cleavage cracks are the initial damage modes produced in germanium. Since most of the cleavage traces on the polycrystalline specimen contained pits and some of the fractures on the single crystal specimen followed residual polishing scratches, fracture initiation during the impact event was significantly assisted by surface defects of microscopic proportions. The scarcity of observed damage sites and the orientations of the cleavage traces suggested that they were produced by two overlapping impacts. Detection of germanium damage for a single impact at this drop diameter and velocity would require application of an etch (or possibly Nomarski interference contrast at high magnification after careful cleaning). It is not possible from this evidence to determine whether the observed cleavage was produced by the hydraulic penetration mechanism, the perimeter tensile stress mechanism, or a sequence of the two mechanisms. The dense arrays of fine cracks were not associated with surface defects of microscopic proportions. The originating mechanism sequence for these fractures is also unexplained at this time.

Both samples were subsequently exposed in the AFML erosion facility for an additional period of 30 seconds so that a total of 200-300 impacts (60-85 drops/cm<sup>2</sup>) would be anticipated. Both samples underwent continued cleavage and crack array formation so that these damage modes were sparsely distributed over the surface. The cleavage traces illustrated in Fig. 93 and 94





Figure 93. Optical Micrograph in Oblique Reflected Light of Cleavage Traces and Crack Array in Polycrystalline Germanium after 6 sec Exposure to 1 in/hr Rainfall at 730 fps in AFML Facility (60X)

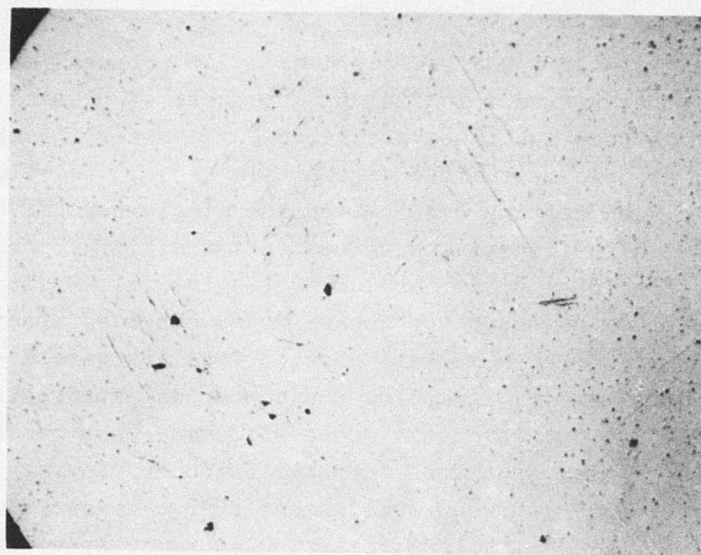


Figure 94. Optical Micrograph in Oblique Reflected Light of Cleavage Traces in Polycrystalline Germanium after 36 sec Exposure to 1 in/hr Rainfall at 730 fps in AFML Facility (35X)

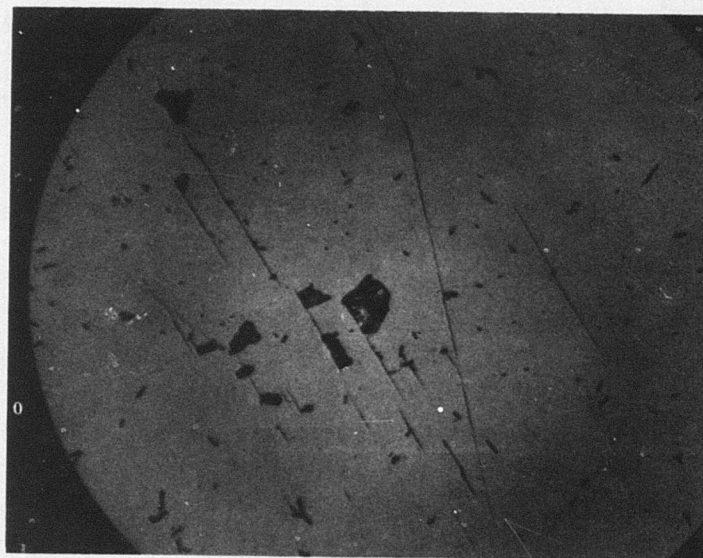


Figure 95. Optical Micrograph in Oblique Reflected Light of Cavity Initiation and Scratch Initiated Damage in Polycrystalline Germanium after 36 sec Exposure to 1 in/hr Rainfall at 730 fps in AFML Facility (240X)



are remarkably similar, differing primarily in propagation length. In other microscopic fields, the onset of pitting was observed by the same mechanism described earlier for the zinc selenide and arsenic trisulfide as shown in Fig. 95 (similar cleavage initiated pitting occurred on the single crystal specimen). Fig. 95 also illustrates the effectiveness of fracture nucleation by residual scratches during the initial erosion period. The onset of the other damage modes observed after the 20 sec. exposure to the AFML/Bell erosion facility were also observed on this sample, including one conchoidal surface relief fracture. Similar densities and modes of damage were observed on the single crystal specimen. Crystallographic cleavage was confirmed by comparing fracture alignment over a large fraction of the specimen surface while maintaining a common specimen orientation. The micrographs contained in Fig. 96 illustrate this for the traces oriented at approximately  $40^\circ$  angle with respect to the longer axis of the photograph. The orientations of the prominent cleavage traces shown in Fig. 96a are consistent with those anticipated for a precursor ring of  $\leq 1$  mm diameter; however, no obvious ring pattern was observed on either sample exposed in the AFML facility. Fig. 96b also contains a fine crack array illustrating how these arrays tended to remain localized developing greater differences in surface height rather than extending across the surface (as the cleavage fractures did) with increasing exposure to the rainfield.

Application of the etchant to the polycrystalline sample clearly revealed the cleavage fractures as shown in Fig. 97 and 98. Consistent with the crystallographic sites monitored on the as-eroded surface, microscopic inspection of the etched surface indicated that the grain and twin sites did not contribute importantly to fracture initiation. The etched surface revealed more clearly the contribution of residual scratches to fracture initiation and propagation. A greater frequency of compact crack and damage arrays were apparent on the etched sample than on the as-eroded sample. Cracks radiated from the larger cavities on this specimen suggesting that even at this early erosion stage

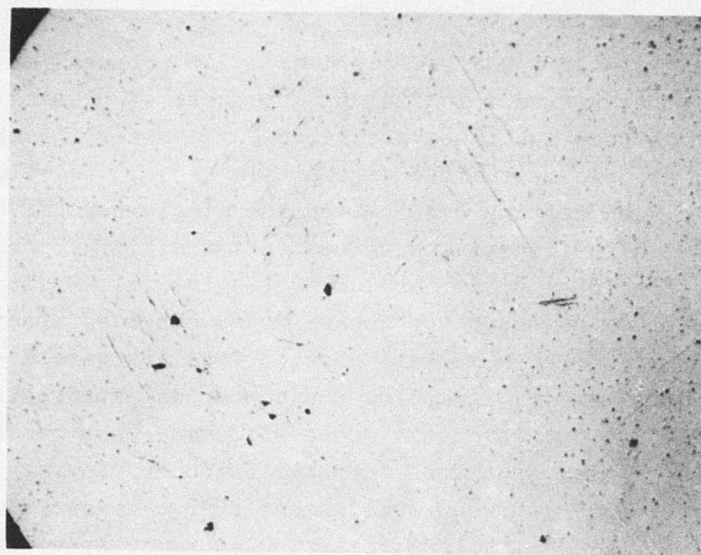


Figure 94. Optical Micrograph in Oblique Reflected Light of Cleavage Traces in Polycrystalline Germanium after 36 sec Exposure to 1 in/hr Rainfall at 730 fps in AFML Facility (35X)

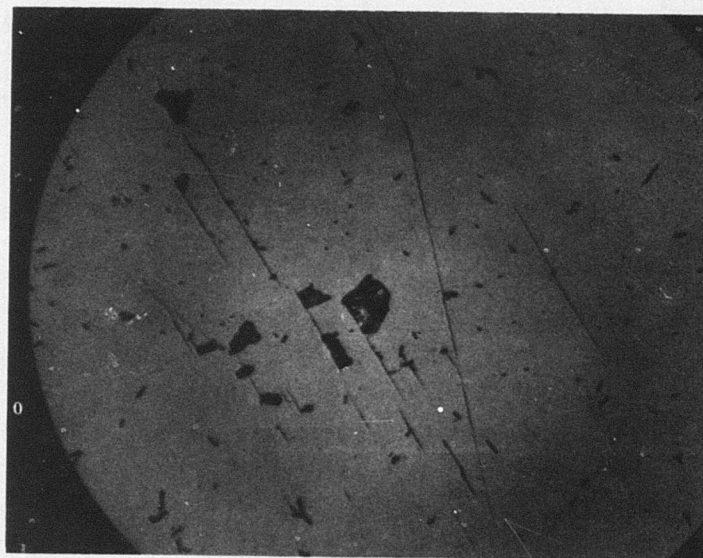


Figure 95. Optical Micrograph in Oblique Reflected Light of Cavity Initiation and Scratch Initiated Damage in Polycrystalline Germanium after 36 sec Exposure to 1 in/hr Rainfall at 730 fps in AFML Facility (240X)



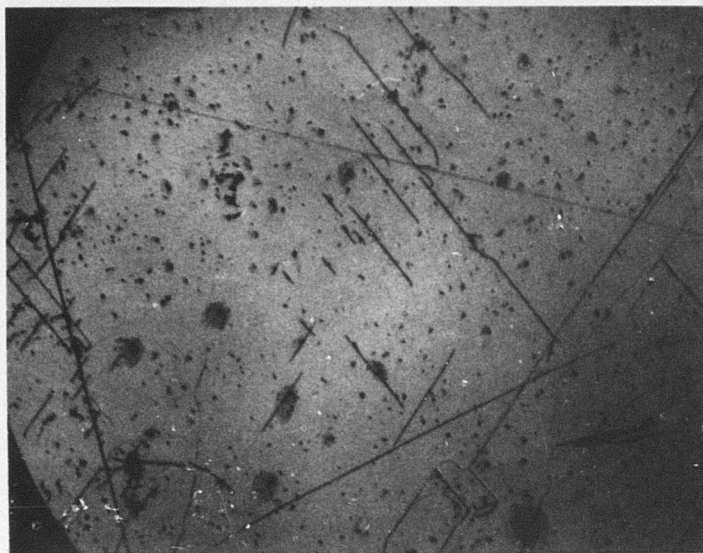


Figure 97. Optical Micrograph in Oblique Reflected Light of Etched Polycrystalline Germanium after 36 sec Exposure to 1 in/hr Rainfall at 730 fps in AFML Facility (70X)

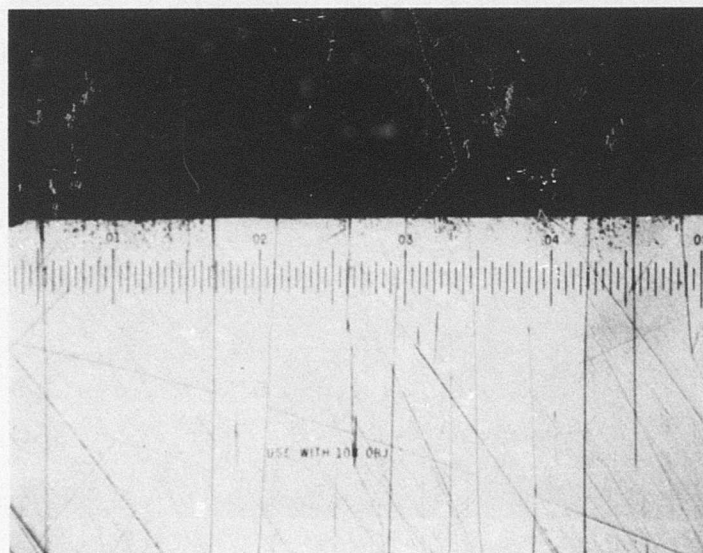
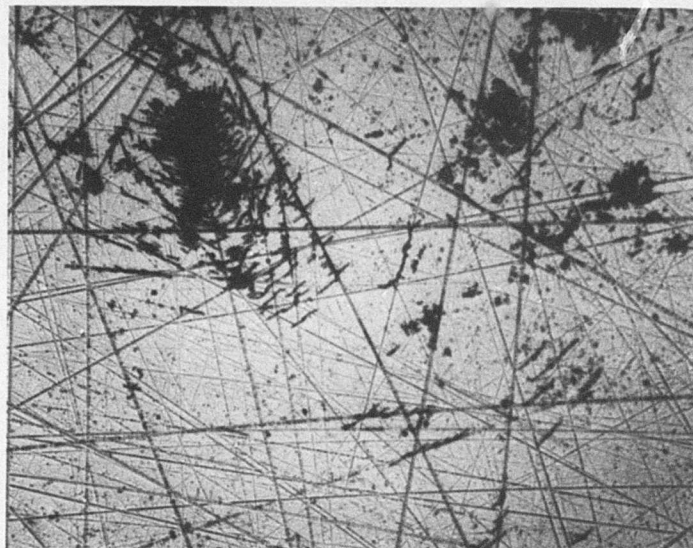


Figure 98. Optical Micrograph in Oblique Reflected Light of an Etched Cross-Section of Polycrystalline Germanium after 20 sec Exposure to 1 in/hr Rainfall at 730 fps in AFML Facility (40X)

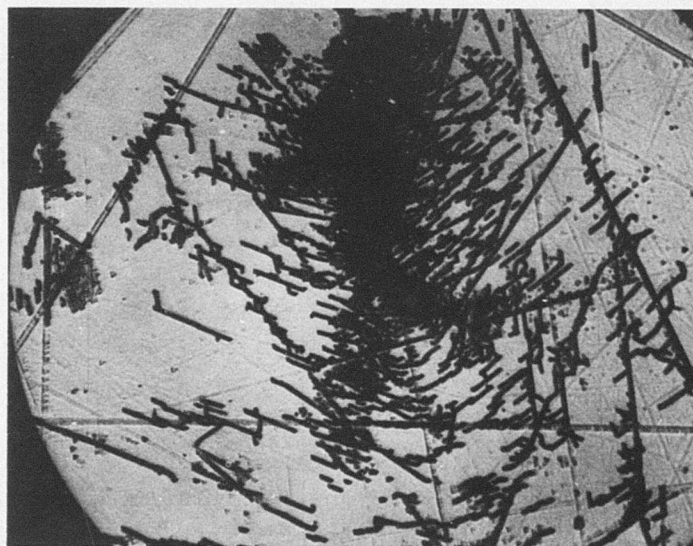
the hydraulic mechanism damaged the surrounding wall material (note the pit in the lower left corner of Fig. 97). Such a mechanism would explain the rapid increase of the cavity dimension with erosion exposure observed during the tests in the AFML/Bell facility.

Fig. 99 and 100 illustrate a damaged area on the single crystal germanium specimen. For this specimen, the etching procedure yielded an overetched condition which indicated more clearly that a dense array of microcracks (and possibly dislocations) existed at the sites of concentrated damage. Unlike the fine grinding damage observed on metallographic cross-sections of a polycrystalline specimen which were etched during various stages of surface preparation, this damage is intensely localized. For the former surfaces, the scratches appeared as linear arrays of overlapping, shallow equilateral triangles whose lateral dimensions were defined by the scratches. The more extensive the general surface damage (i.e., the larger the grit size), the larger and greater the density of the pits. However, the pyramidal pits still tended to be sufficiently shallow to be studied by optical microscopy, frequently terminating in flat faces when the depth of damage had been reached. In contrast, although the etch procedure was appropriate for such scratched surface conditions, the cleavage and scratch damage due to drop impact is very deeply attacked. Attempts to photograph meaningful views of the central region shown in Fig. 99b failed because the penetration depth exceeded optical depth of focus and appeared to be on the order of microns. This area resembles the compact crack array shown in Fig. 90 and both figures illustrate the preferential fracture propagation by straight line segments. In the earlier erosion stage shown in Fig. 99b, a large fraction of the fractures were aligned along the two cleavage directions passing around the intervening arc of approximately  $60^\circ$  by short, jogged connections or following a residual scratch. The depths of such cleavage cracks and damage arrays is surprising since the widths of the as-eroded cleavage cracks at this stage were often less than 1000Å since



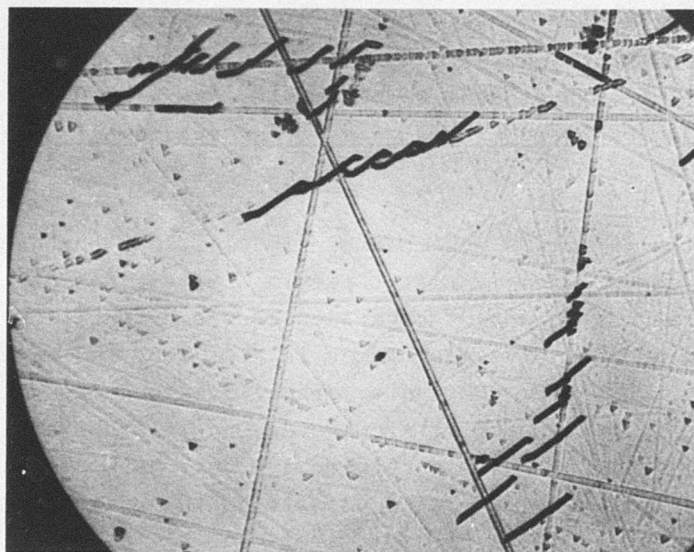


(a) (80X)

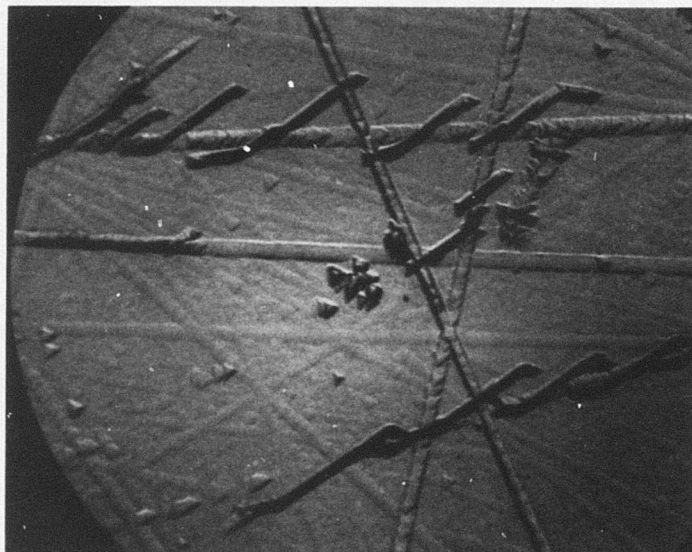


(b) (240X)

Figure 99. Optical Micrographs in Oblique Reflected Light of Etched  $\langle 111 \rangle$  Orientation Germanium after 36 sec Exposure to 1 in/hr Rainfall at 730 fps in AFML Facility



(a) (240X)



(b) (600X)

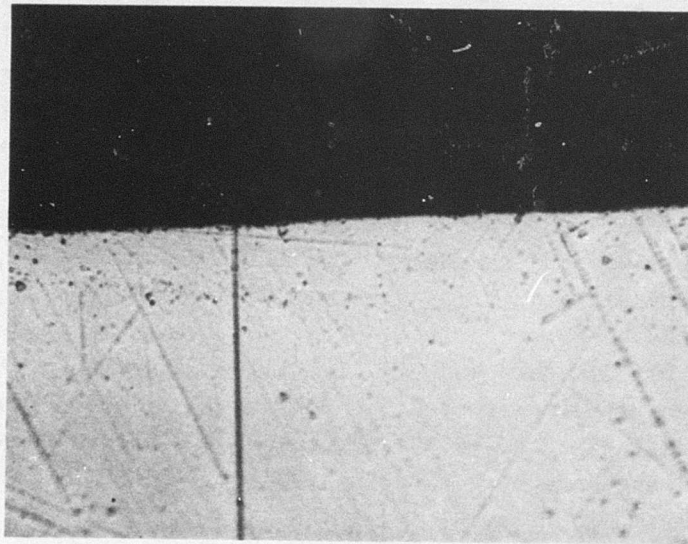
Figure 100. Optical Micrographs in Oblique Reflected Light of Etched  $\langle 111 \rangle$  Orientation Germanium after 36 sec Exposure to 1 in/hr Rainfall at 730 fps in AFML Facility



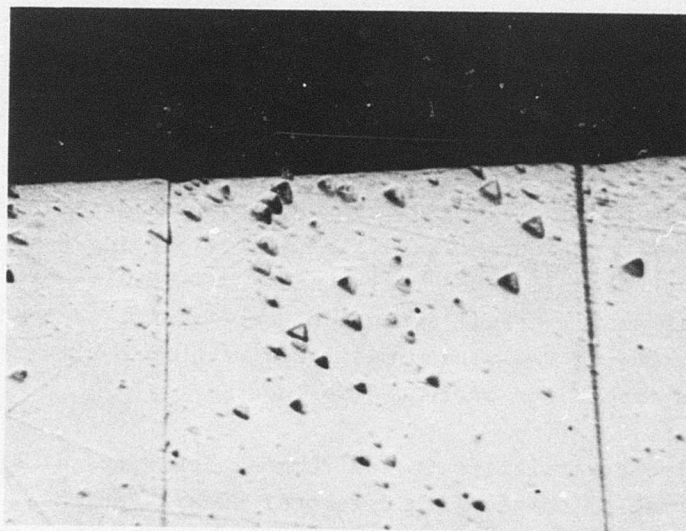
microprobe line scans did not indicate a detectable change in specimen current; large crack widths would also have been revealed during cross-section studies of an eroded polycrystalline specimen.

In the periphery region shown in Fig. 100, the damage intensity lessened sufficiently to permit limited characterization by optical microscopy. Comparison of the orientations of the etch pits and the cleavage traces in Fig. 100b indicated that the cleavage traces propagated primarily along one  $\langle 111 \rangle$  direction and initiated motion along a second  $\langle 111 \rangle$  direction. There is a striking difference between the very dark cleavage lines and the shallow, flat-bottomed pits of the undamaged polishing scratches (these probably arose during the  $6\mu\text{m}$  diamond rough polishing step). The substructure of the cleavage lines could not be clearly resolved but appeared only as etched linear cavities in which individual pits could not be distinguished. Note particularly in Fig. 100b that even light erosion damage to the residual scratch causes a sudden and large increase in both etch pit density and etch penetration depth. The micrographs of Fig. 99 and 100 indicate that the residual scratches accelerate the rate of erosion by both initiating cleavage fracture and providing a preferential path for fracture propagation. However, the large number of cleavage traces and the presence of irregular pit clusters in Fig. 100 indicate that successive drop impacts would quickly produce a sufficiently large density of microcracks and flaws to initiate cleavage fracture in the absence of such preferential initiation sites.

Metallographic cross-sections were prepared of the sample exposed for 20 sec. in the AFML/Bell erosion facility. During preparation, it was noted that exposed grains oriented close to the  $\langle 111 \rangle$  direction yielded tetrahedral pits and as the misorientation increased, the pyramidal shapes become distorted until for large deviations in orientation no surface pitting was observed. Fig. 101b illustrates the fine pyramidal pits observed



(a) Reference Edge (400X)



(b) Eroded Edge (400X)

Figure 101. Optical Micrographs in Oblique Reflected Light of an Etched Cross-Section of Polycrystalline Germanium after 20 sec Exposure to 1 in/hr Rainfall at 730 fps in AFML Facility  
(Refer to Figure 98 for an Overview)

after manual polishing of  $.3\mu\text{m}$   $\alpha$ -alumina or  $.05\mu\text{m}$   $\alpha$ -alumina for grains close to the  $\langle 111 \rangle$  orientation. Inspection of the germanium beneath the eroded surface indicated larger, well-defined pits occurred in the grains close to the  $\langle 111 \rangle$  orientation which were characteristic of selective attack at dislocations and microcracks (the latter is the probable origin). In contrast, only one such pit was observed along the length beneath the opposite face whereas a small cluster was observed on the side where a chunk had been forced free. Fig. 98 contains a survey field of these pit clusters and Fig. 101 illustrates the difference in the etch pit dimensions at appropriately oriented grains beneath the back face (Fig. 101a) and beneath the eroded face (Fig. 101b). The damage pits extended as deeply as  $100\mu\text{m}$  beneath the specimen surface.

#### 4. Sapphire and Spinel

Sapphire, single crystal aluminum oxide, is the most erosion resistant of the current window materials. The optical transmittance is appropriate for lower power laser, iridome, and sensor applications over a wavelength range from  $1500\text{\AA}$  to  $5\mu\text{m}$ . The advantages of sapphire include almost complete inertness to all common reagents and gases at low to moderate temperatures, a high melting point, Knoop hardnesses of 1500-2200 depending on crystalline orientation, flexure strengths exceeding  $5 \times 10^4$  psi, large rupture moduli, good resistance to thermal shock, and a relatively small thermal expansion coefficient. Indeed, sapphire is one of the few window materials which can withstand supersonic rain impact for prolonged periods.

Sapphire crystallizes in the rhombohedral crystal structure but is normally indexed with hexagonal axes. For the crystals studied herein, the c-axis was inclined approximately  $60^\circ$  from the specimen surface. Sapphire does not show macroscopic plasticity below approximately  $900^\circ\text{C}$ .<sup>(57)</sup> However, direct transmission electron microscopy of dislocations introduced by microhardness indentations at room temperature has established that extensive slip occurred on both the (0001) plane and {1012}



planes; some orientations also produced slip on the  $\{10\bar{1}1\}$  planes.<sup>(52)</sup> Also observed were rhombohedral twin and less frequently basal twin formation. Polished sapphire specimens which had been mechanically abraded with 0.25 micron diameter diamond powder also revealed dense dislocation arrays, indicating both basal and nonbasal plane slip had occurred.<sup>(58)</sup> Consequently, localized microplastic deformation can be produced in sapphire specimens at room temperature.

Fracture studies of sapphire have established pronounced orientation effects.<sup>(57)</sup> The specimens with the c-axis oriented at  $60^\circ$  to the surface normal (the orientation of the specimens studied in this report) failed by conchoidal fracture propagation. The specimens with the c-axis oriented  $0^\circ$  (parallel) to the surface normal failed by a combination of mechanisms primarily composed of the  $\{10\bar{1}2\}$  plane cleavage together with some conchoidal fracture contribution. Cantilever beam fracture experiments yielded similar results, showing fracture does not propagate along the basal plane (which would require separation of charged planes) but instead propagated closely along the  $\{10\bar{1}0\}$  plane and more erratically (including a conchoidal contribution) along the  $\{10\bar{1}2\}$  plane.<sup>(59)</sup>

Some rain erosion data have been previously reported for sapphire, particularly for long duration rain erosion experiments. In the 400 m/sec study cited earlier, the incubation period for mass loss of sapphire was around 9000 seconds which was approximately 30 times the incubation period of the next most resistant material tested: hot pressed magnesium oxide.<sup>(52)</sup> Data were also given for the effect of crystal orientation: sapphire exposed with the c-axis parallel to the specimen surface required 650 seconds to produce a 10 mg mass loss whereas with the c-axis perpendicular to the specimen surface required 190 seconds for the same mass loss. There is some question concerning the quality of the sapphire used in their work; however, since they indicate that an approximately 50% increase in exposure



time to specified weight loss by annealing the specimen to reduce growth strain. Unfortunately, the orientation work (based upon their curves) appears to have been done on the as-received specimens rather than post-annealed specimens. In another study, impact on the (0001) basal plane ( $0^\circ$ ) by a 3 mm diameter cylinder of water at 650 m/sec yielded a hexagonal pattern of cracks (analogous to the ring patterns observed herein) whose sides consisted of {1010} cleavage planes.<sup>(60)</sup> Impact by a cylinder of water on a {1010} plane ( $90^\circ$ ) yielded two large, parallel cracks which deviated from close conformity to crystal-line cleavage.<sup>(60)</sup>

Magnesium aluminum spinel crystallizes in cubic structure with the magnesium atoms occupying tetrahedrally coordinated sites and the aluminum atoms occupying octahedrally coordinated sites. This material is relatively hard (Knoop number 1170) with similar index of refraction, transmission bandwidth, and chemical inertness to those of sapphire. Unlike sapphire, this material would be free of the anisotropy in mechanical and optical properties arising from the crystal symmetry. To date, difficulties in annealing growth strains has limited the size of crystalline specimens and led to relatively high prices (comparable to sapphire). No data on the rain erosion properties for spinel was located in a review of the previous literature.

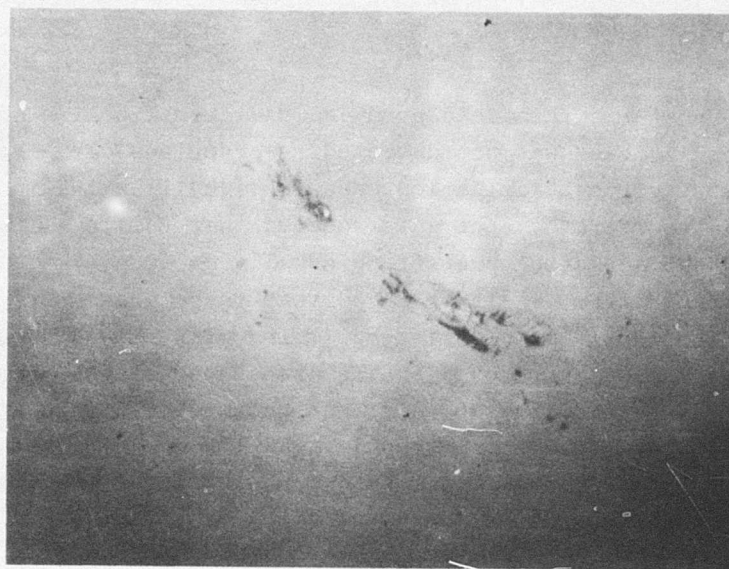
Sapphire specimens cut from crystals grown by the Czochralski process were exposed to the AFML/Bell erosion facility at 730fps for periods of 20 and 60 sec. These crystals were oriented for optimum optical properties: c-axis  $60^\circ$  from the surface normal. Preliminary microscopic examination of the specimens showed them to be free of volume defects such as striae, bubbles, inhomogeneities, etc. and the surfaces to be very well prepared with only a few polishing digs and microscopic fractures. For these rainfield exposures, virtually no damage was detected and the sapphire proved to be far more resistant than the other materials tested in this program. No evidence of cracks, fractures, or pits (within sound material) could be detected. It is

possible that the rainfield produced additional polishing digs; if so the increase was not detected. Scrupulous cleaning and subsequent surface examination under oblique illumination or Nomarski interference contrast revealed that very small areas of wrinkled surface structure were gradually eroding by the formation of tiny pits. It is believed that these areas were surface preparation digs filled during polishing with flowed material which was gradually removed by the drop impacts. The rate of removal was so slow that no distinction between the 20 and 60 second samples could be detected. Examples of this damage are shown in Fig. 102 but it must be emphasized significant surface attack has not begun.

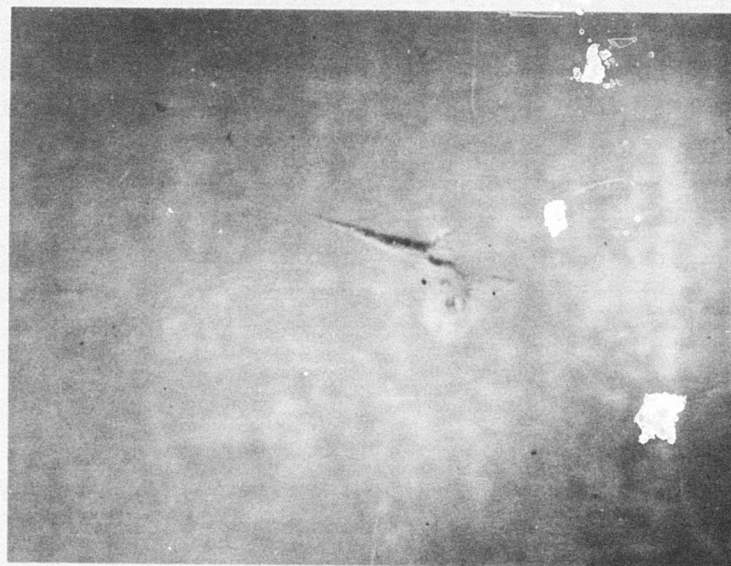
Specimens cut from spinel single crystals to yield {111} surface orientations were exposed to the AFML/Bell erosion facility at 740 ft/sec. for periods of 20 and 90 seconds. This material is also far more resistant than the other materials examined in this work but significantly less resistant than sapphire. Although the initial crystal and surface quality were comparable to that of the sapphire, a higher density of the same surface wrinkling and microscopic pitting mechanisms were detected after rainfield exposure. However, only a small total number of sites were involved and again the damaged sites were difficult to locate. A small degree in damage progression could be discerned when comparing the 20 and the 90 second exposure specimens. Examples of spinel erosion are shown in Fig. 103 and their appearance is closely similar to those shown in Fig. 102 for sapphire.

#### C. OXIDE-BASED GLASSES

In contrast to the crystalline materials for which crystalline cleavage, crystalline slip, intergranular and transgranular fracture are all sensitive functions of the material fabrication processes and impurity contents, the deformation and fracture of homogeneous, well-annealed glasses should be relatively insensitive to fabrication processes. Variations in fracture strengths between different glass compositions, such as within the silicate-based glasses, probably result from variations in Young's modulus,



(a) 360X



(b) 640X

Figure 102. Optical Micrographs in Oblique Reflected Light of Sapphire after 60 sec Exposure to Standard Rainfield





(a) 600X



(b) 500X

Figure 103. Optical Micrographs in Oblique Reflected Light of Spinel after 90 sec Exposure to Standard Rainfield



the existence of microphase structures, the density of silicon-oxygen bonds, and the mean oxygen bond strength.<sup>(61)</sup> Since Young's modulus is not a strong function of glass composition and the bond density is proportional to the  $2/3$  power of the silica concentration, neither of these properties would be expected to depend strongly upon composition. The mean bond strength may, however, depend significantly upon the concentration and distribution of the cation content. The mechanical moduli and strengths are summarized in Table III; it is somewhat surprising to note the small deviations between the properties of soda lime glass (which contains approximately 25% of oxide substitutions) with those of fused silica.<sup>(53,62)</sup>

The theoretical strengths of glasses ( $3 \times 10^6$  psi) are considerably greater than the measured strengths (5,000 - 15,000 psi). This has been explained by Griffith's suggestion that fracture is surface initiated at pre-existing minute surface flaws which dramatically lower the macroscopic strength (this mechanism can also be operative in brittle crystalline and polygranular materials.<sup>(63)</sup> In a glass, the initiated fracture is not confined to any crystallographic plane but instead propagates in a direction perpendicular to the tensile component of the instantaneous stress. The resultant fracture surface shows a characteristic structure: an initial, smooth mirror region close to the nucleation site surrounded by a transition misty region which finally passes into a region of gross roughening called hackle. The misty region results from initial branching and the hackle from extensive branching of the crack tip which forms subsidiary fracture surfaces during propagation to dissipate the excess energy generated by the exothermic fracture thermodynamics.<sup>(64)</sup> However, on the microscopic scale and nanosecond time scale relevant to the drop impact this propagation sequence characteristic of slow strain-rate loading may not occur.

A conventional soda lime glass was studied in this rainfield erosion investigation. This composition class has been historically important and dominates current glass production. The

basis for this system is the addition of sodium oxide to act as a flux in the silica system, of calcium oxide to improve the chemical durability, and of both aluminum and magnesium oxides to suppress devitrification.<sup>(65)</sup> An additional interest in the soda lime formulation was to directly compare the rainfield erosion of the annealed surface with the thermally-tempered surface. The thermal tempering technique has long provided a simple and inexpensive procedure for strengthening certain types of glassware.<sup>(65,66)</sup> The glass article is heated until the entire volume is slightly fluid and then the surface is suddenly chilled by jets of gas or immersion in molten baths. The outer layer quickly solidifies into a hard shell and the interior flows sufficiently to maintain continuity throughout the volume. At this point, there is a temperature gradient through the specimen but not a stress gradient. As the glass continues to cool, the interior slowly contracts establishing a uniform compressive stress of perhaps 20,000 psi at the surface which gradually and monotonically passes into a lower magnitude tensile stress at the specimen center. Consequently, the strength of a simple solid shape of glass can be increased two-fold to four-fold.

Conventional formulations of a borosilicate glass, an ion-exchange strengthened glass, and a calcium aluminosilicate glass were also studied in this rainfield erosion investigation. In the borosilicate system, boron oxide is added to the silica matrix together with small amounts of sodium oxide and aluminum oxide. The boron oxide acts as a fluxing agent, but yields a glass whose coefficient of thermal expansion is significantly smaller and whose chemical durability is greater than those of soda lime formulations.<sup>(65)</sup> In the ion-exchange process, a residual compressive stress is established in the surface by exchanging a fraction of the sodium cations with the larger diameter potassium cations.<sup>(66)</sup> The process is carried out by immersing the specimen in a potassium oxide (or binary mixture) bath and the chemical potential difference between the oxide bath composition and the original glass composition provides the driving force for the diffusion exchange. The resulting stress gradient is much

greater than that of the thermally-tempered glass; the peak compressive stress at the surface exceeds 80,000 psi and this transforms to a small tensile force approximately .2 mm into the interior. Consequently, the glass will spontaneously shatter when a crack penetrates such a distance. Direct applications of this effect have been exploited, but it prevents any significant shaping or finishing operations after the ion-exchange treatment. For the erosion exposures employed in this work, the maximum damage penetration was probably 5 microns or less so that the glass surface may be considered to be under a high compressive stress at all erosion damage sites. Calcium aluminosilicate glass compositions (approximately 33%  $\text{SiO}_2$ , 33%  $\text{Al}_2\text{O}_3$  and 33%  $\text{CaO}$ ) have been developed to extend optical transmission limits to longer infrared wavelengths. Soda lime glass transmits less than 75% light at 2.8 microns, fused silica glass at 4.0 microns, and calcium aluminosilicate glass at 4.4 microns for uncoated 2 mm thickness sections. However, the latter glass is also free of small absorption peaks which appear in the other oxide-based glasses. In addition to the improved infrared optical properties, the calcium aluminosilicate glass also has significantly larger mechanical strength and modulus parameters than the soda lime and borosilicate formulations.<sup>(53,62)</sup> Unfortunately, only limited information has been published on the rainfield erosion of the oxide-based glasses. In the 400 m/sec rainfield study cited earlier, a lead glass, quartz (infrasil), and calcium aluminate were tested yielding incubation periods for mass loss of 4, 7, and 11 sec., respectively.<sup>(52)</sup> These times would indicate these glasses to be relatively poor in performance since their germanium specimen also yielded a 10-11 sec. incubation period. A direct comparison to the data reported herein is not possible since these glass compositions were not investigated. However, qualitative comparison of the appearances of the eroded specimens of borosilicate glass and germanium indicated the mass loss incubation period for the borosilicate glass was probably one-half to two-thirds of that observed for polycrystalline germanium. Qualitative data has been reported



for a series of glasses exposed to a 733 fps rainfield at an unknown drop size.<sup>(67)</sup> The data is summarized here: normal soda lime: severe damage 5 min.; crown glass: moderate to severe damage 6-9 min.; partially thermally tempered glass: deep pitting 10-20 min.; a thermally hardened glass (composition designed for this process): moderate to severe damage 40-80 min.; several ion-exchanged glasses: light to moderate damage 70 min. for two formulations and severe erosion 180-210 min. for third formulation; calcium alumina-silicate glass: moderate erosion 40 min.; and zinc selenide: light to moderate surface damage but bulk cracking 10 min. Although some concept of erosion resistance ranking can be derived from this data, concurrent variations in erosion severity, specimen thickness, and damage mechanisms severely restrict comparison with the work reported herein.

#### 1. Annealed Soda Lime Glass

The soda-lime glass used in the AFML/Bell erosion tests was prepared by unknown techniques. The soda-lime glass used in the AFML erosion tests was fabricated by the float process with special instructions to the vendor to cut the specimens from a previously unused sheet and take precautions to avoid surface damage during cutting. Initial examination of the specimens under Nomarski interference contrast, oblique illumination, and transmitted light in both the etched and unetched conditions (5% hydrofluoric acid for 40 seconds) established the number of defects to be very small for the specimens received from both procurements.

A soda lime glass specimen was exposed to a 730 fps rainfield in the AFML erosion facility for 6 seconds. During this exposure it is estimated the glass specimen received 40-60 impacts (11-17 drops/cm<sup>2</sup>). Optical inspection over the entire surface revealed several surface relief fractures and an occasional scratch. Since this density of defects is comparable to that of the as-received specimens and the drop impact sites were unknown, this sample was then subjected to an additional exposure of three minutes. Examination of a second specimen



exposed for 30 seconds revealed several additional surface relief fractures had been produced during the longer exposure but revealed no evidence for crack formation (including examination under Nomarski interference contrast).

Examination of the specimen exposed to the AFML rainfield for an additional three minutes revealed the first stage of visible damage. It is estimated that this specimen received  $800 \pm 200$  drop impacts ( $270 \pm 60$  drops/cm<sup>2</sup>). The general mode of damage observed over the surface was a sparse distribution of surface relief fractures. The initial fracture structures have the same general form and dimension as those to be described later for the ion-exchanged and the calcium aluminosilicate glass specimens. These fracture surfaces are formed when tensile stresses acting on a subsurface flaw initiation site direct the subsurface fracture to propagate back to the exterior surface (undercutting a surface fragment).<sup>(68)</sup> An example shown in Fig. 92 was produced during withdrawal of a Vickers microhardness indenter after applying a 100 g load on the polycrystalline germanium surface. The central origin site of the drop impact fractures characteristically consisted of a roughened core region comprised of a dense distribution of minute, jagged projections suggesting that this region had been crushed. Simple median vent cracks characteristic of pointed indentors were not generally observed in the oxide-based glasses, although such sealed vertical fractures would have been difficult to detect.<sup>(68)</sup>

The surface relief fractures observed for the ion-exchanged and the calcium aluminosilicate glasses which are far more resistant to rainfield erosion generally propagated up towards the surface. The critical distinction between the surface relief fracture systems formed in the soda lime glass from those observed in the more resistant glasses is the capability of these water drop impacts to introduce additional subsurface flaws originating at (or possibly below) the central core region and extending these fracture surfaces horizontally and vertically beneath the original relief fracture. Consequently, the soda lime fracture

systems can be locally enlarged by the continuing formation of a network of subsurface fractures which undermine the original fracture sites. This is analogous to one mechanism responsible for enlarging the walls of fracture cavities in materials such as zinc sulfide. Examples of this mechanism appear in Fig. 104a (focused at the depth of the deeper set of horizontal fractures) and Fig. 104b (vertical penetration - this latter fracture is probably a median vent crack). Application of quasistatic loads to spherical indenters on soda lime glass exceeding the fracture threshold by more than 50% produced subsurface horizontal fractures and loads exceeding the threshold by more than 300% produced median vent crack formation.<sup>(68)</sup> For these cases, unlike the dynamic event, far more extensive damage occurred concurrently.

A comparison of the morphology of the surface relief fractures of the soda lime glass with those of the resistant glasses indicated that in the former system the surfaces were rougher whereas in the latter systems the surface was smoother and the hackle markings were finer. It can be speculated that this difference arose from a more rapid propagation of impact driven fracture in the soda lime system. The roughness would result from the crack tip responding more sensitively to the rapid changes in the dynamic stress field whereas the slower moving crack tips in the more resistant glass would respond via discrete steps (i.e., microhackle and rib markings).

Concurrently, surface fractures originating at the fracture sites were produced which radiated away to link up with adjacent surface fractures. This link-up mechanism was infrequently observed over much shorter distances on the resistant glass surfaces for longer exposure durations. A pair of linked surface relief fractures are shown in Fig. 105a although at this early stage the crack resealed sufficiently well that it is just resolved on the original photograph. A thorough search over the entire surface under oblique illumination revealed two compact fracture arrays and two linear crack systems only (an example of



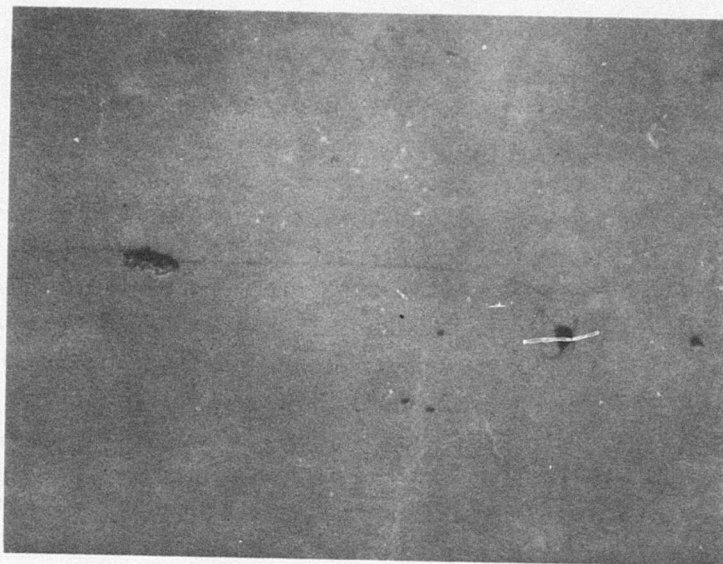
(a) Polarized Reflected Light Micrograph of Subsurface Relief Fracture (600X)



(b) Transmitted Light Micrograph of Median Vent Fracture (400X)

Figure 104. Soda Lime Glass after 3 min. Exposure to 1 in/hr Rainfall at 730 fps in AFML Facility





(a) Oblique Reflected Light Micrograph of Initial Crack Extension (400X)



(b) Oblique Reflected Light Micrograph of Initial Crack Arrays (280X)

Figure 105. Soda Lime Glass after 3 min. Exposure to 1 in/hr Rainfall at 730 fps in AFML Facility



each is shown in Fig. 105). At this early stage, the other crack network was also sufficiently well-sealed to be difficult to photograph. The linear crack mechanism for link-up across the surface is far more important than the compact fracture arrays since this mechanism contributes to the transmission loss (as shown in Fig. 106 for further exposure) and provides the basis for subsequent microscopic and macroscopic mass loss via the formation of networks of fractures and cavities. The crack shown in Fig. 105a extended an equal distance out of the photograph terminating in a simple fork. Thus, a series of impacts were required to generate visible cracks with appreciable length and sufficient fracture surface structure to prevent resealing.

A third soda lime specimen was chemically polished with 5% hydrofluoric acid for 3 minutes before exposure in the AFML erosion facility for four minutes. It was anticipated that this treatment would eliminate sites of exceptional weakness since the density of defects revealed by ion-exchange techniques were dramatically reduced after the application of hydrofluoric acid.<sup>(69)</sup> Such a chemical polish is known to strengthen glass surfaces subjected to bend bar tests by removing very small defects and enlarging the crack radii of larger defects. Inspection of this specimen after a four-minute exposure to the rainfield did not reveal a noticeable decrease in the density of damage (perhaps a factor of two change would be required) and both the dimension and type of damage were unchanged. It is possible that a more effective chemical polish (agitated 10% hydrofluoric acid for 4 minutes) would have removed a deeper surface layer together with a greater fraction of critical and subcritical flaws<sup>(12)</sup>; however, all such treatments enlarge small significant flaws and so significantly degrade optical performance.

An additional exposure of this specimen in the AFML erosion facility for six minutes produced an erosion state at the onset of transition to the formation and expansion of cavity networks responsible for optical degradation and subsequent mass loss. Fig. 106 and 107 contain micrographs illustrating how

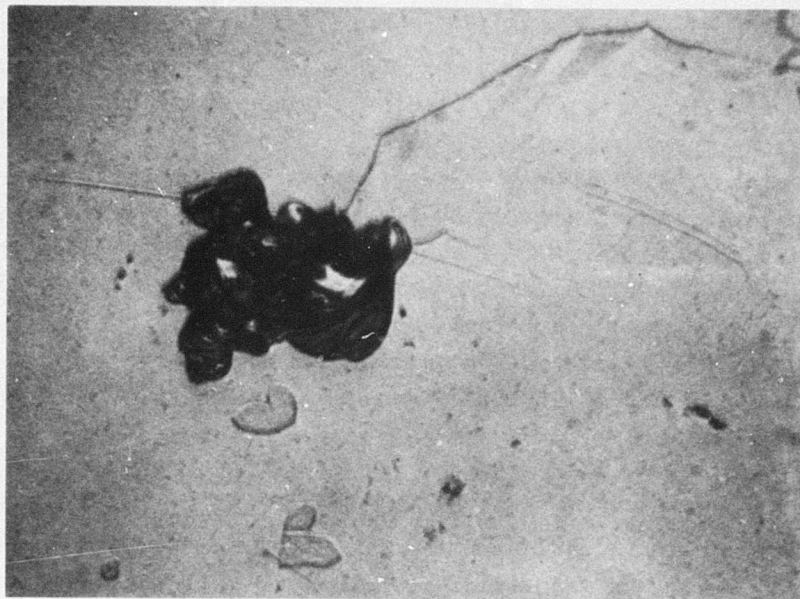


Figure 106. Optical Micrograph in Oblique Reflected Light of Erosion Cavity in Soda Lime Glass after 10 min. Exposure to 1 in/hr Rainfall at 730 fps in AFML Facility (200X)

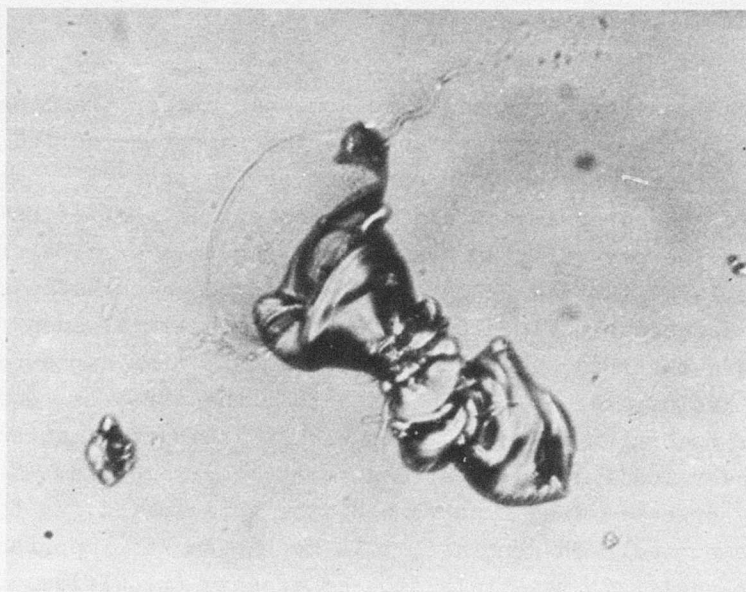


Figure 107. Optical Micrograph in Oblique Reflected Light of Linear Crack Array in Soda Lime Glass after 10 min. Exposure to 1 in/hr Rainfall at 730 fps in AFML Facility (320X)

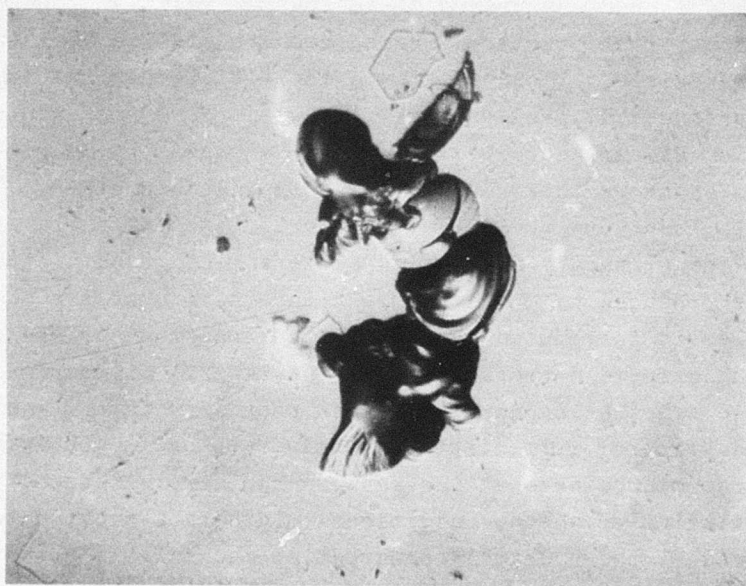
cracks originating at surface relief fractures now simultaneously extend across the surrounding surface and penetrate into the surrounding glass. Also illustrated are sites where phase inhomogeneities have been removed. The fracture system shown in Fig. 106 appears to have originated adjacent to an etched scratch in the glass surface (a more obvious example is shown in Fig. 110a). Note also that subsequent impacts removed at least two small periphery surface fractures from its edges. Note also that the surface cracks now are sufficiently misregistered to significantly reflect light. Fig. 107 shows a surface crack segment of comparable length to the segment shown in Fig. 105a. However, this crack has a significantly greater height differential, jogs and forks occur more frequently (onset of two-dimensional crack networks), and small surface relief fractures form frequently along the network. An undercut surface just before dislodgement appears at the left edge together with a large fracture fork. Fig. 108 contains micrographs illustrating the enlargement of surface relief cracks by edge progression. In Fig. 108a the micrograph under transmission illumination shows an undercut extension of an existing surface relief fracture system and in Fig. 108b the micrograph shows an advanced system produced by this extension mechanism. This mechanism would become important at a more advanced stage of erosion as a means of mass removal within larger and more extensive networks of subsurface fractures.

A soda lime glass specimen was rough polished for several minutes on a metallographic wheel covered with a silk cloth impregnated with 1 micron diamond paste. In addition to producing a dense aligned array of 1 micron scratches, this treatment superimposed a set of coarse scratches (due to contamination) which permitted study of the effect of several levels of damage to the erosion response of the glass surface. This is particularly interesting since such scratch dimensions would be expected to gradually form on exposed optical parts. This specimen was first exposed in the AFML rain erosion facility for 30 seconds (an estimated  $200 \pm 50$  impacts) after which optical inspection revealed a low density of damage consisting of surface relief fractures.





(a) Transmitted Light Micrograph of Surface Fracture Enlargement after 3 min Exposure (200X)



(b) Bright Field Reflected Light Micrograph of Surface Fracture Array after 10 min. Exposure (320X)

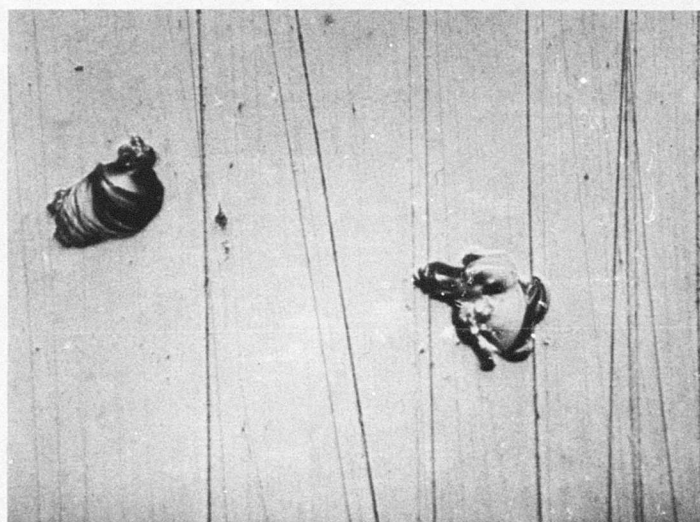
Figure 108. Soda Lime Glass Exposed to 1 in/hr Rainfall at 730 fps in AFML Facility



The damage density appeared to be somewhat higher than that observed on the annealed surface for the same time period - perhaps by a factor of two. In contrast to the lower strength materials, the drop impact did not show evidence of extending or enlarging the pre-existing cracks. During this erosion exposure, only one large surface relief fracture formed along a major scratch as shown in Fig. 109a. Since no additional such fractures were observed during an additional 3.5 min. exposure in the AFML rainfield, it is concluded that the stresses required for this mechanism are not attainable for this combination of drop impact loading and substrate fracture parameters. Many suitably oriented drop impacts would be anticipated for this exposure period. In contrast, this mechanism was important in the less resistant materials such as arsenic trisulfide, zinc selenide, and germanium. The majority of damage did not form along the major scratches or align along the direction of the minor scratch paths as for example in Fig. 109b. Instead, although the cracks appeared to influence fracture propagation in surface relief fractures, scratches appeared to be less important (and possibly less effective) as initiation sites than the damage produced by previous drop impacts. Some preferential initiation of surface relief fractures at the scratch roots was observed as shown in Fig. 110a for a typical example. A fracture core structure would typically originate tangential to the scratch and propagate away at an acute angle. Such a structure could be produced by the concurrent interaction of the compressive stresses introduced beneath the surrounding surface by the impacting drop with propagation of the lateral microcracks by hydraulic penetration into the crack root structure. The data obtained were not sufficient to resolve whether the original transverse microcracks at the scratch roots were responsible for initiation or whether additional microcrack substructure introduced by the hydraulic penetration mechanism (during the rainfield exposure) contributed importantly.<sup>(70)</sup> As observed in other scratch-sensitive systems, sites located at the acute angle intersection of two scratches were particularly vulnerable to microcavity formation as shown in Fig. 110b.

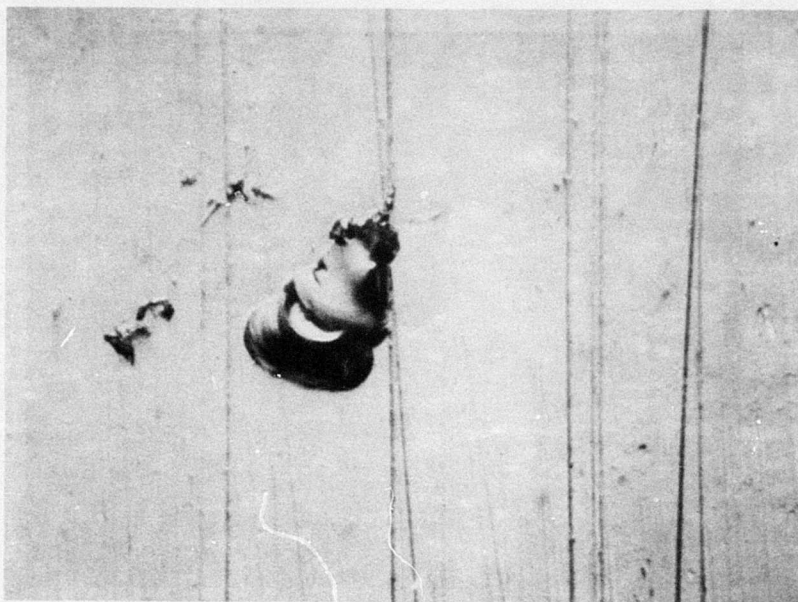


(a) Oblique Reflected Light Micrograph of Scratch Initiated Fracture Surface after 30 sec Exposure

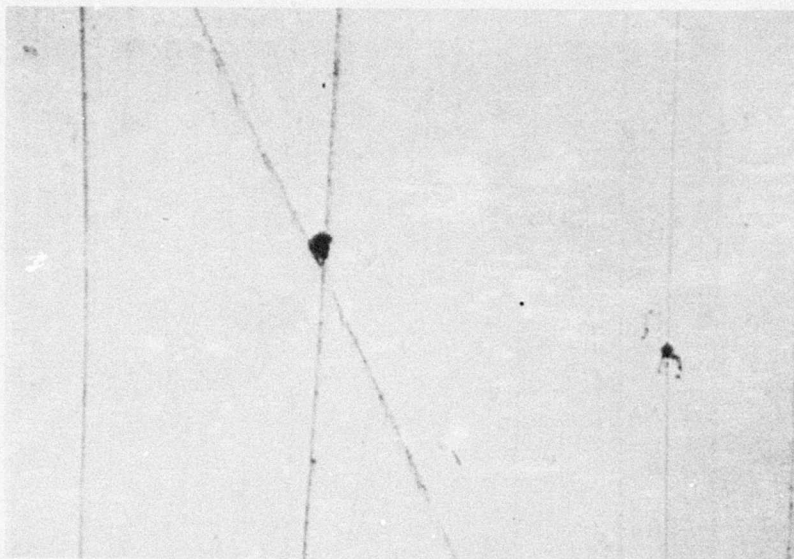


(b) Erosion Damage after 4 min Exposure

Figure 109. Influence of Surface Scratches on Erosion of Soda Lime Glass Exposed to 1 in/hr Rainfall at 730 fps in AFML Facility



(a) 320X



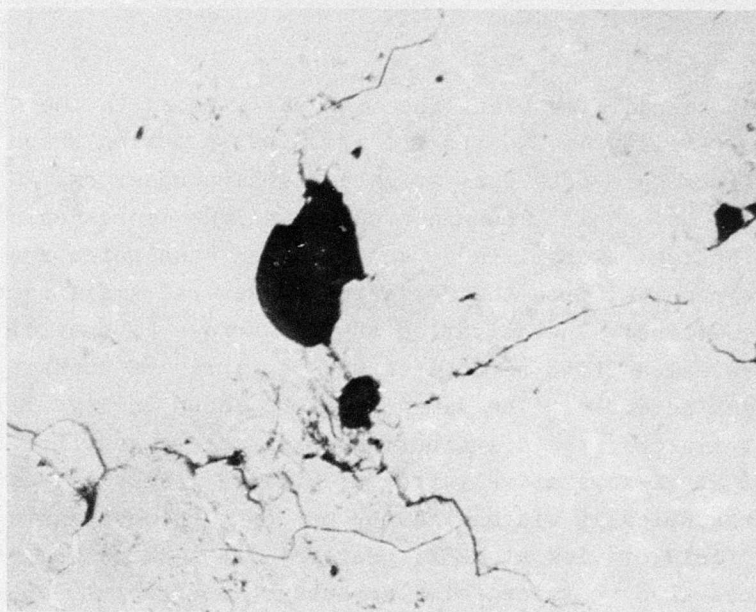
(b) 400X

Figure 110. Optical Micrographs in Oblique Reflected Light of Typical Scratch Initiated Damage in Scratched Soda Lime Glass after 4 min. Exposure to 1 in./hr. Rainfall at 730 fps in AFML Facility



A soda lime glass specimen was exposed in the AFML/Bell erosion facility at 730 fps for two minutes during which each microscopic site was estimated to have undergone  $20 \pm 10$  drop impacts. This exposure produced slight macroscopic losses in the optical transmittance and specimen mass which are believed to have resulted from the formation of several small macroscopic spall cavities. Investigation of the surface by optical microscopy revealed it to be covered with an array of surface pits and crack networks. The damage network shown in Fig. 111 is perhaps typical; the distribution of damage ranged from fields of view at 125X relatively free of visible cracks and cavities to macroscopically visible cavity networks which spanned the entire field of view at 125X. Several sites which had resisted mass loss also contained similar subsurface fracture networks and several sequential drop impacts at these sites would have measurably increased the mass loss. The incubation period for mass loss is the time required to establish a distribution of such networks of surface and subsurface fractures over the specimen surface. The requirement for such pre-existing networks also explains why the incubation time for mass loss depends sensitively upon a velocity exponential (4-7 for supersonic rain erosion) since the damage produced by each successive drop impact depends critically upon the pre-existing damage.<sup>(52)</sup>

At this stage of damage, the fracture structures described for the lightly eroded Air Force specimens have been eliminated and the crater walls tend to adopt steep angles of descent and polygonal surface shapes. The original surface relief fractures have been eliminated and nearly all damage sites radiate away cracks so that networks often span more than a square millimeter over the surface. In general, surface cracks propagated along jogged and branched paths; and, although the path direction frequently changed, it appeared that at this stage that the successive drop impacts readily initiated and continued crack propagation. Consequently, cracks quickly formed extensive networks which were associated with angular cavities running along the crack surface and fracture surfaces extending



(a) Nomarski Interference Contrast



(b) Transmitted Light

Figure 111. Optical Micrographs of Cavity and Associated Crack Network Formed in Soda Lime Glass after 2 min. Exposure to Standard Rainfield (140X)

deeply into the specimen. These surface crack networks frequently radiated away from the periphery of large cavities weakening the surrounding surfaces. This damage mode is shown in Fig. 112. Consequently, although only minimal losses have occurred in macroscopic properties, the incubation period was essentially completed for this exposure to the rainfield environment.

During the next two minutes of exposure in the AFML/Bell facility significant transmittance and weight losses occurred as the cavity walls and the enclosed crack networks were dislodged by subsequent impacts. Concurrently, the subsurface fracture networks were driven deeper into the specimen since the cavity surface exposed the subsurface crack networks to direct attack by hydraulic penetration. After this exposure period, patches of macroscopic damage were readily observed with the unaided eye although the damage was confined primarily to surface spalling of microscopic dimensions. Further exposure to the rainfield produced catastrophic deterioration as macroscopic cavities dominated the surface damage. After 5 minutes exposure, the original surface was completely removed, and after an exposure of 6 minutes cracks had penetrated through the  $3/8$  in. specimen thickness. Light transmission through the specimen was reduced to zero after an exposure time of slightly over 4 minutes.

## 2. Thermally-Tempered Soda Lime Glass

A sample of this tempered glass was exposed to the AFML/Bell rain erosion facility for 4 minutes. The residual compressive state effectively suppressed fracture initiation and propagation in this glass. Whereas such an exposure duration would be sufficient to destroy a borosilicate glass specimen and severely damage the surface of a soda lime glass specimen, only small microscopic craters and crack networks were observed on the surface. Typical fields of view are shown in Fig. 113 and 114. These cracks and cavities were significantly smaller than those observed on similarly exposed annealed soda lime glass. Cavities



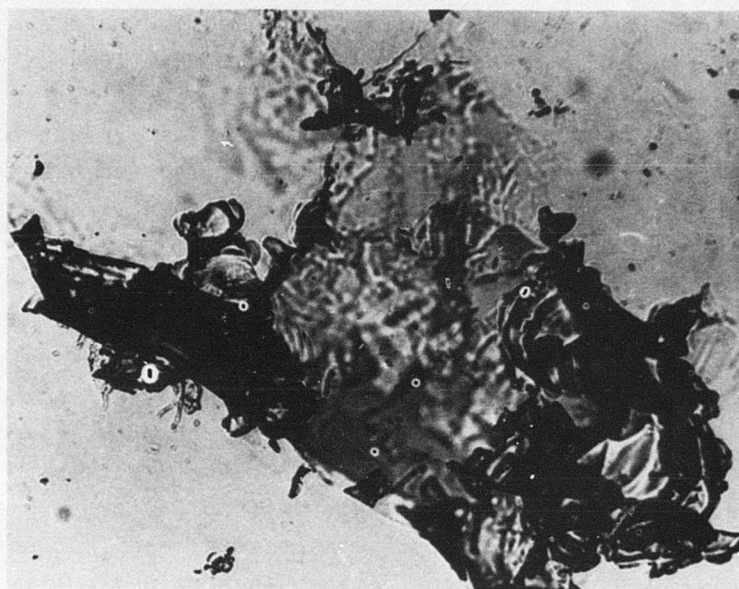
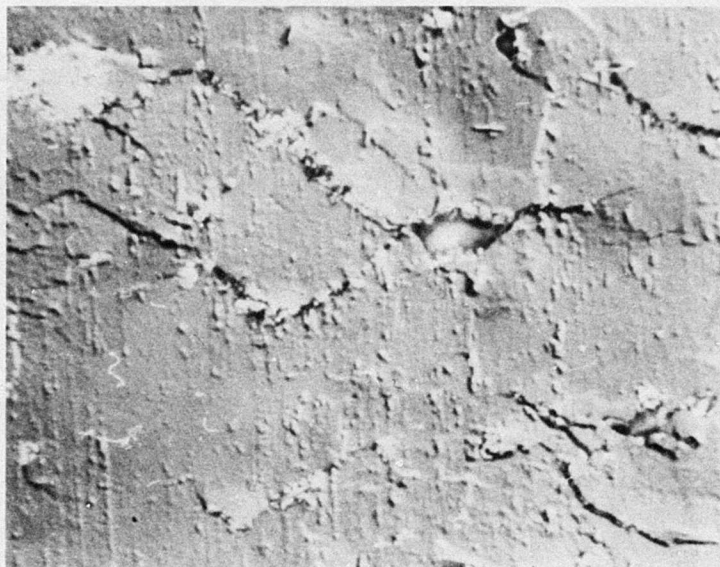
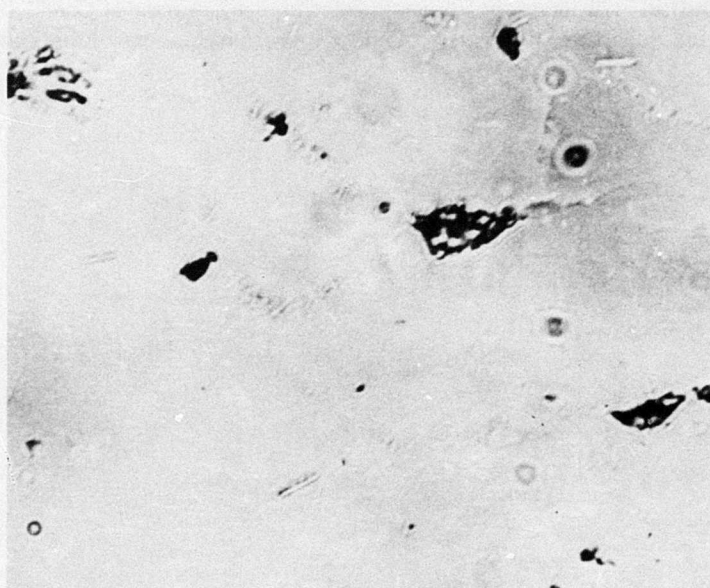


Figure 112. Optical Micrograph of Network of Cavities and Cracks in Soda Lime Glass after 4 min.  
Exposure to Standard Rainfield (140X)



(a) Nomarski Interference Contrast



(b) Transmitted Light

Figure 113. Optical Micrographs of Cavity and Associated Crack Network in Tempered Soda Lime Glass after 4 min. Exposure to Standard Rainfield (600X)



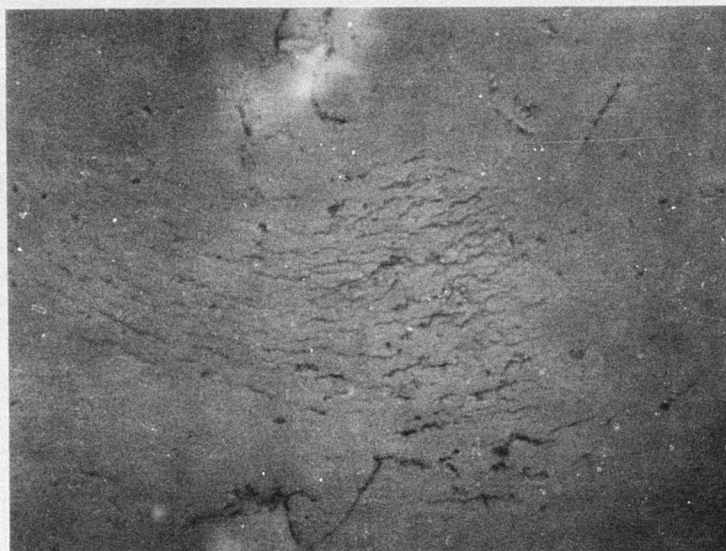


Figure 114. Optical Micrograph in Nomarski Interference Contrast of Crack Network Formed in Tempered Soda Lime Glass after 4 min. Exposure to Standard Rainfield (650X)



on the tempered surface were angular shaped, forming along the surface crack networks where subsequent impacts dislodged fragments which were previously undercut by small subsurface fracture networks analogous to the mechanism observed for cavity formation on the annealed soda lime specimens. Both the subsurface fracture networks and the spall cavities tended to be isolated (surface link-up of surface damage appeared to be inhibited) preventing the formation of large craters surrounded by damaged wall structures. Relatively few surface cracks could be detected that were associated with the observed subsurface damage for this exposure during which a large number of drops struck each site.

In this system, the rain drop impacts appeared to propagate fractures beneath surface sites free of subsurface damage with great difficulty. First, only the peak tensile stresses produced by the drop impact were capable of extending surface flaws as indicated by the short lengths and frequent jogs characteristic of cracks in this system. Second, the high residual compressive strength tended to tightly seal the fine surface cracks against hydraulic penetration by subsequent drop impacts. Consequently, Nomarski interference contrast was required for their detection by optical microscopy revealing the crack as a slight displacement at the surface. In some cases, a series of short, discontinuous cracks extended for distances less than a millimeter. These cracks were closely spaced and oriented in a common direction suggesting that the residual compressive stress had sufficiently inhibited crack propagation that only a series of short crack segments could be propagated from isolated initiation sites. This isolation presents a sharp contrast to the annealed soda lime glass and the borosilicate glass in which the average crack lengths could extend to macroscopic dimensions in the advanced erosion state.

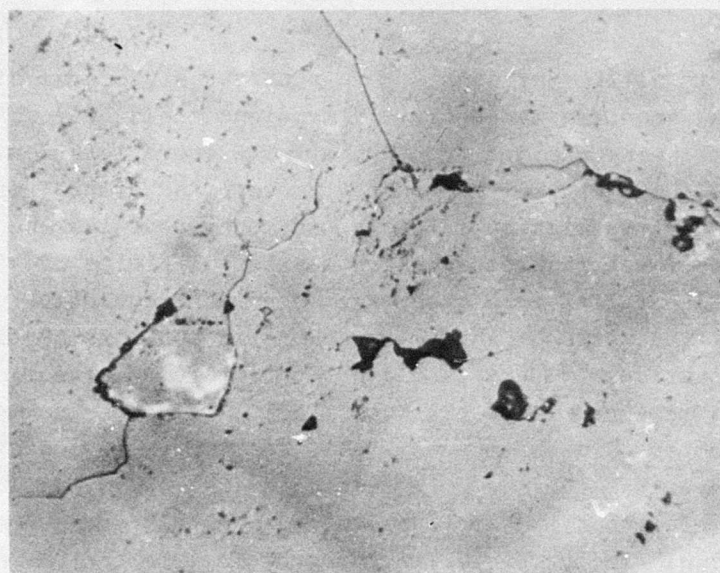
A similar phenomenon was the generation of closely spaced patterns of discontinuous cracks such as the field shown in Fig. 114. In these crack systems the energy of subsequent

impacts would be dissipated into enlarging the series of cracks, significantly reducing the magnitude of further crack propagation. Comparison of the span of these crack fields with comparable systems for the annealed soda lime glass and the borosilicate glass again indicated that the residual compressive state restricted the dimension of the damage produced per impact.

Continuation of the rainfield exposure for another two minutes (total six minutes) significantly increased the density of fine crack networks and produced some large (but shallow) spall cavities. Significant increases also were observed in the density and penetration depth of the subsurface fracture structure. During the next two minutes of rain exposure (total eight minutes) the extensively formed surface crack networks begin to enable dislodgement of numerous small fragments producing a dense array of shallow cavities with relatively complex geometries. Both the surface and subsurface damage continued to increase with additional exposure to the rainfield. This combination of impact loading and substrate fracture parameters were incapable of propagating long continuous surface cracks and forming large associated subsurface fractures (in comparison with the untreated soda lime glass). Consequently, the damage observed under microscopic examination in the advanced states of rainfield erosion arose from a dense array of fine crack networks and small spall craters in contrast to the large spall cavities formed on the annealed soda lime glass. This was consistent with the greater ratio of light transmission loss to weight loss observed for the tempered glass data as indicated in Section IV.

### 3. Borosilicate Glass

The shortest exposure duration of 10 seconds in the AFML/Bell erosion facility produced significant damage to the borosilicate glass surface although each microscopic site probably received only  $2 \pm 1$  drop impacts. An example of the crack networks formed is shown in Fig. 115. Although the intensity of damage was not uniformly distributed, relatively large surface cracks which could extend over a centimeter in length and



(a) Nomarski Interference Contrast



(b) Transmitted Light

Figure 115. Optical Micrographs of a Crack Network in Borosilicate Glass after 10 sec Exposure to Standard Rainfield (140X)



penetrate to millimeter depths were observed at several sites. Such damage spanning macroscopic dimensions could be readily detected with the unaided eye. Other sites were less heavily damaged although optical microscopy in both the simple reflection and the transmission illumination modes revealed the existence of surface crack networks in nearly all fields of view. Small surface relief fractures were observed frequently, particularly at the sites of surface crack forks and intersections. At some locations the cracks did not penetrate to significant depths and remained isolated; these fields may have received a smaller number of drop impacts. Last, small pits were distributed randomly over the surface. Inspection of the cavity wall surfaces revealed that they were frequently comprised of an array of conchoidal fractures similar in morphology to the surface relief fractures. Even for this very short exposure period, the link-up and extension of surface cracks and their concurrent penetration into the glass interior at large angles (frequently larger than  $60^\circ$ ) indicated an advanced stage of the incubation period had already been attained.

Exposure in the AFML/Bell erosion facility for 20 seconds produced a relatively uniform array of damage over the borosilicate glass surface which appeared to have moderately increased in severity when compared to the more heavily eroded areas on the specimen exposed for 10 sec. Although macroscopic damage was uniformly distributed over the surface to the unaided eye, cavities were restricted to microscopic dimensions as was observed for the 10 sec. specimen. The most significant difference between the 10 and 20 sec. specimens was the rapid rate at which the various surface cracks and subsurface fractures linked up to form damage networks which extended across the specimen surface. Under microscopic inspection the surface was seen to be completely covered with arrays of sizable fractures and sometime undercut over macroscopic dimensions.

The circular arc patterns analogous to those described earlier for the soda lime based glasses were also observed on

this specimen as shown in Fig. 116. In this glass, the arcs originated with lengths of 50 microns or less with little vertical penetration and extended outward to a radii of approximately 0.4 mm or so (determined from several randomly selected patterns) whose depth of penetration increased as the radius increased. The penetration angles were oriented so the outer cracks beyond approximately 2 mm resembled arc sectors of the Hertzian ring crack patterns. The radius, depth of penetration, and crack spacing of the arc pattern were all larger than those observed for the other oxide-based glass systems.

After 30 sec. the induction period for mass loss had been completed. The entire surface was covered with a dense array of readily visible cracks. Interestingly, the cracks had a strong arc character and over 20 complete or nearly complete ring crack patterns (composed of arc sectors with associated conical subsurface fractures analogous to zinc sulfide) could be readily discerned. Typical fields of view are shown in Fig. 116 to 118. Although the ground specimen sides prevented a cross-sectional view, the depths of penetration appeared to be limited to a couple of millimeters. Under the optical microscope, the entire surface was observed to be densely interconnected with two-dimensional networks of surface cracks which extended deeply into the substrate so that areas of macroscopic dimensions were frequently undercut by a continuous network of subsurface fractures. Indeed, nearly all surface cracks were associated with significant fracture penetration into the interior. Microscopic pits and cavities were densely distributed and macroscopic cavities were sparsely distributed. Under transmission illumination in the microscope, the damage was observed to be more severe than that shown in Fig. 112 for soda lime glass producing significant macroscopic optical degradation.

Consequently, the critical damage mechanism for borosilicate glass is the formation of surface cracks which extend over the surface to form large two-dimensional arrays and which penetrate deeply into the interior to undercut the overlying

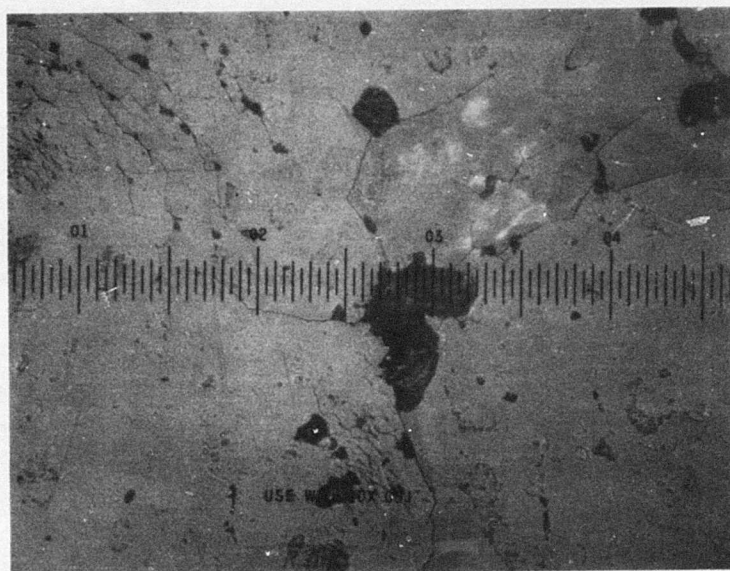
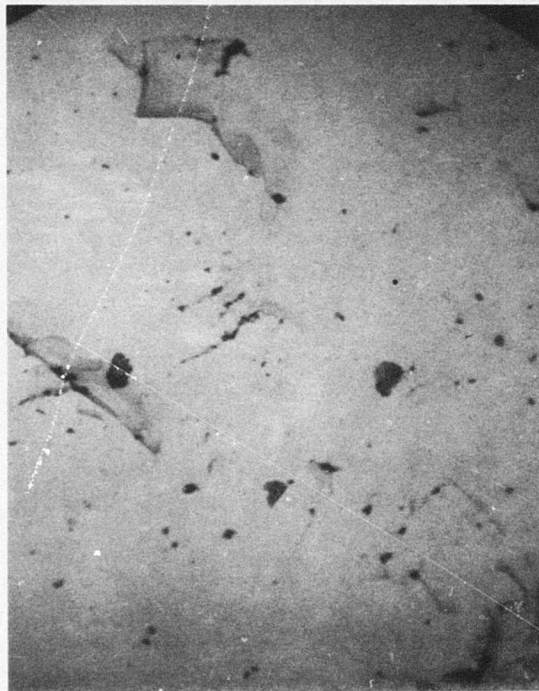
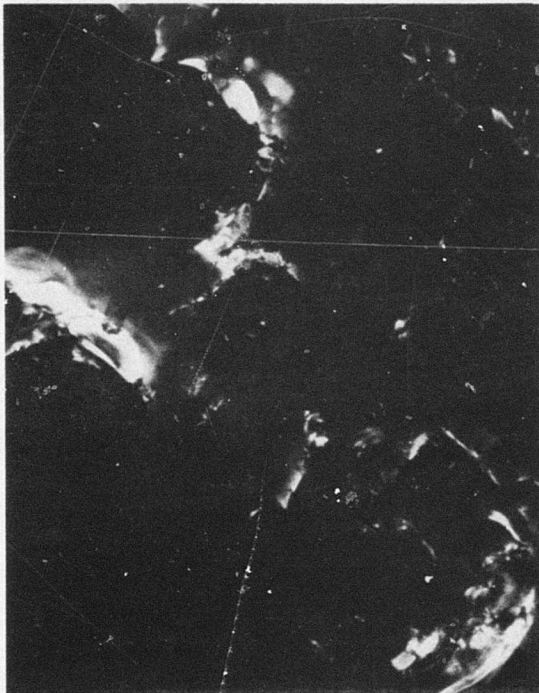


Figure 116. Optical Micrographs in Oblique Reflected Light of Borosilicate Glass after 20 sec Exposure to Standard Rainfield (100X)





(a) Bright Field

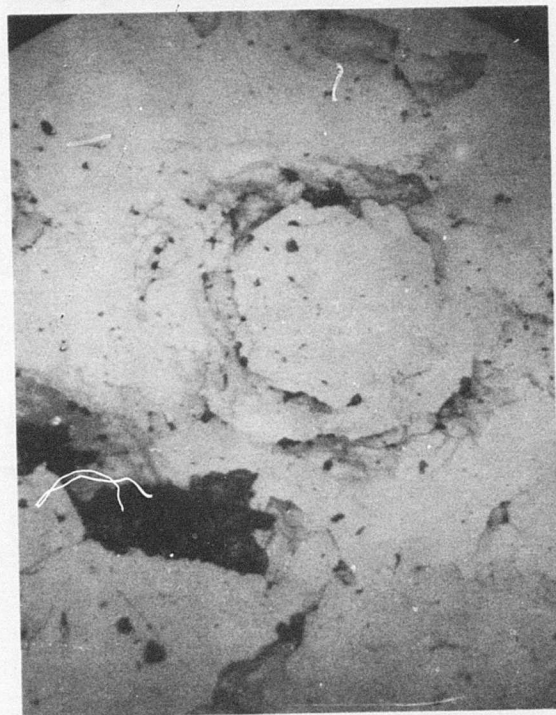


(b) Polarized Light

Figure 117. Optical Micrographs of Bulk Damage in Borosilicate Glass after 10 sec Exposure to Standard Rainfield (35X)



(b) Polarized Light



(a) Bright Field

Figure 118. Optical Micrographs of Ring Crack Pattern Formed in Borosilicate Glass after 30 sec Exposure to Standard Rainfield (35X)

glass. These subsurface networks render the glass vulnerable to the expulsion of macroscopic particles upon subsequent rainfield exposure and significantly degrade the optical transmittance. Examination of the 10 sec. exposure specimen at magnifications ranging from 7X to 400X with a variety of illumination modes indicated most but not all cracks possessed an arc-like character following a circular curvature. Although small crack segments such as shown in Fig. 115 might appear to be randomly oriented, the entire crack structure approximated a circular arc as shown in Fig. 117 and 118. The frequent jogs and forks appeared to result from both a tendency for fork formation in borosilicate glass as shown in Fig. 115 and crack realignment during propagation by randomly positioned drop impact. In this system, crack extension probably occurred by all of the mechanisms discussed in the section of drop impact: hydraulic penetration, dynamic Hertzian tensile stresses, and lateral outflow over surface discontinuities. Examination of the subsurface fracture structure frequently revealed a prominent rib mark from which microhackle radiated further into the interior. On the 20 and 30 sec. specimens, this suggests that of the anticipated 5-10 impacts which struck such a fracture only one or two had the proper orientation to extend the fracture significantly. Such extension was produced by the hydraulic penetration mechanism; no other mechanisms would be operative at these depths. Relatively large fracture misregistrations must exist to permit such penetration by the impacting drop.

Subsequent exposure for 60 seconds or longer in the AFML/Bell erosion facility produced a change in damage morphology. A significant fraction (10-20%) of the surface was dislodged, forming macroscopic and microscopic cavities. The remaining surface area sustained a further increase in the density of microscopic crack arrays and interior fractures. Continued rainfield exposure to 2 min. duration removed more than 90% of the original surface, yielding a very rough surface comprised primarily of macroscopic cavities. The mean depth of damage was several millimeters and some interior fractures



extended four millimeters beneath the original surface. The exposure of the cavity wall flaws and facet intersections to direct drop impact accelerated this removal process so that the borosilicate specimen had been rendered unusable during the shortest duration of the soda lime tests. The results of a series of erosion exposures as a function of impact velocity are summarized in Table VII.

The sequential history of the ring crack pattern formation was explored by etching (40 sec. immersion in 5% HF) the specimens exposed for 10 and 20 sec. in the AFML/Bell erosion facility. In the eroded state, only partial ring patterns were observed on the 10 sec. specimen whereas complete ring patterns were observed on the 20 sec. specimen. Application of the etchant revealed a large number of previously invisible cracks together with a dense distribution of very small surface flaws.

Although these additional cracks and fracture surfaces emphasized the circular character of the damage both on the macroscopic and microscopic scale and more clearly defined the arc geometries, they did not reveal any additional perimeter portion of the partial ring patterns. Consequently, the initial impacts for this erosion and substrate system can only introduce a portion of the circumferential crack systems together with their associated conical subsurface fractures. However, these partial crack systems subsequently interact with the perimeter tensile stresses of appropriately oriented drop impacts (approximately concentric) to complete the circular perimeter. Thus, the completed ring patterns represent an admixture of several coupled crack patterns rather than the enhancement of a pre-existing flaw network from the initial impact. Such a mechanism is consistent with the marked asymmetries and eccentricities which were observed on most ring patterns (the example in Fig. 118 was relatively well-formed). The residual influence of these ring structures is surprising; several sites on the 60 second exposure specimen have circular cylinders of the original

surface from which the surrounding surface has been removed. This is believed to be analogous to observations of glass bead produced erosion in which subsequent exposure removed the material lying in between the initial ring crack patterns. The inner radii of these crack patterns is comparable with the outer radii of the arc crack patterns, 0.4 to 0.5 mm, observed during the early stage erosion.

#### 4. Ion-Exchanged Glass

Ion-exchanged strengthened glass specimens were exposed in the AFML/Bell erosion facility at 730 fps for periods of 20 and 60 sec. Visual examination of the specimens with the unaided eye indicated a dense field of fine bubble-like structures which could be resolved with the optical microscope to consist of arrays of isolated microscopic damage. Principal damage modes consisted of the surface relief fractures, isolated cracks, and concentric arc-shaped crack arrays, as shown in Fig. 119. In contrast to the soda lime and the borosilicate glasses, the predominant fraction of damage in this system did not link-up but instead remained isolated. Consequently, optical transmission and weight loss underwent negligible degradation since depth penetration was minimal.

No evidence for subsurface optical degradation due to fracture penetration could be detected when examining the specimens in the optical microscope with transmitted light illumination. Although a small increase in damage density was observed for the longer erosion exposure, crack extension and surface relief fracture enlargement were not important at this stage of erosion. This rainfield and substrate system only yielded the initial propagation of severe flaws but not the extension of existing surface cracks along the surface or into the interior. Consequently, the isolated cracks quickly terminated and the surface relief fractures tended to remove clusters of surface flaws. This glass system did not undergo either the multiple depth initiation of lateral surface relief cracks originating from the



Figure 119. Optical Micrograph in Nomarski Interference Contrast of Surface Damage Formed in Ion Exchanged Glass after 60 sec Exposure to Standard Rainfield (140X)



central damage core as did the soda lime glass or the crack link-up extension as did the borosilicate glass. The isolation of the microscopic damage features prevented any degradation in optical transmission or mass loss.

Most of the structures tended to have approximately circular shapes although a small fraction had elliptical and irregular shapes. An example of a surface relief fracture system is shown in Fig. 120 which was produced when a droplet struck two defects spaced approximately 20 $\mu$ m apart. On the top side, the rib marks (circumferential markings produced by momentary arrest of the fracture front) and the microhackle marks (lines oriented in the fracture propagation direction analogous to river patterns produced by cleavage fracture in metal fractography) indicated this lateral relief fracture propagated as a single event. However, the lower lateral relief fractures propagated independently; the right point source probably initiated a fracture at this time. It is not clear whether the left point source subsequently initiated the fracture during the original or during a subsequent impact.

As noted earlier, these fracture systems originated at a central core composed of a broken region of jagged irregular surfaces. From this core, surface relief fractures propagated back to the exterior surface producing a fracture mirror. Examination of replicas of several relief fractures by transmission electron microscopy at magnifications of 30,000X did not reveal evidence of the roughness associated with the onset of crack tip instability (mist). Consequently, although the propagation markings acted analogous to those described for quasistatic initiated glass macrofracture, these relief fractures seemed to show little crack tip instability and branching suggesting lower propagation velocities. Microhackle lines were prominent in this glass system and generally served as a mechanism for vertical linking up of isolated crack tips along the fracture front. These lines were generally straight indicating the fracture front propagated along a direct radial path. Although cracks

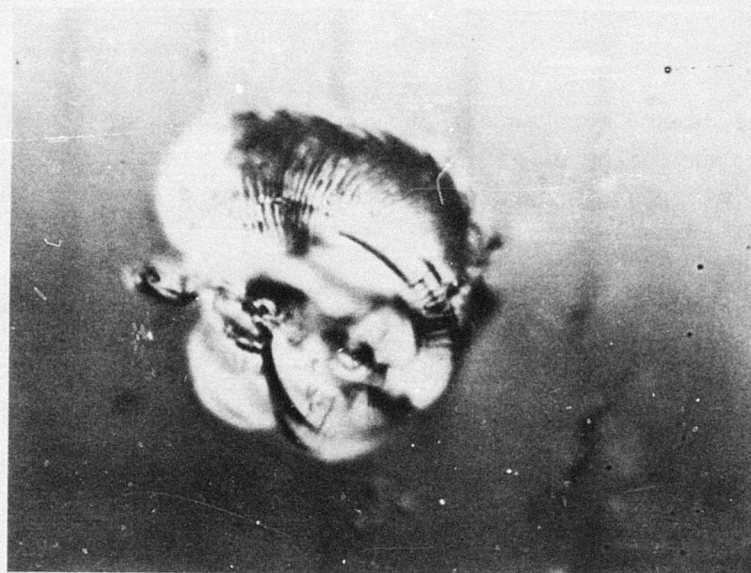


Figure 120. Optical Micrograph in Bright Field Reflected Light of Surface Relief Fracture Formed in Ion Exchanged Glass after 60 sec Exposure to Standard Rainfield (900X)

occasionally propagated away from the fracture core as shown in Fig. 121 for calcium-alumino silicate glass, this damage structure was less important in the ion-exchanged glass and any such cracks quickly terminated. The circumferential rib marks were frequently observed but their relationship to glass properties and fracture characteristics is not understood.

An optical microscopy and replica transmission electron microscopy study was undertaken to characterize the differences in fractography of the ion-exchanged glass from the less resistant soda lime and borosilicate glasses. This work indicated very little if any fracture penetration into the interior of the ion-exchanged glass occurred in contrast to those glasses. Furthermore, the lateral extension of the surface cracks in the ion-exchanged glass was very short, generally less than 100 $\mu$ m after 60 seconds exposure in the AFML/Bell erosion facility, preventing the formation of two dimensional surface damage networks. The crack morphology both under Nomarski interference contrast illumination and replica examination indicated that the short cracks were completely isolated terminating in a single fracture unlike soda lime glass which revealed moderate crack tip branching (refer for example to Fig. 107) and borosilicate glass which underwent extensive branching at analogous crack tips. It is believed that the finely spaced crack arrays (shown in Fig. 119) effectively dissipated the drop impact energy with minimal crack extension and interior damage. Most striking of the replication observations was the high frequency of isolated damage in which a linear trace was formed by a discontinuous line of cracks, elliptical chips and parallel crack propagation (splitting and rejoining). In addition, very small relief fractures frequently lay along short cracks. However it was not possible to clearly determine the initiation and sequential propagation of damage from this data. Unlike the soda lime and borosilicate glasses in which the surface relief fracture systems could be readily extended (refer for example to Fig. 108), the replica investigations of microhackle markings indicated that



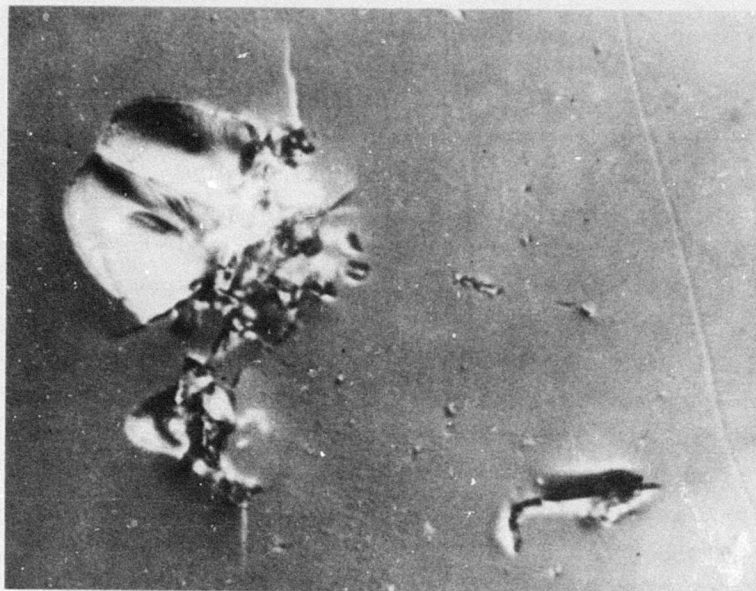
only small fractions of the surface edges could be freed by subsequent drop impacts at this stage of erosion damage.

As noted above, the initial damage consisted primarily of small isolated fracture structures and short, parallel crack arrays so that the rate of damage with rainfield exposure duration decreased with continued exposure. Once the most sensitive surface flaws had been eliminated, relatively few subsequent impacts were capable of propagating significant fractures through the high residual compressive stress (probably greater than 80,000 psi). Although it would be tempting to compare the ion-exchanged and the thermally-tempered strengthened glasses, the large disparity between exposure times reported herein precludes such an evaluation.

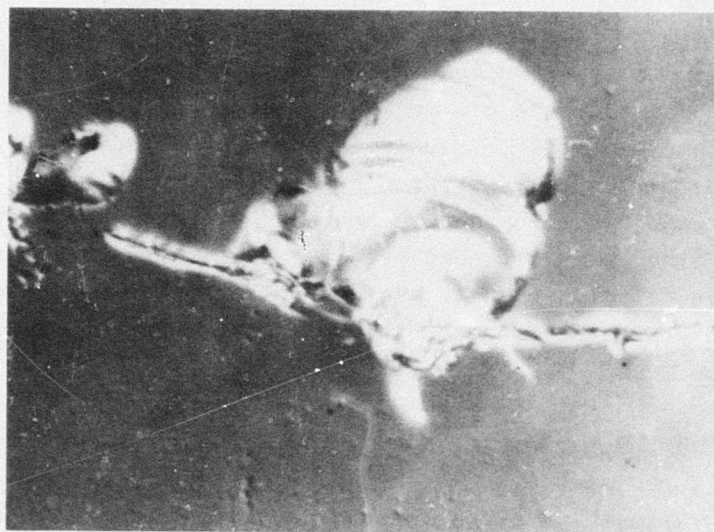
#### 5. Calcium Aluminosilicate Glass

Calcium aluminosilicate glass specimens were exposed in the AFML/Bell rain erosion facility at 730 fps for periods of 20 and 60 sec. The distribution and mode of damage observed resembled that described above for the ion-exchange strengthened glass. Both glass systems effectively confined the drop impact event to localized sites preventing the creation and extension of large fractures upon subsequent impacts. The lower magnification photograph of the ion-exchanged glass shown in Fig. 119 provides an illustration of the damage sustained by the calcium aluminosilicate surface for the same erosion exposure.

In general, rainfield erosion of the calcium aluminosilicate glass resulted in a lower density of arc crack patterns than for the ion-exchanged glass. The surface relief fracture systems tended to be less circular and instead one or more segments predominated as shown in Fig. 121. However, the basic structure of a central core surrounded by lateral relief fractures was observed for this system also. Comparison of the surface relief fracture details of the two glass systems indicated a greater prominence for rib and Wallner (interference at the



(a)



(b)

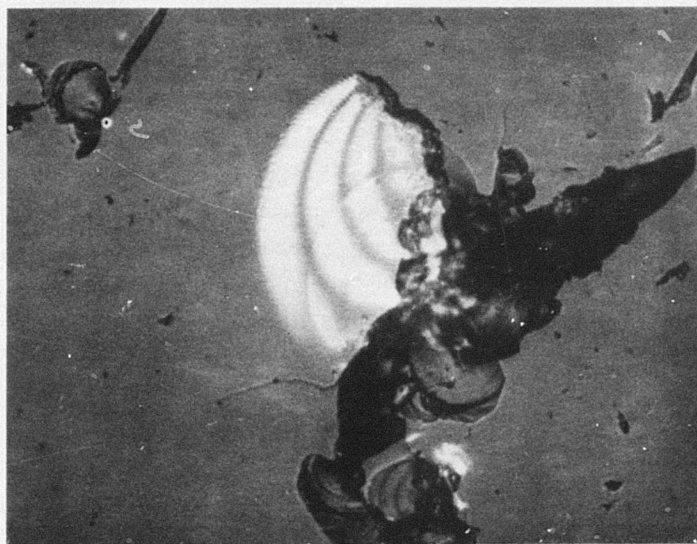
Figure 121. Optical Micrographs in Oblique Reflected Light of Grooves and Surface Relief Fractures Formed in Calcium Aluminosilicate Glass after 60 sec Exposure to Standard Rainfield (620X)

crack tip by sonic waves generated by secondary sources) markings but a decreased incidence of microhackle markings. Relatively few microhackle markings were observed on the calcium aluminosilicate glass fractures; specific searches on surface replicas examined at magnifications up to 20,000X indicated that the crack tip propagation generally did not propagate by this mechanism. Only this glass system contained a significant density of nicks and grooves as shown in Fig. 121 and grooves several microns wide and several hundred microns long occurred rather frequently. The roots of such grooves preferentially initiated surface relief fractures as illustrated in Fig. 121. Adjacent surface relief fractures were sometimes connected by cracks; however such cracks did not branch or fork but instead quickly terminated at each end. A densification mechanism in this glass structure may enable successive droplet impacts to enlarge the crack width and blunt the crack tip rather than deeply extending the fracture surface.

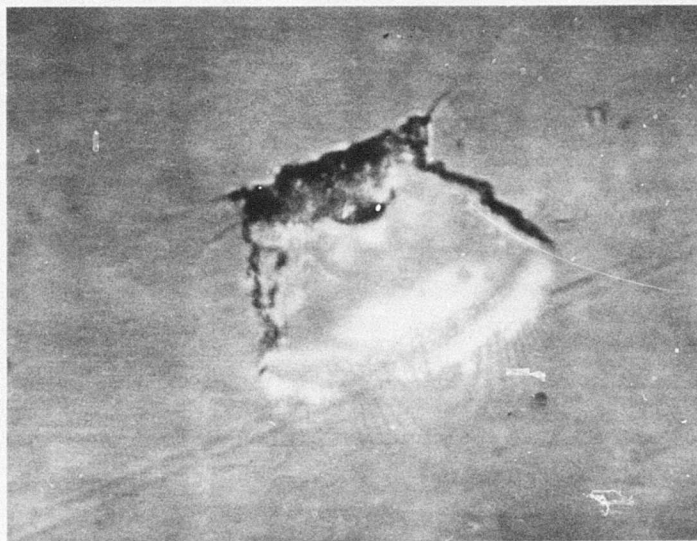
Many of the surface relief fractures were apparently generated by a sequence of impacts so that both sealed and separated surface relief fractures undercut the original glass surface during the early erosion stages. Examples are shown in Fig. 122 of undercut surfaces associated with well developed fracture cores which preceded mass removal. These photographic fields were illuminated with a green filter which produced well-defined interference fringes from which a mean angle of descent could be derived.

Examining Fig. 122a, a narrow, finely spaced fringe system is superimposed over a broad, widely spaced fringe system. The narrow fringe system was produced by interference between light waves reflected from the upper and lower surfaces of the undercut glass. Each fringe displacement corresponded to a variation in height of  $.18\mu\text{m}$  so that the upper edge descended at a mean angle of  $9^\circ$  with respect to the exterior surface. Similar calculations for the fringe spacings at the sides of the fracture shown in Fig. 122b both yielded descent angles of  $14 \pm 1^\circ$ .





(a) 500X



(b) 800X

Figure 122. Optical Micrographs in Green Reflected Light Illustrating Interference Fringes Formed in Calcium Aluminosilicate Glass after 20 sec Exposure to Standard Rainfield

Measurement of several additional descent angles conformed to the range 10-15° indicating such angles to be typical. However, this method of measurement is prejudiced against angles 25° or steeper since the fringe widths and spacings become so narrow that detection and measurement would be difficult. For comparison, a surface relief fracture measurement yielded a 7° angle of descent for a soda lime specimen and several measurements yielded approximately 18° angles of descent for surface arc fractures on the borosilicate glass specimen exposed for 20 sec.

The widely spaced circumferential fringe system shown in Fig. 122a was produced by Fizeau interference between light waves reflected from the upper and lower fracture surfaces across the separation gap. Each fringe displacement corresponded to .28 $\mu$ m so a separation angle of 2° is calculated at the edge of closer spacings and 1° at the edge of wider spacings. The three fringe displacements indicated the crack entrance to be approximately .8 $\mu$ m across and further drop impacts would quickly remove the undercut surface by the hydraulic penetration mechanism. Such fringe patterns were very rarely observed suggesting that the average fracture surface separation was less than several thousand angstroms. Examination of the lower photograph showed the interference fringes produced by the undercut surface to extend beyond the boundary of reflection produced at the fracture surface separation. Apparently an appreciable separation width is required to allow conspicuous reflection although this data does not allow an estimate of this width. Examination of the fringes produced at the center of the sealed fracture indicated a gradual rise angle of 3° which probably preceded a sudden jump to the exterior surface (since the surrounding side fringes indicate twice as large a rise angle).

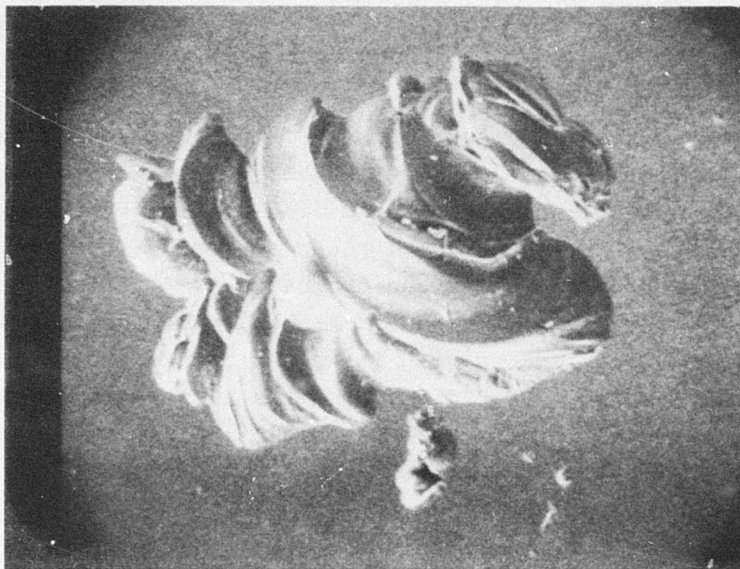
Fractures originating at the fractured cores and grooves tended to rise to the surface rather than penetrate into the substrate as observed for the soda lime system and prolonged exposure tended to yield elongated elliptical systems in contrast to the circular systems observed for the ion-exchanged

glass. The apparent decrease in relief-fracture rate with exposure time suggests the concerted action of two fracture mechanisms. The first mechanism is fracture initiation at sites of flaws present in the original glass surface which would conform to first order kinetics and dominated the initial phase of the incubation period. The second mechanism is the interaction of subsequent drop impacts with flaws and damage produced by previous impacts which would conform to a slower fracture rate requiring a number of impacts to generate additional fracture systems.

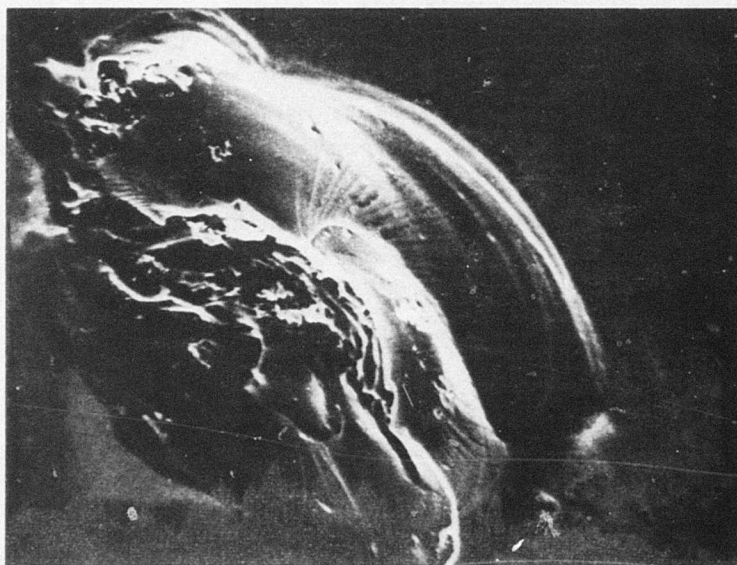
A scanning electron microscopy study was begun of the 20 sec. specimen of the calcium aluminosilicate glass and then extended to the 20 sec. specimen of the ion-exchanged glass. Fig. 123a illustrates the edge chipping which was important during the incubation stage of the calcium aluminosilicate glass. The original fracture event produced the crevice systems in the upper righthand corner together with the large semicircular surface relief fracture. Both the structure of the complex series of outer relief fractures and higher magnification view showing the misalignment of the coarse microhackle markings indicated that the area of surface loss was increased 30 to 50% by subsequent drop impacts along the edge. Although the edge chipping also occurred in the less erosion resistant glasses, it was less important because of the lower probability for chipping and the much greater damage introduced by alternative fracture propagation mechanisms.

Figure 123b illustrates a typical surface relief fracture system in the ion-exchanged glass. The fracture originated in the central core area consisting of broken, irregular glass surfaces. Subsequently, three mirror fracture surfaces originated from this area to radiate back to the surface. The pronounced microhackle markings point along the direction the fracture surface propagated and less prominent rib marks indicate arcs of momentary fracture front arrest. The propagation of the relief fracture front from the inner relief fracture mirror to the





(a) Calcium Aluminosilicate Glass



(b) Ion-Exchanged Glass

Figure 123. Scanning Electron Micrographs of Surface Relief Fractures after 20 sec Exposure to Standard Rainfield (650X)

exterior surface can be traced from the spiral microhackle pattern. The spiral hackle pattern clearly indicates how the crack tip maintained continuity along the perimeter as it advanced. Micrographs at 3,000X and higher revealed typical river pattern convergence in the direction of fracture propagation. Views at similar magnifications of the base of the opposite fracture mirror indicated that this mirror plane had been undercut. Subsequent drop impacts removed some of the heavily damaged core and probably the origin site also. At the lower corner, higher magnification views revealed microhackle misalignment indicating that subsequent impacts also damaged this area (edge chipping).

#### IV. TRANSMISSION CHARACTERISTICS OF WINDOW MATERIALS

Erosion of the exterior of supersonic aircraft or missiles such as windows, or structural components, may be experienced during penetration of rainfields at low altitudes or clouds of ice crystals at higher altitudes under tactical or evasive flight conditions. Transparent materials for windows or enclosures on aircraft and missiles that have the desired transmission in the infrared or visible electromagnetic spectrum suffer from major problems of fracture, surface frosting or pitting due to impacts of rain, sand and ice particles during flight. Therefore, to meet the current and future requirements for all-weather subsonic and supersonic aerospace vehicles, knowledge of the rain, dust, and ice erosion characteristics of windows, coatings and structural materials must be obtained and new and improved erosion resistant materials developed. This research and development effort has been initiated in order that serviceable materials may be available within the next few years.

##### A. MEASUREMENTS OF TRANSMISSION LOSSES

The change in optical quality of window materials after damage by liquid or solid particle impact is of considerable concern in aircraft or missile applications. For optically transparent materials the change in quality was assessed by a subjective method in which the bar type resolution pattern shown in Fig. 124 is resolved through the plastic or glass material before and after erosion damage. In this evaluation specimens were photographed before and after testing. The uneroded specimen was superimposed over the resolution target and photographed at a 6X magnification to illustrate the loss in quality after exposure to a standard rain environment.

For optical and infrared materials the change transmittance before and after exposure for various lengths of time to an erosive environment was determined objectively using a spectrophotometer. The optical materials were scanned over a range from 0.65 - 2.10 microns (6500 to 21,000Å) using a Model 14 Cary Recording Spectrophotometer.





**Figure 124. Resolution Target**

The infrared materials are sometimes used all the way to one end or the other of their spectral transmission ranges. Near the absorption limits their transmittance is greatly affected by thickness. Therefore, in evaluating the I.R. transmittance it is desirable to define the actual thickness of material used in obtaining the spectral transmission scans. For example, a material having a transmittance of 30% at 8 microns with a 4mm thickness, may have a transmittance near 10% for a 12 mm thickness. With this in mind the thicknesses of the infrared materials used in these tests were carefully measured before carrying out the transmission scans shown in Fig. 125.

The transmittance measurements (which include losses due to reflection at the surfaces) were made using a Perkin-Elmer Model 621 spectrophotometer. Spectral reflection reducing coatings are available for infrared materials which increase the transmission substantially. These coatings are at least a thousand Angstroms in thickness and when sufficiently thick can offer significant protection in reducing the surface damage of infrared materials due to rain drop impacts.

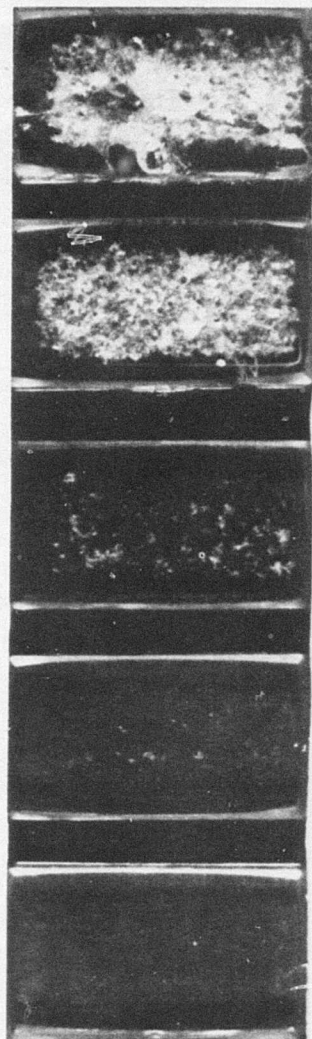
The general nature of the erosion damage for the specimens of the glasses and organic polymers listed in Section I can be seen in Fig. 126-132. The overall features and microscopic details of the erosion process for each material has been described in Section III.

Comparative mass losses for these materials are shown in Fig. 133 for the glass specimens and in Fig. 134 for the organic polymers. Each mass loss measurement recorded represents a different specimen; it is therefore possible that some variation in the shape of the mass-loss curves and the magnitude of the mass loss can be expected if additional specimens were tested. Such variations arise due to the initial condition of the surface of the specimen and the corresponding number of sites nucleated on a specimen's surface which contribute to large-scale material removal. The curves provided in Fig. 133 and 134





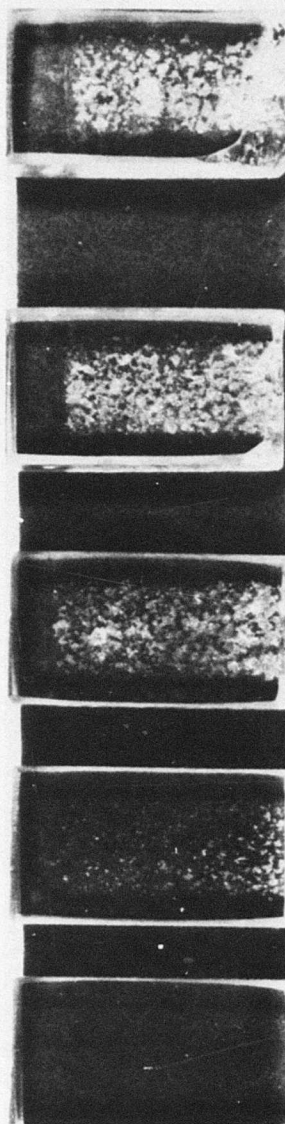
Rain Erosion Tests  
 1 Inch/hr Rainfall - 1.8 mm Drop Size  
 730 ft/sec (500 mph)



Specimen No.	SN-1	SN-2	SN-3	SN-4	SN-5
Time of Exposure, min	0	2	4	5	6
Mass Loss, Milligrams	0	3	15	282	Fractured Large Pieces

Figure 126. Rain Erosion of Annealed Soda Lime Glass

Rain Erosion Tests  
1 Inch/hr Rainfall - 1.8 mm Drop Size  
730 ft/sec (500 mph)

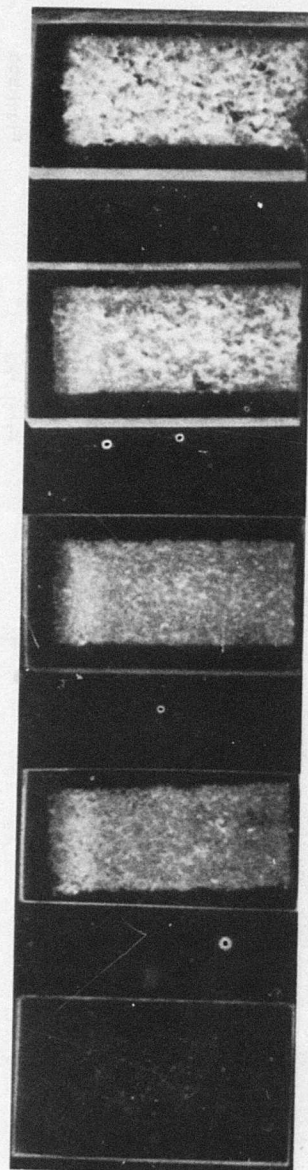


Specimen No.	SLT-1	SLT-2	SLT-3	SLT-4	SLT-5
Time of Exposure, Minutes	4	6	8	10	12
Mass Loss,	0	6	24	Fractured and Chipped	Fractured and Chipped

Figure 127. Rain Erosion of Tempered Soda Lime Glass



Rain Erosion Tests  
 1 Inch/hr Rainfall - 1.8 mm Drop Size  
 730 ft/sec (500 mph)

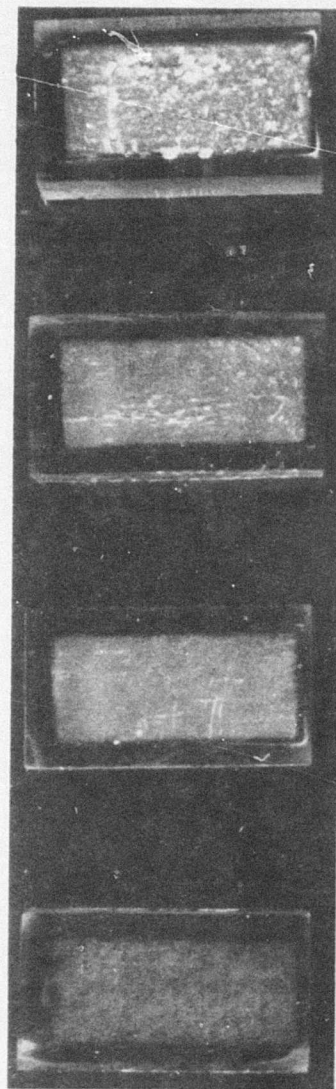


Specimen No.	Time of Exposure, Minutes	Mass Loss, Milligrams
PM 1	0.5	4
PM 2	1.0	16
PM 3	1.5	34
PM 4	2	79
PM 5	2.5	227

Figure 128. Rain Erosion of Polymethylmethacrylate



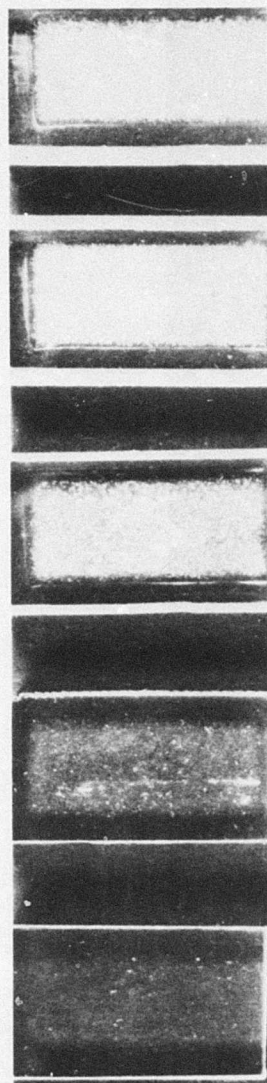
Rain Erosion Tests  
 1 Inch/hr Rainfall - 1.8 mm Drop Size  
 730 ft/sec (500 mph)



Specimen No.	PS 1	PS 2	PS 3	PS 4
Time of Exposure, Minutes	2	4	6	8
Mass Loss, Milligrams	0	6	42	86

Figure 129. Rain Erosion of Polysulfone

Rain Erosion Tests  
 1 Inch/hr Rainfall - 1.8 mm Drop Test  
 730 ft/sec (500 mph)

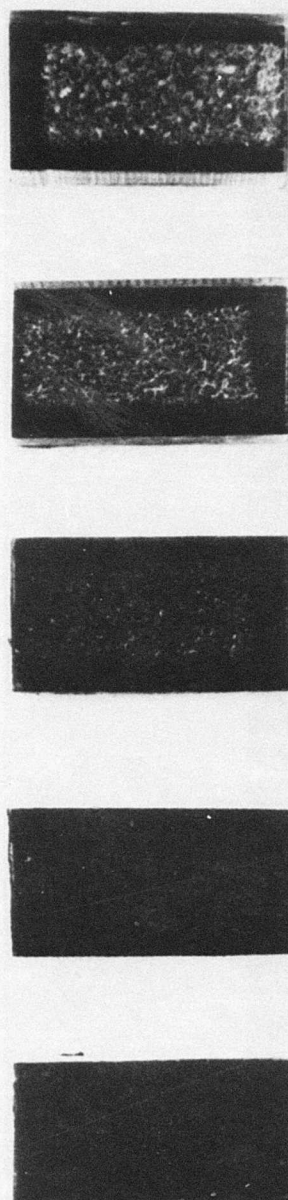


Specimen No.	UL-1	UL-2	UL-3	UL-4	UL-5
Time of Exposure, Minutes	2	4	6	8	10
Mass Loss, Milligrams	3	6	25	58	93

Figure 130. Rain Erosion of Polycarbonate



Rain Erosion Tests  
1 Inch/hr Rainfall - 1.8 mm Drop Size  
730 ft/sec (500 mph),

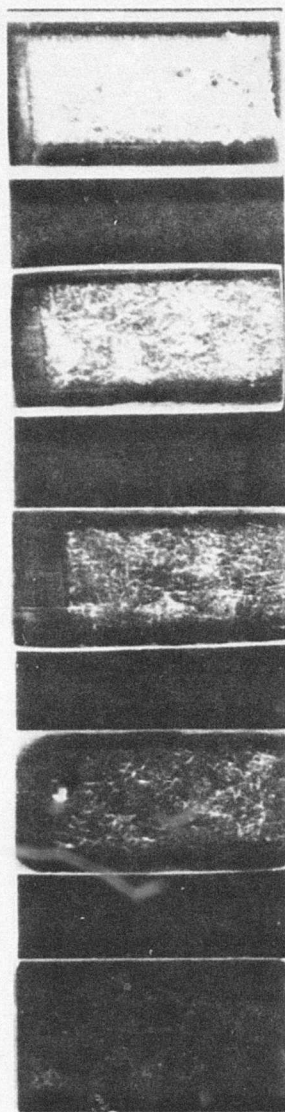


Specimen No.	L-1	L-2	L-3	L-4	L-5
Time of Exposure, Minutes	2	4	6	8	12
Mass Loss, Milligrams	5	10	28	62	134

Figure 131. Rain Erosion of Coated Polycarbonate



1 Inch/hr Rainfall - 1.8 mm Drop Size  
730 ft/sec (500 mph)



Specimen No.	N-1	N-2	N-3	N-4	N-5
Time of Exposure, Minutes	2	3	4	6	8
Mass Loss, Milligrams	0	2	18	24	173

Figure 132. Rain Erosion of Nylon

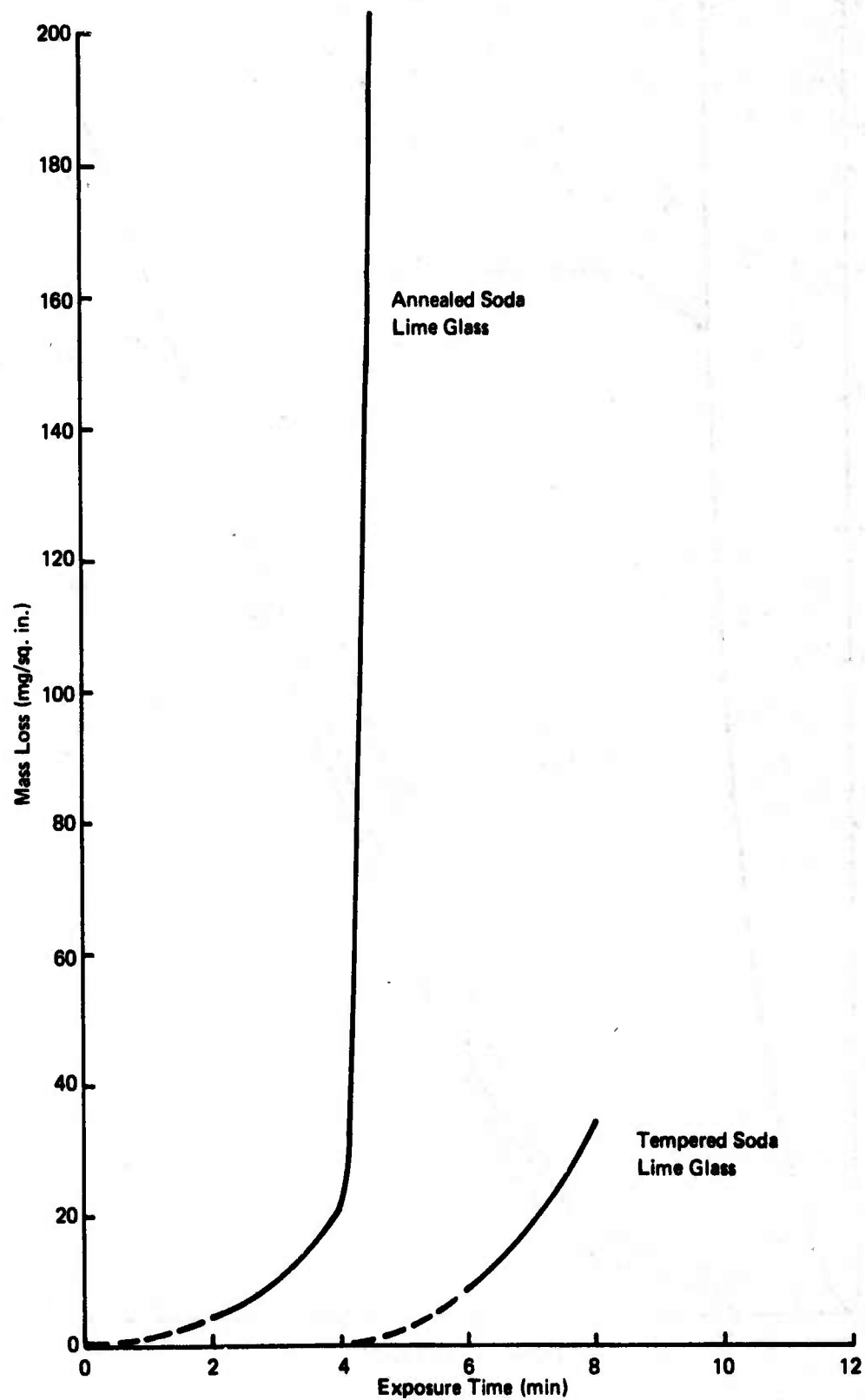


Figure 133. Mass Loss as a Function of Exposure Time for Soda Lime Glass

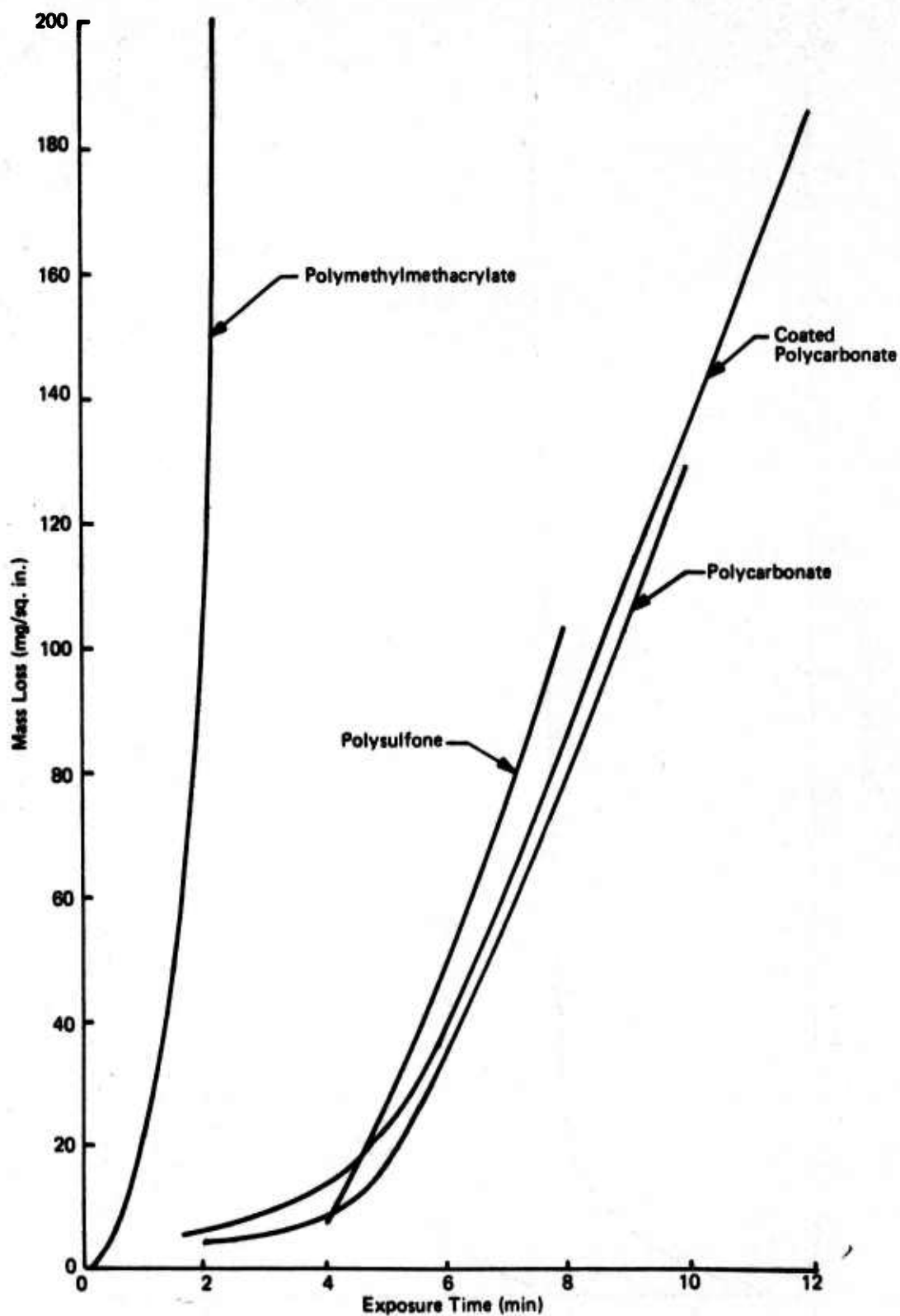


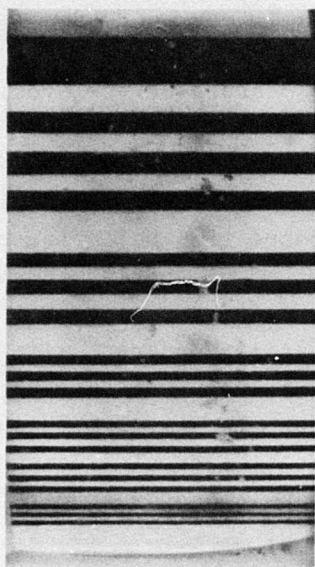
Figure 134. Mass Loss as a Function of Exposure Time for Polymeric Materials



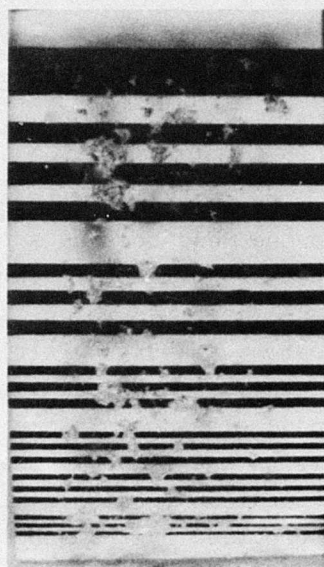
are only intended to provide a relative measure of the erosion resistance of the materials tested.

In the case of the transparent materials evaluated it is not the mass loss as a function of exposure time which is the important parameter, but the degradation of visibility through these materials which is of major concern. The effect of the erosion damage on visibility through these transparent materials is assessed by viewing a bar type resolution target through the eroded glass or plastic specimens as shown in Fig. 135 through 141. A quantitative measure of the effect of erosion damage on the transmission of light through these transparent materials is provided by the spectral scans taken with a Model 14 Cary Recording Spectrophotometer over the visible and near infrared range of the electromagnetic spectrum. The scans recorded in Fig. 142 through 148 show the loss in transmittance of radiation over wavelengths from 0.5 to 2.1 microns as a function of exposure to the rain erosion environment. The specimen designations with suffix zero denote uneroded specimens of the material; the other suffixes on specimen designations correlate with the specimens shown in Fig. 126 to 132.

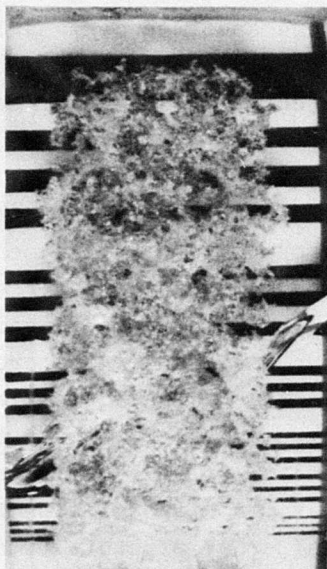
The following trends can be observed between mass loss and light transmittance. The transmittance curves for soda lime glass in Fig. 142 and 143 show that tempering reduces the transmittance by less than four percent compared with annealed soda lime glass, however there is a tremendous increase in the erosion resistance of the tempered compared to the annealed soda lime glass as seen in Fig. 133. Light transmission through the tempered glass is only reduced by 20 percent after a 6 minute exposure to the rain environment; whereas, the transmission is essentially zero in the annealed glass after an exposure time of 5 minutes. The curves in Fig. 142 and 143 show that the erosion damage degrades the transmittance at all wavelengths within the range from 0.5 to 2.1 microns to the same degree. It is concluded that tempering has a negligible effect on the light transmission characteristics of the soda lime glass, but



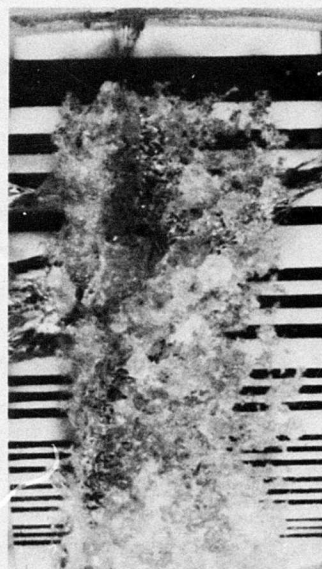
(a) Specimen SN-2: 2 min Exposure



(b) Specimen SN-3: 4 min Exposure



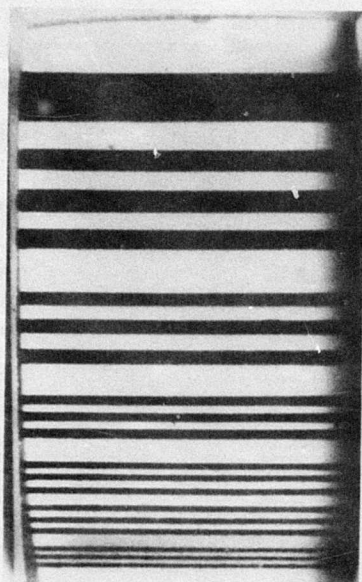
(c) Specimen SN-4: 5 min Exposure



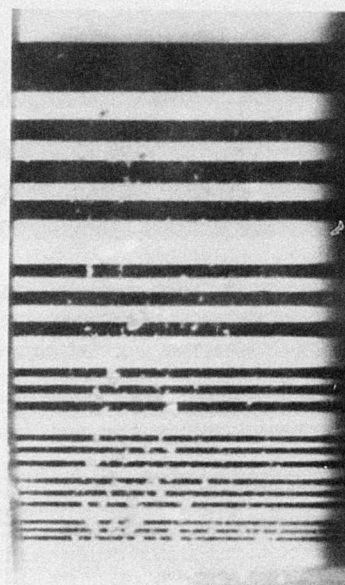
(d) Specimen SN-5: 6 min Exposure

Figure 135. Resolution Pattern Viewed Through Eroded Specimens of Annealed Soda Lime Glass

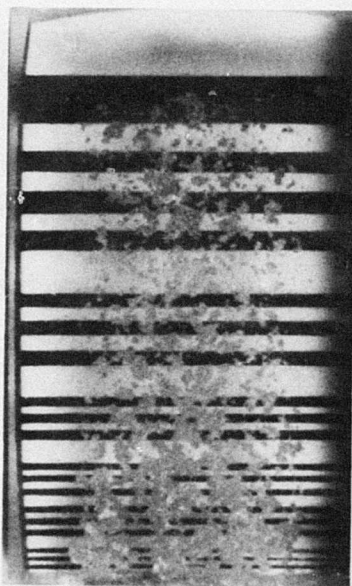




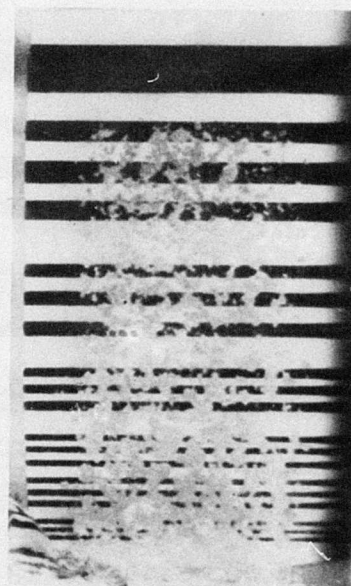
(a) Specimen SLT-1: 4 min Exposure



(b) Specimen SLT-2: 6 min Exposure



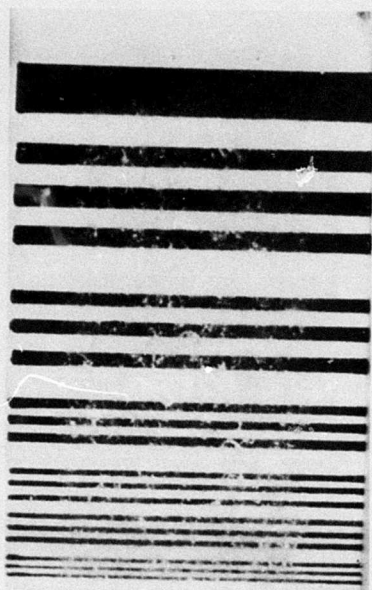
(c) Specimen SLT-3: 8 min Exposure



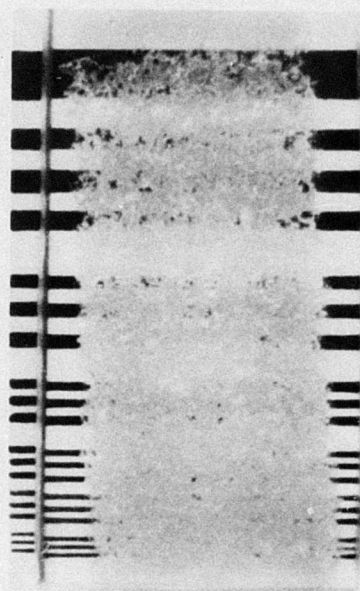
(d) Specimen SLT-4: 10 min Exposure

Figure 136. Resolution Pattern Viewed Through Eroded Specimens of Tempered Soda Lime Glass

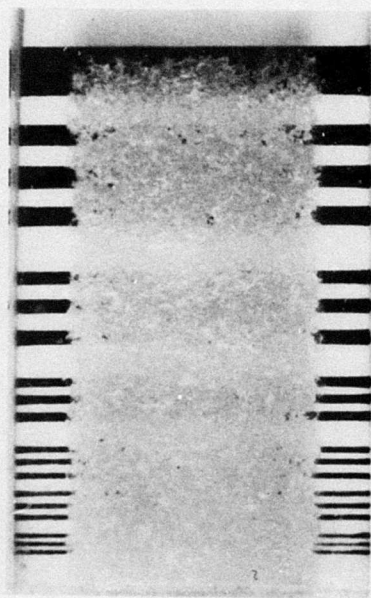




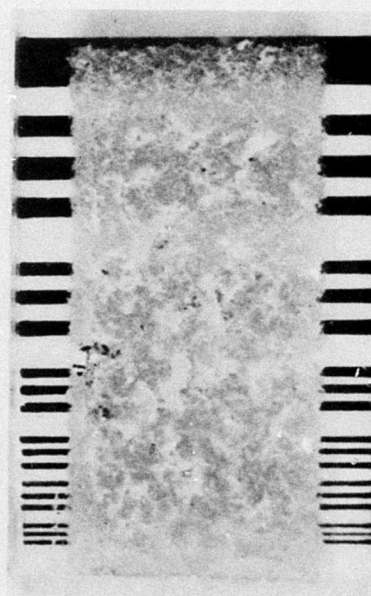
(a) Specimen PM-1: 0.5 min Exposure



(b) Specimen PM-2: 1.0 min Exposure

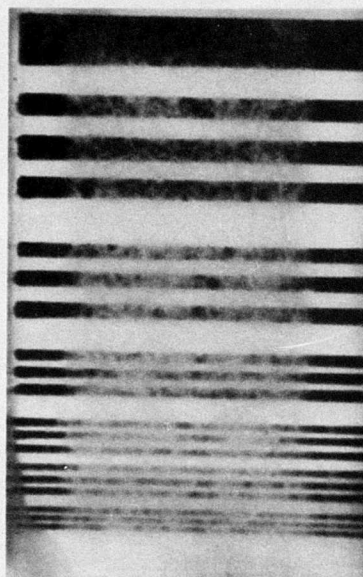


(c) Specimen PM-3: 1.5 min Exposure

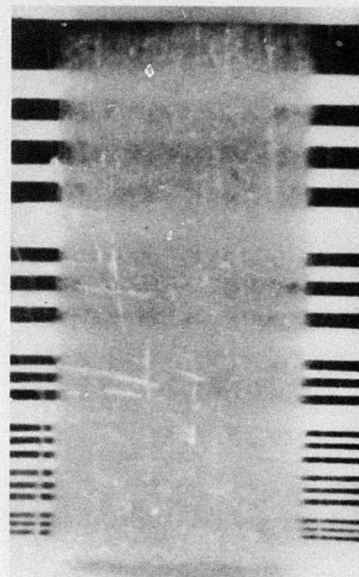


(d) Specimen PM-4: 2.0 min Exposure

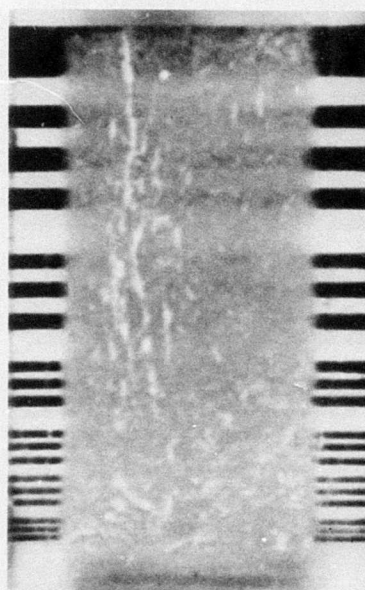
Figure 137. Resolution Pattern Viewed Through Eroded Specimens of Polymethylmethacrylate



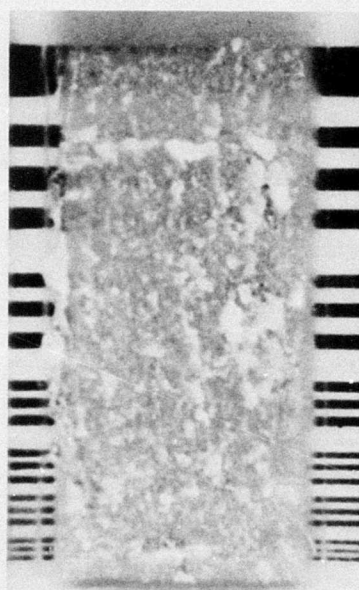
(a) Specimen PS-1: 2 min Exposure



(b) Specimen PS-2: 4 min Exposure



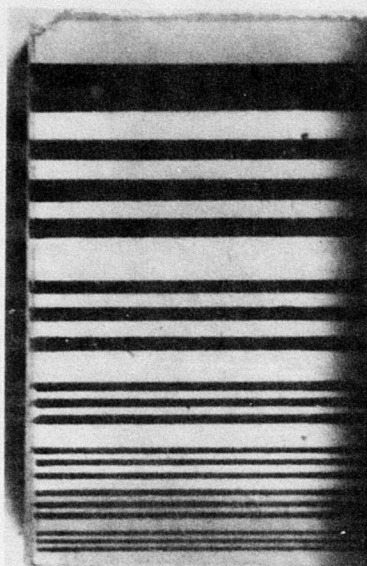
(c) Specimen PS-3: 6 min Exposure



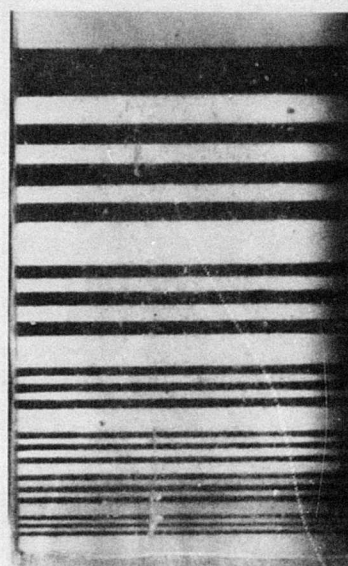
(d) Specimen PS-4: 8 min Exposure

Figure 138. Resolution Pattern View Through Eroded Specimens of Polysulfone

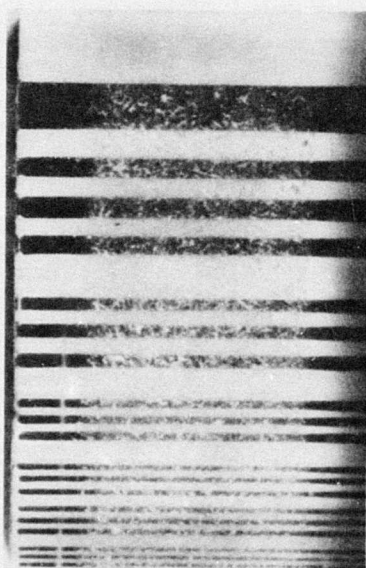




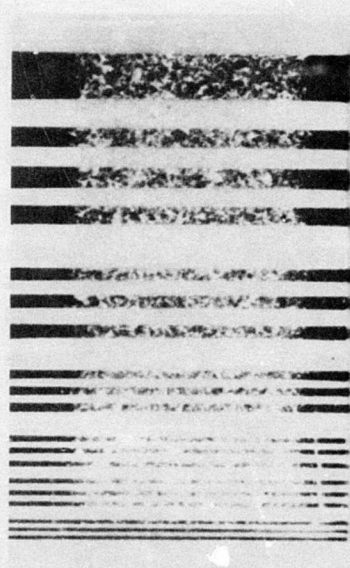
(a) Specimen UL-1 2 min Exposure



(b) Specimen UL-2 4 min Exposure



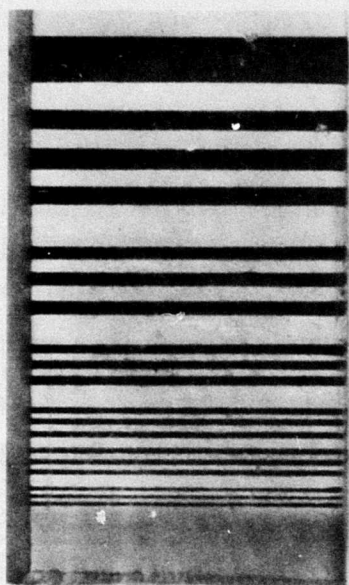
(c) Specimen UL-3 6 min Exposure



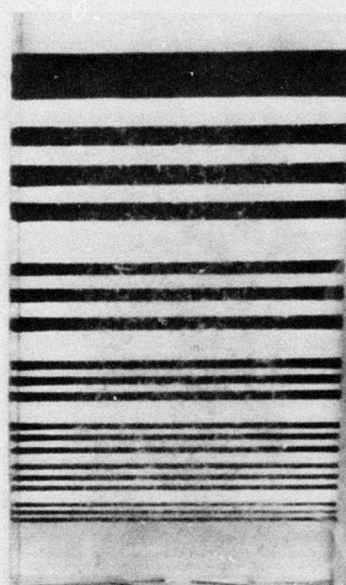
(d) Specimen UL-4 8 min Exposure

Figure 139. Resolution Pattern Viewed Through Eroded Specimens of Polycarbonate

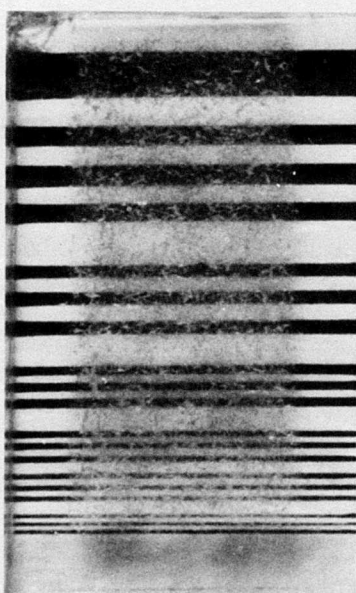




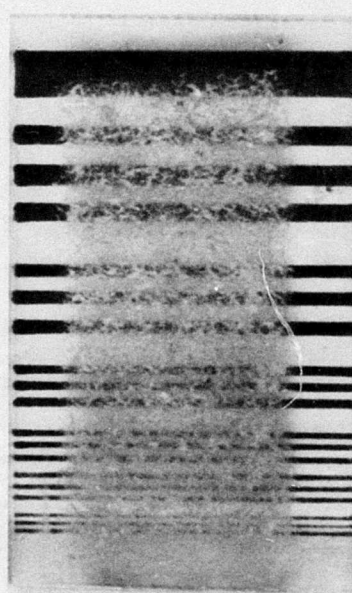
(a) Specimen L-1: 2 min Exposure



(b) Specimen L-2: 4 min Exposure

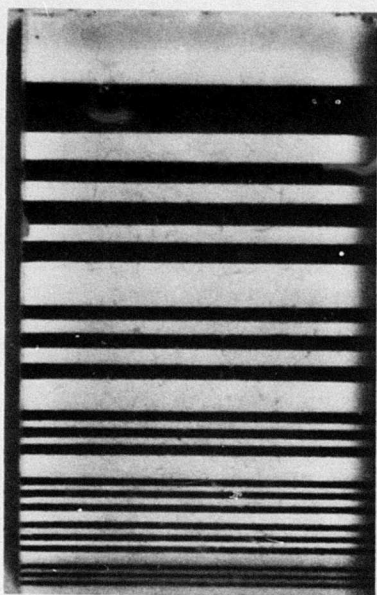


(c) Specimen L-3: 6 min Exposure

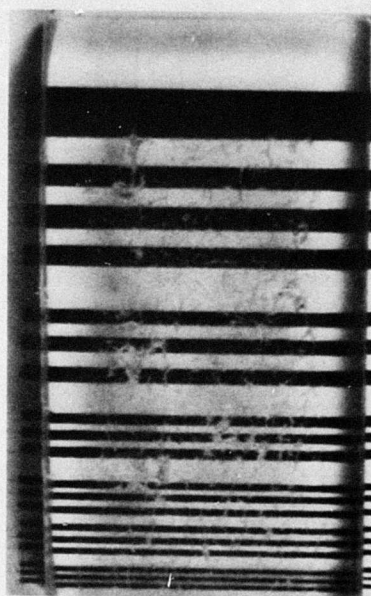


(d) Specimen L-4: 8 min Exposure

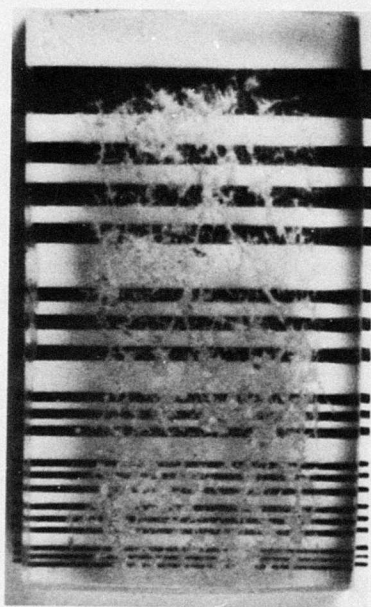
Figure 140. Resolution Pattern Viewed Through Eroded Specimens of Coated Polycarbonate



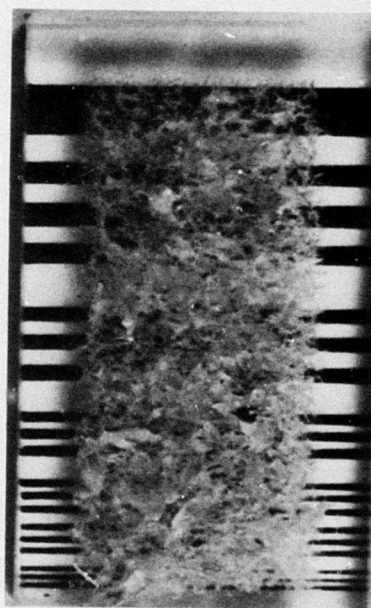
(a) Specimen N-1: 2 min Exposure



(b) Specimen N-3: 4 min Exposure



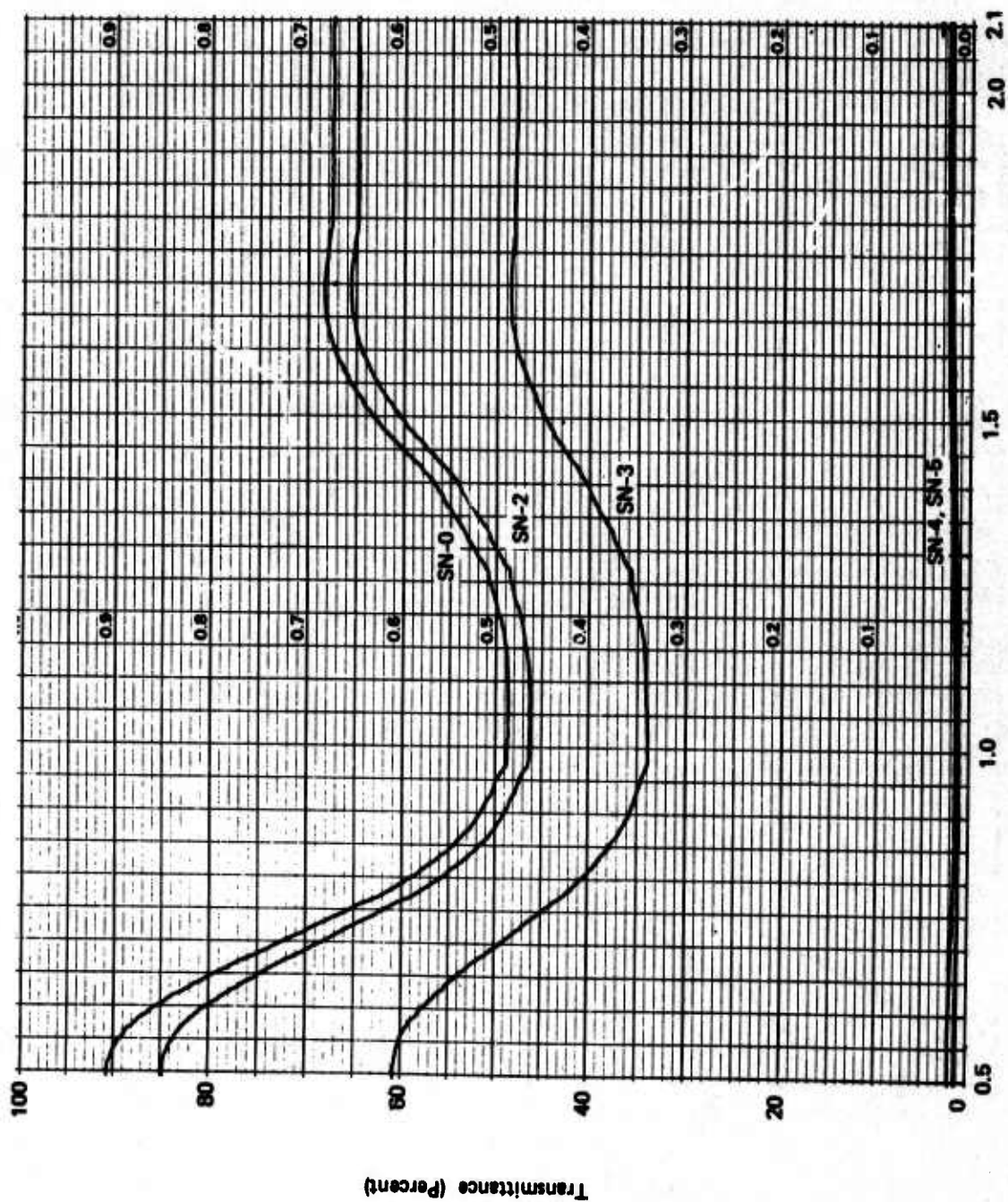
(c) Specimen N-4: 6 min Exposure



(d) Specimen N-5: 8 min Exposure

Figure 141. Resolution Pattern Viewed Through Eroded Specimens of Nylon





Wavelength in Microns

Figure 142. Spectral Transmittance of Annealed Soda Lime Glass



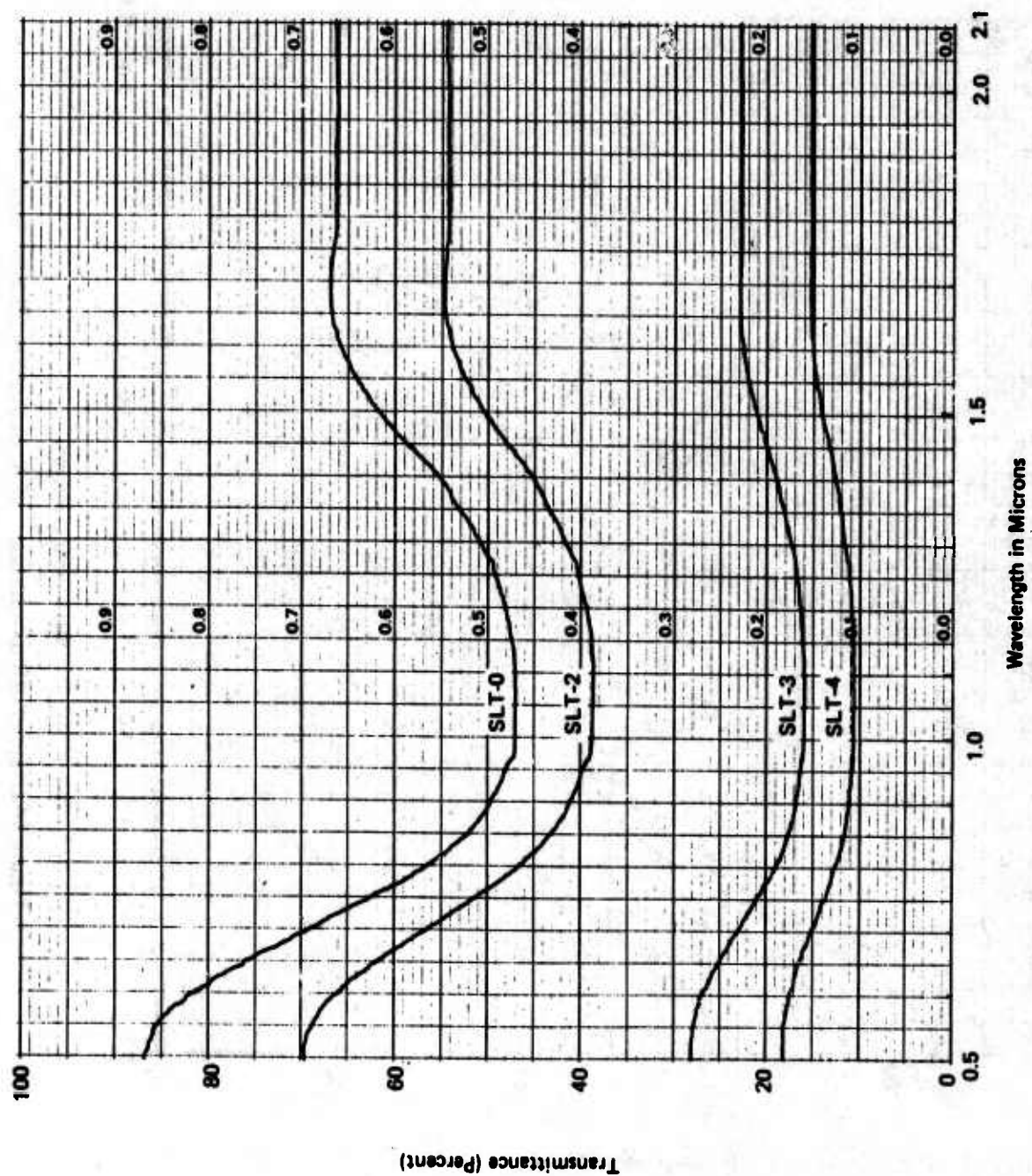


Figure 143. Spectral Transmittance of Tempered Soda Lime Glass

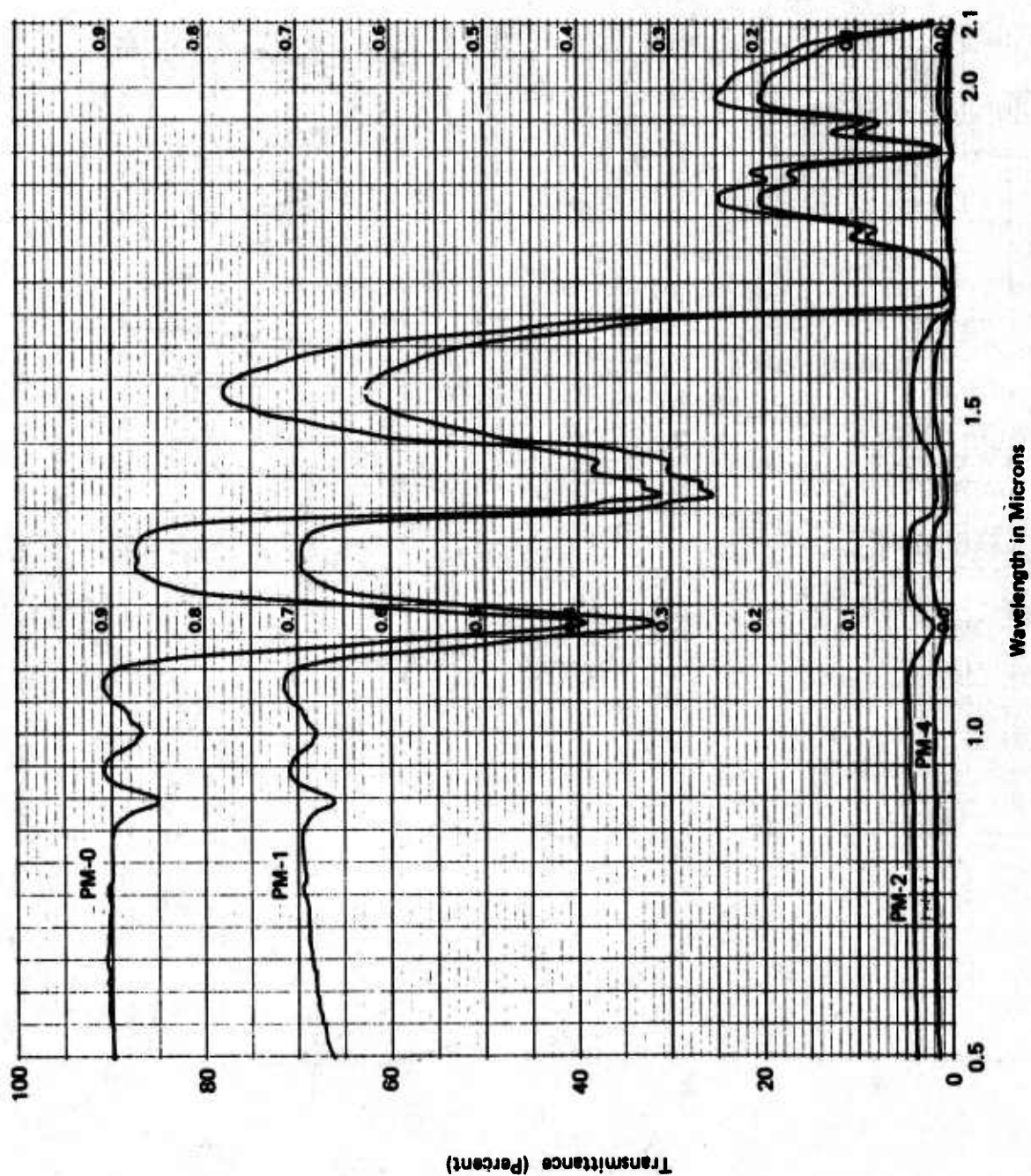


Figure 144. Spectral Transmittance of Polymethylmethacrylate

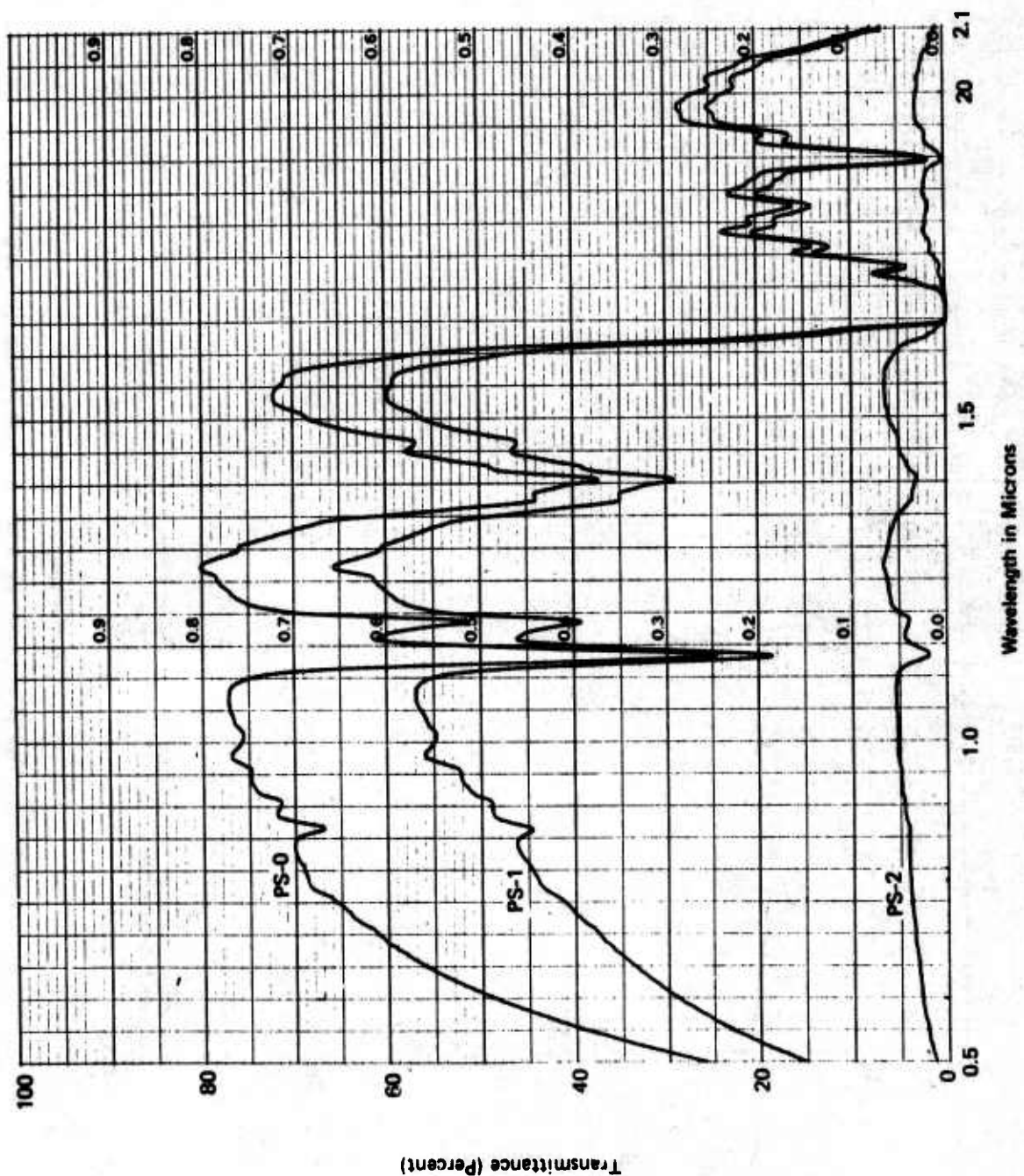


Figure 145. Spectral Transmittance of Polysulfone



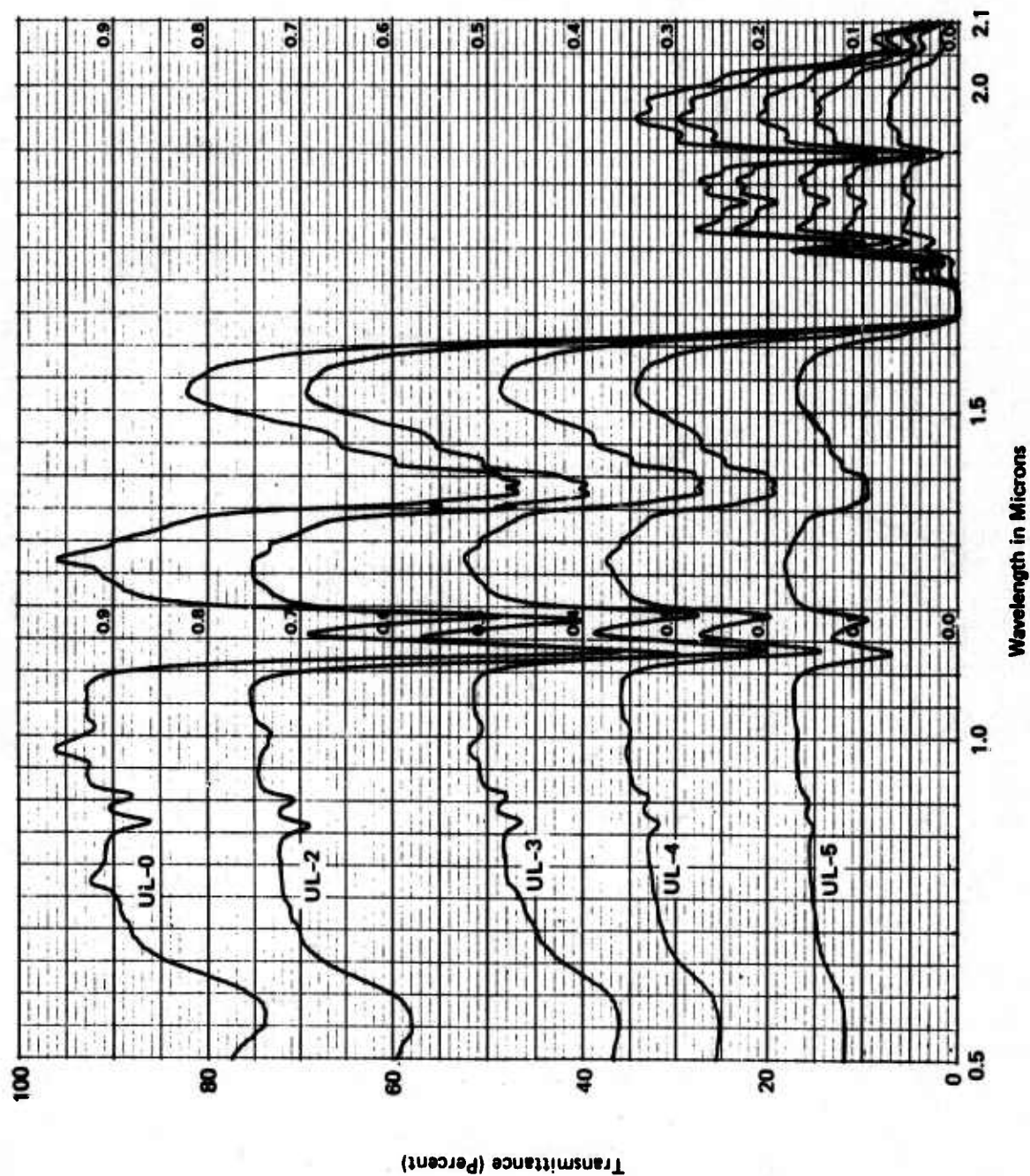


Figure 146. Spectral Transmittance of Polycarbonate

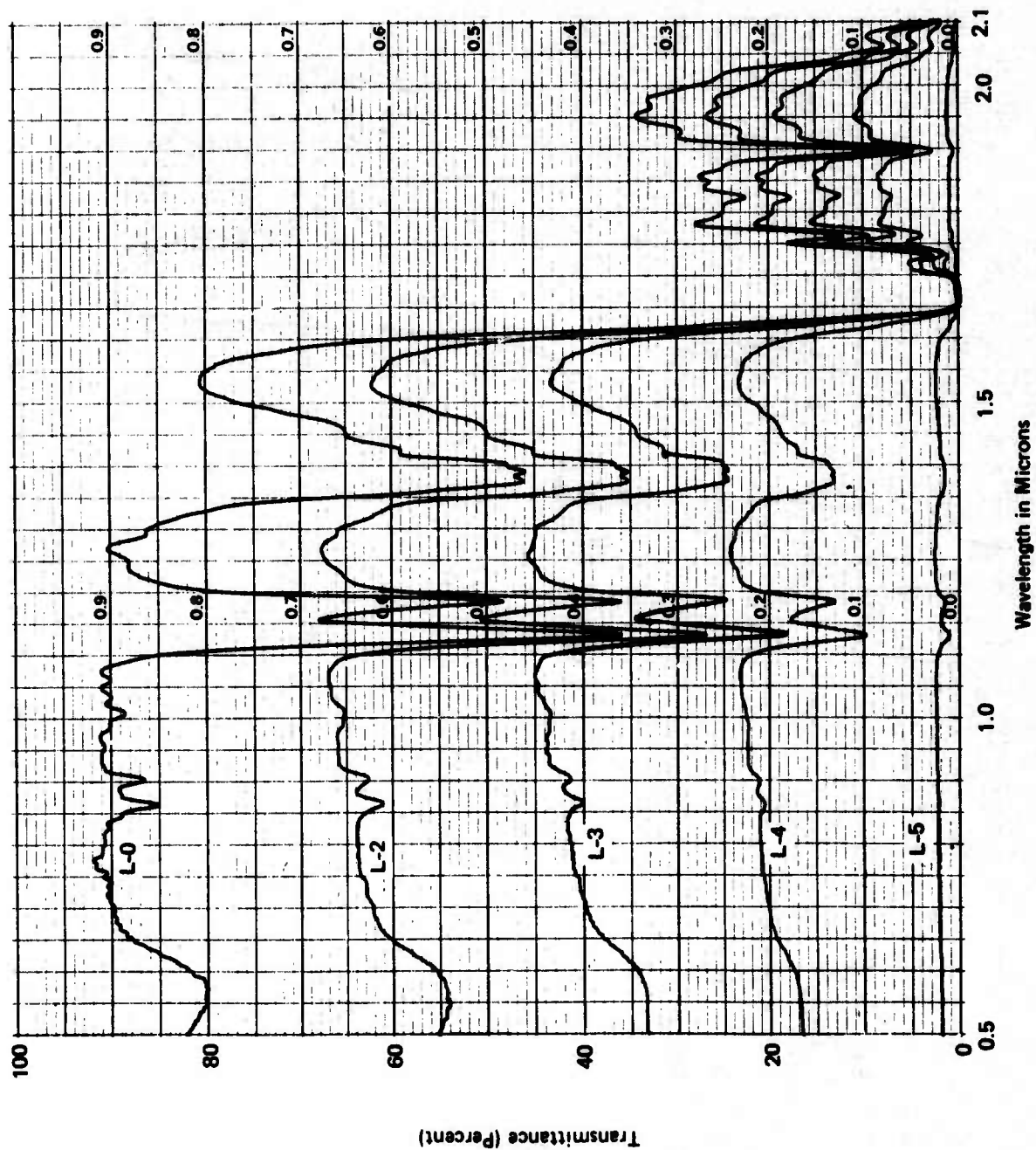


Figure 147. Spectral Transmittance of Coated Polycarbonate

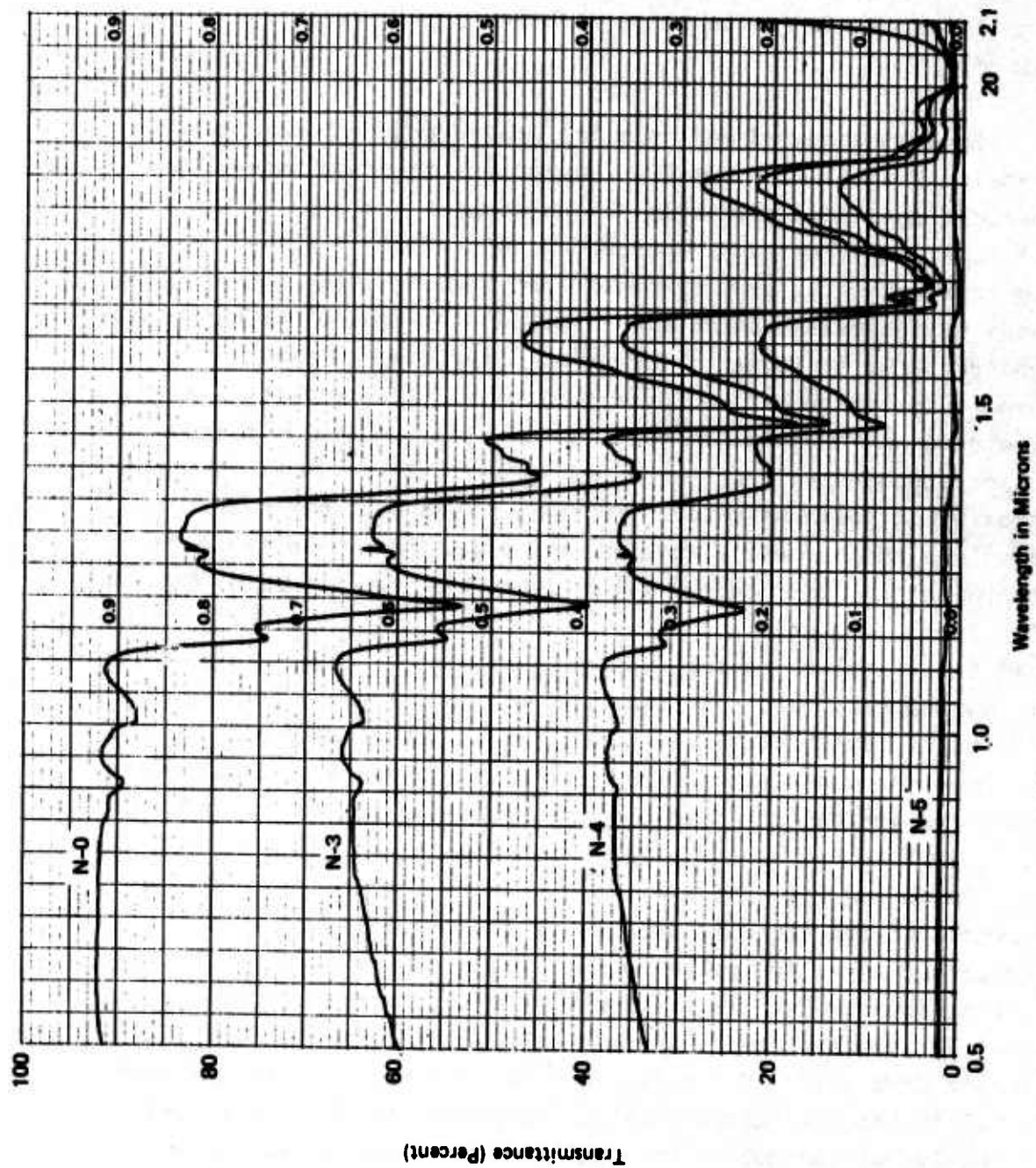


Figure 148. Spectral Transmittance of Nylon



greatly improves the erosion resistance and correspondingly the length of the exposure to the rain environment during which a high level of transmittance of electromagnetic radiation is maintained.

Both an uncoated and melamine coated polycarbonate were tested. The melamine coating reduced the transmittance of the uneroded specimens primarily in the wavelengths ranging from 0.7 to 1.3 microns by 5.0 percent with negligible effect on the higher wavelengths as determined from Fig. 145 and 146. On the basis of the mass-loss data in Fig. 134 the coated polycarbonate appears to have slightly less erosion resistance than the uncoated polycarbonate. Correspondingly, the transmittance of electromagnetic radiation through the eroded melamine coated polycarbonate specimens generally was 10 percent lower than the uncoated polycarbonate for comparable exposure times. For both materials the percent reduction in transmittance was found to be greatest at the lower wavelengths and decreased uniformly with increasing wavelength. From these tests it must be concluded that the melamine coating does not improve the erosion resistance of the polycarbonate substrate and actually appears to contribute to an accelerated rate of scatter. The microscopic details of the erosion process for the coated and uncoated polycarbonate specimens are described in Section III.A.

Comparing Fig. 145 and 147 the general features (peaks and valleys) of the transmittance curve for polysulfone are quite similar to those for polycarbonate above a wavelength of 1.1 micron; however the transmittance of uneroded polysulfone is about 10 percent lower than polycarbonate for wavelengths ranging from 1.1 to 2.0 microns. The thickness of the specimens is 0.5 inches for both materials. As seen in Fig. 134 the rate of erosion of the polysulfone is somewhat higher than that measured for polycarbonate, however the transmittance curves in Fig. 147 for eroded specimens of polysulfone show that the transmittance is greatly reduced before a measurable mass loss occurs and is practically zero when the mass loss is still negligible.

Schmitt<sup>(71)</sup> has pointed out the difference in the transmission losses for polysulfone as compared to polycarbonate even though the mechanical properties for these two materials are comparable (refer to Table II). Schmitt's conclusion is based on an extensive series of rain erosion tests for impact velocities ranging from 585 to 880 fps. Microscopic details of the differences in the erosive response of polysulfone and polycarbonate in the very early stages of the erosion process are reported in Section III.A.

Polymethylmethacrylate eroded very rapidly (Fig. 134) and the transmittance was reduced to zero in less than one minute exposure to the rainfield. From the nylon specimens tested it is difficult to determine if the incubation period of the mass-loss curve (not shown in Fig. 134 due to the large variations in the measurements) is greater or less than that for polysulfone and polycarbonate. The percentage of transmittance for nylon deduced from Fig. 148 is slightly less than that measured for polycarbonate up to an exposure time of 6 minutes. The loss of transmittance in nylon at each exposure time is nearly uniform over the range of wavelengths.

#### B. INFLUENCE OF EROSION DAMAGE ON TRANSMISSION

In the current program at Bell, the transmittance of infrared radiation through progressively-eroded IR transmitting materials is measured with a Perkin-Elmer Model 621 spectrophotometer. The transmittance,  $T$ , of electromagnetic radiation is evaluated as a function of the wavelength of the incident beam. For a radiation absorbing material of thickness  $d$ ,

$$T = \frac{(1-r^2)e^{-ad}}{1-r^2e^{-2ad}} \quad (39)$$

where

$$r = \frac{(n-1)^2 + k}{(n+1)^2 + k} \quad (40)$$

is the reflectivity of the interface when radiation strikes the plane surface of the material at normal incidence in air and  $a$  is the absorption coefficient.

$$a = \frac{4\pi k}{\lambda n} \quad (41)$$

where  $k$  is the absorption constant,  $\lambda$  denotes the wavelength of the radiation, and  $n$  is the index of refraction.

Multiple water droplet impacts on zinc selenide and zinc sulfide, for example, over a velocity range which may have an upper limit in excess of Mach 1 will produce internal fracture facets within the material with only minor disruption of the surface, as described in Section III.B. Initially, sub-microscopic flaws will develop which may or may not have an effect on the infrared transmission. The complex network of internal fractures which subsequently develops should have a significant effect on the infrared transmittance. The expression in Eq. (39) would now have to include additional exponential terms representing scattering due to the erosion process. The internal scattering of the incident beam is generally taken into account as an additive factor to the absorption coefficient. This erosion scattering coefficient will be a function of the exposure time, the parameters characterizing the erosive environment, and the parameters characterizing the erosion behavior of the material. It would consist of two factors: the primary term resulting from reflection of radiation from the internal fracture interfaces and a second term resulting from absorption at crystal defects generated by the water drop impacts.



## V. INDENTATION EVALUATIONS

The small impacting particles sample very small domains on the surface of a material specimen exposed to an erosive environment. The indentation test is most representative of these conditions. The Hertzian fracture test can be used to determine the relative fracture toughness of the near-surface material, the densities of surface flaw size, and the residual stresses in the near-surface material.<sup>(72)</sup> The Hertzian fracture test is sensitive to small changes in fracture toughness and the magnitude of favorable residual stress states introduced by thermal or chemical processes. With a significant cost factor governing the number of specimens which can be tested to provide fracture data, the Hertzian fracture test procedures permit a number of tests to be performed on the surface of a relatively small specimen.

Ring fracture initiation due to quasistatic loading by solid spherical indenters was measured for several of the glasses listed in Table 3. The experimental arrangement for ring fracture measurements is shown in Fig. 149. The specimen is loaded by a very small glass bead ranging in diameter from 150 to 550 $\mu\text{m}$  or a sapphire bead ranging in size from 400 $\mu\text{m}$  to 3200 $\mu\text{m}$ . The sapphire spheres are used for the harder glasses to reduce the fracturing of the spherical indenter during loading.

Johnson, et.al.<sup>(73)</sup> showed that a more rigid indenter than the test surface gives an increase in fracture strength of the material, and a less rigid indenter has the opposite effect. If the elastic modulus of the indenter is different from that of the test material frictional forces are brought into play at the interface which modify the Hertzian contact stresses. Static and dynamic tests on glass plates showed a consistent increase in the apparent fracture stress of about 50 percent using spherical steel indenters compared with glass indenters.

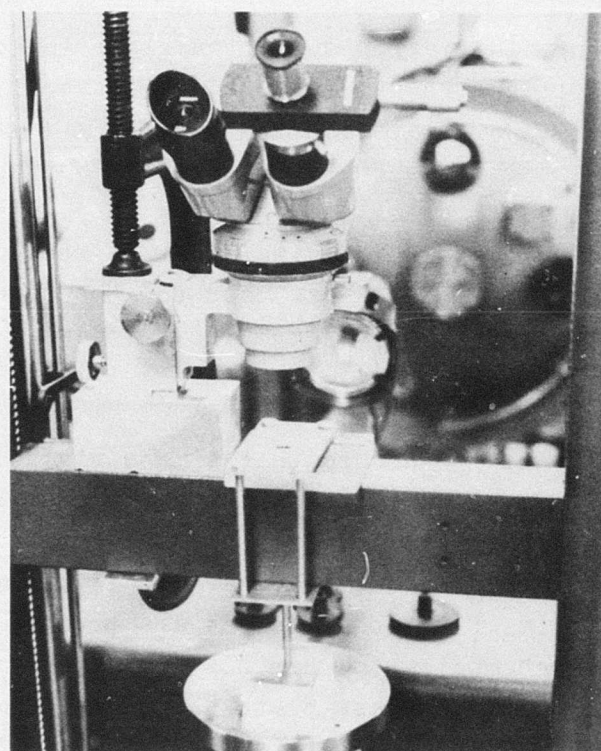
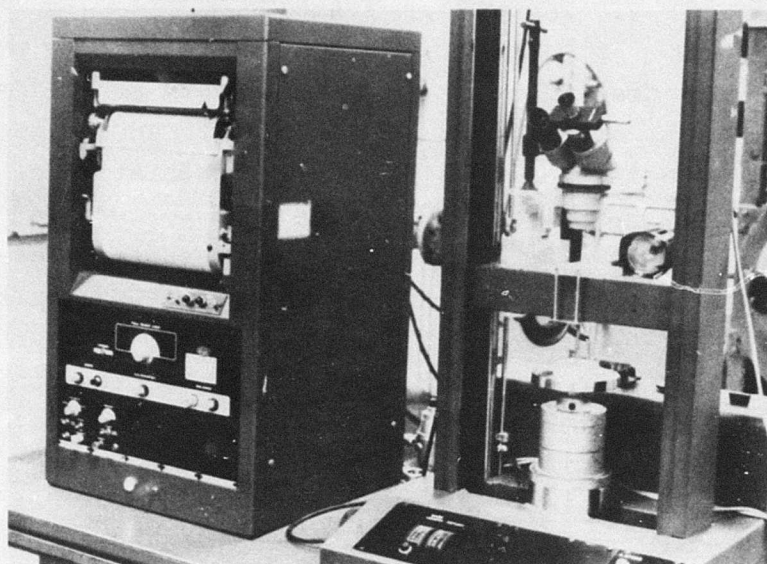


Figure 149. Experimental Arrangement for Indentation Test Evaluations

Static indentation tests were also carried out on sapphire using a steel ball and a tungsten carbide ball. A 50 percent increase in the fracture stresses was found for the tungsten carbide over the steel ball: the Young's modulus for tungsten carbide is more than three times the value for steel. These results are consistent with the influence of the frictional stress on the magnitude of the tensile radial stress component and further confirms that a more compliant indenter reduces the contact stress at fracture while a more rigid one increases it. In view of these results the quasistatic loading conditions for fused silica and borosilicate glass were identical to those used for the investigation of the erosion process due to multiple glass bead impacts. (5-8)

The experimental procedure involved viewing the contact of the sphere against the specimen from the base side of the transparent specimen with a microscope. Oblique illumination was used to aid in the observation of a ring fracture. The specimen is loaded at a moderate rate. When a ring fracture is observed to develop, the loading is stopped, the load level recorded, and the diameter of the ring fracture is measured with the filar micrometer eyepiece at a magnification of 40X. A new location on the surface of the specimen at least three bead diameters from the previous site is used for the next loading. Fifty tests are carried out for each loading condition.

The histograms in Fig. 150 show some of the data for fused silica. The corresponding cumulative distribution curves are shown in Fig. 151 for the applied loads and in Fig. 152 for the ring fracture diameters. The 50 percent probability values of the fracture load and ring fracture diameter can be obtained from these curves for each loading condition.

The average values of the fracture loads and ring fracture diameters for several of the glasses listed in Table 3 are tabulated in Table 11. Significant differences are evident in the magnitude of the applied load required to produce a ring



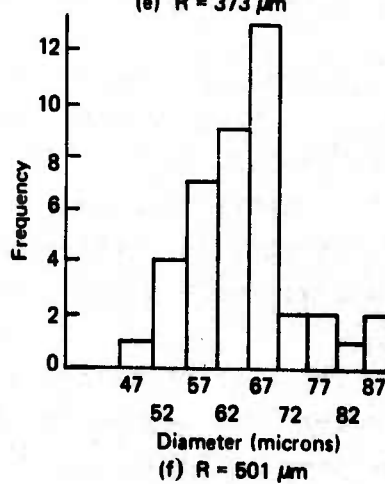
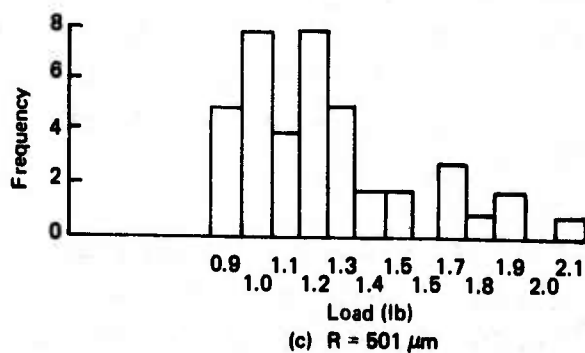
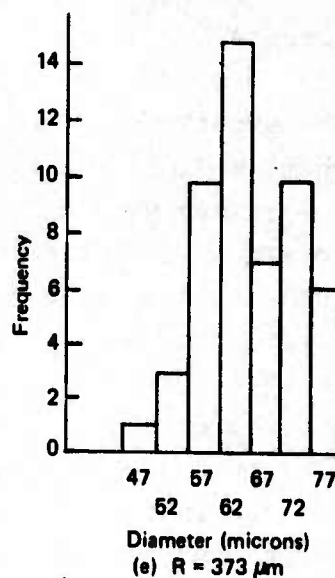
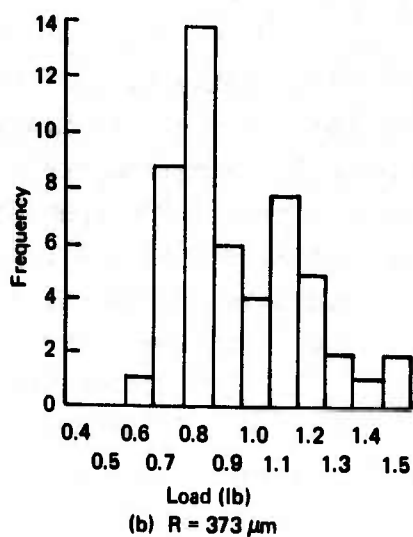
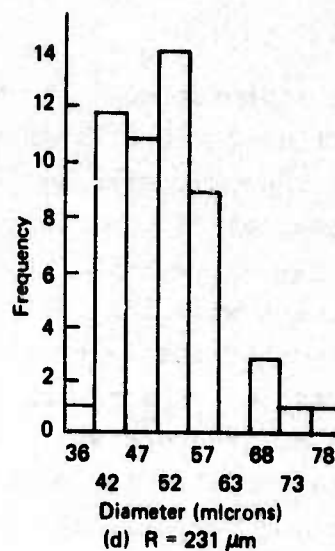
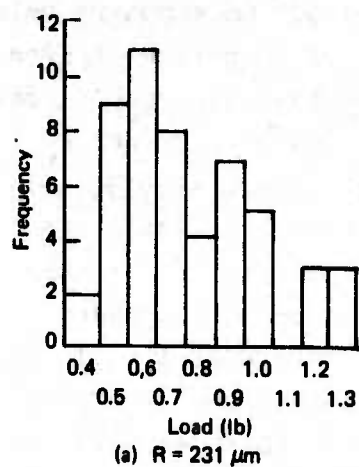


Figure 150. Fracture Loads and Ring Fracture Diameters for Fused Silica

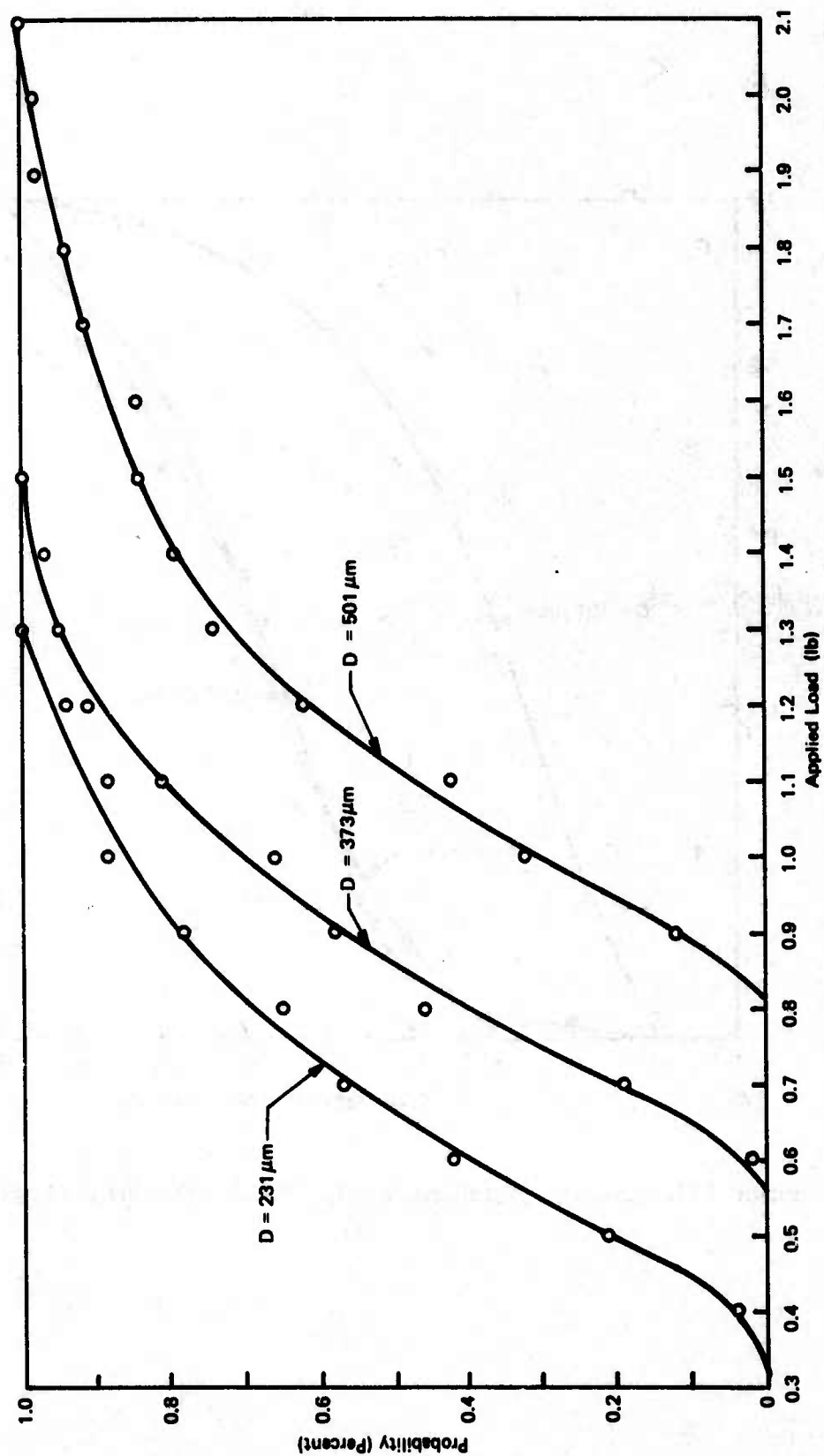


Figure 151. Cumulative Distribution for Indenter Loads for Ring Fracture Initiation in Fused Silica

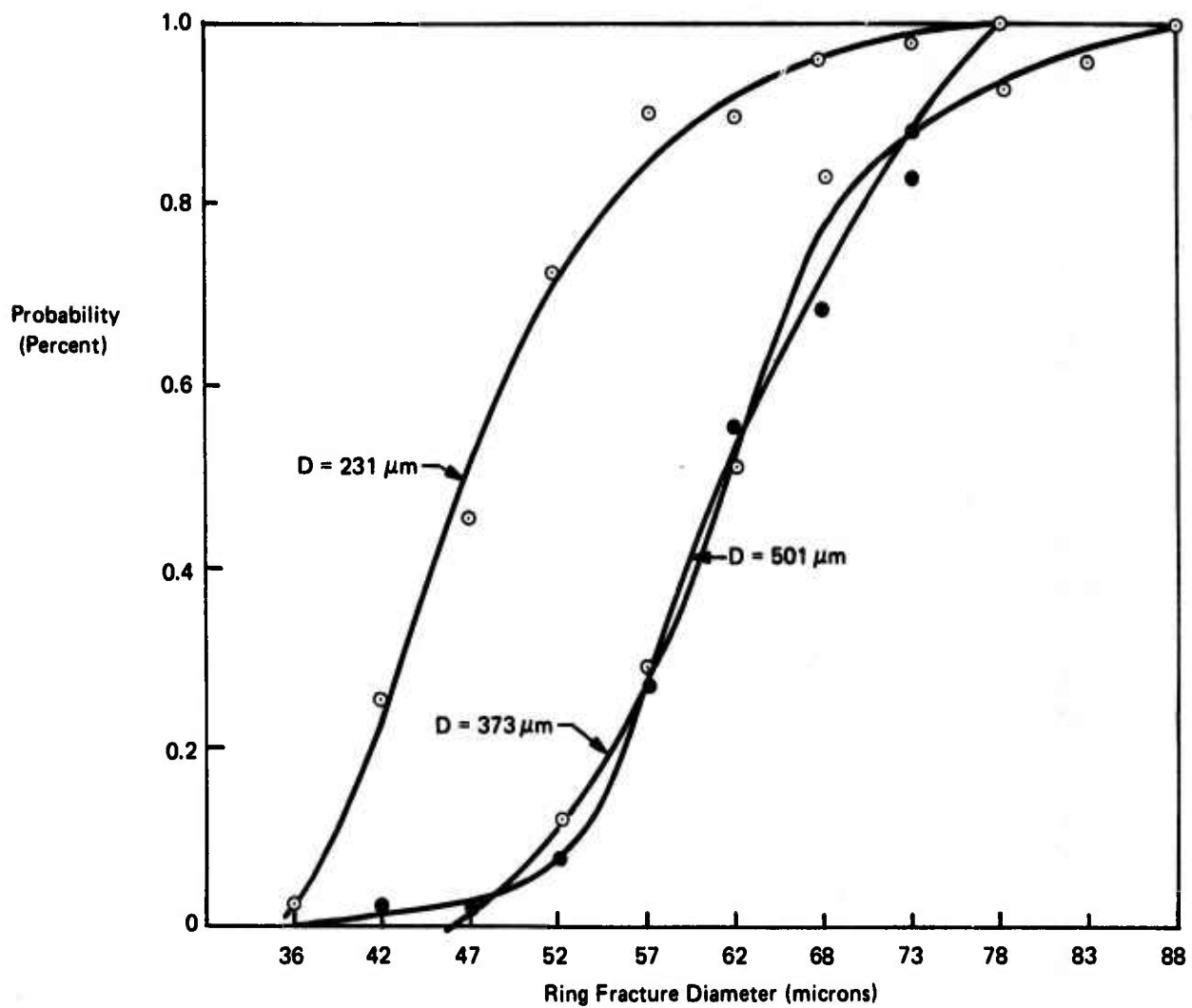


Figure 152. Cumulative Distribution for Ring Fracture Diameters in Fused Silica



TABLE 11  
AVERAGE VALUES OF FRACTURE LOADS AND RING DIAMETERS

<u>Glass</u>	<u>Indenter</u>	<u>Fracture Load (lb.)</u>	<u>Ring Fracture Diameter (<math>\mu</math>m)</u>
Fused Silica	501 $\mu$ m glass	1.26	64.8
	373 $\mu$ m glass	0.95	64.8
	305 $\mu$ m glass	.90	59.7
	231 $\mu$ m glass	.76	51.0
Borosilicate	539 $\mu$ m glass	2.60	109.5
	415 $\mu$ m glass	2.10	96.0
	286 $\mu$ m glass	1.75	78.0
	210 $\mu$ m glass	1.10	62.0
	148 $\mu$ m glass	0.66	41.1
Soda Lime (annealed)	410 $\mu$ m sapphire	3.83	80.6
Soda Lime (tempered)	410 $\mu$ m sapphire	5.60	98.4
Cortran	410 $\mu$ m sapphire	7.30	119.2
Chemcor ,	410 $\mu$ m sapphire	8.20	102.6

fracture in the various glasses. The glasses in Table 11 can be ranked according to their resistance to ring fracture formation in terms of the average applied load. The ranking indicated in Table 11 would be Chemcor, Cortran, soda lime tempered, soda lime annealed, borosilicate, and fused silica. This ranking does not correspond to that obtained from the fracture stress evaluated from bend tests<sup>(53)</sup> recorded in Table 3. The fracture behavior due to the localized loading is definitely different than that observed in conjunction with more conventional fracture evaluation procedures.

Quasistatic indentation measurements were made using 135 and 290 micron diameter glass beads impressing specimens of borosilicate glass and fused silica from the same lots used in the impact tests. The glass beads were also identical to those used in the erosion evaluations. The load required for ring fracture initiation was recorded along with the diameter of the ring fracture. Fifty runs were made for each test condition and the average value of the ring fracture diameter is plotted in Fig. 153 for the 290 micron glass bead.

Using Eq.(21) and the load when the fracture initiates, the quasistatic value of the contact radius can be determined from Hertz's theory. Substituting Eq.(25) into Eq.(21) provides the Hertzian relation plotted in Fig. 153 between the contact radius and the impact velocity for a 290 micron glass bead over a range of impact velocities. The measured ring fracture diameters for borosilicate glass and fused silica are also plotted in Fig. 153 for the dynamic loading conditions. The threshold for damage initiation under impact conditions can be evaluated from the static loading. The experimental results for borosilicate glass indicate that the threshold is somewhat higher than that determined from Eq.(21) and (25).

The tendency for multiple ring fracture formation is clearly indicated in Fig. 153. Multiple ring fractures predominate for fused silica at 200 and 300 fps with the outer ring forming

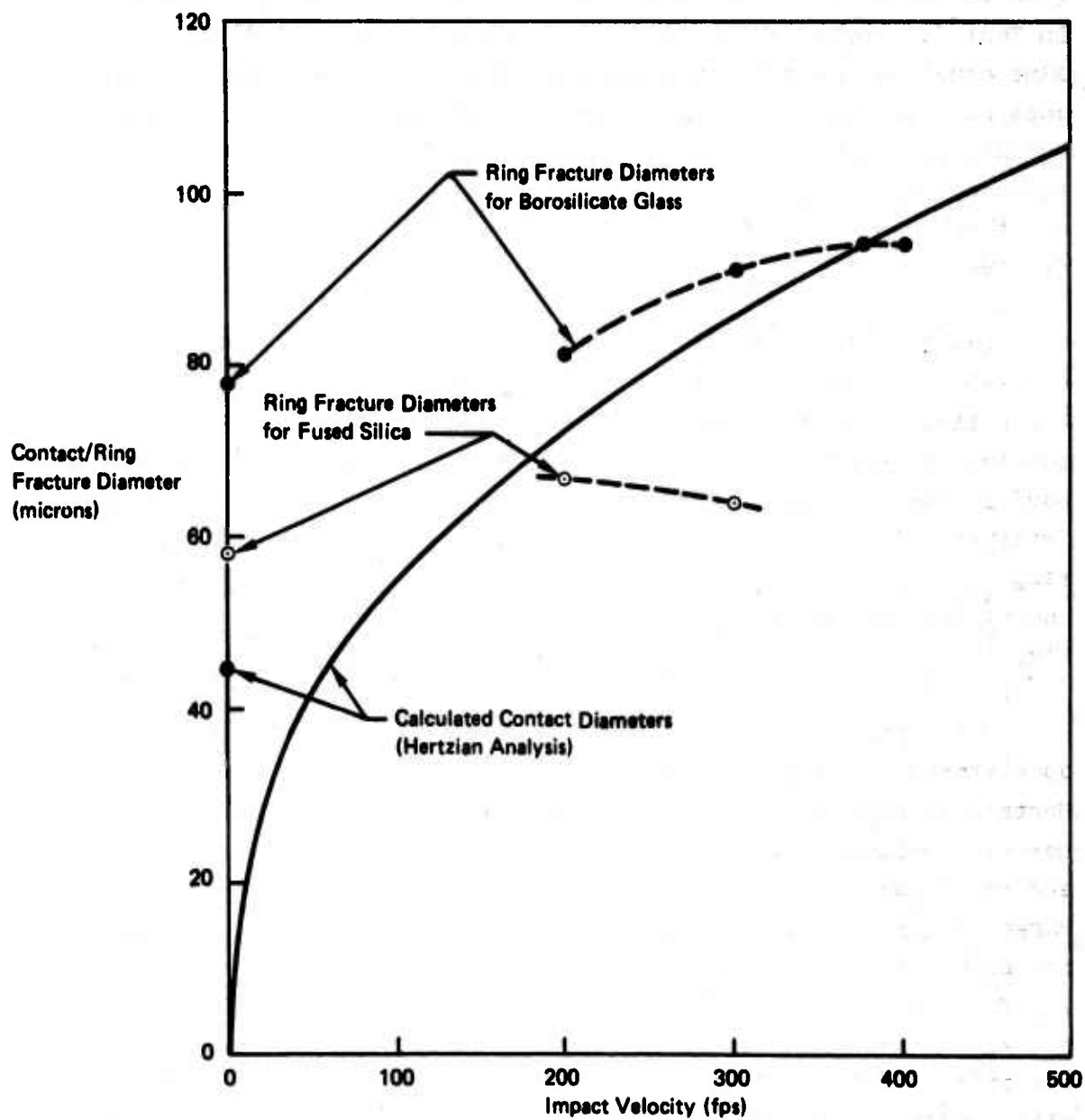


Figure 153. Static and Dynamic Ring Fracture Diameters due to 290-micron Glass Bead in Borosilicate Glass and Fused Silica



slightly beyond the maximum contact radius computed from the Hertzian analysis and a tendency for multiple ring fracture formation is beginning to occur in the borosilicate glass at 400 fps. The creation of multiple ring fractures implies that the transient stresses generated at an intermediate stage of the compression phase of the impact are sufficient to initiate ring fractures. Additional ring fractures are produced as a larger area reaches the critical stress level. The process stops when the maximum contact area is reached where it is still possible for a crack to develop just outside this region before the critical stress level decreases as the applied load subsides.

Results from indentation tests by other investigators<sup>(74)</sup> using spherical tungsten carbide indenters with diameters from 0.80 to 12.68 mm on soda-lime glass revealed radial cracking was initiated after the critical load was reached for cone formation. Radial cracking occurred for the smallest indenters with a diameter of 0.80 mm at loads only slightly in excess of the critical value for cone fracture initiation. The same tendency has been observed by Tsai and Kolsky<sup>(75)</sup> at loads several times the threshold values for 25.4 mm diameter steel balls impacting glass plates. Lawn, et.al.<sup>(74)</sup> pointed out that the observed radial crack patterns were more typical of pointed indenters. It was suggested that at suitably high loads small spheres are capable of producing irreversible flow in the material and of penetrating the surface. These effects are aided by the fact that the expanding contact area tends to encompass the surface trace of the cone crack at higher loads and suppress further cone extension.

The tendency for radial cracking is not evident in the indentation tests carried out at Bell even when the applied load was raised to several times the critical fracture load. Radial cracking was also not observed in the dynamic impact tests for small glass beads impacting glass plates. This difference in the Bell data and that of Lawn, et.al.<sup>(74)</sup> is difficult to explain, especially in view of the analysis and experimental

evidence provided by Johnson, et.al.(73) that the fracture stress for glass plates is considerably higher for steel indenters than for glass indenters.

## VI. SUMMARY

The spatial and temporal distributions of the transient stresses generated in elastically-deformable bodies with the elastic properties of zinc selenide, polymethylmethacrylate, and soda lime glass have been evaluated for an idealized representation of a liquid drop impacting a plane surface. The origin and extent of the damage due to a single drop impact on these materials, while not completely understood mechanistically, are beginning to become evident and the appropriate relations established with the mechanical properties using the calculated stress distributions. The development of regions of significant tensile stresses within the target material is clearly shown. Calculations for both the static and dynamic stress distributions for the equivalent impact conditions indicate that the dynamic tensile stresses are considerably higher than the static stresses in the region near the surface outside the contact area. The transient stress evaluations also provide a more accurate representation of the critical tensile stresses and the attenuation of the direct compression pulse propagating through the specimen in terms of the applied pressure than the simple one-dimensional analyses which have been used for this purpose.

The analytical approach used has its inherent shortcomings which include the lack of obtaining the stresses at the surface in the vicinity of the Rayleigh wave front and the fact that it is only applicable to the earliest stages of the impact event before lateral outflow dominates. However it does appear that the period of the collision covered by the analysis is where the damage within the material originates, and the evaluation of the stresses by this procedure is economical when compared with the finite difference schemes currently being developed by others. In general the idealized model reasonably approximates the results from the numerical analyses with regard to the water drop shape profile in the initial stage of the impact when the compressibility of the water in the drop is most significant.



The erosion mechanism evaluations based on the experimental data obtained during this funding period is summarized below. The information provided is a condensation of the more detailed account of the microscopic observations presented in Section III.

Rain erosion of CVD zinc selenide at 695 fps produced ring cracks at the surface which then propagated into the interior along conical paths. Subsequent impacts produced subsurface damage more rapidly than surface damage; the ring centers resisted the further introduction of damage but the lateral outflow phase of the drop collision produced chipping at the exterior edges of the circumferential cracks. Continued exposure to the rainfield ultimately produced an array of overlapping ring cracks, pitting within the enlarged circumferential cracks, and a random distribution of nicks, cracks, and small cavities. Concurrently, the conical subsurface fractures were extended deeply into the interior of the specimen and a complex system of subsurface fractures evolved. Fracture proceeded via cleavage on {110} planes: the characteristic mechanism of bulk fracture.

Exposure of CVD zinc sulfide to the rainfield at 695 fps produced significantly less damage than that observed on the CVD zinc selenide at twice the exposure time. Surface damage consisted of incomplete arrays of fine circumferential cracks together with small isolated pits. Surface cracks were composed of very short segments with frequent discontinuities suggesting the critical fracture stress to be comparable to the impact tensile stresses. The density and dimension of subsurface fractures were also smaller, consisting of conical segments which interacted less effectively with transmitted illumination. Fracture in this system was also along {110} cleavage planes; however, in this system a fraction of the subsurface fractures originated at subsurface sites.

Rainfield exposure of the hot-pressed zinc sulfide at 730 fps produced a greater number of ring crack structures of larger dimension than found in the CVD zinc sulfide. These could be

readily discerned by the unaided eye with transmitted light. The surface cracks were composed of a discontinuous series of fine pits suggesting grain ejection such that the grain loss was proportional to the subsurface fracture dimension. Associated conical subsurface fractures penetrated deeply into the interior. A fraction of the smaller subsurface fractures also appeared to initiate at subsurface sites. Surface cavities in this system were initiated both within the circumferential crack arrays and at isolated locations. These cavities rapidly enlarged during subsequent rainfield exposure. The surrounding material was damaged as incoming drops struck cavity wall protruberances and penetrated cavity wall cracks to impose hydraulic loadings. Further impacts readily dislodged and removed this weakened material. Fracture propagation occurred by intergranular separation.

Arsenic trisulfide glass was almost instantly demolished upon rainfield exposure at 730 fps. Short duration exposures at 500 fps produced moderate surface damage but extensive subsurface damage. This latter damage measurably degraded the optical transmittance and caused bulk fracture. Optical degradation was primarily associated with extensive subsurface fracture which developed upon subsequent drop impacts at sites along the outer perimeter of the ring crack patterns. Loss of structural strength resulted from the penetration of isolated fractures over macroscopic distances into the specimen interior. Both well-defined ring crack structures and random arrays of disjointed cracks were distributed over the eroded surface. Residual polishing scratches were preferentially attacked, yielding large and damaging fractures upon initial impact. Fractures propagated by the conchoidal mechanism characteristic of glasses and glassy polymers. Hydraulic loadings were particularly effective in this glass due to the combination of low fracture stress, hardness, and elastic modulus which facilitated water penetration into exposed cracks.

Damage initiation in the polygranular and single crystal germanium system proceeded via cleavage fracture along {111} surfaces and formation of compact crack arrays. Fractures preferentially propagated along the scratches when aligned tangential to the transient tensile stresses; in contrast cleavage fractures with this alignment preferentially initiated along the length of scratches oriented at large angles to this direction. A maximum of two successive impacts were required to produce discernable damage. Continued rainfield exposure rapidly covered the specimen with a pattern of cleavage fractures. Pit formation was initiated by subsequent lateral outflow impacts against the cleaved surfaces. Further exposure resulted in larger cavities produced by growth of the cleavage pits and also formation of isolated conchoidal fractures. During the final stage before measurable mass loss, both mass loss and transmittance degradation resulted primarily from the rapid growth of cavities to macroscopic dimensions.

Sapphire and spinel effectively resisted rain exposure at 730 fps; only slow removal of flowed material from polishing defects was observed. Prolonged exposure at 845 fps opened polishing digs and gradually introduced a distribution of fine pits and subsurface fractures with dimensions less than  $2\mu\text{m}$ . Such damage negligibly influenced the specimen properties so that these materials were far more resistant than the other materials evaluated in this program.

Borosilicate glass underwent the most rapid erosion of the oxide-based glasses at 730 fps. Exposure to several sequential impacts (perhaps 4-5) produced partial ring crack structures and random crack arrays whose associated subsurface fractures penetrated macroscopic distances into the interior. Fewer impacts produced less densely distributed surface cracks of shallow depth which propagated along jogged and forked paths. Etching revealed an additional dense distribution of isolated, minute flaws. Continued rainfield exposures caused the surface crack arrays to quickly link-up: first into interlocking two-dimensional



networks which covered the surface and then extended into the interior producing three-dimensional fracture networks. At this stage macroscopic cavity formation accelerated as drop impacts dislodged undercut fragments and exposed the weakened interior surfaces to direct impacts.

Soda lime glass generally required several sequential impacts to produce detectable damage. Initial damage consisted of isolated surface relief fractures and sealed microscopic cracks. Macroscopic fractures and ring fracture segments were not formed in this system. Continued exposure produced microscopic surface cracks which linearly propagated along jogged and forked paths. Jogs and forks provided preferential sites for surface relief fractures and angular-walled cavities. Concurrently, existing surface relief fractures were enlarged by formation of adjacent surface relief fractures and subsurface fractures below the original structure. Subsequent impacts upon the enlarged surface cavities produced radial cracks which propagated into the surrounding material. Exposure of scratches preferentially initiated surface relief fractures at the scratch roots and also cavity formation at the acute angles formed by intersecting scratches. Exposure of a specimen polished with hydrofluoric acid yielded only a limited retardation in damage formation. The most effective source for damage initiation and propagation appeared to be a microscopically non-discernible network of minute, sealed flaws produced by prior impacts.

After longer rainfield exposures an interlocking two-dimensional network of microscopic cracks with shallow depths covered the surface. This completed the incubation period for mass loss since further exposure developed a three-dimensional fracture network and microscopic fragments were dislodged from the surface. Although mass loss occurred by the same mechanism as for borosilicate glass, exposure durations for soda lime glass for both the incubation period and for a selected mass loss were more than doubled since the fracture propagation distances per impact and the dislodged fragment volumes were significantly smaller.

Thermally tempered soda lime glass exposed to the standard rainfield established it to be more resistant than the conventional soda lime glass. The exposure durations required to attain a selected mass loss were more than doubled relative to conventional soda lime glass but the mechanistic sequence for forming an interlocking three-dimensional crack network for mass loss remained the same. The residual compressive stress both reduced the mean crack propagation length and resealed previously formed cracks. The resultant cracks were finely structured, containing a high density of jogs and forks, but not contributing significantly to optical degradation. Structural integrity was also conserved over a significantly longer time period and bulk fracture required penetration through the zone of compression. Lateral outflow impact contributed proportionately more to the erosion process in the thermally tempered glass than in the borosilicate and the soda lime glasses.

The ion-exchanged strengthened glass and the calcium aluminosilicate glass responded similarly to rainfield exposures at 730 fps for relatively short durations. Investigations by other workers have established their resistance to macroscopic erosion to be comparable to or greater than that of the best thermally tempered glass. In contrast to the other oxide-based glasses, drop impacts produced only isolated damage with little tendency for extension and link-up of surface cracks and for subsurface fracture initiation. The most prominent early damage was surface relief fractures, however cracks, nicks, and compact crack arrays (discontinuous) were also observed. The rate of damage appeared to decrease with continued exposure suggesting that a number of sequential impacts were required to produce flaws of critical dimension at sites initially devoid of such flaws. In contrast to the fine surface cracks formed in the thermally tempered glass, surface cracks in these glass systems were coarser and not as effectively sealed but instead propagated over very short distances without evidence of jogs or forks.

Initial exposure of polysulfone to the standard rainfield produced some complete ring structures whose perimeters contained annuli of surface ripples together with a higher density of fragmentary ripple patterns. Continued rainfield exposure produced a uniformly rippled surface together with shallow microscopic craters. At this stage substantial optical degradation was observed indicating that the rippled structure efficiently scattered visible wavelengths. Further rainfield exposure resulted in cavity and crevice formation due to the concerted action of the imposed impact stresses and surface strain hardening. Residual scratches were preferentially eroded, localized cavities initiated along fine scratches, and coarser scratches enlarged into crevices. Initial mass loss resulted from hydraulic uplifting of small undercut fragments (analogous to the glass surface relief fractures). Further rainfield exposures preferentially enlarged the crevices, particularly the enlarged scratches, forming fracture surfaces extending deeply into the interior. Removal of larger fragments ranging up to macroscopic dimensions occurred between closely spaced cracks and crevices and at sites of crack intersections.

Both uncoated and melamine-coated polycarbonate underwent similar rain erosion behavior at 730 fps. The initial exposures produced small patches of shallow ripples and microscopic craters, indicating less ductility than polysulfone. The more brittle character resulted in a number of concurrent deformation modes with continued rainfield exposure: surface cracks in microscopic craters, shallow conchoidal fractures, linear crevice networks, and vertical conchoidal fractures. Preferential scratch fracture and enlargement were less important. Further exposure produced crevice enlargement and scratch extension through the hydraulic penetration mechanism. Mass loss occurred by the same process described for polysulfone at approximately the same rate. The melamine coating inhibited the initial ductile deformation but exerted only a minor influence on subsequent fracture and crevice formation.



Exposure of nylon to the rainfield at 730 fps initially produced arc-shaped regions of shallow damage composed of surface wrinkling, fine microcracks, and irregular cleavage. These regions appeared to be responsible for early exposure transmission losses. However, very deep fractures of near normal orientation formed exclusively beneath residual scratches. Continued rainfield exposure extended and enlarged these fractures to form a three-dimensional network of intersecting cracks and crevices. Subsequent impacts produced mass loss as undercut surface fragments were uplifted by the imposed hydraulic loadings applied to the internal surfaces.

Water drop impacts on polymethylmethacrylate produced well-defined ring cracks with each impact. The fracture annuli were composed primarily of dense arrays of fine, short cracks together with a sparse distribution of deeper fractures initiated along residual scratches. Pits formed on the exterior edges of a few of the circumferential crack segments during the initial impact. Continued exposures produced complex arrays of intersecting surface cracks at sites of fracture annuli overlaps together with dramatic enlargement of scratch initiated fractures. Subsequent hydraulic penetration into these regions led first to rapid crevice growth together with fine fragment loss followed by formation of cavities and intersecting fracture networks. Ultimately, the original ring crack patterns were obscured as the surface was covered with crevices and growing cavities. An extensive network of subsurface fractures continued to be produced within the expanding cavities.

The response of borosilicate glass to rainfield exposures (1.8 mm drop diameter) was determined as a function of impact velocity:

- 300 fps - negligible damage
- 400 fps - sparse distribution of small fractures and pits
- 500 fps - uniform distribution of small fractures together with growth of three-dimensional fracture networks and cavities at some sites

- 600 fps - uniform distribution of three-dimensional fracture networks and cavities formed by small segments of ring crack structures
- 730 fps - rapid growth of macroscopic three-dimensional fracture networks and cavities formed by large segments of ring crack structures

This velocity sequence can be generalized to correspond to the drop impact damage behavior observed for the inorganic materials and glasses considered here. At 500 fps arsenic trisulfide underwent formation of incomplete and complete ring crack patterns during the initial impact and each subsequent impact extended subsurface fractures over macroscopic distances. At 730 fps concurrent central subsurface damage and radial cracks would be anticipated. The CVD zinc selenide, displaying the next lowest erosion resistance underwent formation of complete and incomplete ring crack structures during the initial or the first two sequential impacts at 730 fps. Hot-pressed zinc sulfide and borosilicate glass underwent formation of ring crack segments spanning less than  $180^\circ$  during the initial impacts. Several sequential impacts were required to complete the ring geometry and propagate subsurface fractures to macroscopic depths. The CVD zinc sulfide underwent a similar erosion morphology but the impact event was less damaging, propagating fractures over shorter distances.

Germanium resisted the formation of ring crack structures at 730 fps; instead only microscopic cleavage and conchoidal fractures were formed by the first two sequential impacts. Soda lime glass and tempered soda lime glass initially underwent only microscopic surface relief fractures and a number of sequential impacts were required to initiate and propagate cracks along the surface and into the interior. Calcium aluminosilicate and ion-exchanged glasses effectively isolated the early stage damage yielding only individual damage sites spanning less than  $100\mu\text{m}$ . Spinel and sapphire resisted early stage damage entirely at 730 fps.

## VII. CONCLUSIONS

The fractures in the inorganic materials and glasses produced by multiple water drop impacts were found to propagate by the same mechanisms as observed for quasistatic loadings. The relative ranking of the erosion resistance of the glasses was found to show a correlation with the fracture loads determined from spherical indenter evaluations. However the deformation and fracture of the organic polymers exposed to the rain environment could not be readily related to the available mechanical properties. For all material classes the observed erosion modes and rates depended sensitively upon the drop diameters, impact velocity, material fabrication, and surface preparation.

A correlation has been suggested in which the incubation time for mass loss was an exponential function of microhardness.<sup>(52)</sup> It is surprising that a property which requires the extensive development of internal fractures should respond sensitively to microplasticity. The erosion rates for the important materials, magnesium oxide, silicon, and spinel (our data) all deviate significantly from Hoff and Rieger's function<sup>(52)</sup> and these deviations would be anticipated if the erosion is assumed instead to be primarily a function of fracture strength and crystallographic response. Furthermore, the rate of optical degradation, the primary property of interest, was not simply proportional to this incubation period and weaker materials could undergo bulk fracture from isolated crack propagation before the incubation period was completed.

Engineering designs should be based upon the degradation rate of the property such as optical transmission or fracture propagation together with an appreciation of the material response to the drop impact event. For example, CVD zinc sulfide has a microhardness which is less than one-half that of germanium but underwent rain erosion at a significantly slower rate than germanium based on comparisons with hot-pressed zinc sulfide. However, reported fracture thresholds for bend bar failure of these materials are similar. Furthermore, initiation and propagation



of cavities on the germanium surface is more rapid than on the zinc sulfide surface. Initial impacts on the germanium surface produce primarily cleavage fractures with uplifted edges whereas initial impacts on the CVD zinc sulfide produce primarily sealed surface cracks and conical sectors of subsurface fractures. Consequently, the lateral outflow impact and subsequently the hydraulic penetration mechanisms effectively enlarge the surface openings and initiate pits along the cleavage traces (especially at the cleavage intersections) of germanium. The same mechanisms inefficiently interact in zinc sulfide for which most of the fracture propagation during subsequent exposure occurs within the substrate. Since cavity wall erosion is particularly effective, both the density and dimension of cavities increase rapidly to produce the more rapid optical and structural degradation observed in germanium. A similar discrepancy is predicted for the rates of rain erosion of silicon and spinel which have comparable microhardnesses.

Calcium aluminosilicate and ion exchanged glasses, spinel, and sapphire all effectively resisted fracture propagation for the imposed water drop impacts. The two glasses responded similarly to a moderate erosion exposure undergoing a distribution of isolated surface relief fractures, surface cracks and nicks. Prolonged exposure at 850 fps gradually introduced a fine array of minute pits and subsurface facets in spinel and sapphire but these materials would resist mechanical and optical degradation for perhaps an order of magnitude longer than the other materials.

The initial response of the plastics varied significantly ranging from the annuli of surface ripples produced in polysulfone to the annuli of dense crazes produced in polymethylmethacrylate. Low damage thresholds for both ductile and brittle deformation were deleterious since both plastics underwent total opacity for moderate exposure durations. Unlike the inorganic materials, crevice formation due to hydraulic stress enlargement of fractures was more important than simple conchoidal

fracture or direct cavity formation. Exposure to the rainfield first initiated fractures (the polysulfone underwent plastic deformations which then nucleated fractures) which were extended and enlarged to produce a coarse network of crevices. All of the polymer materials were scratch sensitive, resulting in deeper, isolated fractures at these sites. In the final stage, mass loss occurred as undercut fragments were dislodged.

The following general picture of the rain erosion process emerges from the mechanism studies. In materials of low and moderate strength, the initial water drop impacts under the standard conditions employed here (730 fps and 1.8 mm drop diameter) produced a circular damage pattern analogous to that predicted by the Hertzian model. A central zone which resisted damage was surrounded by an annular zone of crack segments in brittle materials and surface ripples in polysulfone. In brittle materials, the cracks apparently formed a surface step which faced toward the impact center since preferential pit initiation was produced on the exterior edge by tangential water flow during drop collapse. Circular patterns were formed for low fracture strength materials such as arsenic trisulfide glass and polymethylmethacrylate plastic whereas increasing fracture strengths for zinc selenide and zinc sulfide were associated with reduced damage dimensions and increased erosion resistance. Preferential fracture propagation at surface scratches depended inversely upon the fracture strength such that very large, deeply penetrating fractures formed in arsenic trisulfide glass at scratch sites. For the oxide-based glasses, a similar association was obtained with microspherical indenter fracture thresholds. Germanium and soda lime glass did not undergo ring formation but conformed to the same erosion sequence in which fractures were initially introduced by transient radial stresses and then lateral outflow impact against surface discontinuities. The latter mechanism was most important for materials whose crack openings left discontinuities such as cleavage in germanium. Subsequent impacts produced an interlocking network of surface fractures which propagated into the interior. Concurrently,

cavities initiated and propagated as undercut fragments were dislodged by subsequent impacts, critical flaw sites were directly impacted, and lateral outflow continued. These processes produced fracture misregistration so that the water penetrated into the crack networks and cavity wall structures producing large hydraulic stresses which dominated subsequent fracture propagation. Consequently, the establishment of a three-dimensional network completed the incubation period for mass loss (extrapolated from the constant erosion rate stage) so that subsequent impacts dislodged exposed surface fragments and further extended the crack network into the interior. However, optical degradation depended both on the crack network and upon the cavity content, while the bulk strength depended upon the anomalous propagation of isolated fractures so that neither property of interest could be simply related to the incubation period. Instead these properties depended upon the crack initiation, crack propagation length per impact (fracture strength), material substructure, surface preparation, etc. so that a simple lifetime estimate was not reliable.



## VIII. RECOMMENDATIONS

Although the limited test data prevented a fundamental understanding of the material response to the drop impact event, some preliminary suggestions for increasing subsonic and low supersonic erosion resistance can be derived from the work completed. Obviously, more resistant materials can be selected. When cost considerations permit, oxides such as magnesium oxide, sapphire, and spinel at wavelengths less than  $5\mu\text{m}$  should be acceptable. Other possible candidates for this wavelength range include calcium fluoride, magnesium fluoride, silicon, and zinc sulfide. For shorter wavelengths the oxide-based glasses are particularly attractive since they are less expensive and more readily procured. However, a surprising range of erosion resistance was observed. Note that two glasses of primary interest, borosilicate compositions and fused silica, underwent rapid erosion. Calcium aluminosilicate glass and strengthened formulations were more resistant.

The plastic data were not clearly defined due to the intrinsic complexity of the mechanical response of these materials and the tendency to modify the basic polymer with additives. However, nylon and polycarbonate underwent the slowest rate of optical degradation, resisting the catastrophic onset of opacity observed for polysulfone and polymethylmethacrylate (the former responding primarily as a ductile material and the latter responding primarily as a brittle material). Consequently, some intermediate mechanical response would appear to be the optimal condition.

It became clear even from the limited test data available that simple material fabrication and preparation procedures can substantially improve their erosion resistance. A good surface polish which minimizes residual scratches will significantly impede the initiation of erosion damage in the lower strength materials. A good chemical polishing cycle which eliminated defects without chemically leaching the surface would

certainly be desirable. This is particularly important for the low strength materials when one or two sequential impacts can produce a critical flaw. A surface treatment which introduces a residual compressive stress appears to be very effective in reducing the erosion rate during all stages of erosion. The inexpensive and simple thermal tempering process is recommended for all applications which can tolerate the inherent dimensional requirements. Similarly, a careful thermal anneal to minimize residual fabrication stresses can significantly reduce the erosion rate. Development of halide salts for optical elements have shown solid solution doping, fusion casting, and forging procedures can dramatically improve the fracture resistance for these materials. These improvements are anticipated to also significantly improve the erosion resistance. Etching the surface to remove flaws and hot-pressing materials can improve material strength; however, the effect on erosion resistance and optical scattering can be deleterious unless carefully optimized and controlled.

Materials of low fracture thresholds and materials which tend to deform leaving sudden discontinuities in surface profile, such as polymethylmethacrylate and germanium can be covered with thin layers to diminish the influence of lateral outflow. For example, a substantial reduction in the rate of cleavage formation and in the areal fraction of erosion craters were observed for a germanium specimen covered with an antireflective coating 1.5 $\mu$ m thick. An appreciable increase in the incubation period occurred for drop impacts at 695 fps. This improvement resulted because the coating shielded the germanium surface from direct impact, externally sealed the openings of surface flaws (Griffith defects), and reduced the abruptness of cleavage discontinuities at the surface. Obviously, such a coating would be necessary for materials which have measurable water solubilities or undergo stress corrosion effects in the presence of water.

In the 8-12 $\mu$ m range, there is no material currently available which possesses both good rain erosion resistance and also good infrared transmittance. For these materials, a compromise approach based upon layered structures may be the most effective means for achieving the desired levels of rain erosion resistance.



# REFERENCES

1. Morris, J. W., Jr., Mechanistic Investigation of Rain Erosion, AFML TR-69-287, Part II, September 1969.
2. Morris, J. W., Jr., and Wahl, N. E., Erosion Characteristics of Aerospace Materials, AFML TR-70-265, November 1970.
3. Adler, W. F., Morris, J. W. Jr., and Wahl, N. E., Supersonic Rain and Sand Erosion Research: Characterization and Development of Erosion Resistant Materials, AFML-TR-72-85, May 1972.
4. Adler, W. F., and Vyhna, R. F., "Rain Erosion of Ti-6Al-4V", paper presented at the Fourth International Conference on Rain Erosion and Associated Phenomena, Meersburg, West Germany, May 1974.
5. Adler, W. F. and Sha, G. T., Analytical Modeling of Subsonic Particle Erosion, AFML-TR-72-144, July 1972.
6. Adler, W. F., Analytical Modeling of Liquid and Solid Particle Erosion, AFML-TR-73-174, September 1973.
7. Adler, W. F., Analysis of Multiple Particle Impacts on Brittle Materials, AFML-TR-74-210, September, 1974.
8. Adler, W. F., "Erosion of Fused Silica by Glass Beads," Erosion, Wear, and Interfaces with Corrosion, ASTM STP 567, 294 (1974).
9. Peterson, F. B., "Some Considerations of Material Response Due to Liquid-Solid Impact," Trans. ASME, J. Basic Engineering, Paper No. 72-WA/FE-27.
10. Jenkins, D. C., and Booker, J. D., "The Impingement of Water Drops on a Surface Moving at High Speed," in Aerodynamic Capture of Particles, E. G. Richardson (editor) New York: Pergamon Press, 1960.
11. Bowden, F. P., and Brunton, J. H., "The Deformation of Solids by Liquid Impact At Supersonic Speeds," Proc. Roy. Soc. (London), A263, 433 (1961).
12. Bowden, F. P., and Field, J. E., "The Brittle Fracture of Solids by Liquid Impact, by Solid Impact, and by Shock," Proc. Roy. Soc. (London), A282, 331 (1964).
13. Fyall, A. A., "Single Impact Studies with Liquids and Solids," Proc. Second Conference on Rain Erosion, Meersburg, West Germany, (August 1967).

14. Brunton, J. H. and Camus, J. J., "The Flow of a Liquid Drop During Impact," Proc. Third Int. Conf. on Rain Erosion and Associated Phenomena, Elvetham Hall, Hampshire, England.
15. Rochester, M. C. and Brunton, J. H., "The Influence of the Physical Properties of the Liquid on the Erosion of Solids," Paper presented at the ASTM Symposium on Erosion, Wear and Interface with Corrosion (June 1973).
16. Rochester, M. C. and Brunton, J. G., "Surface Pressure Distribution During Drop Impingement", Paper presented at the Fourth International Conference on Rain Erosion and Associated Phenomena, Meersburg, West Germany, (May, 1974).
17. Field, J. E., Camus, J. J., Gorham, D. A., and Rickerby, D. G., "Impact Damage Produced by Large Water Drops," Paper presented at the Fourth International Conference on Rain Erosion and Associated Phenomena, Meersburg, West Germany, (May, 1974).
18. Huang, Y.C., "Numerical Studies of Unsteady, Two-Dimensional Liquid Impact Phenomena", PhD Dissertation, Department of Mechanical Engineering, University of Michigan (1971).
19. Engle, O. G., "Waterdrop Collisions with Solid Surfaces," J. Res. Nat. Bur. Stand., 54, 281 (1955).
20. Heymann, F. J., "High-Speed Impact Between a Liquid Drop and a Solid Surface," J. Appl. Phys., 40, 5113, (1969).
21. Huang, Y. C., "Three Stage Impact Process in Liquid Impingement", Paper presented at the Fourth International Conference on Rain Erosion and Associated Phenomena, Meersburg, West Germany, (May, 1974).
22. Hwang, J. B. G., "The Impact Between a Liquid Drop and an Elastic Half-Space," PhD Dissertation, Department of Mechanical Engineering, University of Michigan (1975).
23. Blowers, R. M., "On the Response of an Elastic Solid to Droplet Impact," J. Inst. Maths. Applics., 5, 167 (1969).
24. Kreyenhagen, K. N., personal communication.
25. Engel, O. G., "Damage Produced by High-Speed Liquid-Drop Impact," J. Appl. Phys., 44, 692 (1973).
26. Adler, W. F., Discussion of "Effects of Fatigue and Dynamic Recovery of Rain Erosion" by A. F. Conn and S. L. Rudy, ASTM STP 567, December 1974, pp. 261-269.
27. Rice, M. H. and Walsh, J. M., "Equation of State of Water to 250 Kilobars", J. Chem. Phys., 26, 824 (1957).

28. Hertz, H., "On the Contact of Elastic Solids", Miscellaneous Papers, London: MacMillan and Company, 1896; 142.
29. Huber, M. T., "Contribution to Theory of Contact of Elastic Solids," Ann. Phys., (Leipzig), 14, 153 (1904).
30. Love, A. E. H., "The Stress in a Semi-Infinite Solid by Pressure on Part of the Boundary," Trans. Royal Soc. (London) A288, 377 (1929).
31. Hertz, H., "On the Contact of Rigid Elastic Solids and on Hardness," Miscellaneous Papers, London: MacMillan and Company, 1896; p. 163.
32. Tsai, Y. M., "Dynamic Contact Stresses Produced by the Impact of An Axisymmetrical Projectile on an Elastic Half-Space," Int. J. Solids Structures, 7, 543 (1971).
33. Kinslow, R., Rain Impact Damage to Supersonic Radomes, Tennessee Technological University Report TTU-ES-74-3 (October, 1974).
34. Asay, J. R., Lamberson, D. L., and Guenther, A. H., "Pressure and Temperature Dependence of the Acoustic Velocities in Polymethylmethacrylate," J. Appl. Phys., 40, 1768 (1969).
35. Barker, L. M., and Hollenbach, R. E., "Shock-Wave Studies of PMMA, Fused Silica, and Sapphire," J. Appl. Phys., 41, 4208 (1970).
36. Schuler, K. W., "Propagation of Steady Shock Waves in Polymethyl Methacrylate," J. Mech. Phys. Solids, 18, 277 (1970).
37. Engel, O. G., "Mechanism of High-Speed Waterdrop Erosion of Methyl Methacrylate Plastic," Journal of Research of the National Bureau of Standards, 54, 51 (1955).
38. Walker, W. A., and Sternberg, H. M., "The Chapman-Jouguet Isentrope and the Underwater Shockwave Performance of Pentolite," The Fourth Symposium on Detonation, Naval Ordnance Laboratory, White Oak, Md., 12-15 October 1965, pp. 27-38.
39. Werwick, J. H., "Structure and Properties of Some Intermediate Phases," Physical Metallurgy (R. W. Cahn, Editor) New York: North-Holland, 1965.
40. Wolff, G. A., and Border, J. D., "Microcleavage, Bonding Character and Surface Treatment in Materials with Tetrahedral Coordination," Acta Cryst., 12, 313 (1959).
41. Pappis, J., "Chemical Vapor Deposition of IR Laser Window Materials," Conference on High Power Infrared Laser Window Materials, AFCRL-71-0592.



42. Freiman, S. W., et.al., "Influence of Microstructure on Crack Propagation in ZnSe," J. Am. Ceram. Soc., 58, 406 (1975).
43. Kulia, S. A. and Posen, H., "Texture Studies in ZnSe," Third Conference on High Power Infrared Laser Window Materials, Vol. II Materials, November 12-14, 1973, AFCRL-TR-74-0085 (II), 14 February 1974, Special Reports, No. 174
44. Dobson, C. D., "The Technology of Gallium Arsenide Lasers," Gallium Arsenide Lasers, (Gouch, C. H., Editor) New York: Wiley (1969).
45. Peterson, T. L., unpublished data.
46. Rice, R. W., et.al., "Fracture Mirror, Strength, Flaw Size Relations in Polycrystalline Ceramics," Am. Ceram. Soc. Bull., 53, 317 (1974).
47. Dakshinamourtry, S., and Preece, C. M., unpublished data.
48. Ferguson, W. J. and Rice, R. W., "Effect of Microstructure on the Ballistic Performance of Alumina," Materials Sci. Research (W. W. Kriegel and H. Palmour III, Editors), 5, 271, New York: Plenum Press (1971).
49. Katz, R. N. and Brantly, W. A. "Fractography of High Boron Ceramic Subjected to Ballistic Loading," Materials Science Research (W. W. Kriegel and H. Palmour III, Editors) 5, 271, New York: Plenum Press (1971).
50. Raytheon Product Brochure, July, 1975.
51. Pohanka, R. and Rice, R., "The Compressive Strength Behavior of CVD ZnSe," Fifth Laser Window Conference.
52. Hoff, G., and Reiger, H., "Rain Erosion of Infrared Transmitting Materials," Proc. Eleventh Symposium on Electromagnetic Windows, (N. E. Poulos and J. D. Walton, editors) (1972).
53. Mecholsky, J. J., Rice, R. W., and Freiman, S. W., "Prediction of Fracture Energy and Flaw Size in Glasses from Measurements of Mirror Size," J. Am. Ceram. Soc. 57, 440 (1974).
54. Johnson, O. W. and Gibbs, P., "Brittle Fracture of Germanium", Metallurgical Society Conferences, 20 (D.C. Drucker and J. J. Gilman, editors) New York: Gordon and Breach Science Publishers, 315 (1963).
55. Greenwood, J. H., "The Measurement of Fracture Speeds in Silicon and Germanium," Int. J. Frac. Mech., 8, 183 (1972).

56. Craig, J. V. and Pugh, E. N., "Fracture of Germanium at Room Temperature", Acta Met., 15, 1309 (1967).
57. Conrad, H., "Mechanical Behavior of Sapphire," J. Am. Ceram. Soc., 48, 195 (1965).
58. Hockey, B., "Plastic Deformation of Aluminum Oxide by Indentation and Abrasion," J. Am. Ceram. Soc., 54, 223 (1971).
59. Wiederhorn, S., "Fracture of Sapphire," J. Am. Ceram. Soc., 52, 435 (1969).
60. Field, J. E., "Stress Waves, Deformation, and Fracture Caused by Liquid Impact," Phil. Trans. Roy. Soc., A260, 86 (1966).
61. Doremus, R. H., Glass Science, New York: John Wiley and Sons, Inc., (1973).
62. Freiman, S. W., Personal Communication.
63. Schonert, et.al., "Influence of Temperature and Environment on Slow Crack Propagation in Glass," Fracture 1969, (P. L. Platt, editor) London, Chapman and Hall, (1969).
64. Mechanical Behavior of Materials, (McClintock, F. A. and Argon, A. A., Editors), Reading, Mass. Addison-Wesley Publishing Company, Inc., (1966).
65. Shand, E. C., et.al., Glass Engineering Handbook, New York: McGraw-Hill Book Co., Inc. (1958).
66. Shoemaker, A. F., "Strengthening of Glass and Glass Ceramics," Mechanical Engineering, 91, 30 (1969).
67. King, R. B., "Rain Erosion Part IX: An Assessment of Inorganic Non-Metallic Materials," Royal Aircraft Establishment Technical Report No. 69253, November (1969).
68. Lawn, B. R. and Wilshaw, T. R., "Indentation Fracture: Principles and Applications," J. Mat. Sci. (in press).
69. Ernsberger, F. M., "Properties of Glass Surfaces," Annual Review of Materials Science, 2, 529 (1972).
70. Holland, L., The Properties of Glass Surfaces, New York: John Wiley and Sons, Inc. (1964).
71. Schmitt, G. F., "Rain Droplet Erosion Mechanisms in Transparent Plastic Materials," presented at the Mechanical Failure Prevention Group Meeting on the Role of Cavitation and Erosion in Mechanical Failures, Boulder, Colorado, 31 October to 2 November (1973).

72. Wilshaw, T. R., "The Hertzian Fracture Test," J. Phys. D. Appl. Phys., 4, 1567 (1971).
73. Johnson, K. L., O'Connor, J. J. and Woodward, A. C., "The Effect of Indenter Elasticity on the Hertzian Fracture of Brittle Materials," Proc. Roy. Soc., A334, 95 (1973).
74. Lawn, B. R., Widerhorn, S. M., and Johnson, H. H., "Strength Degradation of Brittle Surfaces: Blunt Indenters", National Bureau of Standards preprint.
75. Tsai, Y. M., And Kolsky, H., "A Study of the Fracture Produced in Glass Blocks by Impact," J. Mech. Phys. Solids, 15, 263 (1967).



AD

BO14124

AUTHORITY:

AFWAL

1tr, 19 NOV 82

